Optical Flow Velocimetry : optimization, benchmarking and application to system identification, modelling and control of shear flows

Antonios Giannopoulos

ÉCOLE SUPERIEURE DE PHYSIQUE ET CHIMIE INDUSTRIELLE
SORBONNE UNIVERSITY

DOCTORAL THESIS

Optical Flow Velocimetry: optimization, benchmarking and application to system identification, modelling and control of shear flows

Author: *Antonios* GIANNOPOULOS

Thesis defended the 6_{th} of July 2021 in Paris, France. **Jury composition:**

Jean-Luc Aider	Director of Research	ESPCI Paris	**Supervisor**
Olivier Cadot	Professor	University of Liverpool	**Jury member**
Valérie Ferrand	Associate Professor	Université fédérale Toulouse Midi-Pyrénées	**Jury member**
Philippe Guibert	Professor	UPMC-Sorbonne University	**Jury member**
Nicolas Mazellier	Director of Research	University of Orleans	**Jury member**
Jacques Borée	Professor	ENSAM	**Reviewer**
Dimitrios Mathioulakis	Professor	National Technical University of Athens	**Reviewer**

"*It is the voice of life which calls us to come and learn.*"

(Inscription on bell in Hayes Hall Bell Tower, Buffalo, New York)

ÉCOLE SUPERIEURE DE PHYSIQUE ET CHIMIE INDUSTRIELLE
SORBONNE UNIVERSITY

Abstract

ESPCI Paris and Photon Lines

Doctor of Philosophy

Optical Flow Velocimetry: optimization, benchmarking and application to system identification, modelling and control of shear flows

by Antonios GIANNOPOULOS

An integrated and fruitful journey of an Optical Flow Velocimetry system in various fluid mechanics study cases is presented: From its development and benchmarking, to the application of its results in instability analysis, modelling, dynamics prediction and control of shear flows. Regarding development, the software (algorithm, Graphics User Interface) and hardware parts (camera, workstation, laser) part of the system are presented and discussed. Furthermore, the system is benchmarked on various experimental and synthetic fluidic datasets. We explore its spatial precision from simple step displacements test-cases, to synthetic homogeneous isotropic turbulence datasets and then grid-generated turbulence and finally a bluff body turbulent wake. After the advantages regarding spatial resolution and computational speed of the system comparing to other state-of-the-art velocimetry systems are presented, a novel pressure reconstruction method is described and validated using the global turbulent kinetic energy budget in the turbulent wake of a D-shaped body, resolving scales down to the sub-Kolmogorov range. Then, Optical Flow measurements are used for modelling and system identification of two experimental datasets: On one hand the forced Turbulent Boundary Layer of a flat plate and on the other the Backward-Facing Step flow, for a maximum $Re_h = 3090$. Modern data-driven methods are utilised for this purpose: a statistical learning approach and a Neural Network machine-learning approach. Last but not least, more light on the 3D instability of the Backward-Facing Step is shed as well, followed by a novel open-loop control strategy to reduce the volume of the recirculation bubble. Such a full exploitation of a velocimetry system shares crucial insight on the importance of experimental, non intrusive methods such as Optical Flow Velocimetry, in the study of complex flows; flows that are often extremely costly or impossible to resolve numerically.

ÉCOLE SUPERIEURE DE PHYSIQUE ET CHIMIE INDUSTRIELLE
SORBONNE UNIVERSITY

Abstract

ESPCI Paris and Photon Lines

Doctor of Philosophy

Optical Flow Velocimetry: optimization, benchmarking and application to system identification, modelling and control of shear flows

by Antonios GIANNOPOULOS

Un parcours intégré et fructueux d'un système de vélocimétrie à flux optique dans divers cas d'étude de la mécanique des fluides est présenté : Depuis son développement et son évaluation comparative, jusqu'à l'application de ses résultats dans l'analyse de l'instabilité, la modélisation, la prédiction de la dynamique et le contrôle des écoulements cisaillés. En ce qui concerne le développement, le logiciel (algorithme, interface utilisateur graphique) et les composants matériels (caméra, station de travail, laser) du système sont présentés et discutés. En outre, le système est évalué sur divers ensembles de données fluidiques expérimentales et synthétiques. Nous explorons sa précision spatiale à partir de cas tests de simples déplacements par paliers, d'ensembles de données synthétiques de turbulence isotrope homogène, puis de turbulence générée par grille et enfin d'un sillage turbulent d'un corps bluffant. Après avoir présenté les avantages du système en termes de résolution spatiale et de vitesse de calcul par rapport à d'autres systèmes de vélocimétrie de pointe, une nouvelle méthode de reconstruction de la pression est décrite et validée en utilisant le bilan global de l'énergie cinétique turbulente dans le sillage turbulent d'un corps en forme de D, en résolvant les échelles jusqu'au domaine sub-Kolmogorov. Ensuite, les mesures de flux optique sont utilisées pour la modélisation et l'identification du système de deux ensembles de données expérimentales : D'une part, la couche limite turbulente forcée d'une plaque plane et, d'autre part, l'écoulement de la marche descendante, pour un maximum de $Re_h = 3090$. Des méthodes modernes basées sur les données sont utilisées à cette fin : une approche d'apprentissage statistique et une approche d'apprentissage automatique par réseau neuronal. Enfin, l'instabilité tridimensionnelle de la marche descendante est également mise en lumière, suivie d'une nouvelle stratégie de contrôle en boucle ouverte visant à réduire le volume de la bulle de recirculation. Une telle exploitation complète d'un système de vélocimétrie nous donne un aperçu crucial de l'importance des méthodes expérimentales et non intrusives telles que la vélocimétrie optique dans l'étude des écoulements complexes, qui sont souvent extrêmement coûteux ou impossibles à résoudre numériquement.

Acknowledgements

I would like to thank my thesis advisor Dr. Jean-Luc Aider for his positive and open-minded supervision. I would also like to thank my parents Olga and Giorgos; without their support and influence regarding scientific thinking and valuing knowledge rather than a consumerist lifestyle i would not have been the person i am today. I would like to thank all the people close to me in the good and bad times during the thesis, particularly Sabrina, Pablo, Giannis, Nefeli, Carlo, Samantha, Luis, Lea, Alexis, Felipe, Emily. For the scientific discussions and comments i would also like to thank B.Semin, J.E. Wesfreid, Tao Liu, P. Fortrin, P. Chatelier, P. Petitjeans, P-Y. Passagia, N. Mazellier, Guy Cornejo Maceda, A. Avranas, J.-G.Inigo, D.Mathioulakis, Gaurav Prabhudesai, J.Laurent, T.Darnige and Luis Benetti Ramos. For the countless hours of scientific discussion and fruitful collaboration i would like to thank Pierre-Yves Passaggia.

Contents

List of Figures

List of Tables

List of Abbreviations

PIV	Particle Image Velocimetry
OF	Optical Flow
ANN	Artificial Neural Networks
CUDA	Compute Unified Device Architecture
CV	Control Volume
FTDANN	Focused Time Delay Artificial Neural Networks
FFT	Fast Fourier Transform
FTD	Focused Time Delay
GPU	Graphics Processing Unit
HIT	Homogeneous Isotropic Turbulence
LTI	Linear Time-Invariant
MSE	Mean Squared Error
MIMO	Multiple Input Multiple Output
RA	Recirculation Area
SI	System Identification
T-S	Tollmien-Schlichting
TBL	Turbulent Boundary Layer
POD	Proper Orthogonal Decomposition
PKE	Perturbation Kinetic Energy
2D-2C	2 Dimensions- 2 Components

Part I

Introduction

Purpose and scope of the thesis

The present thesis was carried out in laboratory of PMMH, ESPCI, in the context of the french industrial PhDs (CIFRE) under the organisation of the french National Technological Research Association (ANRT). The industrial partner was Photon Lines, a leading supplier of optical hardware and software solutions in France and the United Kingdom.

The thesis had a double goal: On the one hand, the goal was to develop and benchmark a fast, accurate, and integrated Particle Image Velocimetry (PIV) system, based on an Optical Flow (OF) algorithm. PIV is an important non-intrusive measurement methodology in order to obtain velocity fields using only images of a particular flow; it has been applied in the fluid mechanics research and industry since 40 years (Stanislas, Okamoto, and hler, 2003). By PIV system development we mean the development of the software and its harmonious and optimized functionality with the hardware components of a fast camera, a pulsating laser and an optimised workstation. For these reasons, the said system was benchmarked in various experimental and synthetic PIV datasets. Various image datasets from fluid experiments outside the PIV scope were also tested. We focused on all aspects of such a benchmarking study: PIV computational time, spatial resolution, disk space occupancy; characteristics which were compared with various other state-of-the-art cross-correlation PIV solutions. As part of this industrial collaboration between PMMH and Photon Lines, i have been an active member of the R&D team and participated in all the development phases of conception, software integration and debugging, hardware dimensionalisation, testing and final verification what is currently a PIV product soon to be launched by Photon Lines.

The second goal regarded the use of this system in fluid mechanics experiments of transitional and turbulent flows: particularly focusing on modelling, system identification and control. Transition to turbulence is an important phenomenon to understand, since many structures and dynamics that appear in the transitional regime continue to exist and have an important role in the turbulent regime (Sirovich, 1987). It can also give inspiring ideas on how to delay this transition, hence control optimally the studied turbulent flow. Understanding and controlling turbulent flows has thus great potential to reduce the devastating human environmental impact of the transportation industry, including ground vehicles, trains, ships and aeroplanes. Such studies, can play a definitive role in the reduction of CO_2 emissions as regulated recently in the European Union 2030 emission target plan EU-Council, 2014; Parliament and EU, 2013 and the 2050 climate neutral plan Parliament and EU, 2020; regulations will not have any environmental impact unless other countries, and particularly the commercial companions countries outside the European Union (that host a large part of its production lines), follow as well.

Thesis chronological unfolding

The thesis was conducted in the laboratory PMMH of ESPCI Paris, located in the Jussieu campus of the University of Pierre and Marie Curie, under the supervision of Professor Jean-Luc Aider, and the R&D department of Photon Lines SAS, under the supervision of managers Julien Romain and Eric Drean. Chronologically, the thesis lasted 3.5 years (6 months extra than the average PhD in France due to the Covid-19 crisis) and below can be found briefly the main landmarks: The first year consisted in gaining expertise in the OF velocimetry experiments in a hydrodynamic channel. A dynamic library, created in Microsoft Visual Studio and containing all the OF velocimetry functions was integrated in the software Eyemotion of See Fast Technologies (part of Photon Lines) in the form of a plugin. Eyemotion is a native code image acquisition software containing a large variety of built-in offline and online (during acquisition) image processing tools; image compression, binarisation, convolution, image cropping, Roberts/Sobel filter to name a few. It is compatible with a large variety of cameras (PCO, BASLER, Zylon, etc). A software development using OPENCV and Microsoft visual studio was used to integrate the OF tools in this platform. The Graphic User Interface (GUI) of the said PIV plugin was also designed for maximum functionality and user comfort. The first year also included the moving of the experimental setup of the lab from the campus of ESPCI to the campus of UMPC/Paris VI University. The setup consisted of a 3 meters long gravity-driven hydrodynamic channel. The process was long and complicated and lasted 3 months; the opportunity was used to improved the experimental setup. A new tower for the upper tank was constructed, improved flow straighteners were dimensionalised tested (home-made, industrial ones and 3D-printed at PMMH were tested); dimensioning and integrating a new smart and vibrationless pump was also achieved, together with positioning the channel on top of antivibratory plastic material to reduce vibrations. All these ameliorations lead to diminishing the turbulence intensity in the channel from $2-3\%$ to 0.7%. A parametric study was also conducted to obtain the optimal number of polyamid PIV particles in the hydrodynamic channel according to the measurement plane.

The second year consisted in the conception and implementation of two novel machine-learning studies for the dynamics prediction and order reduction of turbulent boundary layer and the backward facing step experiment conducted in the lab hydrodynamic channel, using the OF velocimetry. Such methods can be proved important in order to have fast diagnostic tools of system with complicated dynamics, using only local and simple accessible sensors. A transition to turbulence study was also conducted for the 3D instability of the BFS flow before testing various open-loop control strategies as well. The results were presented in various conferences and journal papers listed in the general conclusion section. A first working proof presentation of the real-time PIV system on a hydrodynamic channel experiment was presented in the presence of the CEO of Photon Lines SAS as well.

The third year we proceeded in the software and hardware optimization of the final PIV product: The choice of Workstation and further benchmarking of the algorithm was made, regarding turbulent spectra precision and pressure reconstruction. A pulsating laser synchronisation was tested successfully during image acquisition software that hosted the PIV algorithm as well. A final PIV system presentation was presented in July 2020. First client interest begun in April 2020, providing positive feedback. Since then we have processed and presented OF PIV results of image datasets of more than 6 potential industrial and academic

clients, and received positive feedback.

During all of three and a halfyears of the PhD program i followed the official schedule of the R&D team of Photon Lines SAS, taking part in monthly meetings and brainstorming sessions regarding the various products and activities of the team.

Thesis text structuring

The organisation of the present thesis unfolds in the following way: First, we start with the PIV algorithm description and its main parameters and speed performance comparing to Cross-Correlation PIV, followed by the integration of the algorithm in the software tools of Photon Lines. We then present benchmarking studies of the system regarding spatial resolution and turbulent spectra precision in various experimental and synthetic datasets. A pressure and acceleration reconstruction methodology using these Optical Flow measurements will be presented as well. The design of an online, real-time PIV system will be presented after. This is the first part of the thesis.

The second part consists of the presentation of the forced turbulent boundary layer flow and 2 data-driven approaches: a dynamic observer method to obtain a reduced-order model using statistical learning, as well as an artificial neural network (ANN) system identification approach to reduce the order of the system and reconstruct the velocity fields using local visual sensors.

In the third part, we will present the transition to turbulence of the Backward-Facing Step (BFS) flow, its Kelvin-Helmholtz instability as well as the 3D instability, using 2D-2C PIV. A novel open-loop approach to control will be presented as well, which successfully reduced the recirculation bubble volume size by 64%. A ANN method, similar to the one presented in chapter three, will be also applied in the same flow to reduce the order of the system and predict the dynamics using visual sensors placed right next to the step. Last but not least, general information regarding publications, courses and conferences attended will be presented, together with the final conclusions.

Part II

Optical Flow Velocimetry: Development and benchmarking

Chapter 1

PIV method introduction

Particle Image Velocimetry (PIV) has been widely used for almost 40 years in fluid dynamics research and the industry and carries a long history of techniques which have gradually improved over the years (Westerweel, 1993; Scarano and Riethmuller, 2012). A flow is seeded by tracer-particles of low Stokes number and it is illuminated with a laser sheet, as illustrated in figure 1.1. Digital PIV (DPIV) uses two separate images that record the displacement of particles in such a flow over a dozen pixels. This method has been used extensively and gave rise to different correlation methods to analyse these image pairs in order to obtain a snapshot of a vector fields in a plane from two instantaneous images. At this point, two methods stand out: On one hand, Particle Tracking Velocimetry (PTV) is traditionally used to analyse particle tracks from series of images where the tracks are used to obtain the velocity and acceleration from sparse particles in an images. On the other hand PIV uses Cross Correlation (CC) boxes to determine the mean displacement of particles from a correlation box based on a couple or more instantaneous images of the flow. While this approach is widely used in experimental fluid dynamics, different algorithms have been developed in order to calculate the correlation between two successive frames.

The most widely used strategy for PIV considers CC-based algorithms, where most are based on Fast Fourier Transform (FFT) to calculate the CC more efficiently than direct correlation. Such algorithms have been extensively used across the literature and have been adapted to a large range of flows. Despite its efficiency and high accuracy, FFT-based cross-correlation algorithms present a few drawbacks. First, the size of the correlation box does not evolve linearly with the number of pixels. In fact, because of the nature of the FFT, the length of the correlation box evolves as a powers of 2 and can hardly be adapted below 16 pixels. In the field of PIV, various CC PIV algorithms were used as benchmark and compared for various dataset during the 4 PIV challenges Stanislas, Okamoto, and Kahler, 2003; Stanislas et al., 2005; Stanislas et al., 2008; Kähler et al., 2016. In addition, Foucaut, Carlier, and Stanislas, 2004 showed that overlapping the correlation boxes beyond 50% did not improve the quality of the correlation, nor the accuracy of the gradients. In fact, the cut-off frequency is only dependent on the size of the correlation box and remains constant where wavenumbers greater than 2.8 times the size of the correlation box followed a top-hat filter which translates into a sinus cardinal in Fourier space. This bound is extremely important, and shows that in order to improve the accuracy of the correlation, one may either use very large images with a very dense seeding, or design a fast algorithm that can perform equivalently than direct correlation which does not suffer the curse of the box size. The same group recently showed that George and Stanislas, 2020 when PIV is used to measure turbulence, it can be treated as a time-dependent signal and hence the noise between different realisations and different interrogation volumes is statistically independent.

Optical Flow (OF) algorithms, first introduced in the machine vision field by Horn and Schunck, 1981, provided an interesting alternative to solve motion estimation problem. The

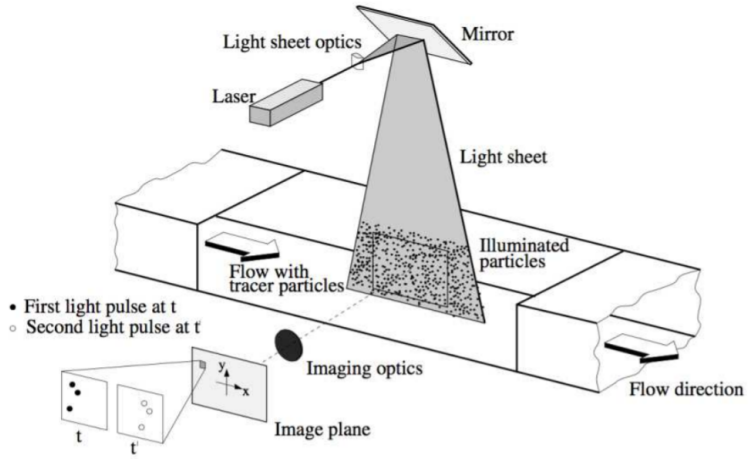

FIGURE 1.1: A classic 2D PIV experimental setup, as illustrated by Raffel, Willert, and Kompenhans, 1998.

estimation relies on finding the optimal $[u,v]$ to achieve the energy minimization of an objective function which consists of a data energy term (based on brightness conservation assumption) and a regularization energy term. Let $\mathbf{x} = (x,y)$ denote the position of a pixel in the two-dimensional domain Ω, where $\mathbf{x}\ \varepsilon\ R^2$ and ω (x) = (u,v) the velocity vector. Let $I(x,y)$ be the brightness function. The original Horn and Schunck (HS) method can be formulated as minimizing the quantity J in the full image domain Ω:

$$J(u,v) = \int_{\Omega} \left[(I_x u + I_y v + I_t)^2 + \lambda^2 \left(|\bigtriangledown u|^2 + |\bigtriangledown v|^2 \right) \right] dxdy \tag{1.1}$$

where $\bigtriangledown$ denotes the gradient operator in two dimensional directions and $\|\cdot\|$ the Euclidean norm, and λ a weighting parameters between two terms. The formula can be solved with calculus of variations. Their application in the field of PIV followed years after, with the studies of Quénot, Pakleza, and Kowalewski, 1998; Ruhnau et al., 2005 and have been since increasingly used in fluid mechanics laboratories (Gautier and Aider, 2013; Giannopoulos and Aider, 2020b). Even if such OF algorithms give dense velocity fields (one vector per pixel), it seems that their spatial resolution was no better than standard cross-correlation Fast-Fourier Transform (FFT) PIV algorithms, although ranked among the top 5 for various benchmarking tests in the so-called PIV challenges (Stanislas, Okamoto, and Kahler, 2003; Stanislas et al., 2005). Recently, Seong et al., 2019 showed that OF can be used additionally to improve cross-correlation PIV results. Turbulent data sets are an excellent case for the comparison of PIV algorithms: they contain high gradients, large velocity differences inside the same field, and are governed by universal laws for their relative spectra. Hence, they can be used for benchmark and further understanding the advantages and disadvantages of each algorithm. Very recently, machine learning algorithms have been also tested to perform PIV with promising expectations for the future of the community Rabault, Kolaas, and Jensen, 2017a; Dosovitskiy et al., 2015a; Cai et al., 2020. Moreover, Schmidt and Sutton, 2019; Schmidt and Sutton, 2020 proposed a wavelet-based OF method to improve the resolution and accuracy of standard Cross-Correlation PIV, which is somewhat close to windowing the correlation box but provides more flexibility on the sample size.

Different approaches using neural networks have been also recently coming to the foreground of the PIV community. They have a great potential since the number of easily accessible large datasets are getting larger and larger and the machine learning tools faster, optimized and freely distributed in toolboxes like PyTorch for Python (pytorch, 2021). A first proof of concept was presented by Rabault et al. (Rabault, Kolaas, and Jensen, 2017b), and after this multiple studies were followed with faster and more accurate results (J.Rabault et al., 2018; Dosovitskiy et al., 2015b). Moreover, an efficient optical-flow based PIV solution using deep learning was presented and made freely available under the name PIV-LiteFlowNet a year ago (Cai et al., 2019).

Chapter 2

Cross-Correlation-based PIV

The principle of CC for PIV regards in calculating the correlation matrix between successive images of particle-illuminated flows. The peak in the CC matrix gives the displacement vector, as seen in figure 2.1. The present section presents the error measurement strategy for the CC algorithm originally developed by Meunier & Leweke Meunier and Leweke, 2003a. This open source CC PIV software is called DPIVsoft (Meunier and Leweke, 2003b) ; it is a standard CC algorithm optimized for large velocity gradients. It is freely distributed for MATLAB and it will be used for the benchmarking comparisons of chapter 4.

In their original work, Meunier & Leweke analysed errors generated two-dimensional CC PIV algorithms (with window shifting), when high velocity gradients are present. In classical CC-based PIV, a first bias error is due to the difference between the Lagrangian displacement of a particle and the real velocity. This error has been calculated theoretically as a function of the velocity gradients, and is shown to reach values up to 1 pixel if only one window is translated (Meunier and Leweke, 2003a). However, it becomes negligible when both windows are shifted in a symmetric way. Meunier & Leweke also showed that a second error source is linked to the image pattern deformation, which decreases the height of the correlation peaks. In order to reduce this effect, the windows in DPIVSoft are deformed according to the velocity gradients in an iterative process (Meunier and Leweke, 2003a; Passaggia, Leweke, and Ehrenstein, 2012a; Camassa et al., 2018; Passaggia et al., 2020; Shanmughan et al., 2020). The problem of finding a sufficiently reliable starting point for the iteration is solved by applying a Gaussian filter to the images for the first correlation. The approach of Meunier & Leweke implemented in DPIVSoft thereby minimises the displacement error in an iterative manner, finding the optimal displacement and deformation for the correlation box. The results were found to recover the same accuracy than commercial software for still and moving images of particles.

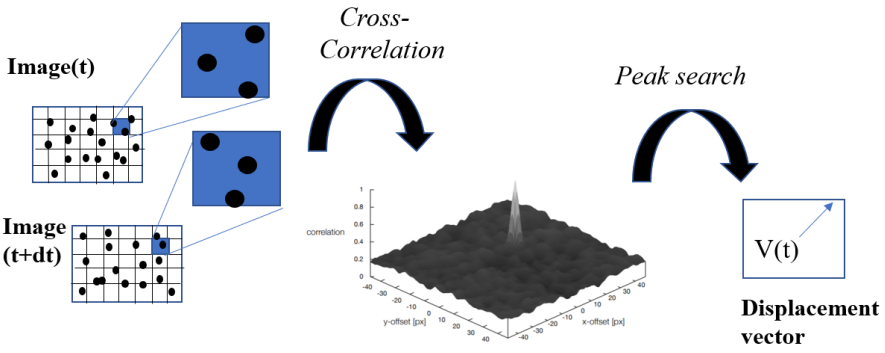

FIGURE 2.1: Sketch of the cross-correlation and peak-search process to estimate velocity vectors from a couple of successive images.

2.1 Parameter discussion : Correlation window size

The size of the correlation box is set by different parameters such as the particle size, particle density, and particle displacement Kähler, Scharnowski, and Cierpka, 2012. In the following benchmarking studies, we will analyse the effect of the box size with dimensions increasing with powers of 2, since the present CC is performed using Fast Fourier Transform (FFT) which requires samples with powers of 2 to improve its accuracy. Thereby, squares boxes with sizes 16, 32, and 64 pix^2 will be considered.

2.2 Parameter discussion : multiple pass and pyramid levels

The FFT-based CC implemented in DPIVSoft is performed in an iterative way over successive passes such that each iteration is performed not only once but iterated several times in order to converge towards optimal box displacements and optimal box shape modification (Meunier and Leweke, 2003b). Hence, at the end of each iteration, the displacement vector is stored and used as an update for the shapes and displacement of the correlation window. In practice, no more than 5 iterations were found to be necessary in order to converge correlations in each window. The second part of the iterative scheme deals with pyramid levels which are implemented in DPIVSoft in a multigrid manner. At first, boxes with size $4X$ (where X is the final size of the correlation box) are used for the cross correlation and iterated as discussed previously. Then, a second grid is considered (i.e. with size $2X$) which is twice smaller than the original grid and therefore gives rise to four times more vectors. An additional level is computed to reach the final box size X with up to 5 sub-iterations in order to obtain the final velocity field.

The next section addresses the second strategy analysed in this chapter, which uses the OF method. We will show later that both methods present different accuracy and robustness to unresolved measurements.

Chapter 3

Optical Flow for PIV

A variational OF method was first proposed by Horn and Schunck Horn and Schunck, 1981 to solve motion estimation problem. The estimation relied on finding the optimal displacement field $[u, v]$ to achieve the energy minimisation of an objective function which consists of an intensity energy term (based on brightness conservation assumption) and a regularisation energy term. Although firstly introduced in the field of machine vision, OF methods have been applied in the field of fluid mechanics as well; various OF algorithms were benchmarked multiple times in the 4 international PIV challenges (Stanislas, Okamoto, and Kahler, 2003; Stanislas et al., 2005; Stanislas et al., 2008; Kähler et al., 2016). Most of them were found of equivalent precision and spatial resolution with CC PIV algorithms for most of the benchmarks. Even a 3D PIV OF algorithm was benchmarked in such a 3D PIV challenge Kähler et al., 2016, giving a performance amongst the top 5 competitors.

Among other OF efforts tested on PIV applications, we mention that a hybrid CC-OF PIV method was presented by Liu et al., 2020b. Furthermore, Wang, He, and Wang, 2020 used a multi-pyramid-type scheme optimisation algorithm (used traditionally in OF) in order to globally minimise an objective function consisting of a CC term, a penalty term for smoothness and an empirical smoothing parameter. They thus obtained superior resolution results comparing with standard CC PIV and outperforming OF for small vortex resolution, but losing from OF for error analysis in particle concentration, particle image diameter, large displacements and image noise. CC PIV and OF have also been used as a benchmark for biological image dataset like in Vig, Hamby, and Wolgemuth, 2016. OF showed clear advantages in order to extract additional biophysical/chemical information such as local vorticity or net polymerisation rates from speckle microscopy. Last but not least, OF algorithms have been increasingly more applied in experimental machine learning control and system identification studies with quite satisfying results (Giannopoulos and Aider, 2020c; Giannopoulos and Aider, 2020a; Gautier and Aider, 2015b).

3.1 A dense Optical Flow PIV algorithm

The algorithm presented consists in a dense iterative Lukas-Kanade OF algorithm (Champagnat et al., 2011). It was developed at ONERA, and then optimized for the case of real time calculations at the laboratory of PMMH at ESPCI PARIS (Gautier and Aider, 2013). It is written in C++ language, implemented with CUDA C functions. This means that the core calculations of the algorithm are performed in the GPU and are optimally parallelized with the NVIDIA libraries that are freely distributed. The advantage of this algorithm compared to a standard FFT-PIV algorithm is its high computational speed when implemented with CUDA functions; it has been tested to be around 50 times faster than state-of-the-art PIV software (C.Pan et al., 2015; Champagnat et al., 2011). This algorithm was used by Davoust, Jacquin, and Leclaire, 2012; Sartor, Losfeld, and Bur, 2012 to fast post-process their snapshots for a turbulence jet flow study and for an investigation of the interaction between a shock wave and a turbulent boundary layer, respectively. The code has been used numerous

times both for time-resolved PIV measurements. A high spatial resolution was proven in various physics experiments by Varon et al., 2017 as well as for flow control experiments Gautier and Aider, 2013; Gautier, 2014; Gautier and Aider, 2015a; Varon et al., 2019. Another comparison Liu et al., 2015a showed superior performance for OF in comparison with CC PIV regarding spatial resolution.

The algorithmic core idea of OF consists in minimising a criterion containing the difference of intensities and gradients of intensities of 2 successive flow images. Mathematically, the most direct method to do this consists in the following: for each pixel m, we search the displacement $\boldsymbol{V}(\boldsymbol{m})$ that minimises the sum of square differences between the intensity field around m ,I^t, for time t and a second one for time $t^{'} = t + dt$ shifted by $\boldsymbol{V}(\boldsymbol{m})$,$I^{t^{'}}$:

$$\sum_{k \in \mathcal{N}(m)} \left(I^t(k) - I^{t^{'}}(k + V(m)) \right)^2 \tag{3.1}$$

,where $\mathcal{N}(m)$ is a square IW centered in pixel m and of size $2 * KR + 1$. KR is an acronym for the parameter Kernel Radius, as defined in figure 3.1. The estimated displacement at the iteration step $i, V_i(m)$, is thus calculated such as $V_i(m) \sim V(m)$. It is proven though that $V(m) \sim V(k)$ can be assumed at each pixel k inside the IW to ensure fast convergence (Le Besnerais and Champagnat, 2005). This assumption leads to the following equation:

$$\sum_{k \in \mathcal{N}(m)} \left(I^t(k) - I^{t^{'}}(k + V_i(k) + V(m) - V_i(k)) \right)^2 \tag{3.2}$$

A first order expansion around $k + V_i(k)$ of equation 3.2 leads to the form below:

$$\sum_{k \in \mathcal{N}(m)} \left(I^t(k) - I^{t^{'}}(k + \boldsymbol{V_i}(k)) - \nabla I^{t^{'}}(k + \boldsymbol{V_i}(k))^T \Delta \boldsymbol{V}(k) \right)^2 \tag{3.3}$$

We set the above expression to zero and define the operator H:

$$H = \sum_{k \in \mathcal{N}(m)} \nabla I^{t^{'}}(k + V_i) \cdot \nabla I^{t^{'}}(k + V_i)^T \tag{3.4}$$

where H is defined as the Gauss-Newton approximation of the Hessian. Now solving for the displacement V_m leads to the following expression:

$$\boldsymbol{V}(m) = \mathrm{H}^{-1} \sum_{k \in \mathcal{N}(m)} \nabla I^{t^{'}}(k + \boldsymbol{V_i}) \left(I^t(k) - I^{t^{'}}(k + \boldsymbol{V_i}) + \nabla I^{t^{'}}(k + \boldsymbol{V_i})^T \boldsymbol{V_i} \right) \tag{3.5}$$

The computed displacement $V(m)$ will then be used as a better estimation $V_{i+1}(m)$ at the next iteration until converging. We mention though that the integration on the IW $\mathcal{N}(m)$ in equation 3.5 is in fact replaced by a convolution function (or a Gaussian Blurring) over the whole snapshot, which implies that the IW is really warped instead of simply shifted. This method as it is though, can only resolve very small displacements, around $1-2$ pixels. To increase the maximum displacement a standard computational pyramid reduction scheme is implemented, particularly a Burt-Andelson one (Adelson et al., 1983). Going up one level in the pyramid means reducing the size of the image by 2 at each direction, as seen in figure 3.1. A better initial solution is calculated in the upper level, which is used to pass in the lower levels, always minimizing iteratively the criterion 3.5. This is continued until we reach the original image size. More pyramid levels help calculate larger displacements, with no upper theoretical limit in the displacement. Practically though for most datasets, the pyramid reduction method leads to a maximum displacement of up to 20 pixels. Hence, the

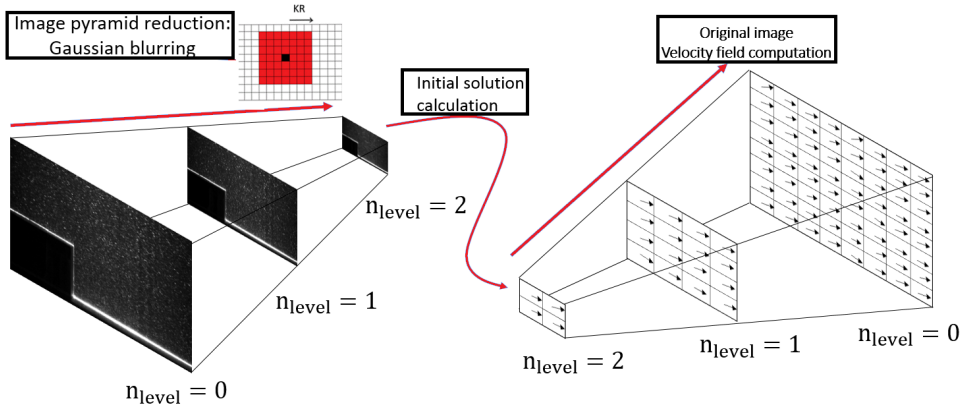

FIGURE 3.1: A Burt-Andelson pyramid reduction scheme that allows for a calculation of displacements up to 20 pixels. Kernel Radius definition.

3 main user parameters are the number of Gauss-Newton iterations to converge, the size of the interrogation window noted as KR and the number of pyramid levels.

Regarding the handling of the boundaries, OF suffers as every window-based algorithm the fact that particles move outside the picture frame. The solution used in OF relies on dynamic masks, which are updated at each iteration. Excluded pixels are either those whose current displacement vector is located outside of the image or those whose IW contains more than 80 of already excluded pixels. Displacement vectors are computed for the remaining pixels; the missing pixels are then filled with the nearest valid vectors before the next iteration.

The algorithm being in the OF family, can be used for type of experiments apart from PIV ones. Every image dataset of high contrast and distinct gradients (up to a limit of the maximum displacement of 20 pixels) can be used to calculate displacements. This fact has been tested for more than 15 datasets not coming from PIV experiments. In the example below, during a collaboration with the acoustofluidics team of PMMH (particularly L. Lebollon), the velocity of blood platelets was successfully measured in a microfluidic channel 3.2. In another example, during a collaboration with University of Paris Diderot (Professor Matthieu Labousse), we managed to calculate velocity fields of Liquid films emulsion, for the purpose of vortex detection. Results are presented in figure 3.3. In a third example in figure 3.4, we present velocity field measurements ombroscopy images of microjets (experiment from : J.L. Aider and J.-E. Wesfreid). Multiple client datasets coming from industry clients of Photon Lines were also processed to asses the algorithm; the results of which cannot be presented due to confidentiality reasons. The development of a complete PIV system using this algorithm was carried out during the present thesis. Such a development consisted in the software and hardware part design and testing as well as its rigorous benchmarking on challenging flows, results which will be presented in the sections below.

3.2 Parameter discussion : Kernel Radius

KR is defined in pixels and is the size of the Gaussian convolution window performed at each pixel, for each pyramid level. Larger values yield more smoothed-convoluted results, that are on the other hand more robust to noise and particle density variations. Smaller values may increase the spatial resolution but also the spatial noise of the measurement. It plays a secondary role in the computational time.

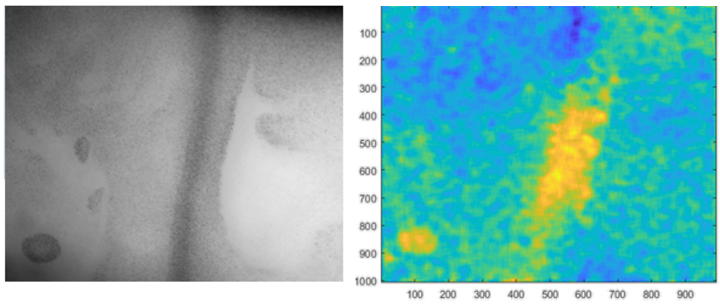

FIGURE 3.2: Blood platelets flow image (left) and velocity field calculation using OF (right). Experiment from: L.Bellebon, PMMH.

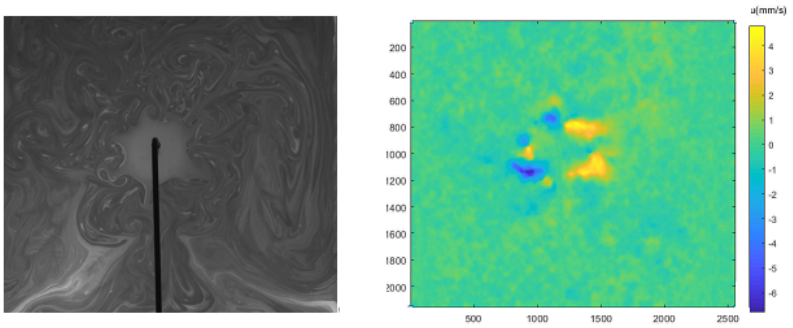

FIGURE 3.3: Liquid film emulsion experiment and corresponding velocity field calculation using OF.

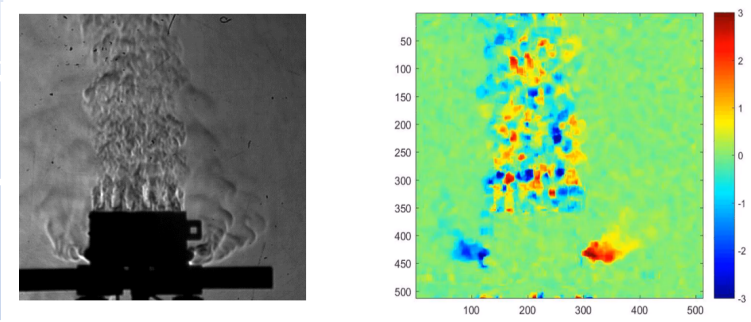

FIGURE 3.4: Velocity field calculation using OF on a microjet Ombroscopy image dataseta.

3.3 Parameter discussion : Pyramid levels

Multipyramid computational schemes are standard algorithms widely used in computations; they provide a better initial condition estimation for the iterative scheme and increase drastically the number of maximum possible particle displacement. At each pyramid level, the upper level is obtained by applying a low-pass filter, hence downsampling the image size by a factor of 2. In the present algorithm a Burt-Andelson pyramid (Adelson et al., 1983) is implemented. This specific parameter was introduced so that more than 2 pixels displacements can be calculated ; a typical problem of initial OF algorithms Horn and Schunck, 1981. With the increase of pyramid levels there is no upper limit on the maximum displacement that can be calculated, practically though we rarely observe a non-fictitious velocity of more than 20 pixels.

3.4 Parameter discussion : Gauss-Newton iterations

The standard number of Gauss-Newton iterations for the minimisation criterion to converge is 5-7, for the majority of datasets. The lower limit of the iterations can go down to 2 with no problem for most datasets, with a more than double result in computational speedup. Hence, a lower number of iterations is favourable for experiments that require rapid velocity calculations like in Gautier et al., 2015; Gautier and Aider, 2015b.

Chapter 4

Optimal window size, filtering effects and benchmarking : Optical Flow vs Cross-Correlation PIV

The content of this chapter is based on the article: *A.Giannopoulos, P.Y.Passaggia, N.Mazellier, J.L.Aider, Optimal window size, filtering effects and benchmarking : Optical Flow vs Cross-Correlation PIV, to be submitted in Experiments in Fluids.*

This section analyses the spatial resolution of two Particle Image Velocimetry (PIV) algorithms applied to turbulent flows. Cross-correlation (CC) and an iterative multi-pyramid Optical flow (OF) algorithm are compared side by side through various tests. The first analysis considers still images, which are used to evaluate the cut-off frequency induced by each algorithm, while a step response analysis highlights the capabilities of each method to minimise the effect of unresolved velocity gradients. Benchmarks then consist of various turbulent datasets, that go down to the sub-Kolmogorov scale. Particularly, three different data sets are used to analyse the velocity spectra and the Turbulent Kinetic Energy dissipation estimation. In the first dataset, a synthetic PIV dataset of homogeneous isotropic turbulence (HIT) is processed and compared with Direct Numerical Simulation (DNS) results. In the second dataset, a grid turbulence wind tunnel experimental dataset is processed to calculate velocity spectra, which are compared with Laser Doppler Velocimetry spectra. In the third dataset, the turbulent flow produced in the near wake of a D-shaped bluff body is examined and velocity spectra are compared alongside with hot-wire measurements. These results all point to the fact that, although OF is more diffusive and up to 5% less accurate than CC, the numerical diffusion improves the calculation of sub-window unresolved gradients and allows for directly measuring the onset of the viscous subrange from experimental measurements.

4.1 Benchmarking analysis outline

To this date, we were only able to find few comparative studies that analyses how OF, Direct-Cross-Correlation, and FFT-based CC perform with respect to one another (Liu et al., 2015b; Liu et al., 2020b; Champagnat et al., 2011). In this paper, we begin with the same ideas than Foucaut, Carlier, and Stanislas, 2004 and analyse still images to understand how band-pass filtering compares between OF and CC. In particular, we will show that CC is twice more accurate than OF with a band-pass filter 50% smaller for CC than OF. The analysis will be extended to the step displacement analysis to understand how unresolved velocity gradients affect both CC and OF. In particular, we will extend the framework developed in Kähler, Scharnowski, and Cierpka, 2012 and analyse the statistics (mean and variance) of the step response. We will show that OF provides consistent results, independent of the Kernel Radius (KR) used, and minimises the variance of unresolved gradients even for small values

of $KR = 8$. As a reminder we mention here that the side of the interrogation window in the OF algorithm has a size of $2 * KR + 1$ pixels. Moreover, the KR will be found to provide optimal results (smallest error and minimum velocity gradient variance) when it is equal to the size of the particle. On the other hand, CC shows a different behaviour and increasing the window size improves the accuracy while minimising the variance of the velocity gradients. Hence, the best compromise is obtained for square correlation windows of 32×32 px^2 as already observed in the literature. We will therefore draw a clear picture on the advantages and disadvantages of each method when applied to either laminar or turbulent flows.

Then, we will analyse a two-dimensional Homogeneous Isotropic Turbulence (HIT) dataset generated from a Direct Numerical Simulation (DNS) without noise. We show that CC PIV is again less diffusive than OF and predicts a more accurate dissipation spectrum, although OF is able to outperform CC for small distances between vectors, which improves the the spectrum in the deep viscous regime when compared with the DNS data. Finally, we will consider the case of a turbulent flow behind a regular grid and the case of a turbulent wake behind a D-shaped bluff body. These results show that optical aberrations such as particles defocusing are limiting for both CC and OF. However, OF correlation boxes are only limited to the size of the particle itself whereas for CC, the correlation window size is limited by the particle size itself Kähler, Scharnowski, and Cierpka, 2012. Our results will reveal on both test cases that CC is outperformed by OF when attempting to directly measure the Kolmogorov subrange.

Regarding the 3 PIV datasets studied in the present chapter, the mean displacement for each experiment was found to be approximately 4 *pix* for the Homogeneous Isotropic Turbulence (HIT) dataset, 8 pix for the grid- generated turbulence experiment and 12 pix for the case of the turbulent wake behind a D-Shaped bluff body. For all experiments, the mean radius of the particles was approximately 3 *pix* except for the case of the D-shaped wake where the particles were defocused and attained radius sizes close to 6 *pix* in average. Hence, square correlation boxes of 32 *pix* in length for the first three cases and 64 *pix* in length for the case of the wake were used in order to obtain 9 particles for the cross correlation for each experiment.

4.2 Filtering effect of Optical Flow and Cross Correlation

4.2.1 Steady particle images : Noise response analysis

A single experimental field of still particles was used to study the filtering effect of each approach. We tested still images obtained from Passaggia et al., 2020 which are neutrally buoyant PIV particles at rest in a stratified fluid experiment. The average particle radius is 1.5 *px* while the mean particle concentration is 0.07 (px^{-2}).

Window size / Method	Number of fields	Mean disp. long x(pix)	Mean disp. along y(pix)	Std dev. σ_u(pix)	Std dev. σ_v(pix)
16×16 CC	1	-0.008	0.0032	0.207	0.0452
32×32 CC	1	-0.003	0.0014	0.160	0.0159
64×64 CC	1	-0.004	0.0012	0.067	0.0164
16×16 OF	1	-0.008	0.004	0.174	0.128
32×32 OF	1	-0.008	0.003	0.112	0.061
64×64 OF	1	-0.007	0.002	0.086	0.044

TABLE 4.1: Systematic and random errors computed from no motion PIV maps.

Particle images can be considered as a two-dimensional discretised signal where particles are based on the pixel size. Assuming that the displacement of the particles is close to null, there only remains the noise from the camera, the experimental setup such as the misalignment or optical aberrations to only cite a few. following Foucaut, Carlier, and Stanislas, 2004, we proceed with a spectral analysis and compare how both CC and OF respond to nearly-zero-displacement images. In particular, we adapt their analysis and assume that the interrogation window used in both methods can be modelled by the convolution of the particle image sample with a square window, whose Fourier transform corresponds to a multiplication by a *sinc* function in the spectral domain. As suggested by Lourenco, 2000, the power spectra of the noise images can be expressed as:

$$E_{ii} = E_{noise}\left(\frac{\sin(kX/2)}{kX/2}\right)^2, \tag{4.1}$$

where E_{noise} is the white noise level introduced by measurement errors. In the present study, E_{noise} corresponds to the intercept at the smallest wave numbers of the spectrum measured from OF and CC which is assumed to have the form given by equation (4.1). The results are compared in Fig. 4.1(a) and (b) for CC and Fig. 4.1(c) and (d) for OF with $E_{noise} = 78.5\times10^{-3}\,pix^3$ and $58.6\times10^{-3}\,pix^3$ respectively for E_{11} and E_{22} for CC and $E_{noise} = 158\times10^{-3}\,pix^3$ and $97.5\times10^{-3}\,pix^3$ respectively for E_{11} and E_{22} in the case of OF.

For both methods, the noise level is therefore twice higher for E_{11} than for E_{22} in agreement with the values of the standard deviation in Table 4.1 and the study of Foucaut, Carlier, and Stanislas, 2004. In fact, Foucaut, Carlier, and Stanislas, 2004 argue that this difference may be attributed to the type of sensor used which transfers data between the two successive images which is also performed along the x direction by our CCD camera which is equivalent to the one used in Foucaut, Carlier, and Stanislas, 2004. This is also consistent with the fact that the particles in the present still images are neutrally buoyant in a stratified fluid which further mitigates the vertical motions. The error between the horizontal and the vertical component of the noise are reported in Table 4.2 and varies differently between OF and CC. Cross correlation provides systematically smaller mean displacements than OF. However, there is a substantial difference regarding the standard deviation where OF is weakly dependent on the vertical or horizontal direction while CC is much more sensible and differences are much larger depending on the direction. In the following, the results presented correspond to E_{22} and are generalised to E_{ii}.

The cutoff frequency produced by each PIV method can be seen as the decrease by -3dB between the $E_i i$ measured at the intercept (i.e. $k = 0$). This cutoff corresponds to the lower significant wavenumber for which the velocity is not filtered by the interrogation window size. As shown by the theoretical expression (4.1), the *sinc* function is the standard low-pass filter introduced by the square window whose cutoff wavenumber gives $k_{min} = 2.8$ rad/pix for CC and $k_{min} = 1.34$ rad/pix for OF. This value is shown in Fig. 4.1(a-d) by a vertical dashed line. OF is therefore twice more diffusive than CC and it is therefore necessary to use an interrogation window twice smaller for OF than CC to obtain results with similar cutoff frequencies. In the following, an overlapping of 75% will be used in order to detect easily the *sinc* function although an overlap larger than 50% is not necessary in practice.

Note that in the case of OF, there is no overlapping but the Kernel radius X is considered instead. It is interesting to note that OF produces exactly the same windowing-type filter on the spectra shown in Fig. 4.1(c) and Fig. 4.1(d). The dense approach to the Lucas-Kanade algorithm can therefore be sub-sampled or binned down to near wavenumbers with values of $1.3X$rad/pix.

As a first step, an approach based on spectral computation varying the window size X was carried out. This study shows that the cut-off frequency computed from $k_cX = k_cY = 2.8$

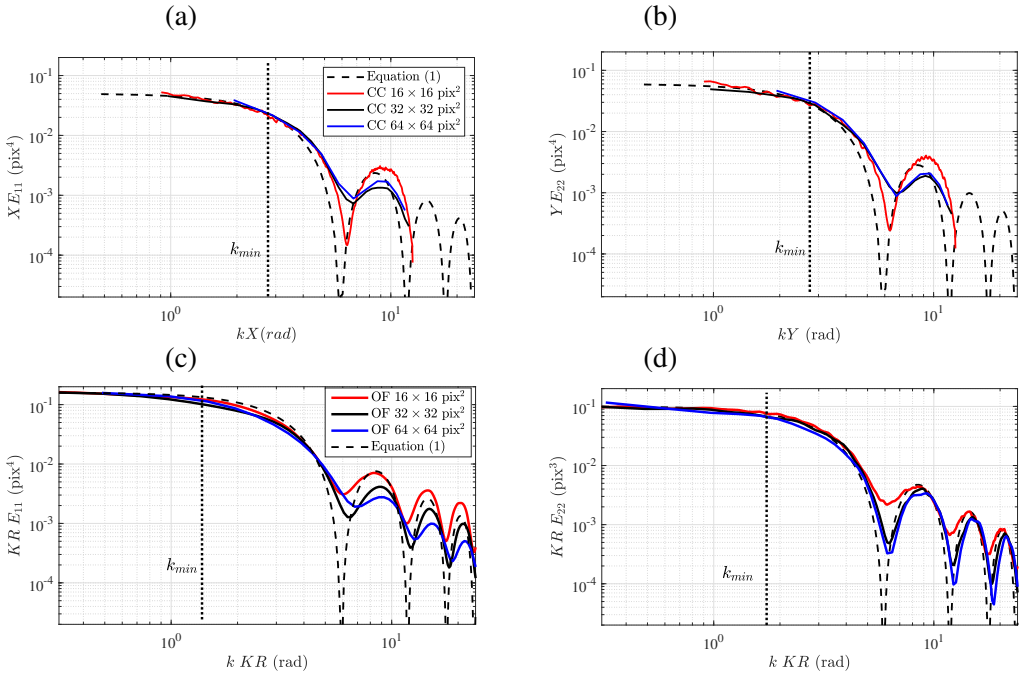

FIGURE 4.1: Power spectra of displacement from no motion PIV maps with 75% overlap for cross correlation in (a) and (b) and optical flow in (c) and (d) along x in (a) and (c) and along y (b) and (d).

remains universal for CC Foucaut, Carlier, and Stanislas, 2004. However, this is not the case for OF where the cut-off wavenumber decreases to $k_c KR = 1.3$ which is nearly twice lower than what is found for CC. In other words, OF is twice more diffusive, both in noise amplitude (see Tab. 4.2) and the cut-off frequency. Note that if this can first appear as a weakness in the algorithm, it will later prove to introduce a numerical-type diffusion which will prove important when considering unresolved velocity gradients and thus, turbulent flows.

In what follows, the representation of the spectra is rescaled with respect to the window size X such that $E_{ii} = E_{ii}(kX)$ for both CC and OF remains universal, independently of the method. The noise level for CC is constant at a value of $17.5 \times 10^{-3} pix^3$, while we obtain $17.5 \times 10^{-3} pix^3$ for OF. Then we compute both spectra varying $Y = X$. The E_{noise} values are 37, 60 and $78 \times 10^{-3} pix^3$ respectively for $Y = X = 16, 32$ and 64 pixels for CC. The E_{noise} values are 63, 103 and $160 \times 10^{-3} pix^3$ respectively for $Y = X = 16, 32$ and 64 pixels for OF.

As noted in Foucaut, Carlier, and Stanislas, 2004, it can be remarked that E_{noise} varies with the inverse of Y and the data can be represented as $YE_{ii}(kX/2)$. Rescaling the wavenumbers with $(X/2)$ and multiplying the left-hand side by the interrogation window size Y, eq. (4.1) writes :

$$YE_{ii} = \zeta \left(\frac{\sin(kX/2)}{kX/2} \right)^2 . \tag{4.2}$$

Fig. 4.1(a) and (b) show these spectra for CC while OF is depicted in Fig. 4.1 (c) and Fig. 4.1 (d) computed for different window sizes (16, 32 and 64 pixels) for square interrogation windows with aspect ratios of 1.

The rescaled spectra given by eq. (4.2) is shown in Fig. 4.1(a-d) alongside the rescaled no-motion spectra measured with CC and OF where a good agreement is obtained for both methods. Note that at low wave numbers, OF shows a small departure when using large kernel radii. Nevertheless $\zeta = E_{noise} Y$ remains essentially constant for all window size of kernel radii and takes a constant value of 0.275 pix^4 for CC and 0.38 pix^4 for OF. This result confirms that similarly to CC, the cut-off frequency obtained with OF due to the *sinc* function

depends only on the window size X in the direction where the spectrum is computed. The noise level E_{noise} depends only on the window size or the kernell radius for CC and OF in a similar fashion. As a conclusion, the best spectrum is obtained for both methods using a rectangular window with a small X to increase the cut-off frequency and a large Y to decrease E_{noise} which is equivalent to the conclusions obtained in Foucaut, Carlier, and Stanislas, 2004.

The best compromise is thus to use square windows for CC or equivalently, a square kernel for OF. We therefore reach the same conclusion than in Foucaut, Carlier, and Stanislas, 2004 where the standard deviation σ_u of the displacement decreases when the window size increases independently of the method. As shown in Foucaut, Carlier, and Stanislas, 2004, σ_u is the square root of the integral of the power spectra and relates to the amplitude of the error. Based on eq. 4.2, σ_u can be directly obtained computing:

$$\sigma_u = \sqrt{\frac{4\zeta I}{XY}}, \tag{4.3}$$

where $I = \int_0^{2\pi} \left(\frac{\sin(u)}{u}\right)^2 du = 1.492$ and $I = 1.418$ when using an overlap of 50%. The value of ζ_1 and ζ_2 obtained from Fig. 4.1(b) and the estimation of σ_u and σ_v computed with eq. 4.2 are reported in Tab. 4.2 for the displacement along x and y respectively using both CC and OF. It is worth emphasising that the values of ζ_1 and ζ_2 are slightly larger for OF than CC for small kernel radii and become essentially similar when increasing the kernel size.

Window sizes	ζ_1 (pix^4)	ζ_2 (pix^4)	σ_u estimated	σ_v estimated
16×16 CC	0.26	0.225	0.304	0.162
32×32 CC	0.28	0.239	0.156	0.116
64×64 CC	0.31	0.250	0.080	0.061
16×16 OF	0.34	0.316	0.324	0.224
32×32 OF	0.38	0.339	0.172	0.124
64×64 OF	0.41	0.357	0.102	0.064

TABLE 4.2: Spectral noise density and estimated standard deviations of noise.

Although the correlation (or interrogation) window sizes or the kernel radii are different, the density ζ is quasi constant for a given direction. The small differences are probably due to an effect of convergence of the spectra. In Table 4.2 the estimated standard deviations compare favourably with the measured values given in Table 4.1.

4.2.2 Step-response analysis

To determine systematically the effective resolution for various interrogation windows and different approaches systematically, the resolution limit can be analysed with a step-like velocity profile, like in Kähler, Scharnowski, and Cierpka, 2012. Such a profile may be thought as an infinitely thin shear layer or a small eddy eddy, given for instance by:

$$\Delta x\,(y) = \begin{cases} 5 \text{ px}, & y \geq 0 \\ 0 \text{ px}, & y < 0 \end{cases} \tag{4.4}$$

The step response is also frequently used in electrical engineering and control theory to analyse the transfer function associated with linear and nonlinear systems. In order to analyse the resolution of CC and OF, the signal (particle image displacement) is changed in space over an infinitely small distance. The response to a step profile is shown in the top profile

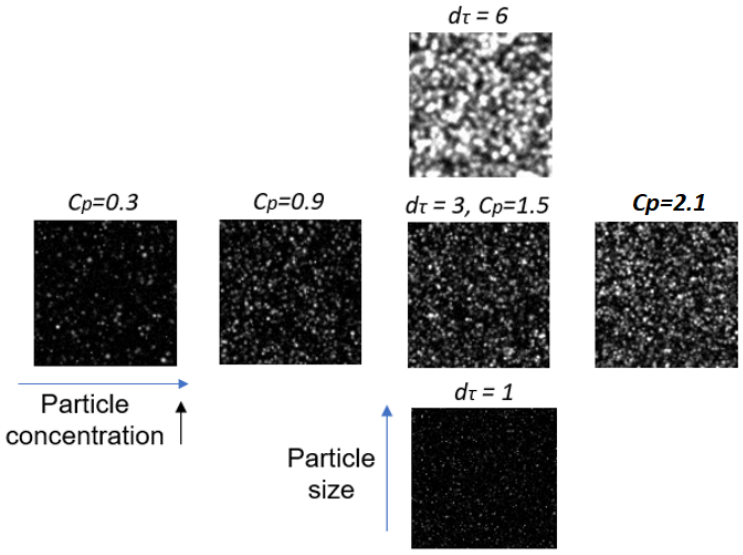

FIGURE 4.2: Examples of tested synthetic images with different particle concentration and particle size. Image size shown is 100×100 px^2.

of Fig. 4.3(a,b) for window-correlation using three different interrogation window sizes X for CC, and four KR sizes for OF. The width of the response function Step Response Width (SRW) can be regarded as the resolution and describes the minimum distance between independent vectors. Only for distances larger than the SRW, the vector is not biased by the aforementioned flow variations.

The sampling introduced by the window function, that is for both CC and OF can therefore be regarded as a convolution between a step or Heaviside function with a square window function with a dimension KR for OF and Y for CC (since the shear is in the vertical direction). The theoretical expression is a piecewise linear ramp of width KR or equivalently Y, which is given by

$$U(y) = \begin{cases} 0, & y < -KR/2, \\ 5/KR \times \mathrm{Y} - 2.5, & -KR/2 \geq \quad y \geq KR/2, \\ 1, & y > KR/2. \end{cases} \tag{4.5}$$

The crucial point though is that not only we are interested in the velocity profile, but also its derivatives and taking the vertical derivative of these profiles:

$$\frac{\partial U}{\partial y} = \begin{cases} 0, & y < -KR/2, \\ 5/KR, & -KR/2 \geq \quad y \geq KR/2, \\ 0, & y > KR/2. \end{cases} \tag{4.6}$$

The second-order derivative can also be analysed using the Fourier transform which is obtained theoretically as a *sinc* function. In what follows, we analyse the Step Response Derivative Amplitude (SRDA) as well as its standard deviation for both CC and OF as a function of the particle size d_τ and particle concentration $Cp = N/(n_x n_y)$, where n_x and n_y are the number of pixels in each direction respectively. Next, we determine how each methods is able to resolve velocity gradients and its implication when applied to turbulent flows. This aspect may shed light on how turbulent flows can be resolved using either OF or CC.

A synthetic PIV image generator provided by Thielicke and Stamhuis, 2014 was used to create the images with varying parameters : maximum particle diameter tested $d_\tau = 6$ pix

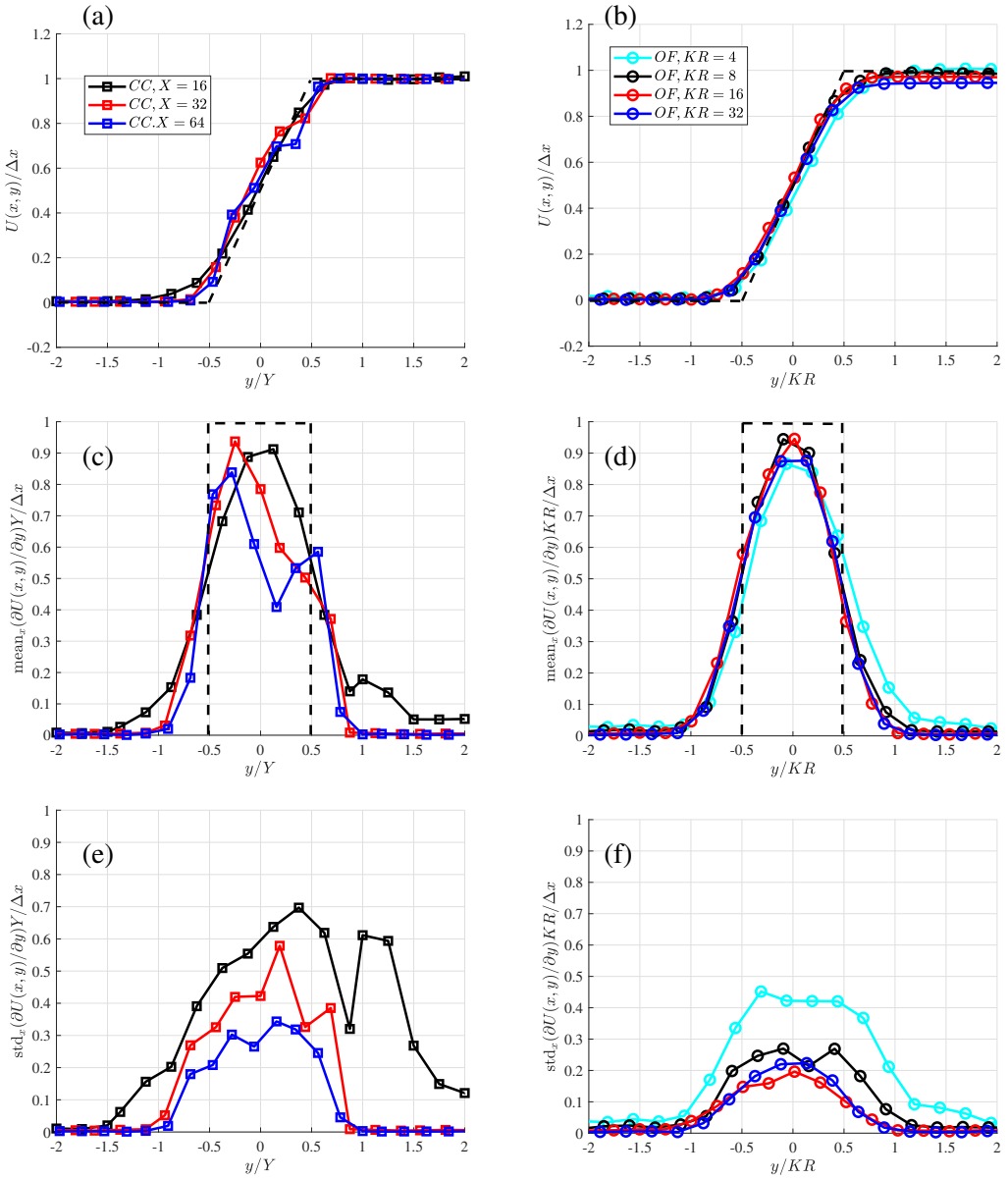

FIGURE 4.3: Step-response analysis showing the mean normalised vertical profile of displacement $U(x,y)$ for (a) CC and (b) OF and for several interrogation window and kernel sizes. Note that the horizontal axis is normalised using the interrogation window size of each method. Mean value of the vertical gradient of velocity computed along the horizontal direction x for CC (c) and OF (d). The theoretical profile is shown with black dashed lines in (a,b,c,d). Standard deviation of the vertical gradient along the spatial direction x for (e) CC and (f) OF. Here the particle size $d_\tau = 3$ pix and $Cp = 2.1$.

and maximum $Cp = 2.7$. The said generator satisfies all the requirements of standard PIV images as defined by Raffel, Willert, and Kompenhans, 1998. The displacement was fixed at 5 pixels. The PIV image generator generates pairs of images illuminated by a laser sheet with a light intensity distribution varying like a Gaussian. The coordinates of the particles, as well as an out of place motion are selected randomly Mendes, Bernardino, and Ferreira, 2020. The thickness of the laser sheet was given a standard value of 0.5. By this value, we mean the out-of-plane distance including the region where laser intensity is larger than I_0/e^2, where I_0 is the maximum intensity and $e = exp(1)$ is Euler's number.

Figure 4.4(a,b) shows the normalised step response, resolved for each method for $d_\tau = 3$ pix and $Cp = 2.1$ which will serve as a reference case. From these figures, the normal direction is normalised with the window size and all curves collapse on the theoretical profile given in eq. (4.5). As observed in Kähler, Scharnowski, and Cierpka, 2012, the step response cannot be smaller than the window size. Note that in Fig. 4.3(b), OF shows slightly less accuracy than CC where up to 5% velocity deficit can be observed for $y/KR > 0.5$ when $KR \geq 16$, which is consistent with the still image analysis.

The gradient is shown in Fig. 4.3(c,d) for both methods. The theoretical profile, given in eq. (4.6) is clearly diffused since the normalised maximum for both CC and OF never reaches 1, but is closer to 0.9 for all methods. This translates into a diffusion effect of 10%, independently from the method used for the analysis. It is interesting to see that CC is less diffusive than OF and that the derivative profile progressively steepens and approaches the theoretical profile when the interrogation window decreases. The conclusion is somewhat different for OF. The mean derivative profile remains self similar, almost independently from the the KR. Note that for $KR = 4$, the method is even more diffusive as the SRW is larger than for $KR > 4$. This aspect will be shown to have interesting implications for the analysis of turbulent spectra for the analysis of synthetic images of turbulence.

More interesting is the standard deviation of the step response shown in Fig. 4.3(e,f) computed along the horizontal direction x. This quantity relates the variance of the gradient, which is directly related to the notion of dissipation and hence, the quality of the spatial gradient resolution. Ideally, each curve in Fig. 4.3(e,f) should be 0 along y. However, the noise in the reconstruction inevitably leads to variations, compared to the mean, shown in Fig. 4.3(e,f). In the case of CC, as the interrogation window increases, the standard deviation decreases to a value of 0.3 for $X = Y = 64$. The case of OF is more interesting since for $KR = [8,16,32]$, the standard deviation peaks at 0.27 for $KR = 8$ and decreases to 0.2 for $KR = [16,32]$. Therefore, the numerical diffusion induced by OF decreases the sensitivity for the step response which is particularly important for the calculation of turbulent flows. In fact, although more diffusive, OF may prove to be more robust in approximating dissipation in turbulent flows. This will be demonstrated in §4.4 on experimental datasets.

As a general conclusion, OF is more diffusive than CC when calculating the step response to an infinitely thin shear layer but also more robust. In fact, Kernel radii with sizes $KR = 4$ and $KR = 8$ outperform results obtained with CC for interrogation windows with dimensions $X = 16$. Recalling from §4.2.1 that the cut-off frequency for OF is twice smaller than for CC, we can conclude that OF can be considered at least as twice more accurate to resolve velocity gradients if one considers sacrificing a few percents for the precision of the actual velocity as compared to CC. Next, we consider the effect of both particle concentration and particle size on the standard deviation of the gradients.

4.2.3 The effect of particle size and particle concentration

A systematic study is now carried out on the effect of particle sizes and particle concentration on the quality of the gradient statistics. As shown in Kähler, Scharnowski, and Cierpka, 2012, the particle size becomes a concern when the particle size increases beyond a third of the size of the correlation window for the SRW. Here, we not really are interested in the mean SRW but in the statistics of the derivatives. Hence, we analyse the standard deviation of the gradients at $y = 0$ for both OF and CC for particle sizes $d_\tau = [1,2,3,4,6]$ and particle concentrations $C_p = [0.1 - 2.7]$. Fig. 4.4(a) shows variations with respect to Cp while Fig. 4.4(b) reports variations with respect to the particle size d_τ, both for a displacement $\Delta x = 5$ pix. For both cases, the standard deviation is nearly constant for OF while decreasing the interrogation window increases the standard deviation for CC. Also, decreasing the particle

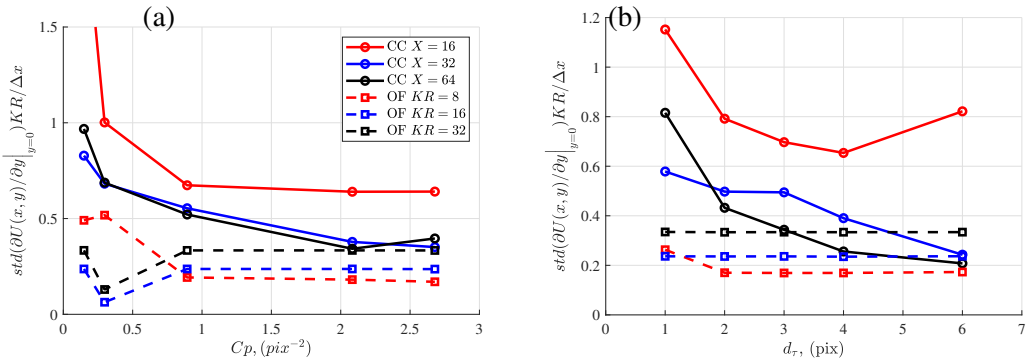

FIGURE 4.4: Maximum of the standard deviation computed in Fig. 4.3(e,f) of the shear as a function of both (a) the particle concentration Cp computed for $d_\tau = 3$ *pix* and (b) the actual particle size d_τ for $Cp = 2$ pix^{-2}. Here the continuous lines corresponds to the results obtained with CC while dashed line correspond to OF.

size and particle concentration degrades the quality of the reconstruction for CC while OF remains essentially insensitive to both parameters.

As a first conclusion, OF provides greater robustness to parameter variations such as particle size and particle concentration, at least for the parameters investigated in this study, which is representative of experiments as will be shown in §4.4 and turbulent flow experiments in general.

As a rule of thumb: OF appears be twice more precise when attempting to resolve velocity gradients but slightly more diffusive when measuring mean displacements from particle images. The optimal KR should therefore be consistent the actual size of the particles and independently from the particle concentration. This will be demonstrated from turbulent measurements computed from both synthetic and real particle image turbulent experiments.

4.3 Two-dimensional turbulent dataset from synthetic images

The dataset used in the present study is available online and provided by Carlier, 2005. It is a synthetic PIV dataset of a forced, time-resolved HIT flow computed from a DNS in two dimensions, where particles are seeded without camera noise nor illumination variations. These therefore correspond to synthetic PIV images from the 4th PIV-Challenge Kähler et al., 2016. In this dataset, the average particle radius is 2 *px* while the mean particle concentration is $Cp = 0.014$ (px^{-2}).

For CC PIV, an interrogation window of 16 and overlap of 75% was used which provided the best compromise between accuracy and resolution. In the case of OF, several kernel radii were considered in order to investigate this interrogation window on the quality of the reconstruction. snapshots of the velocity fields are shown in figure 4.6(a) for the DNS, 4.6(b) for the results from OF and in figure 4.6(c) for CC. It is worth noting that the amplitudes are well measured by both PIV strategies but the border in OF show a lack of resolution as particles may leave or enter through these locations. Further, the gradients seem to be slightly smoothed for both OF and CC for this first visual inspection.

The data are also compared with the actual velocities from DNS and the results are shown for the mean horizontal spectrum in figure 4.5(a), while the compensated spectrum is shown in 4.5(b). Welche's method (Stoica and Moses, 2005) was used for the calculation of the spectra, for which a Hamming window size equal to the full signal length was considered.

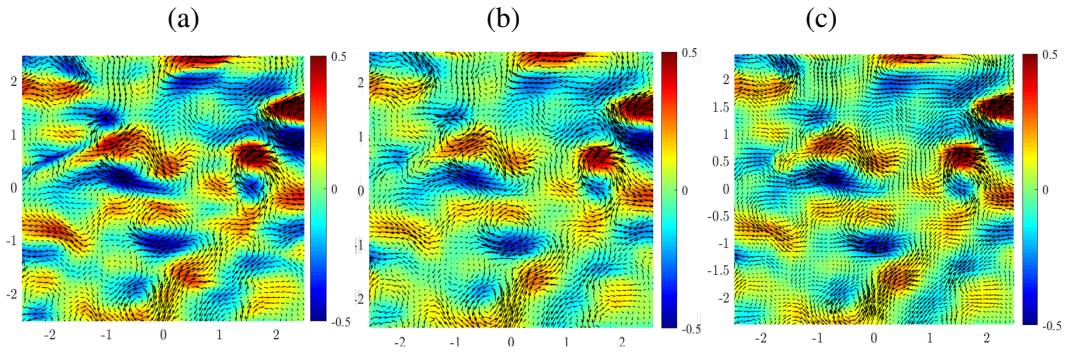

FIGURE 4.5: Instantaneous velocity field results for the two-dimensional homogeneous and isotropic turbulence dataset. DNS results (a), OF results (b), CC PIV results (c).

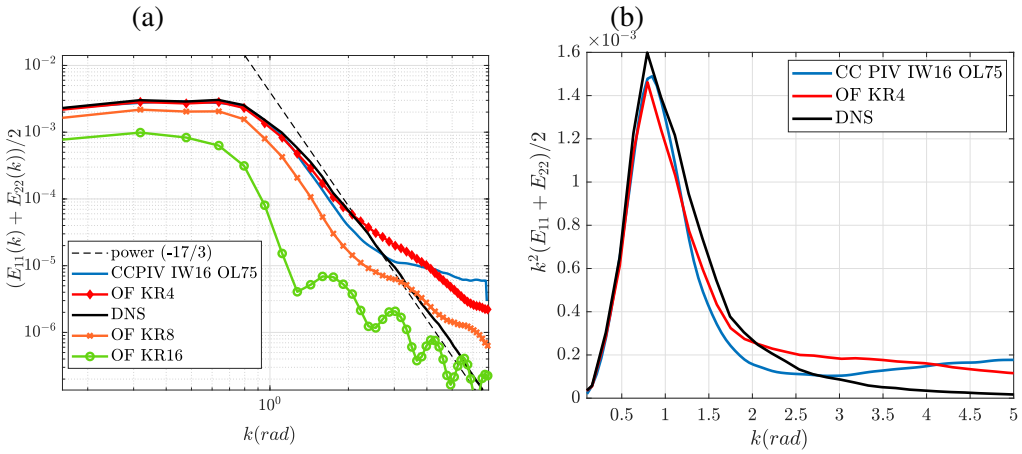

FIGURE 4.6: (a) Velocity spectra comparison for the turbulence homogeneous isotropic dataset. Comparison with spectra from reference DNS data. 10 iterations and 2 pyramid levels kept for OF calculations. (b) Dissipation rate comparison for the turbulence homogeneous isotropic dataset. Comparison with spectra from reference DNS data.

Note that here, we make the assumption of a two-dimensional isotropic and homogeneous flow (Carlier, 2005). In addition, we mention that only 100 snapshots were available for the comparison for the DNS while 1000 PIV snapshots of particles are provided online, but this was not an issue in order to compare the results and obtain conclusive remarks.

The present results show that decreasing the KR improves the quality of the velocity spectrum for OF approach. In fact, the best results are obtained from a KR of dimension $KR = 4$ which for the largest to the smallest scales. Note that this KR size is nearly the size of the particles themselves; this will turn out to be the same for all experiments. The results for CC begin to depart from the DNS for $k \approx 2.8$ rad/pix and a slope of k^{-2} which is the point where the filtering effect induced by windowing was predicted. This estimates therefore remains robust, even for complex flow fields (cf. figure 4.6(b)). In the case of OF, the departure between the two spectra appears at a lower wavenumber. In particular, the spectrum no longer displays a slope of $k^{-17/3}$ but a steeper exponent is found which is an interesting result in itself. This means that for synthetic data, the noise level is low enough so that OF is able to either smooth or capture accurate gradients, even for lengthscales where a spectrum close to k^{-6}. This is also confirmed for the compensated spectrum shown in figure 4.6(b) where for the larger wavenumbers, the compensated energy decreases with increasing k. Note that both CC and OF predict the peak of dissipation at $k = 0.8$ which is very close to

the DNS.

This analysis confirms that the KR necessary to achieve an accurate PIV calculation using OF is close to the particle size itself, which is 4 times smaller than the needed window size by CC. Note that here, the concentration is rather high while for the motionless particle images, the concentration was nearly 2 times lower. Hence, it is important for an accurate OF reconstruction, to ensure that particles are as small as possible and as dense as possible in order to accurately measure velocity gradients. Note that this is not the case for CC, where individual particles must appear individually because of the FFT used for the correlation and the fact that several particles must be present in the interrogation window. Note also that we performed CC using direct correlation and both method yield nearly identical results. As a first rule of thumb, we can therefore conclude that the KR for OF has to be at least twice smaller than the interrogation window for CC in order to obtain comparable measurements. Furthermore, the optimal KR used in this benchmark was four times smaller than the interrogation window size used in CC, which should lead to a twice more accurate result. However, the present test case makes it hard to confirm this assertion.

Next, we apply the same technique to experimental images, obtained in the case of a turbulent flow behind a regular grid and further demonstrate the robustness of OF compared to CC.

4.4 Benchmarking on experimental results

First it should be noted that the velocity fields presented in the following are obtained without pre-processing or filtering of the raw images. In addition, sample snapshots of instantaneous fields are provided as supplementary material with the paper.

In this section, we analyse experimental snapshots ranging from 1.3 Mpx image series for the first case to 29 Mpx image series for the second test case. We therefore first analyse the possible loss of quality for the resolution of the particles and in particular, the fact the defocusing may lead to larger particles.

Kahler *et al.* Kähler, Scharnowski, and Cierpka, 2012 showed that increasing the magnification may enhance the resolution of the measurements but this is remains essentially true when the particle is actually resolved bu the pixel of the camera. On the other hand, optical magnification may lead to detrimental effects, as will be explained later. The particle image diameter as seen from the camera sensor is related to the particle size but other parameters such as the optical magnification. Four key effects are described in Kähler, Scharnowski, and Cierpka, 2012 when particles appear enlarged in the PIV images, as acquired by the optical sensors and correspond to:

- 1. diffraction at the limited aperture of the objective lens
- 2. defocusing
- 3. lens aberrations
- 4. discretization and quantization of the continuous image signal into a discrete signal with pixel size S.

In this subsection, we use the same nomenclature as Kähler, Scharnowski, and Cierpka, 2012 to understand which factor lead to the particle size acquired in our experiments. The enlargement of the particle image due to diffraction and defocusing can be described by the second and third terms under the square root of the following equation proposed by Olsen

and Adrian Olsen and Adrian, 2000:

$$d_\tau = \sqrt{(M \cdot d_p)^2 + (2.44 \cdot f_\#(M+1)\lambda)^2 + \left(\frac{M \cdot z \cdot D_a}{s_0 + z}\right)^2} \tag{4.7}$$

where M is the magnification of the imaging system. Here, d_p is the particle diameter, $f_\#$ is the ratio between the objective lens diameter and the apertures diameter, λ is the wavelength of the scattered light from the particles, z is the objects distance from the focal plane, D_a is the lens aperture diameter, and s_0 the object distance.

The variables used in eq. (4.7) are also summarised in Tab. 4.3. The three terms in the square root of eq. 4.7 correspond to the geometric, diffraction, and defocusing components. In macroscopic PIV, as for instance considered in the present study, z is usually 1 to 3 orders of magnitude smaller than s_0 for well-aligned optical systems Kähler, Scharnowski, and Cierpka, 2012. Thus, for a large numerical aperture (small $f_\#$) and a wavelength in the range of visible light, the particle images are smaller than the pixel size S of the camera sensor, which is typically in the range of 520 μm for the typical CCD cameras used in the present PIV analysis Hain, Kähler, and Tropea, 2007.

In the present analysis, particles are much smaller than the sensor size for the case of 1.3 Mpx images and the particles diameter $d_\tau \approx 2 \pm 1 px$. However, in the case of the 29 Mpx camera, the sensor size is close to the size of the particle $d_p \approx 5\mu m$. However, the lens used in this experiment was a $50mm$ lens with aperture $f_\# = 2.8$. The distance between the laser plane and the objective of the camera was $0.5m$. The spatial resolution is $res = 0.021$mm and the senors gathers 6600 px in the horizontal direction. The size of the sensor was 43.3mm and the magnification for that particular lens was $M = 1$, and only the laser plane distance from the focal plane (z) remains unknown.

Quantity	Symbol	Unit
Particle diameter	d_p	μm
Particle image diameter	d_τ	px
Particle diameter	D	px
Dynamic spatial range	DSR	m/m
Field of view	FOV	m
F-number	$f_\#$	m/m
Discrete sensor size	L	px
Optical magnification	M	m/m
Sensor pixel size	S	μm/px
Spatial resolution	res	m
Step response width	SRW	px
Shift vector components	$\Delta X, \Delta Y$	px

TABLE 4.3: Spectral noise density and estimated standard deviations of noise.

The wavelength of the laser was $523nm$ and using these values in eq. (4.7), only the particles should have appeared with a size of $d_\tau \approx 2 \pm 1 px$. However, defocusing induced by hand manipulations of the lens led to particles with diameter $d_\tau \approx 12 \pm 1 px$. Nevertheless, it will be interesting to analyse the effect of defocusing on the quality of the reconstruction using CC and OF.

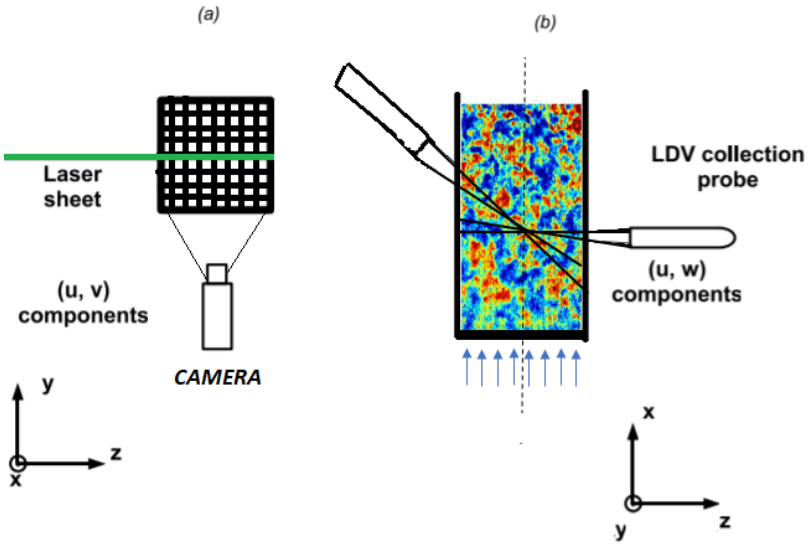

FIGURE 4.7: Grid turbulence experiment sketch. PIV plane and LDV measurement planes. Only u component kept from LDV measurements

4.4.1 Grid-generated turbulence experiment

The experimental grid turbulence data-set was first presented in Mazellier, Danaila, and Renou, 2010, to improve premixed combustion, although no turbulent spectra study was conducted. Nonetheless, the second-order structure function showed that the Kolmogorov spectrum could be measured. Experiments were carried out in an open loop vertical wind-tunnel Mazellier, Danaila, and Renou, 2010. The wind-tunnel cross section was $8x8\ cm^2$. The test-section was $40cm$ long and was allowed easy optical access. The turbulence intensity was 0.4% and the inlet free-stream velocity was $3.7\ m/s$.

In the present experiment, turbulence was generated by perforated plates. Each plate consisted of a mesh of circular holes of 15 mm diameter each, that spans the entire wind tunnel. The holes were arranged in a triangular network with a 24.7 mm spacing. Moreover, the perforation is straight over the entire thickness of the plates and the holes network is chosen such that the tunnels centre line coincide with a hole centre.

The data-set consisted in 1600 snapshots. Examples of instantaneous spanwise and streamwise velocity components computed with OF are shown in Fig. 4.8 (a) and (b) respectively. In this data-set, the average particle diameter is $d_\tau = 3.5\ px$, while the mean particle concentration is $0.014\ px^{-2}$.

The spectra of the streamwise component were calculated on the streamwise profile along the x axis in the middle of the snapshots ($z = 0.03$) and compared with spectra from time-series in the same profile. Two positions were used for the LDV probe: $x = 0.85$ and $x = 1.19$ in the mid-channel plane as shown in Fig. 4.7. Welche's method Stoica and Moses, 2005 was again used for the calculation of the spectra, for which a Hamming window size equal to the full signal length was consistently chosen. The spectra analysis results for various KR and interrogation windows are presented in Fig. 4.9. Interestingly, the results are quite similar when the interrogation window of CC is equal to twice the KR of OF. Nonetheless, only the case of OF with $KR = 8$ allows for capturing the LDV measurements up to $k = 5000$ (rad/m) and the onset of the Kolmogorov subrange. On the other hand, CC-PIV gave best results with an optimal IW $X = 16$. The maximum wavelength with good agreement compared to the LDV measurements is around $k = 2000$ (rad/m). In this test case, CC is not able to capture the Kolmogorov lengthscale.

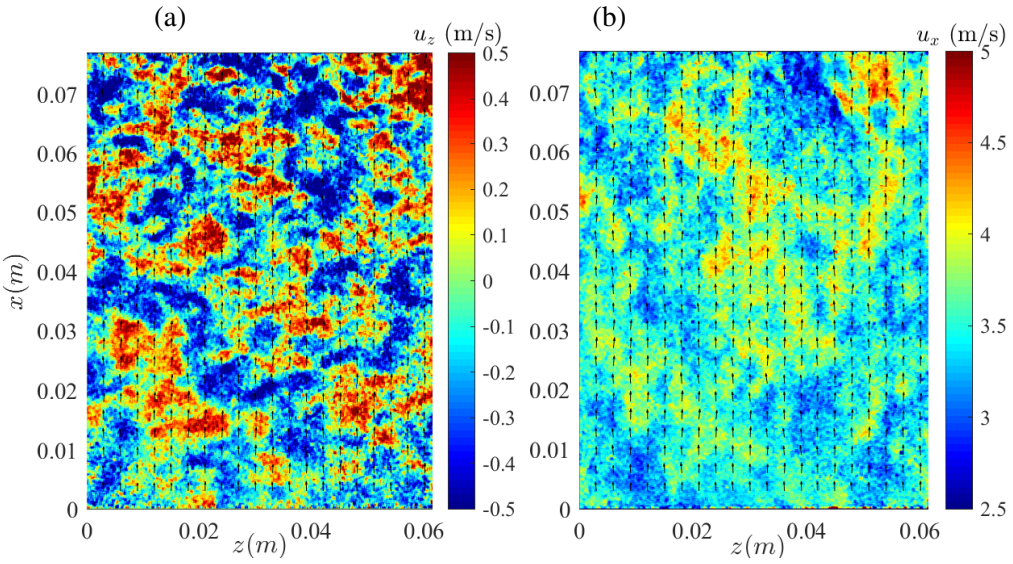

FIGURE 4.8: Instantaneous fields of wind tunnel grid turbulence experiment. (a) Spanwise and (b) streamwise velocity components left and right respectively.

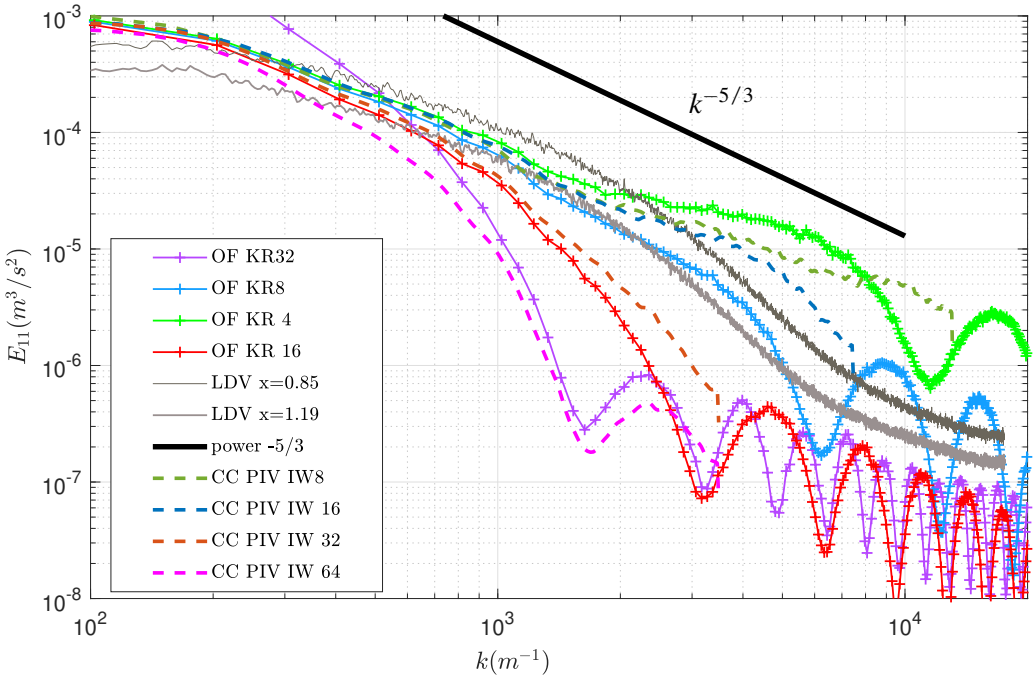

FIGURE 4.9: Time-averaged velocity spectra of the streamwise component in a streamwise profile in the centre of the field, compared with LDV measurements spectra in 2 streamwise positions $x = 0.85$ and $x = 1.19$. Different KR and interrogation windows are tested for OF and CC PIV respectively.

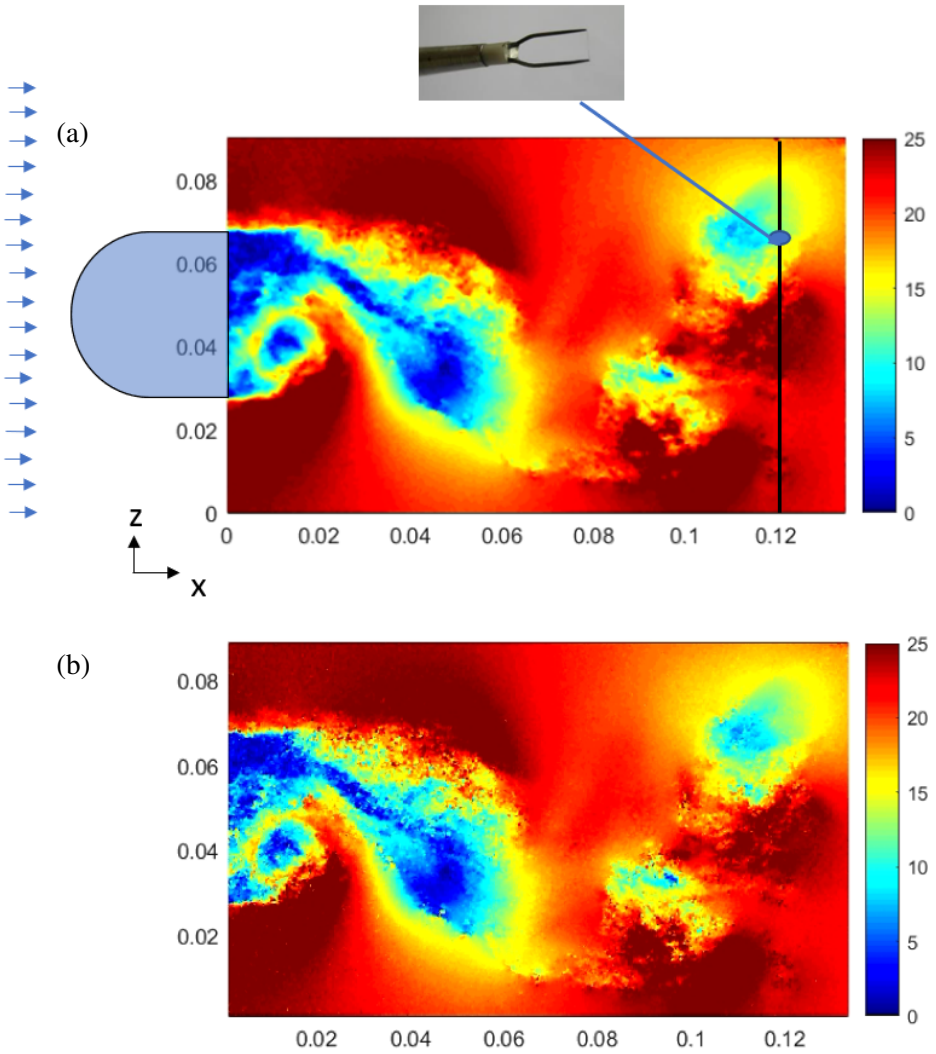

FIGURE 4.10: Instantaneous velocity magnitude ($V = \sqrt{u^2 + v^2}$) computed using OF with $KR = 18$ (top,a) and using CC PIV with $X = Y = 32$ (bottom,b). The black vertical line corresponds to the spanwise profile used to compute the spectra at ($x = 3h$). The blue dot shows the position of the hot-wire probe at $x = 3h$.

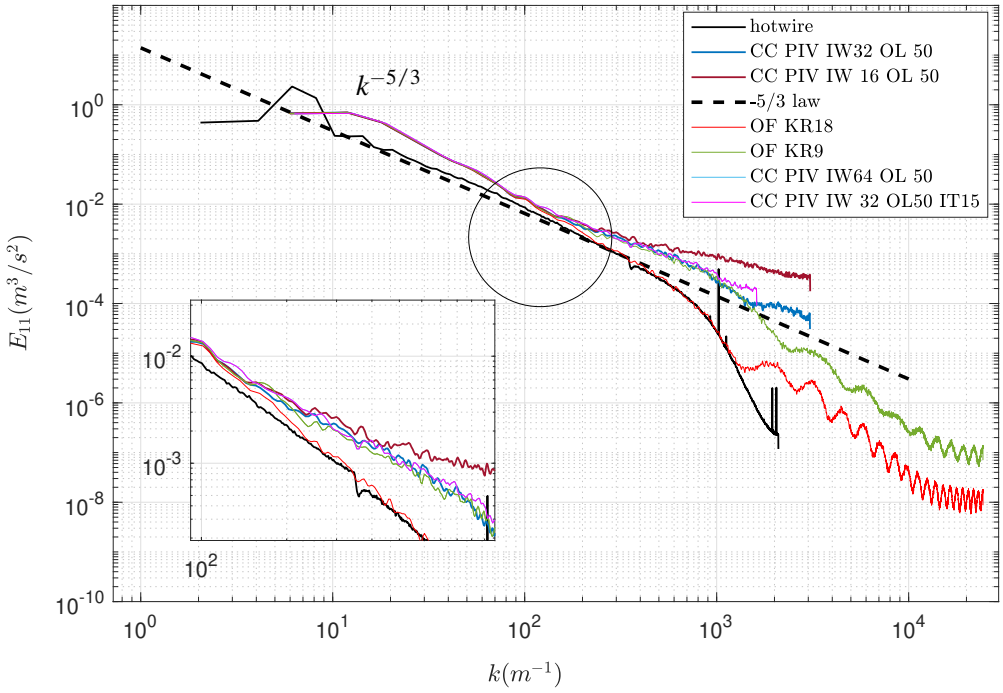

FIGURE 4.11: Velocity spectra comparison for D-shaped turbulent wake flow. Comparison of different OF and PIV parameters with the hot-wire spectrum (in black).

4.4.2 D-Shaped bluff body turbulent wake

The last application considers the near wake of a D-Shaped bluff body. The Reynolds number is $Re_H = \frac{U_\infty \times H}{\nu} \approx 53000$, where the body height $H = 4$ *cm*, the free-stream velocity $U_\infty = 20\ m.s^{-1}$ and the kinematic viscosity of air is $\nu = 15 \times 10^{-6}\ m^2.s^{-1}$. Using a high-definition 29 Mpx CCD camera our objective is to resolve scales from the integral lengthscale down to the viscous sub-range.

The experiment setup and validation of the data are fully detailed in Shanmughan et al., 2020. In the present paper, we analyse a novel dataset consisting of zoomed-in snapshots of the flow in the near wake at $x/H = [0, 3.5]$ and $y/H = \pm 1.125$ with a resolution of 6600 *px* in the horizontal/streamwise direction x and 4400 *px* in the vertical/normal direction y. Sample snapshots are shown in Fig. 4.10(a) for OF and Fig. 4.10(b) using CC where clear differences can already be noticed.

In addition, hot-wire measurements have been carried out at $y/H = 0.5$ and at $x = 3H$ in order to compare the spectra of turbulence, similarly to the case of the grid turbulence. This position corresponds to half the maximum of the mean streamwise velocity profile. The acquisition of the hot-wire was performed at 80 kHz.

The low-speed wind tunnel cross section is 500 *mm x* 500*mm* and is approximately 2000 mm long. The D-shaped model has a cylindrical nose of diameter 40 mm, streamwise and spanwise aspect ratios of 4 and 12.5, respectively. The model was 3-D printed and installed at approximately $14H$ from the inlet of the test section.

The background turbulence level in the test section was measured using the hot-wire anemometer and found to be less than 0.5%. The flow seeded with olive-oil droplets was illuminated by a double-pulsed Nd:YAG laser with a pulse delay short enough to limit the in-plane movement to a quarter of the interrogation window size. 5000 image pairs were acquired at a rate of 0.825 Hz, sufficiently separated in time to recover time-uncorrelated

data sets to obtain turbulent quantities. The ImperX BOBCAT 6620 CCD PIV cameras was synchronised with the laser using a TSI LaserPulse Synchronizer Model 610036, with a delay of 11 μs between each laser pulse while a laser engraved checker board was used for the spatial calibration. Images were acquired with 12 bit-depth resolution. The KAI-29050 sensor is 43.3 mm in size which provides a resolution of $6.5\mu m$ per pixel which is close to the size of the olive-oil droplets used to seed the flow.

Because of the defocusing introduced by hand-manipulation of the lens, the average particle image diameter is $d_\tau \approx 6px$ while the mean particle concentration is 0.004 (px^{-2}). Regarding OF parameters, a KR of 9 and 18 px was tested. For CC PIV, an interrogation window with dimensions $X = Y = 32$ and $X = Y = 16$ and an overlap of 50% was used. An overlap of 75% was also tested but provided worse results for the velocity gradients. Welche's method (Stoica and Moses, 2005) was used once again for the calculation of the spectra, for which a Hamming window size equal to the full signal length was always chosen. Variables are made dimensionless using the free-stream velocity U_∞ and the height of the body H.

The different spectra are presented in Fig. 4.11. We can observe that for such large particles, a KR 3 times bigger than the particle diameter d_τ gives optimal results for OF. The best CC PIV spectrum results were obtained for IW 32 and 64. IW of 16 failed to give satisfying results for such large particles. In any case, the CC PIV fits with the hot-wire spectrum with a cut-off wavenumber of $k = 200$ whereas OF shows excellent agreement up to wavelengths around $k = 1500$. This can be explained with the gradient calculation robustness of OF, for data-sets with low concentration C_p and large particle diameter d_τ.

4.5 Conclusions

A rigorous comparison between OF velocimetry and CC PIV has been presented, down to sub-Kolmogorov turbulent scales and for various PIV image parameters (particle concentration and size). The performances of OF and CC-PIV have been evaluated on various test cases, from still images, step displacement of synthetic images, 2D isotropic turbulence and finally two experimental challenging turbulent flows (grid-generated turbulence and a D-shaped bluff-body turbulent wake).

No-motion velocity fields show that OF and CC provides the same results in terms of noise and transfer function guided by the window size, as shown in Foucault *et al.* Foucaut, Carlier, and Stanislas, 2004. CC provides a lower noise level than OF and a twice higher frequency cut-off for the gradient. Analysing the step-response, we have shown that OF is indeed less accurate and more diffusive, but resolves better the gradients ($std(dU/dy)$ was found twice lower for OF than for CC). Step-motion tests showed that CC and OF behave differently when varying KR and IW compared with the effective particle size d_τ and the particle concentration C_p. OF appears more consistent, keeping lower errors for a wider range of image parameters.

Application to HIT from synthetic images confirms the same trend: OF is more diffusive but more accurate in the spectrum. The grid turbulence experimental data-set showed the same trend down to Kolmogorov length scales: OF is more diffusive but lower KR allows for resolving nearly the entire range of scales. The application to the case of a turbulent wake showed that sub-Kolmogorov spectrum is recovered using OF but not using CC.

Considering all the tested cases, we can conclude that CC PIV can be more precise than OF based on pure velocity calculations. However, OF's diffusion decreases the variance of the velocity gradients. This proves to be a critical advantage when PIV is applied to experimental turbulent flows, with windows nearly the size of the particles. OF is therefore more relevant to study such flows when the camera sensor is able to resolve enough particles

and achieving viscous sub-range resolution. This result opens new alleys to study the effect of small-scale turbulence in high-Reynolds number turbulent flows.

Chapter 5

A rapid PIV system development

5.1 Algorithm integration in software platform of Eyemotion

An intense collaboration with the industrial partner Photon Lines, and particular its R&D team was carried out to implement the algorithms of PMMH lab in the software tools of Photon Lines. Photon Lines has developed the software called Eyemotion; Eyemotion is a native code image acquisition software containing a large variety of built-in offline and online (real-time during acquisition) image processing tools like image compression, binarisation, convolution, image cropping, Roberts/Sobel filters. It is compatible with a large variety of cameras (PCO, BASLER, Zylon, to name a few).

Previous to the thesis, the OF algorithm had been integrated in the form of dynamic library, and was operated in the laboratory of PMMH inside the graphics programming environment of Labview for a number of years (Gautier, 2014). A development using OPENCV and Microsoft Visual Studio was performed to integrate the OF algorithm of the lab inside the software platform Eyemotion of Photon Lines: A common server was setup and accessed by both the author and company engineers in order to have optimal and safe version verification during the debugging and development period. A light benchmarking tool of the algorithm was developed in order to fast check different GPU performances in different machines. The API calls and memory handling of the external functions of the algorithmic core were optimised. A new option has been added in order to save real-time the velocity fields and not the images. This option will save around 50 % of hard disk space, for experiments where saving the images is not needed.

The algorithm performance was analyzed using the NVIDIA Visual Profiler, in order to find and optimize the most computationally costly functions. A time-line of all the functions called can be visualised, together with the FLOPs (Floating Point Operations per second) and bandwidth performances as seen in a screenshot in figure 5.1. It was found that around 50% of the computational time consisted in calls of the convolution function. An optimal library from NVIDIA is used for this function in order to divide calculations of convolution in row and column form. It was verified moreover that the GPU cores occupancy during these function calls is the maximum possible; as seen in figure 5.2 we can see that we reach a satisfying occupancy of more than 80 % (the theoretical maximum occupancy can almost never be achieved practically). The computational speed was around 30 Mb/s of calculation performance for 1 Mp images; a rigorous study on performance using various images and hardware components is presented in section 5.3.

5.2 Graphics User Interface design

A full GUI design for the PIV interface inside the software of Eyemotion was performed, regarding colorbars, vector plots, and visualisation windows, in the same line as other commercial PIV products. Four windows were created. The image acquisition window, the PIV

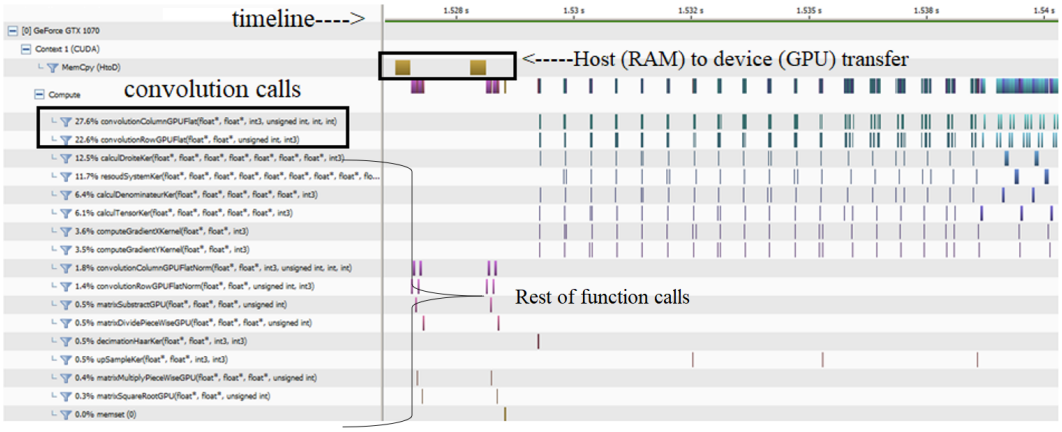

FIGURE 5.1: NVIDIA Visual Profiler analysis of a single displacement field calculation using OF. Convolution functions occupying more than 40 % of computational time.

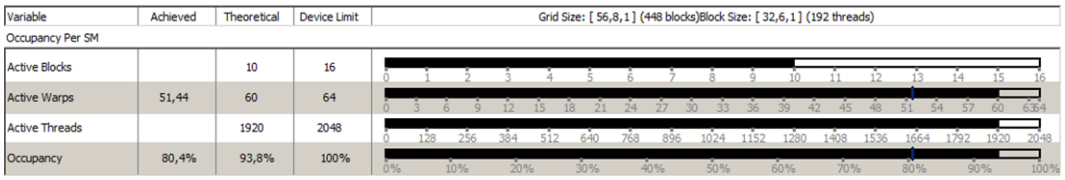

FIGURE 5.2: Occupancy test of GTX 1070 GPU during a velocity field calculation using the NVIDIA Visual Profiler.A satisfying GPU occupancy of more than 80 % observed.

parameters window, the 2D plotting window and the 1D plotting window. In the image acquisition window all the tools of real-time image processing (like filters and cropping) are integrated and can be performed in parallel with the PIV plugin. In the PIV parameters window, a choice is given to the user to visualise velocity components or magnitudes, with or without colours and with or without vectors. The density and size of the vectors is modifiable by the user, although an optimal default proposal is proposed by the software. In the 2D plotting window we can visualise different 2D variables derived by the velocity calculations. The 2D recirculation area, swirling strength and Q-criterion as well as the mean fields and fluctuation kinetic energy was included. A screenshot of the GUI can be seen in figure 5.3. In the 1D plotting window we included the visualisation of all scalar variables derived by the velocity: The total recirculation area, the swirling strength and Q criteria calculated in a window as well as the mean velocity value. The velocity profile along a line defined by the user can be plotted in the same window.

A multi-GPU option, was also integrated and is currently being tested in order to reduce the computational time. A window was integrated showing the list of the available NVIDIA GPUs in the workstation; the user, can select the number of GPUs he wants to use for the calculation in the window GPU, as seen in figure 5.3. When more than one GPUs is selected, the image is divided in 2 parts and each GPU calculates the displacements for each one. An optimal overlapping of the 2 parts of the images is selected in order to correctly reconstruct the full field after the calculations in the separate GPUs is performed. Tests are currently underway to test if this methodology reduces the computational time.

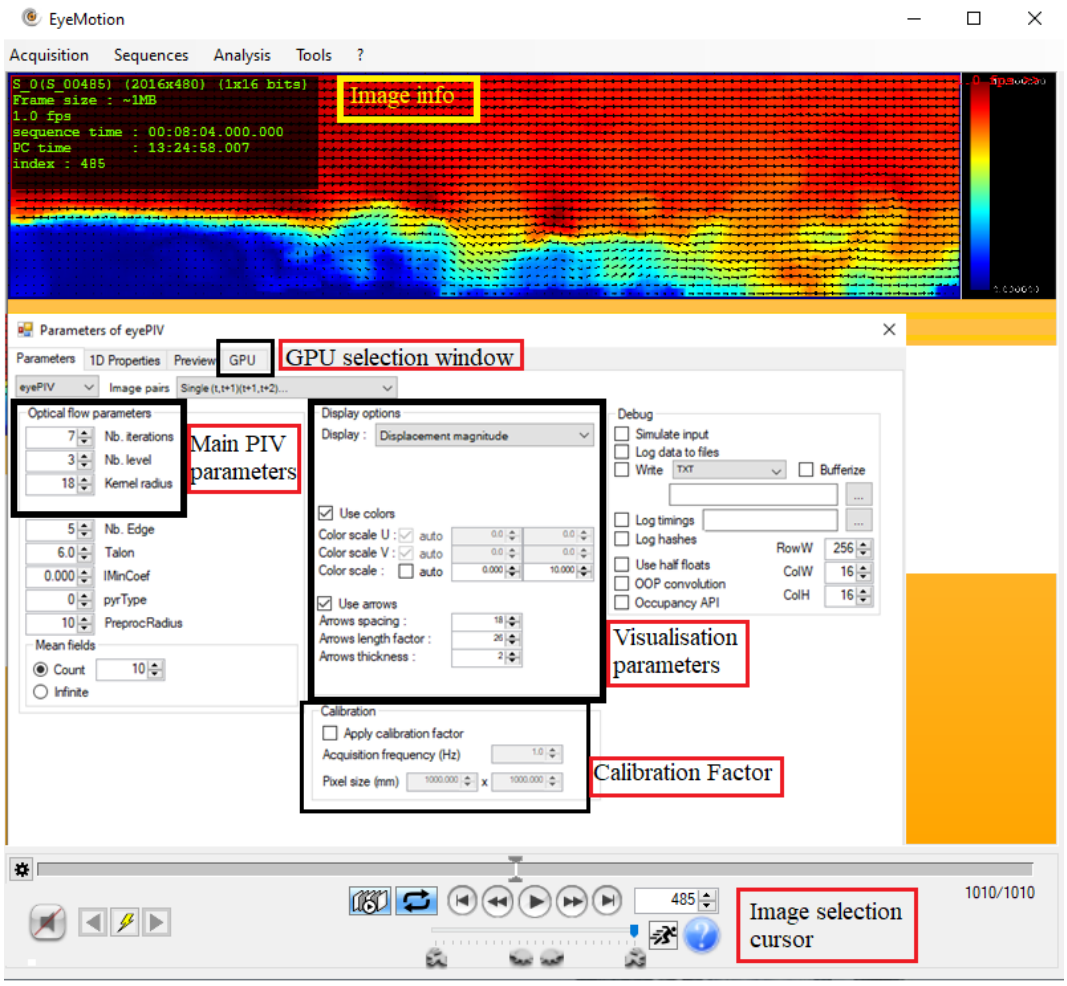

FIGURE 5.3: Screenshot of the designed GUI for the PIV plugin, integrated inside the software Eyemotion of SeeFast Technologies (PhotonLines, 2021). Backward-facing step flow velocity magnitude at $Re_h = 2700$.

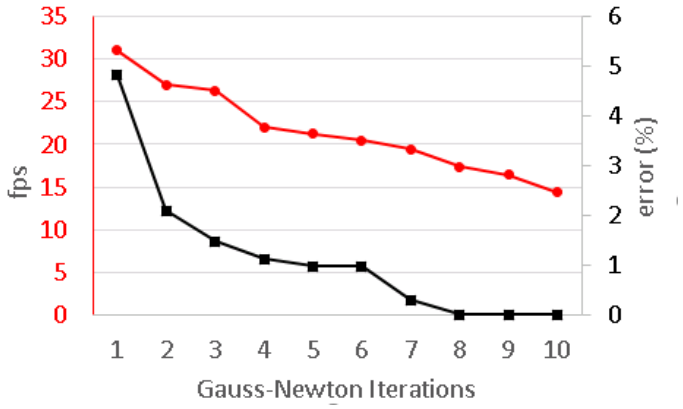

FIGURE 5.4: Number of iterations, introduced error and fields per second sensitivity study for 4.2 Mpixel PIV images using the RTX 2070 NVIDIA GPU.

5.3 Speed performance measurements

There are three main parameters that affect the computation time of the present OF algorithm: the image size and depth, and the number of Gauss-Newton iterations to converge. The number of the maximum iterations of the OF algorithm can be selected by the user and has been rigorously studied in Gautier, 2014. Results using the recent GPU RTX 2070 various number of iterations are presented in 5.4; we mention that the standard number of iterations for the solution of the displacement to converge is 5-7, but keeping a number of iterations as low as 2 can double the computational, speed introducing only a 5 % error. In the case of closed-loop control experiments though, where PIV is used as a sensor, these errors can be negligible, as was seen in Gautier and Aider, 2014.

The image size and depth is also crucial for the computational speed, as shown in figure 5.5. Images up to 30 Mp have been tested. For real-time control experiments, where rapid calculations are needed (Gautier and Aider, 2014), an 8 bit camera sensor can be used; with as many as 3 iterations and a 1 Mp size sensor we can reach more than 100 fields per second of real-time calculation, which is to our knowledge the fastest PIV setup presented. This presents a real opportunity for visual sensors to be used in control experiments and is to our knowledge the fastest PIV algorithm worldwide today.

Last but not least, each NVIDIA GPU generation includes various ameliorations (apart from the clock speed and bandwidth that play and important role). Various GPUs have been tested, showing better results for the newer generations, but without clear answer on which GPU specification is the most important so far. Results of testing of 3 GPUs in the same workstation (Windows 10, 64 bit, 64 Gb RAM and AMD EPYC 7302P 16-Core Processor CPU at 3 GHz) are presented in figure 5.6 for a set of 16 bit images. Further investigation of GPU comparisons are underway; they will shed more light on which GPU specifications are most important for the OF algorithm and how to optimise the hardware setup.

5.4 Speed and disk occupancy comparisons with Cross-Correlation PIV

The computation and saving time performance with a standard commercial CC PIV solution was performed in the same 64*bit* workstation; a Precision 7920 Dell tower with an Intel Xeon GOld 5120 CPU @ 2.2 Ghz and 128Gb RAM. Standard 1 Mp PIV images with 12bit

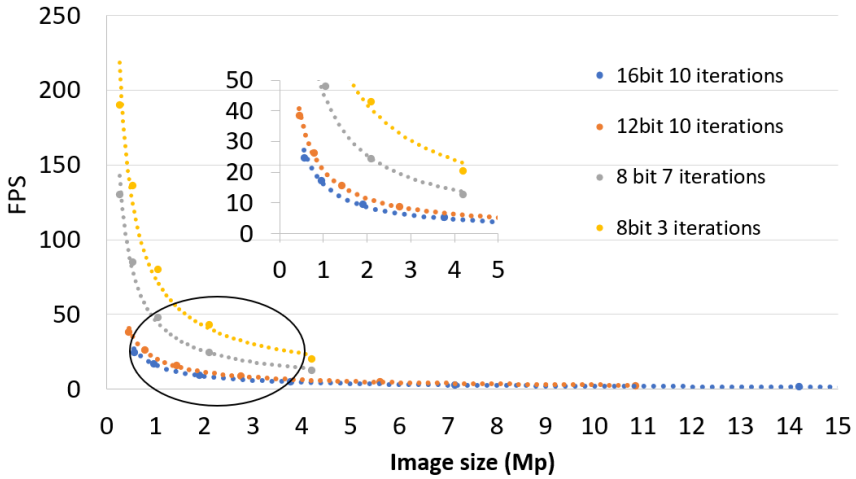

FIGURE 5.5: Influence of image depth and size and number of Gauss-newton iterations on the computational speed. Calculations performed on the NVIDIA RTX 2070.

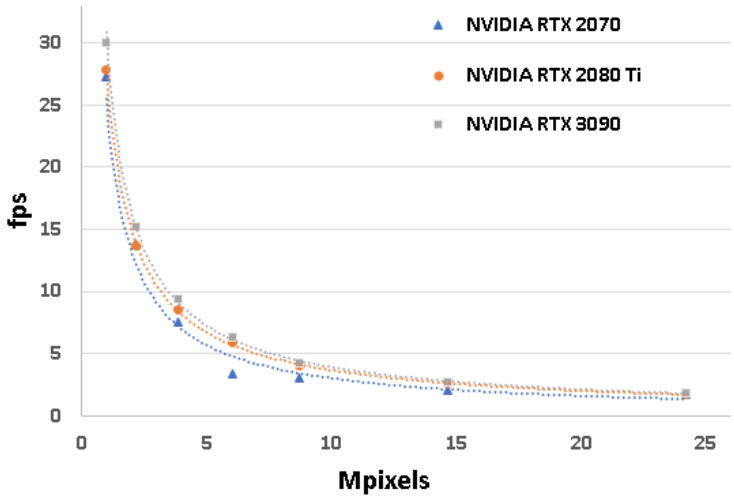

FIGURE 5.6: Fields per second calculated for different image sizes and 7 iterations. 3 different GPUs tested in the same workstation.

	OF	CC PIV
Mb saved field/Mb image	213	23
Mb saved field/vector	7.8e-6	4.8e-6
Mb saved total(image+field)/ vector /image	5.33E-06	1.01E-05
s/field calculated +saved	0.03	1.8
s/vector calculated +saved	1.16E-07	4.4E-05

TABLE 5.1: OF vs CC PIV comparison for overlap of 87.5%. Calculation speed and disk space occupancy.

	OF	CC PIV
Mb saved field/Mb image	15.1	31.3
Mb saved field/vector	1.4 e-5	4.2e-5
Mb saved total(image+field)/ vector /image	1.4e-5	4.2 e-5
s/field calculated +saved	1.25	14.7
s/vector calculated +saved	1.3e-6	2.3e-5

TABLE 5.2: OF vs CC PIV comparison for overlap of 50%. Calculation speed and disk space occupancy.

image depth visualised in figure 5.3 were used. The workstation was equipped with a CUDA-enabled GTX 1080 GPU; both algorithms made use of the GPU for parallel calculations. The CC PIV algorithm tested in this section is the commercial software DaVis 10 from Lavision (LaVision, 2021). Furthermore, the disk occupancy was compared as well. We mention that in Eyemotion, we save the fields in a tif format, whereas DaVis has its proper saving format in a MATLAB structure form (pivmat). The author would like to thank Tao Liu for the post-processing of the results using DaVis 10.

The results for a standard parameter set (size of $IW = 12$, 50% overlap, $512x480$ image size) showed the following the results presented in table 5.1. OF was faster 60 times and occupied 10 times less disk space as well, which verifies previous findings in a similar comparison with state-of-the-art CC PIV algorithms by Champagnat et al., 2011. For a dense field calculation from CC PIV (overlap of 87.5% image size 2016x480, 12 bit image) the comparison showed one order of magnitude difference in calculation. The space occupancy was twice larger for CCPIV as well. Result are presented in table 5.2.

5.5 Hardware part of the PIV system: integration and perspectives

The hardware of the designed PIV system consists of a fast camera, a pulsating or continuous laser (depending on the PIV application), and of course a powerful workstation with a CUDA-enabled GPU. The choice of the GPU is very important. Strong hints revealed in the NVIDIA Visual Profiler analysis (see figure 5.1, suggest that the L-K iterative OF algorithm is mostly a memory-bound application, due to the multiple need of each pixel In the convolution during Gaussian blurring for each pixel. A memory-bound application is a code where memory access is what is slowing down the calculation (in our case GPU memory). Hence GPU bandwidth could be more important than the concurrent threads per streaming multiprocessor (which is proportional to the number of cores). Further investigation of GPU specifications comparisons in the same workstation are currently underway to shed more light. We mention that for compute-bound kernels, the register count typically limits the number of concurrent threads per SM. The laboratory is equipped with various NVIDIA GPUs that are currently being tested: the TESLA K80, RTX 2070, the GTX 1070, GEforce560, and more recently the RTX 2080 Ti and the RTX 3090.

In figure 5.1 we can see the timeline of a single velocity field calculation. Each function calling is displayed together with its computational time on the left. The separable convolution function is called more than 100 times and in total consists of more than 45 % of the total computational time. The convolution function is called during Gaussian blurring, and can be done fully in parallel in an FPGA card. This is one of the long-term strategies of the product development, to transfer the algorithm in FPGA language, which would possibly reduce the computational time since the convolution function is ideally parallelizable in an FPGA card. This study though is beyond the scope of this thesis. The transfer of the matrices from host

(meaning the RAM) to device (meaning the memory of the GPU) was found less than 10 % of the total calculation time and is considered to be eliminated with the unified memory architecture that will be implemented in NVIDIA hardware the next years. The concept of Unified Memory consists in a single memory address space accessible from any processor in a system. The hardware long-term plans of NVIDIA regarding this idea are to install an embarked CPU processor on the GPU card so that no time is wasted in the transfers with motherboard buses.

5.5.1 RAID 0 disk implementation

A new workstation was dimensionalized in order for the motherboard to be able to host multiple GPUs together with a PCI or PCI express camera frame grabber. The timeline of a real-time calculation can be thought as a series of actions of image acquisition, field calculation-field or scalar velocity-derived variable calculation and result saving. A simple schema can be found in figure 5.9. It is often seen that the slowest part of the system can be the saving part in the disk, especially for large images. For this reason a RAID 0 implementation was applied in our workstation; A RAID 0 disk configuration means that when we save a file, it is divided in pieces to be saved at the same time in 2 different disks. That way the writing speed is usually doubled. On the other hand, if one of the 2 disks is faulty then we result in losing all the information, because each file is incremented in pieces during the saving process. In the new workstation the RAID 0 system was tested with extremely satisfying speed results, as presented below: With no RAID 0, on an SSD the writing speed was 299.46 Mo/s. Including the RAID 0 setup on latest generation SSDs the writing speed was tested to be more than quadruple, 1336.5 Mb/s. we mention nonetheless that the developed software, Eyemotion, does not work serially in the acquisition and calculation sequence and has a confidential buffering system to maximize image acquisition and processing flow. Moreover, the option for the user to save in real-time only the velocity fields and not the images was integrated. This solution can be crucial when acquiring large images and can save up to 50 % of hard disk space, for experiments where saving the images is not needed.

5.6 A real-time PIV system

As reported very early by Champagnat et al., 2011, the presented OF algorithm, when implemented in CUDA functions, gives the opportunity of a 50x faster computational time than other state-of-the-art PIV algorithms. A real-time PIV system of this algorithm was first adapted by Gautier and Aider, 2013 in the laboratory of PMMH and is to our knowledge the fasted PIV system today, with a speed of more than 100 fields per second as presented in figure 5.5 in the previous chapter.

This extremely small computational time can not only give the user real-time feedback when he is setting up experimental parameters like Kernel Radius window size, acquisition frequency, maximum particle displacement and number of field to converge to a mean flow, but also give access to further real-time calculations of velocity-derived variables as well, like the recirculation area of a wake or the swirling strength vortex identification criteria. Such post-PIV calculations have already been used as sensors for closed-loop flow control experiments, while the OF algorithm was implemented in the software environment of Labview (Gautier and Aider, 2013; Gautier and Aider, 2014). The above real-time PIV system was integrated in the software of Eyemotion, since the latter gives access to optimized data flow, more simultaneous image processing tools and is compatible with a larger variety of cameras. The user has a variety of post-velocity variables to chose as sensor signals, like recirculation area, vortex identification criteria, fluctuation kinetic energy and more as seen in figure 5.8. A Region Of Interest can also be defined inside the software to restrict the

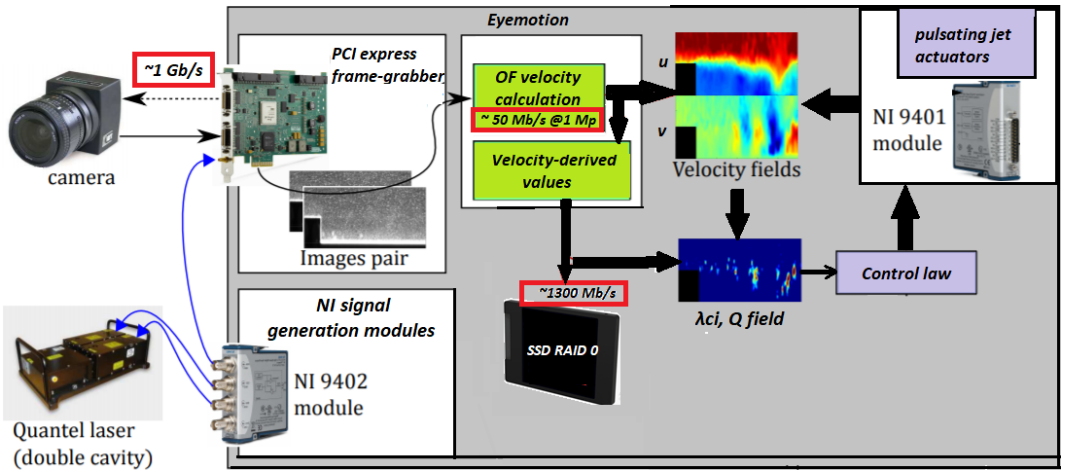

FIGURE 5.7: Real-time experimental setup of the laboratory: a rapid PIV software, synchronising fast camera and pulsating laser for real-time velocity calculations and closed-loop control experiments (Gautier and Aider, 2014).

sensor and velocity calculations in a specialised region of the field. Furthermore, an option is integrated in order to generate actuation signals in a closed-loop form inside the software, according to velocity-derived sensors. The system to generate signals for actuators was successfully tested, using the electropneumatic actuators SMC ITV 1010. This option can give the opportunity to perform optimally closed-loop flow control experiments, based on the visual sensors coming from PIV calculations. A full schematic of the elements such a PIV system with an actuator reaction mode integrated is presented in figure 5.7. A communication module between MATLAB and Eyemotion was also integrated, giving the chance to the user to run MATLAB scripts while acquiring images.

As seen in figure 5.9, 2 PIV modes were integrated: pulsating (used mostly in wind-tunnels) and continuous laser (for use mostly in hydrodynamic channels). In the second case, no need for synchronisation with the laser is needed. We mention though that in the software Eyemotion, the sequence of image acquisition and field calculation is not done in a serial master-slave architecture as seen in the figure 5.9, rather than with a parallelized way using a spacial buffering system; this maximises the data flow. More details cannot be discussed due to confidentiality. The camera-laser synchronisation was tested successfully, using a double cavity laser by Quantel-BigSkylaser.

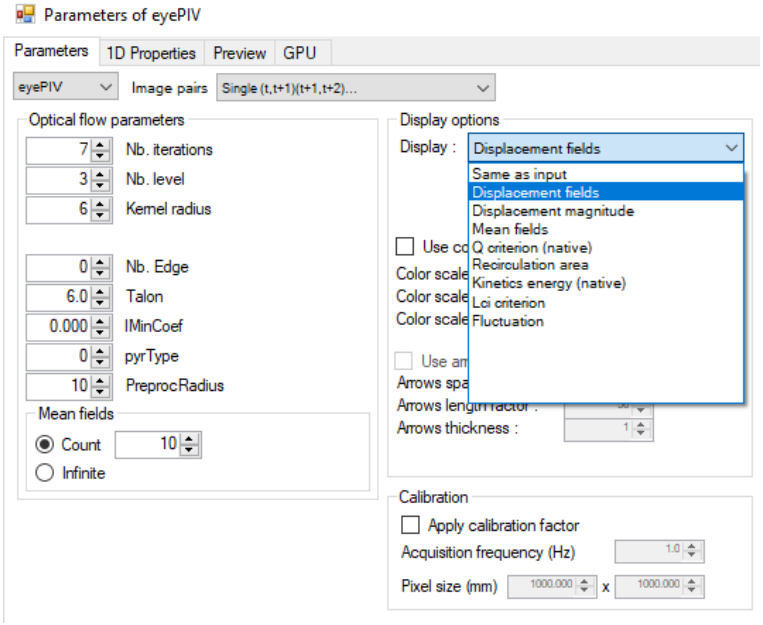

FIGURE 5.8: 2D instantaneous velocity-derived variables list available.

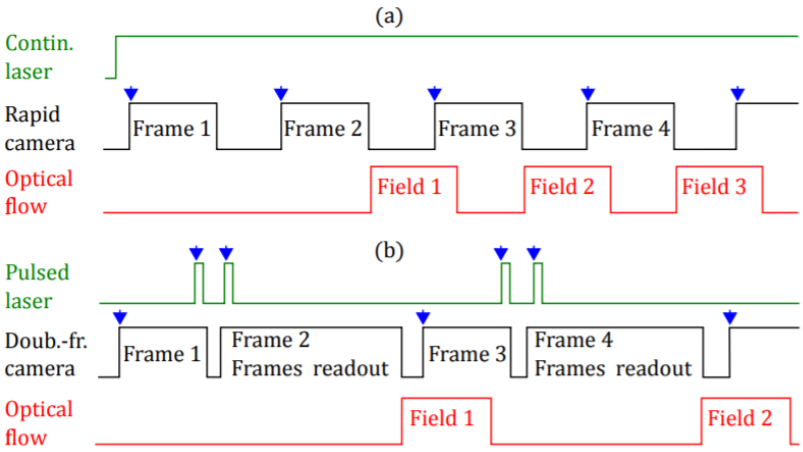

FIGURE 5.9: Sequence diagrams of laser pulse, image acquisition, and field computation.

Chapter 6

Acceleration and pressure reconstruction from non-time-resolved particle image velocimetry: Application to turbulent flows

The content of this chapter is based on the article: *A.Giannopoulos, P.-Y.Passaggia, N.Mazellier, A. Kourta, J.L.Aider, Acceleration and pressure reconstruction from non-time-resolved particle image velocimetry: application to turbulent flows, to be submitted in Physical Review Fluids, 2021*

The present chapter investigates the algorithmic approach to compute acceleration and pressure from single-snapshot Particle Image Velocimetry (PIV), based on Optical Flow (OF). Regarding the pressure reconstruction methodology is based on the recent work of Passaggia et al. (2020). Regarding the acceleration term, we describe a method structured on second-order finite differences and use the vorticity-streamfunction formulation to exclude the pressure term and estimate the local acceleration only from an image pair. The acceleration term is then used to estimate pressure in the two-dimensional plane; a quite satisfying agreement is observed for Direct Numerical Simulation data and synthetic particle images processed with the OF method in the case of two-dimensional homogeneous turbulence. Then, we consider the mean Turbulent Kinetic Energy (TKE) budget in the near wake of a bluff body at $Re = 5 \times 10^4$ and show that all the terms can be accurately estimated using an isotropy assumption. Using highly-resolved PIV measurements in the wake, we are able to recover the pressure spectra as well as the mean pressure-velocity contribution in the energy budget, and provide an accurate estimate of the mean dissipation. More importantly, we show that the pressure-correlation term plays a dominant role in the turbulence kinetic energy budget when analysing the recirculation region area. The present method naturally extends to non-time resolved three-dimensional tomographic measurements where all the components to estimate pressure are readily available.

6.1 Introduction

Particle Image Velocimetry (PIV) is an important non-intrusive experimental technique widely used for almost 40 years in fluid dynamics research and the industry for velocity field measurements (Stanislas, Okamoto, and hler, 2003). Pressure measurement from non-intrusive sensors plays a key role in various applications like fluid-structure interaction, compressible and stratified flows and pipeline monitoring (Sadeghioon et al., 2014; Elsinga et al., 2004;

Rapaka, Gayen, and Sarkar, 2013). An effort to use PIV as such a indirect pressure sensor have been made in the past. In wave experiments, Jensen and Pedersen, 2004 used PIV to determine the acceleration and pressure term, and Koengeter, 1999 investigated the pressure variations in vortical structures occurring in the shear layer behind a surface mounted obstacle. Kindere et al., 2019 relied on Taylor's hypothesis to determine the pressure in a non-time-resolved turbulent boundary layer PIV experiment ; a review of such efforts can be found in (Oudheusden, 2013). Recently, a method to obtain instantaneous measurements of pressure and wave flux in stratified incompressible flows were presented for the first time using combined time-resolved PIV and Synthetic Schlieren (SS) (Passaggia et al., 2020). Only PIV alone was shown to work only in limited cases and the best results were achieved combining SS and PIV to calculate pressure. Results were validated against direct numerical simulations for internal waves focusing above a three-dimensional Gaussian ring.

One of the key quantity to estimate instantaneous pressure from PIV comes from the ability to measure highly accurate time derivatives of the velocity, thereby, the acceleration of the fluid. To this end, triple- and quadruple-pulse PIV experiments were designed, but most authors outlined the difficulty to measure accurate accelerations from such measurements (Ding et al., 2013; Westerweel, Elsinga, and Adrian, 2013). Kurtulus, Scarano, and David, 2007 calculated acceleration from time-resolved PIV measurements using finite differences in the case of a square cylinder flow, but in fact, using finite differences to estimate time derivatives inherently introduces noise, which is particularly hard to control or minimise.

On the other hand, instantaneous pressure measurements is key to turbulent-flows analysis, and in particular, to compute time-averaged budgets of coherent and fluctuating quantities. In this paper, we propose a novel approach to compute acceleration and pressure from single two-dimensional-two component PIV snapshot. More precisely, we use the vorticity equation and the streamfunction to obtain an estimate of the temporal derivative. This quasi two-dimensional method is validated on time-resolved synthetic PIV images computed from a two-dimensional direct numerical simulation of turbulence. The same method is then applied to the TKE budget in the recirculation region of a turbulent flow behind a two-dimensional D-shaped bluff body where PIV is calculated using the OF method. Using the isotropy assumption for the missing terms, we show that the turbulence kinetic energy is accurately predicted everywhere locally. The present method is also more accurate than using the frozen Taylor's hypothesis to estimate acceleration, in particular for regions where the mean velocity is close to zero. These measurements are combined with instantaneous pressure measurements which finally allows for an accurate estimation of the dissipation in the wake which is validated using direct measurements from PIV.

The chapter is structured as follows; section 6.2.3 details the methodology to estimate acceleration and pressure from instantaneous velocity measurements. The method is first validated in section 6.3 on the synthetic dataset of two-dimensional homogeneous isotropic turbulence (HIT), by comparing with the corresponding DNS data. The same technique is then applied to the flow in the wake of a bluff body in section 6.4; further validation will regard the TKE budget calculation, using direct high-resolution PIV measurements and a global budget in the control volume available. Conclusions and perspectives are given in section 6.5.

6.2 Acceleration and pressure from a single PIV snapshot

6.2.1 Projection onto a divergence-free field

The present model-based approach to estimate the temporal derivative from a single snapshot requires certain constraints on the velocity field. We begin with the definition of the

streamfunction ψ which reads

$$\nabla^2 \psi = -\omega, \tag{6.1}$$

where ω is the vorticity vector defined as $\omega = \nabla \times \mathbf{u}$, $\mathbf{u}(x,y,z,t)$ is the velocity vector $\mathbf{u} = (u,v,w)$, $\nabla = [\partial_x, \partial_y, \partial_z]$ is the gradient operator, and ∇^2 is the Laplacian $\nabla^2 = [\partial_{xx}, \partial_{yy}, \partial_{zz}]$. Solving equation (6.1) for ψ provides the solution to the Helmholtz equation with non-homogeneous Neumann boundary conditions $(\nabla \times \psi) \cdot \mathbf{n} = \mathbf{u} \cdot \mathbf{n}$. In the two-dimensional case, in the (x,y) plane, the vorticity and the streamfunction simplify to scalar equations of the form

$$\nabla^2 \psi_z = -\omega_z, \quad \text{with boundary conditions,} \quad \partial_x \psi_z = -v \ \text{ and } \ \partial_y \psi_z = u. \tag{6.2}$$

In the case where the flow is expected to be two-dimensional, equation (6.2) provides a basis to obtain the temporal derivative from the vorticity equation without approximation. In the case of three-dimensional data, equation (6.1) has to be solved which is not a trivial task because of boundary conditions. In what follows, we will be only solving the two-dimensional problem in the case of two-dimensional synthetic data. In the case of a three-dimensional flow in a two-dimensional plane, as for turbulent flows in a 2D plane, we will have to proceed with approximations to the vorticity equation to estimate the temporal derivative.

6.2.2 A quasi two-dimensional approximation to the time-derivative

Assuming that the quality of the PIV data is sufficient to resolve all the details of the flow, we propose an approach to calculate the temporal derivative of the velocity using a single snapshot of PIV. Note that the problem arising from unresolved spatial scales is left for future work. Making the approximation that the flow is essentially driven by its two-dimensional dynamics, the vorticity equation can be used to estimate the temporal derivative of the vorticity in the z direction. The vorticity equation in vector form yields

$$\frac{\mathrm{D}\omega}{\mathrm{D}t} = (\omega \cdot \nabla)\mathbf{u} + \nu \nabla^2 \omega. \tag{6.3}$$

and reduces to

$$\frac{\mathrm{D}\omega}{\mathrm{D}t} = \nu \nabla^2 \omega, \tag{6.4}$$

in the two-dimensional case. In the present analysis, we are restricted to the streamwise and normal velocity components (u,v) and the only contribution of the vorticity is $\omega_z = \partial_x v - \partial_y u$. While this is not an issue for two-dimensional flows where all components of the flow to solve equation (6.4), The three-dimensional case is more challenging.

For instance, in a strongly turbulent flow, where viscosity is small compared to the other terms, the vorticity equation in the (x,y) plane writes

$$\frac{\partial \omega_z}{\partial t} = -u\frac{\partial \omega_z}{\partial x} - v\frac{\partial \omega_z}{\partial y} - w\frac{\partial \omega_z}{\partial z} + \omega_x \frac{\partial w}{\partial x} + \omega_y \frac{\partial w}{\partial y} + \omega_z \frac{\partial w}{\partial z}. \tag{6.5}$$

where the last term is the vortex stretching term component arising from the three-dimensional nature of the flow and the two other production terms correspond to the vortex turning terms.

However, the only terms that can be directly estimated from equation (6.3) for the two velocity components (u,v) in the (x,y) plane are

$$\frac{\partial \omega_z}{\partial t} = -u\frac{\partial \omega_z}{\partial x} - v\frac{\partial \omega_z}{\partial y} + \omega_z \frac{\partial w}{\partial z}. \tag{6.6}$$

Furthermore, using the divergence condition ($\nabla \cdot \mathbf{u} = 0$), we can rewrite the above as

$$\frac{\partial \omega}{\partial t} = -u\frac{\partial \omega_z}{\partial x} - v\frac{\partial \omega_z}{\partial y} - \omega_z\left(\frac{\partial u}{\partial x} + \frac{\partial v}{\partial y}\right). \tag{6.7}$$

Although several terms have been omitted in order to obtain equation (6.7), the latter allows for obtaining a two-dimensional estimate of the temporal derivative term computing the stream function ψ, defined as $(u,v) = \nabla \times \psi$. The problem to solve in order to estimate the temporal derivative writes

$$\frac{\partial}{\partial t}(u,-v) = \nabla \times \frac{\partial \psi}{\partial t} = -\nabla \times \nabla^{-2}\left(u\frac{\partial \omega_z}{\partial x} + v\frac{\partial \omega_z}{\partial y} + \omega_z\left(\frac{\partial u}{\partial x} + \frac{\partial v}{\partial y}\right)\right). \tag{6.8}$$

The first two terms on the right-hand-side of (6.8), in the parenthesis, are the advection terms while the third term is the vortex stretching term. There are therefore 3 terms missing here in the case of a three-dimensional flow for the out-of-plane vorticity ω_z: the out-of-plane advection term $w(\partial \omega_z/\partial z)$, the two vortex turning terms $\omega_z(\partial u/\partial z)$ and $\omega_z(\partial v/\partial z)$. Introducing the mean and fluctuation such that

$$\mathbf{u}(\mathbf{x},t) = \mathbf{U}(\mathbf{x}) + \mathbf{u}'(\mathbf{x},t) \;\text{ and }\; \omega_z(\mathbf{x},t) = \Omega_z(\mathbf{x}) + \omega_z'(\mathbf{x},t) \tag{6.9}$$

where $\mathbf{U}$ and Ω_z are the temporal mean while $\mathbf{u}'$ and ω_z' are the perturbations of the velocity and the vorticity respectively, we could estimate the right-hand side of (6.8) as to approximate the acceleration as:

$$\begin{aligned}\frac{\partial \psi}{\partial t} = -\nabla^{-2}\Bigg[&\left(U\frac{\partial \omega_z'}{\partial x} + V\frac{\partial \omega_z'}{\partial y}\right) + \left(u'\frac{\partial \Omega_z}{\partial x} + v'\frac{\partial \Omega_z}{\partial y}\right) + \Omega_z\left(\frac{\partial u'}{\partial x} + \frac{\partial v'}{\partial y}\right)\\ &+ \left(u'\frac{\partial \omega_z'}{\partial x} + v'\frac{\partial \omega_z'}{\partial y}\right) + \omega_z'\left(\frac{\partial u'}{\partial x} + \frac{\partial v'}{\partial y}\right)\Bigg].\end{aligned} \tag{6.10}$$

Non-homogeneous Neumann-type boundary conditions are given by $\partial v/\partial t = -(\partial^2 \psi)/(\partial t \partial x)$ and $\partial u/\partial t = (\partial \psi)/(\partial t \partial y)$. However, the temporal derivative of the velocity is not measured at the boundary and is therefore remains an unknown in the present analysis. An alternative way to estimate the temporal derivative is to use Taylor's frozen hypothesis which writes

$$\frac{\partial \psi}{\partial t} \approx ((\mathbf{U}\cdot\nabla)\psi)\cdot\mathbf{n}, \tag{6.11}$$

where $\mathbf{U}$ is the time-averaged solution. One could have argued that Taylor's frozen hypothesis derivative could have been used to estimate the temporal derivative solely based on equation (6.11). Although this assumption seems valid at first, it is not providing realistic temporal derivatives in regions where the mean flow $\mathbf{U}$ is small. This is particularly true, for instance in a recirculation region where there exists region where $\mathbf{U} = \mathbf{0}$, that is at the tip of the recirculation region and at the centre of the vortices. Using equation (6.11), the temporal derivative would be null which is incorrect. Instead, the strategy proposed in (6.8) contains a lot more information and could allow for tackling complex flow regions such as recirculation regions. Nevertheless, we use Taylor's frozen condition to estimate the boundary conditions for (6.8) such that

$$\frac{\partial}{\partial y}\frac{\partial \psi}{\partial t} = \frac{\partial u}{\partial t} \approx V\frac{\partial u}{\partial y} \quad \text{and} \quad -\frac{\partial}{\partial x}\frac{\partial \psi}{\partial t} = \frac{\partial v}{\partial t} \approx U\frac{\partial v}{\partial x}, \tag{6.12}$$

Since we do not have access to the temporal derivative at the boundary. Note that when

the mean flow is null, as for instance in the case of homogeneous and isotropic turbulence dataset, homogeneous zero-Neumann type boundary conditions can be considered.

6.2.3 Pressure reconstruction methodology

Pressure estimation in PIV has remained challenging, since acceleration is required in order to obtain an accurate estimation. However, measuring acceleration has remained an extremely challenging task in practice since it is particularly hard to measure acceleration from dense particle images. Depending on how the Poisson problem for the pressure is formulated, acceleration necessarily enters in the equations as

$$\nabla p = -\partial_t \mathbf{u} - (\mathbf{u}\cdot\nabla)\,\mathbf{u} + \nu\nabla^2\mathbf{u}, \tag{6.13}$$

which can be solved in two directions using a least squares to compute $p(x,t)$ or formulated as a Poisson problem as

$$\nabla^2 p = -\nabla\cdot\left((\mathbf{u}\cdot\nabla)\,\mathbf{u}\right), \tag{6.14}$$

with non-homogeneous Neumann boundary conditions

$$\nabla p\cdot\mathbf{n} = \left(-\partial_t \mathbf{u} - (\mathbf{u}\cdot\nabla)\,\mathbf{u} + \nu\nabla^2\mathbf{u}\right)\cdot\mathbf{n}, \tag{6.15}$$

where $\mathbf{n}$ is the normal vector to the boundary. In fact, the only way to get rid from the temporal derivative when computing pressure in a turbulent flow is to consider a fully periodic domain (i.e. together with periodic data) where periodicity naturally eliminates the boundary conditions. The later will be compared with calculations using boundary conditions to evaluate the quality of the prediction of the pressure solving either (6.13) in the least squares sense or the Poisson problem (6.14)-(6.15).

To solve (6.13) with a least-squares approach, we rely on the gradient field calculation, followed by the pressure gradient term calculation. The differentiation matrices are centred second-order stencils on a regular grid. The regularised least-squares Gradient-to-Surface Tikhonov method is then applied to calculate the pressure term (Harker and O'Leary, 2013). The order of the Tikhonov method was chosen equal to 2 and the parameter λ was chosen after a parametric study as $\lambda = 0.02$. Once the instantaneous pressure field is calculated, the first mode of the pressure term, the mean pressure is subtracted in the case of homogeneous and isotropic turbulence or estimated using a local pressure sensor. For the Poisson solver, we use the same method as Passaggia et al. (2020). Note that both the Poisson solver and the least squares solver were validated in their study on the focusing of internal waves on both time-resolved synthetic Schlieren and PIV.

6.2.4 Particle Image Velocimetry with Optical Flow

The OF algorithm tested in the present study is a dense, multi-pyramid Lukas-Kanade Optical Flow algorithm. The first version of the code has been developed at ONERA (Champagnat et al., 2011) and later modified, optimized and adapted to the constraints of real-time measurements by Gautier and Aider, 2015b. The advantage of this algorithm compared to a standard FFT-PIV algorithm is its high computational speed when implemented on GPUs with CUDA functions; it has been proved to be around 50 times faster than state-of the art PIV software (C.Pan et al., 2015; Champagnat et al., 2011). The algorithm consists in estimating at each pixel m the intensity displacement which minimises the sum of square differences between the intensity over a warped interrogation window (IW) of size equal to the Kernel radius (KR) at time t and the intensity over the warped IW at time $t' = t + dt$. The code has been used numerous times both for time-resolved PIV measurements (Varon et al., 2017), as well as for flow control experiments (Gautier and Aider, 2013; Gautier, 2014; Gautier and Aider, 2015a;

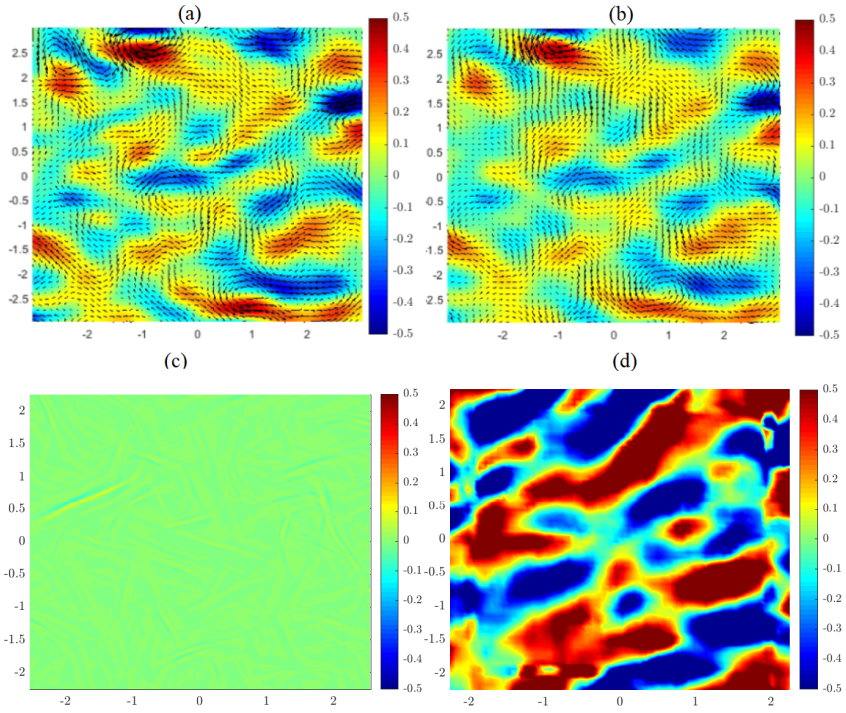

FIGURE 6.1: Instantaneous fluctuation velocity field results for the HIT dataset, DNS (a) and OF (b). Instantaneous divergence fields comparisons, DNS (c), and OF with KR=8 (d).

Varon et al., 2019). The same algorithm was used by Davoust, Jacquin, and Leclaire, 2012; Sartor, Losfeld, and Bur, 2012 to fast post-process their snapshots for a turbulence jet flow study and for an investigation of the interaction between a shock wave and a turbulent boundary layer, respectively. The solver was also recently analysed with respect to cross correlation methods and showed more diffusion but also more robustness than cross-correlation-based PIV methods when applied to turbulent flows and unresolved gradients (Giannopoulos et al., 2021)

6.3 Validation on Homogeneous isotropic 2D turbulence from DNS

The dataset presented here is published open access provided kindly by Carlier, 2005. It is the case of a self-sustained time-resolved Homogeneous Isotropic Turbulent (HIT) computed from a Direct Numerical Simulation, and their corresponding synthetic PIV images. The domain size is 2π and the number of snapshots used to gather statistics is 100. The time step between two images is 0.1 and the density of particles $C_p[N/px^2] = 0.014$, which translate in a displacement $\Delta x \approx 2.5px$ between two successive frames. The corresponding velocity fields from the DNS are shown in figure 6.1(a) and the corresponding solution computed with OF is shown in figure 6.1(b).

The case of two-dimensional isotropic turbulence is interesting to begin with since there is no missing velocity component and that velocity derivatives are not required to estimate pressure because of the periodic nature of the flow. Note that although the flow solution from the simulation is essentially divergence free, that is not the case for the OF results (see figure 6.1(c)). The divergence term is an indication of PIV error since, in the HIT dataset, the third component should be zero. A comparison for the divergence field DNS and the OF/ CC PIV approach shows an error of similar order for the 2 approaches. The KR used for the OF

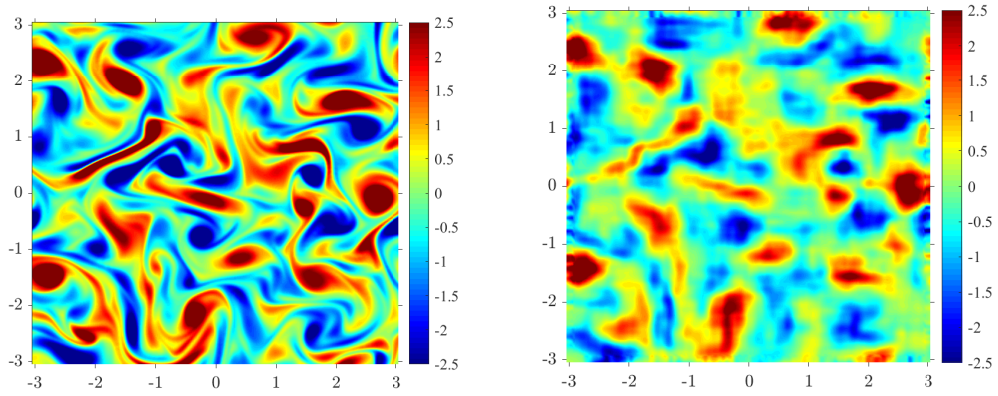

FIGURE 6.2: Instantaneous vorticity fields ω_z from DNS (left) and OF (right).

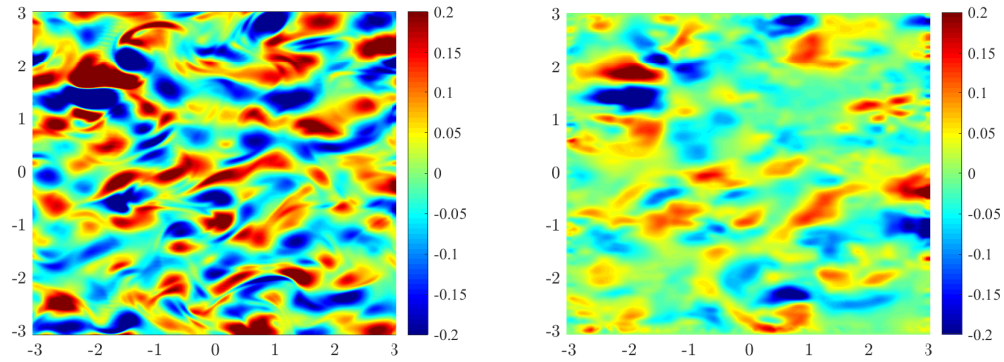

FIGURE 6.3: Instantaneous acceleration term $\partial u/\partial t$ from OF method with Poisson solver (right) and DNS Second order central schema for DNS results (left).

results in this dataset is $KR = 8$ pixels. The solution computed with the OF method therefore introduces a bias which leads to significant discrepancies in the divergence, but this will turn out not to be an issue for the estimation of the time derivative nor the estimation of pressure using least-squares methods (see Shanmughan et al., 2020; Passaggia et al., 2020 for a more complete discussion on this particular issue).

6.3.1 Border effect and filtering

The velocity field, which is our input for the acceleration and the pressure reconstruction algorithm may fail near the borders of the images or in near-wall regions. Border error effects are always present due to the fact that particles can be missing from the frame in two successive images since they may leave or enter the image. Therefore, we removed the first and last rows and columns of vectors for the analysis; particularly we cut each side a number of pixels 24 pixels, which guarantees we observe no border effects during pressure reconstruction, which was proven quite sensitive to this effect.

Furthermore, the gradient calculation used for the vorticity, the acceleration and pressure reconstruction can lead to artefacts in the reconstruction of the acceleration and the pressure field. In the HIT dataset, a spatio-temporal Savitzky-Golay filter was applied in the 3D

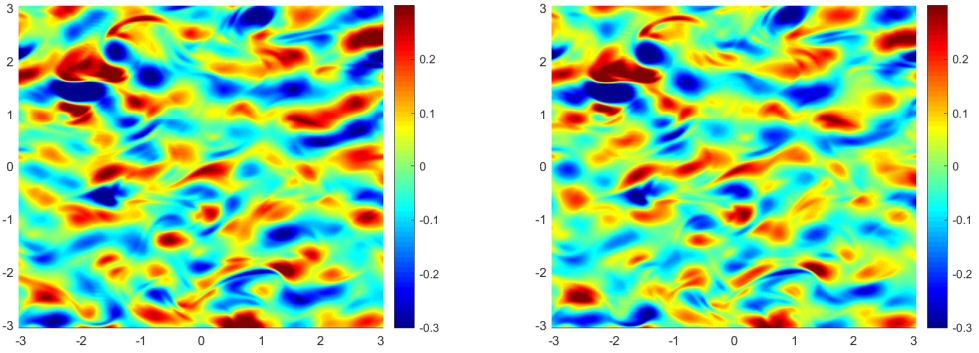

FIGURE 6.4: Instantaneous term of du/dt component first order backward schema for DNS results (left) and fourth order central schema (right).

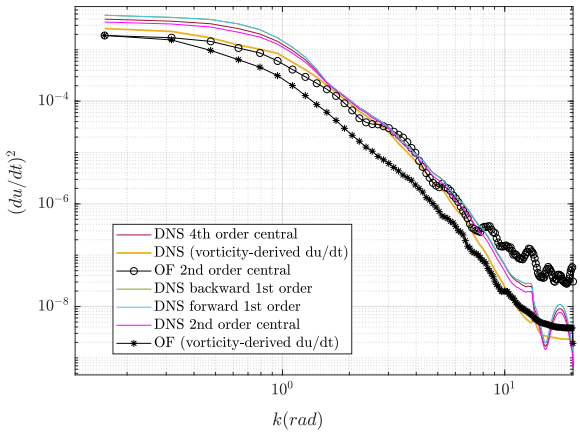

FIGURE 6.5: Acceleration term spectra comparison for different calculation schemes for OF and DNS: Direct finite differences of different orders and vorticity-derived acceleration terms are compared for both datasets.

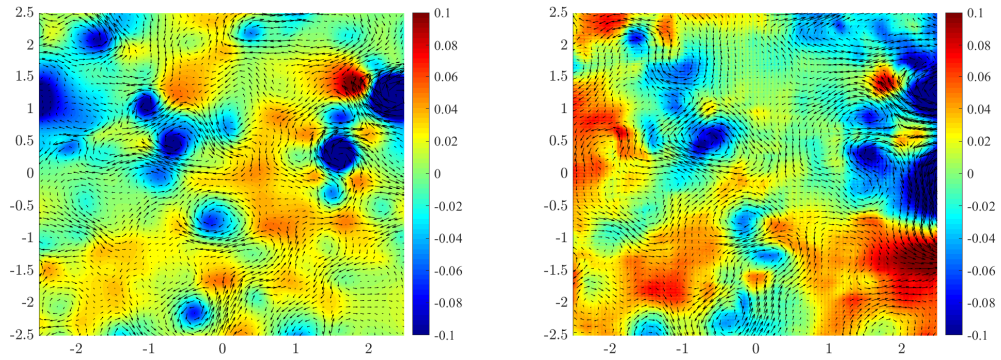

FIGURE 6.6: Instantaneous pressure and velocity vector field for DNS (left) and OF (right).

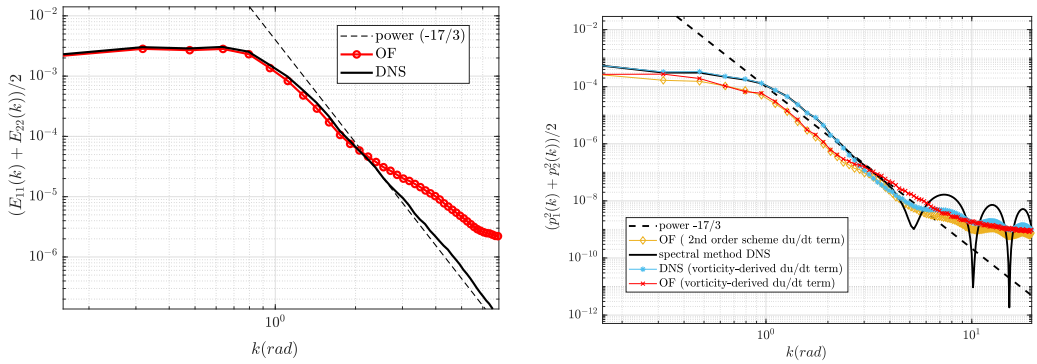

FIGURE 6.7: Time-averaged velocity (left) and pressure spectra (right), compared between OF and DNS. For pressure reconstruction from OF, different schemas are compared for the acceleration part.

matrix containing all the fields. A spatial window with a filter window of 11 pixels in space and 5 time-steps in time appeared to provide the best balance between signal and noise. The results can be found in figure 6.2(a) for the vorticity obtained from the DNS and the vorticity calculated using OF in figure 6.2(b).

6.3.2 Acceleration from single images in HIT

The temporal derivative for both the DNS and OF are estimated using equation (6.6) and equation (6.8). The results are shown in figure 6.3(a) and 6.3(b) for the DNS and OF respectively for $\partial u/\partial t$. The result looks qualitatively similar although very thin regions of the acceleration are clearly not captured. In addition, the temporal derivative was also computed using first and fourth order finite differences since the particular dataset is time-resolved, as shown in figure 6.4(a) and 6.4(b) but are essentially similar. Note that the second order finite difference estimate to $\partial u/\partial t$ is extremely close to the figure shown in 6.3(a) and quantified in figure 6.5 for each scale.

The time-averaged kinetic energy spectrum is shown in figure 6.7(left), where both the DNS and OF are compared. The two spectra are essentially similar for $k \leq 2$ but they differ for larger wavenumbers where the reconstruction with OF shows a less steep spectrum with an exponent close to k^{-2}. The spatial pressure spectrum (averaged in time and space as well) is shown in figure 6.7(right) for the DNS calculated using different methods: we begin comparing the results obtained with the spectral method against the vorticity equation to estimate

the temporal derivative and the least-squares method to compute the Poisson equation. Both methods provide nearly identical results except for $k \geq 4$, where the physics is lost using both methods. Note that both numerical strategies are significantly different but the results are essentially identical. The results obtained using the velocity field computed with OF are shown alongside. For wavenumbers $k \leq 4$, all spectra display the same slope. Here, the temporal term is computed using either second-order finite differences based on different snapshots in time while the second strategy uses the temporal term estimated using the vorticity method. For wavenumbers in the rage $1 < k < 4$, both spectra computed using OF collapse and are differ from the DNS by a factor 4. For lower wavenumbers, that is for $k < 1$, the temporal term estimated using the OF method differs by a factor 2 approximately, which is consistent with the results reported in figure 6.5 where the temporal derivative computed using OF is also more diffusive than for temporal term computed using finite differences. Indeed, as the quality of the data improves, this difference is expected to diminish and all spectra are expected to collapse for low wavenumbers. A fourth order scheme for the pressure calculation is also currently being investigated showing promising results.

In the next section, we use the vorticity-based algorithm to estimate the temporal derivative and provide an estimate of the pressure in the case of three-dimensional turbulence. The aim is to provide an accurate estimate of the transport equation for the TKE in both conservative and non-conservative form, using only 2D-2C PIV. In particular, we show that the present method allows for precisely estimating the TKE dissipation in the near wake of a bluff body.

6.4 Turbulent kinetic energy budget in the recirculation region of a bluff body

6.4.1 Experimental setup

Next, we consider the case of the near wake of a D-shaped bluff body. The experimental setup is also previously described used in the work by Giannopoulos et al., 2021 and analytically described in Shanmughan et al., 2020. It considers a novel dataset consisting of zoomed-in high-definition snapshots performed using a 29 Mpx ImperX CCD camera, with the aim of resolving scales from the integral lengthscale down to the Kolmogorov lengthscale. The low-speed wind tunnel cross section is $500mm500mm$ and is approximately 2000 mm long. The D-shaped model has a cylindrical nose of diameter $H = 40\ mm$. The characteristic lengthscale is the body height H and the streamwise and spanwise aspect ratios of $L/H = 4$ and $W/H = 12.5$, respectively. The model was 3-D printed and installed at approximately $14H$ from the inlet of the test section. The near wake is resolved and in particular, the region at $x/H = [0, 3.5]$ and $y/H = \pm 1.125$ with a resolution of 6600 px in the horizontal/streamwise direction x and 4400 px in the vertical/normal direction y. A KR of 18 pixels was chosen for the OF algorithm.

The Reynolds number is $Re_H = U_\infty H/\nu \approx 5.3 \times 10^4$, where the body height $H = 4\ cm$, the free-stream velocity $U_\infty = 20\ m.s^{-1}$ and the kinematic viscosity of air is $\nu = 1.5 \times 10^{-5}\ m^2.s^{-1}$. In addition, hot-wire measurements have been carried out at different vertical positions for $x = 3H$. In particular, we report turbulence kinetic energy spectra at $y/H = 0.5$ in order to compare the spectra of turbulence. An instantaneous velocity field can been seen in figure 6.8(a).

6.4.2 Pressure reconstruction and spectrum

We first analyse the velocity and pressure spectra obtained by OF in a vertical profile at $x = 3H$, as seen in figure 6.10(a). The velocity spectra are compared with hot-wire measurements,

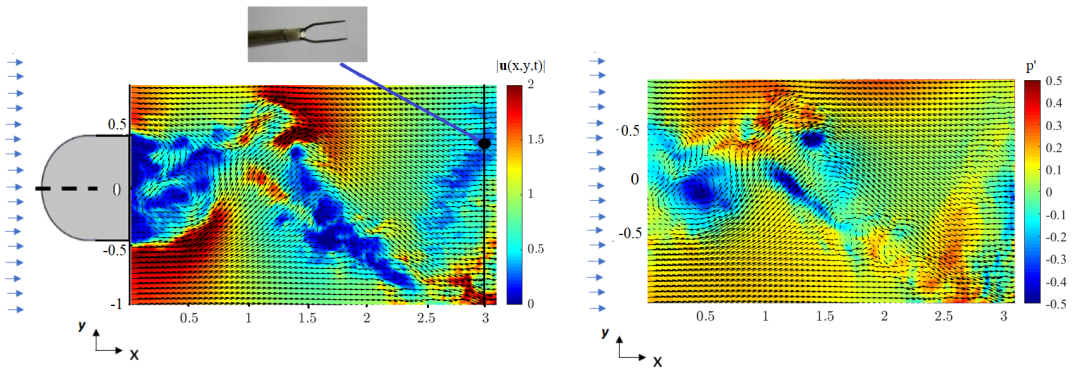

FIGURE 6.8: Instantaneous velocity field of D-shaped turbulent wake dataset and position of hot-wire probe (left) and instantaneous pressure field reconstruction of the same field (right).

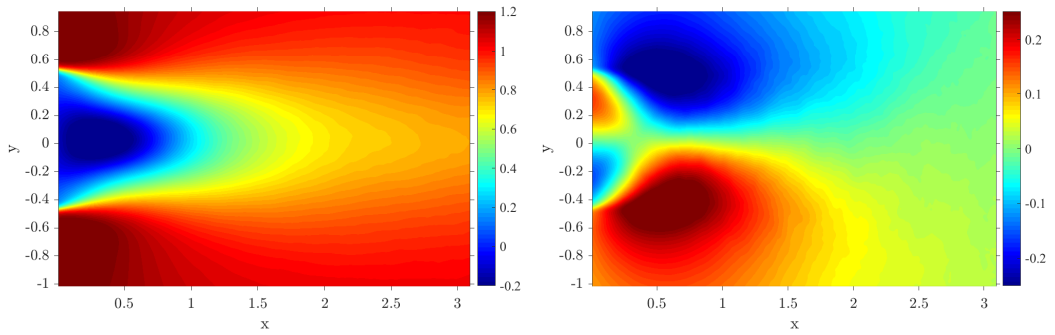

FIGURE 6.9: Mean fields of D-shaped turbulent wake dataset. Streamwise $\overline{u_x}$ (left) and spanwise $\overline{u_y}$ (right) components.

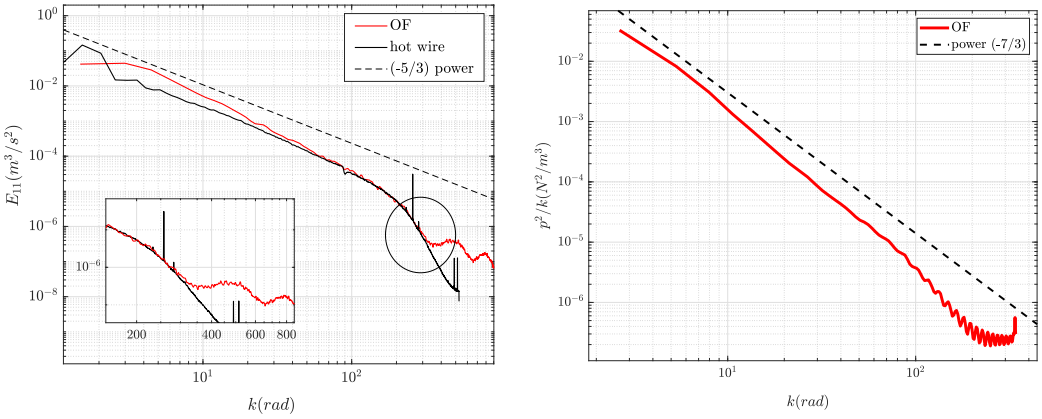

FIGURE 6.10: (a) Velocity spectrum obtained with OF together with the hot-wire measurements spectrum. (b) Pressure spectrum obtained from OF measurements.

showing a good agreement for the larger wavenumbers, in the Kolmogorov cascade and in the viscous subrange, up to $k = 300$. The first 2 modes of the pressure was subtracted, using experimental measurements. A subsampling of the initially calculated velocity vectors (which are the same as the number of pixels in the image) was made in the same order as the KR before the pressure reconstruction, in order to ensure the correct calculation of non-fictitious gradients.

Regarding the pressure reconstruction, the acceleration term computed using the method described in section 6.2.3 is shown in figure 6.10(b). An instantaneous snapshot of the velocity and its corresponding reconstructed pressure reconstruction field are also presented in figure 6.8(a,b). It is worth recalling that in the case of the wake, the mean flow is not null and that the boundary conditions to solve for the estimate of the acceleration are of non-homogeneous Neumann type, given by equation (6.12). These boundary conditions can be seen as advection-type boundary conditions for the velocity as often implemented in numerical solvers Marquillie and Ehrenstein, 2003; Gallaire, Marquillie, and Ehrenstein, 2007; Marquillie, Ehrenstein, Laval, et al., 2011; Passaggia and Ehrenstein, 2018 when collocation points are considered for both the velocity and pressure. The mean velocity fields are shown in figure 6.9 for reference. Note that at the top and the bottom boundaries, the mean vertical velocity entrains fluid into the domain while the outlet only advects fluid parcels out of the domain. At the inlet, both situations occur as velocity perturbations leave the domain in the recirculation region and enter on both sides of the recirculation region. The mean pressure spectra in the profile along $x = 3$, follows the theoretically expected $-7/3$ power law, as seen again in figure 6.10 (George, Beuther, and Arndt, 1984; Tsuji and Kaneda, 2012).

In what follows, we consider the Turbulence Kinetic Energy (TKE) transport equation and assess the quality of pressure reconstruction further, in order to validate our quasi two-dimensional approach.

6.4.3 Direct TKE budget calculation

For this experimental dataset, given that sub-Kolmogorov scales is accessible through PIV as presented in the spectrum in figure 6.10, an extra validation was performed.

The Navier-Stokes equations are first non-dimensionalised using the height of the body H and the free-stream velocity U_∞ such that

$$x_i = x_i^*/H, \quad t = t^* U_\infty/H, \quad u_i = u_i^*/U_\infty, \quad p = p^*/\rho U_\infty^2, \tag{6.16}$$

where the quantities with stars are dimensional variables. The Navier-Stokes equations in non-dimensional form therefore write

$$\frac{\mathrm{D}u_i}{\mathrm{D}t} = -\frac{\partial p}{\partial x_i} + \frac{1}{Re}\frac{\partial^2 u_i}{\partial x_j^2}, \tag{6.17}$$

where $Re = U_\infty H/\nu = 5.5\times10^4$ is the Reynolds number. Taking the dot product of equation 6.17 with the velocity vector u_i', one recovers the kinetic equation

$$\frac{\mathrm{D}k}{\mathrm{D}t} = -\frac{\partial\,(u_i p)}{\partial x_i} - \varepsilon + \frac{2}{Re}\frac{\partial}{\partial x_i}\,(u_i S_{ij}) \tag{6.18}$$

where $k = (u^2+v^2+w^2)/2$ and $S_{ij} = (\partial u_i/\partial x_j + \partial u_j/\partial x_i)/2$ is the symmetric part of the velocity tensor. The flow variables (u_i, p) are then decomposed between a temporal mean (U_i, P) and a turbulent fluctuation (u_i', p')

$$(u_i(x_i,t), p(x_i,t)) = (U_i(x_i), P(x_i)) + (u_i'(x_i,t), p'(x_i,t)). \tag{6.19}$$

and equivalently for the mean and the turbulent kinetic energy,

$$K = (U^2+V^2+W^2)/2 \quad \text{and} \quad k' = (u'^2+v'^2+w'^2)/2. \tag{6.20}$$

From an ensemble averaging of the kinetic energy equation for the fluctuation, one recovers the mean Turbulence Kinetic Energy (TKE) equation

$$\underbrace{U_j\frac{\partial \overline{k'}}{\partial x_j}}_{\text{Advection}} = -\underbrace{\frac{\partial \overline{u_j' p'}}{\partial x_j}}_{\substack{\text{Pressure}\\ \text{diffusion}}} - \underbrace{\frac{1}{2}\frac{\partial \overline{u_i' u_i' u_j'}}{\partial x_j}}_{\substack{\text{Turbulent}\\ \text{transp.}}} + \underbrace{\frac{1}{Re}\frac{\partial^2 \overline{k'}}{\partial x_j^2}}_{\substack{\text{Molecular}\\ \text{visc. transp.}}} \underbrace{-\overline{u_i' u_j'}\frac{\partial U_i}{\partial x_j}}_{\text{Production}} - \underbrace{\frac{1}{Re}\overline{\frac{\partial u_i'}{\partial x_j}\frac{\partial u_i'}{\partial x_j}}}_{\text{Dissipation}} \tag{6.21}$$

where each term is labelled for clarity and averaged using 4530 PIV snapshots. The last term is the dissipation, also noted as $\varepsilon = \frac{2}{Re}\overline{S_{i,j}' S_{i,j}'}$. In particular, we are interested in analysing the role of the pressure diffusion term. The mean reconstructed terms of the TKE transport equation can be found in figure 6.11.

Note that to compute the pressure-diffusion term from equation 6.21, $(\partial\overline{u_j' p'})/(\partial x_j)$, we compute $\overline{u_j'(\partial p'/\partial x_j)}$ since $\partial u_j'/\partial x_j = 0$ by definition. This is particularly important since p' is defined up to constant which vanishes when computing the gradient. The same conclusion can be drawn form the turbulent-transport term in equation (6.21) $(\partial\overline{u_i' u_i' u_j'})/(2\partial x_j)$ which is computed as $\overline{u_j'(\partial u_i' u_i')/(2\partial x_j)}$. In addition, because we only have access to two components of the velocity, that is u' and v', we make use of the assumption of isotropy of turbulence and use the following coefficient

$$\overline{k'}\Big|_{3D} = \frac{3}{2}\overline{k'}\Big|_{2D}, \quad \frac{\partial\overline{u_j' p'}}{\partial x_j}\Big|_{3D} = \frac{3}{2}\frac{\partial\overline{u_j' p'}}{\partial x_j}\Big|_{2D}, \quad \frac{1}{2}\frac{\partial\overline{u_i' u_i' u_j'}}{\partial x_j}\Big|_{3D} = \frac{3}{4}\frac{\partial\overline{u_i' u_i' u_j'}}{\partial x_j}\Big|_{2D}. \tag{6.22}$$

Finally, the dissipation is expressed using Taylor's hypothesis

$$\varepsilon = \frac{2}{Re}\overline{S_{i,j}' S_{i,j}'} \approx \frac{6}{Re}\left(\overline{\left(\frac{\partial u'}{\partial x}\right)^2} + \overline{\left(\frac{\partial v'}{\partial y}\right)^2} + \overline{\left(\frac{\partial v'}{\partial x}\frac{\partial u'}{\partial y}\right)^2}\right) \approx \frac{15}{Re}\overline{\left(\frac{\partial u'}{\partial x}\right)^2}. \tag{6.23}$$

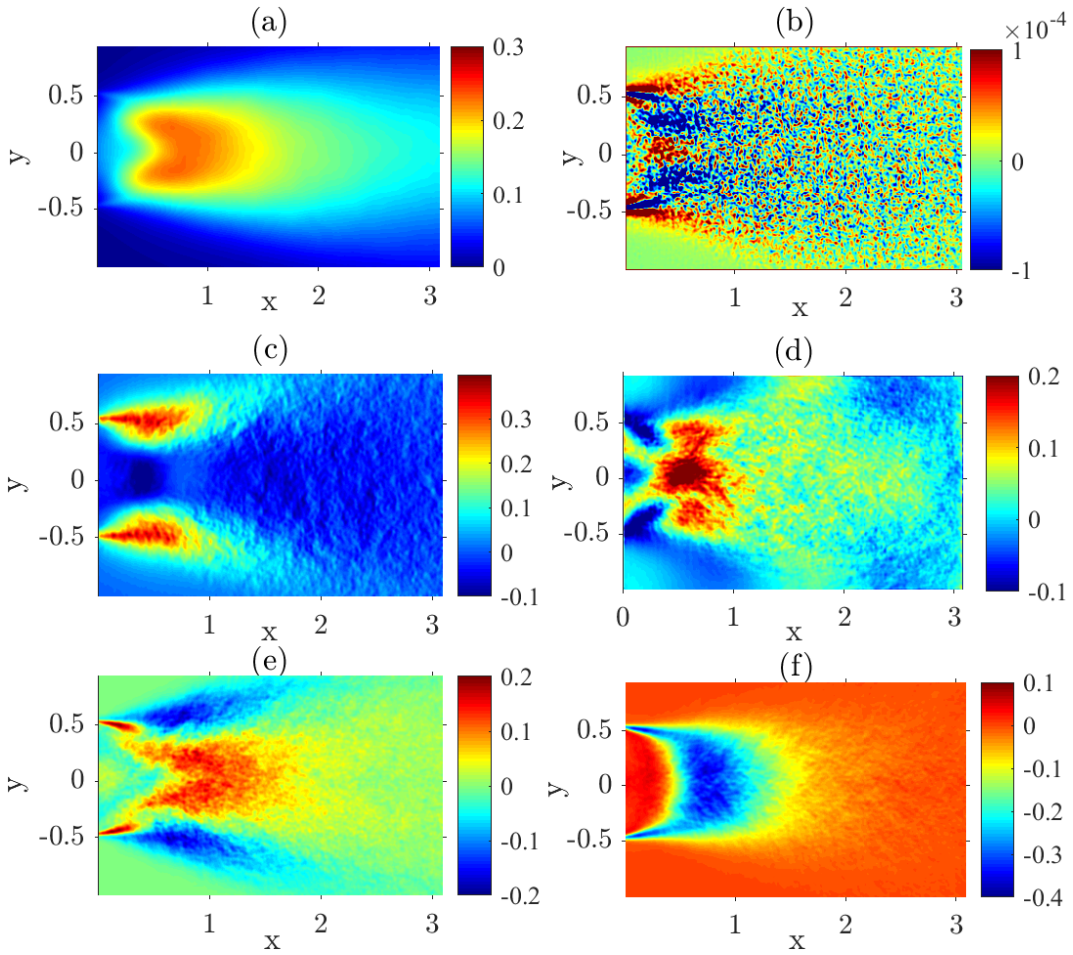

FIGURE 6.11: Contour plots of all the terms of the direct TKE budget: kinetic energy (a), molecular viscous transport (b), advection (c), pressure diffusion (d), turbulent transport (e), production (f) terms respectively.

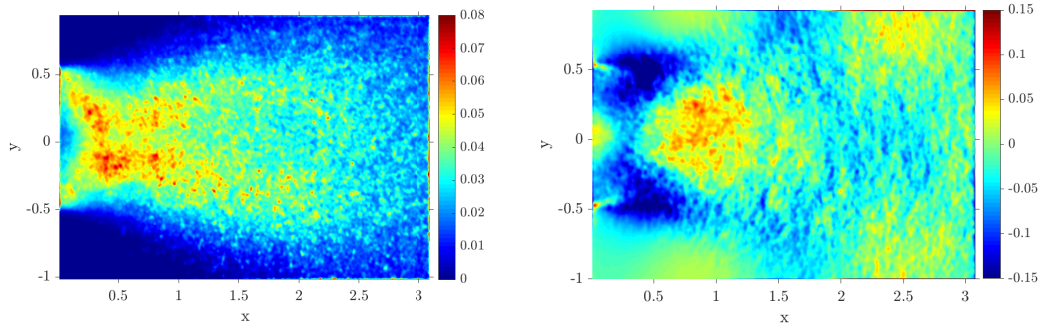

FIGURE 6.12: Dissipation term (left) and summation of all terms of the direct TKE budget calculation (right) in the PIV window.

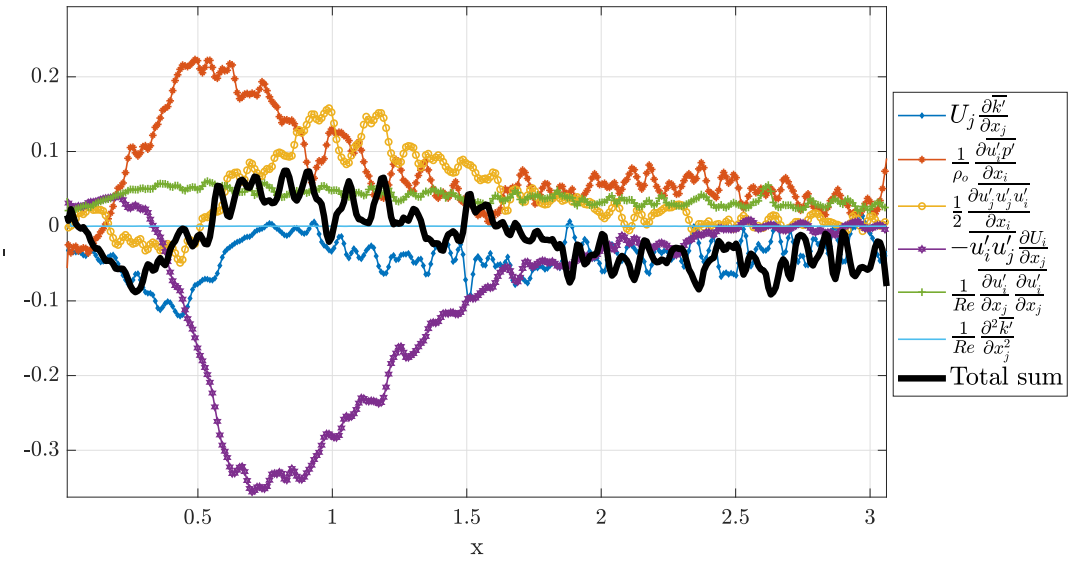

FIGURE 6.13: Direct budget calculation of the TKE transport terms along the middle line. The summation of all the terms leads to a maximum error of less than 10 % for all the wake inside the PIV window.

We begin with exploring the contribution of each of these terms in the streamwise direction, along the middle line, as seen in figure 6.13. At this particular location, the production term and the pressure diffusion term are dominant and even balance one another near the centre of the recirculation region at $x = H/2$. The molecular viscous transport term is three orders of magnitude smaller than all the other terms. In figure 6.12, we observe that the total sum of the budget is less that 10% for most regions of the turbulent wake, and close to 5% in average. To the best of our knowledge, it is the first time that the TKE balance is obtained with such an accuracy from experimental data alone in the case of for a bluff body turbulent wake.

In addition, 29 hot-wire measurements were performed equidistantly on a vertical profile along the y direction, at $x = 3H$ (as presented in figure 6.8) . Comparing hot-wire measurements and PIV data, we can see a good agreement for the mean fields and the terms $\overline{u'^2}, \overline{(\partial u'/\partial t)^2}$, and the dissipation term of the global TKE budget. Results are presented in figures 6.14 and 6.15 for the mean streamwise and mean streamwise fluctuating component of the velocity. We mention that in this very near-wake flow, the two-component X-type hot-wire is not perfectly adapted to measure the large vertical velocity component. Nevertheless, we compare the mean horizontal velocity between the hot wire and OF in figure 6.14(a) and find 5% difference but the width of the wake is well captured. The mean streamwise fluctuations together with the dissipation are shown in figure 6.14(b) and 6.15(c) respectively. Both values are slightly underestimated by the hot wire by approximately 10%, in agreement with the observations from the mean field. Figure 6.15(right) finally compares the mean temporal derivative at the same position in the wake where we can observe an overall agreement, and slight differences between OF and hot-wire measurement as we move away from the centerline. This difference is a direct consequence of the smoothing effect induced by the second-order finite difference scheme. A fourth-order scheme is currently being investigated showing ameliorated promising results.

Finally, we compare the Probability Density Function (PDF) for the pressure measured at the base, at $x = 0$ and $y = \pm 1/4H$. Note that this pressure tap is shift in the transverse direction at $z = 1$ from the tap used to compute the constant of the pressure field (see figure 7

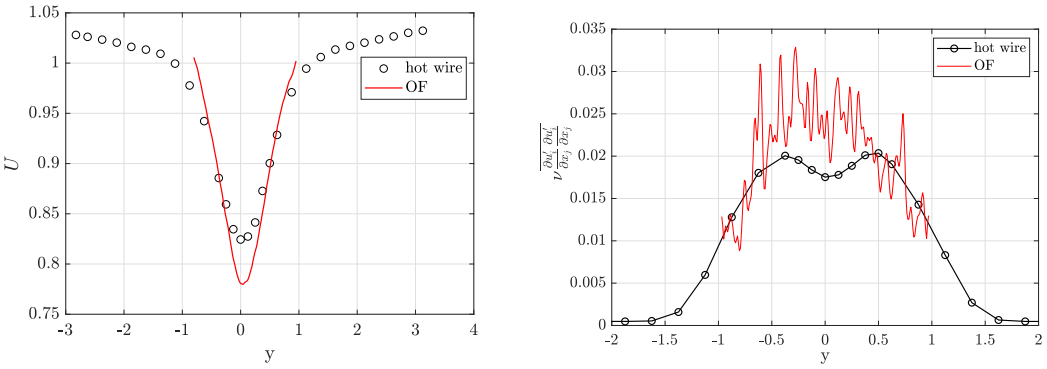

FIGURE 6.14: Hot-wire measurements compared with OF for the mean streamwise velocity profile $U(x = 3H, y)$ *at* $x = 3H$ (left) and dissipation estimated as $\varepsilon = 15/Re\overline{(\partial u'/\partial x)^2}$ from the hotwire and $\varepsilon = 6/Re\left(\overline{(\partial u'/\partial x)^2 + (\partial v'/\partial y)^2 + (\partial v'/\partial x)(\partial u'/\partial y)}\right)$ (right).

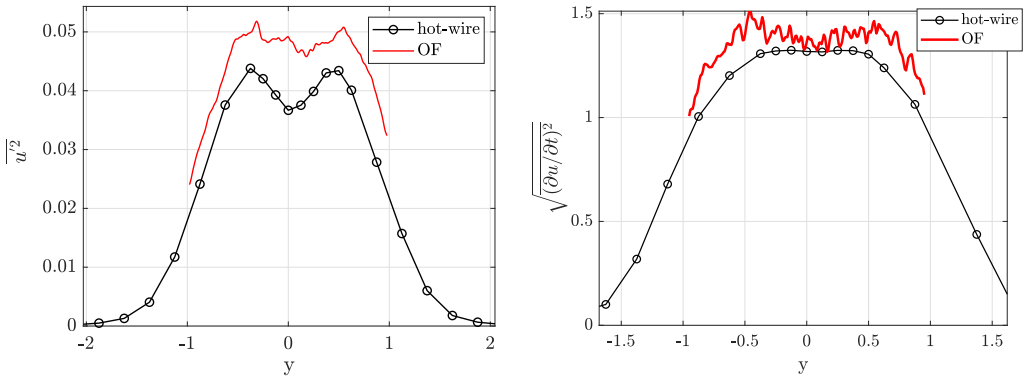

FIGURE 6.15: Same hot-wire OF comparison as figure 6.14 but for (left) the mean streamwise fluctuating component of the velocity field $\overline{u'^2}$ and (right) the mean fluctuating acceleration term $\sqrt{\overline{(\partial u'/\partial t)^2}}$ (right).

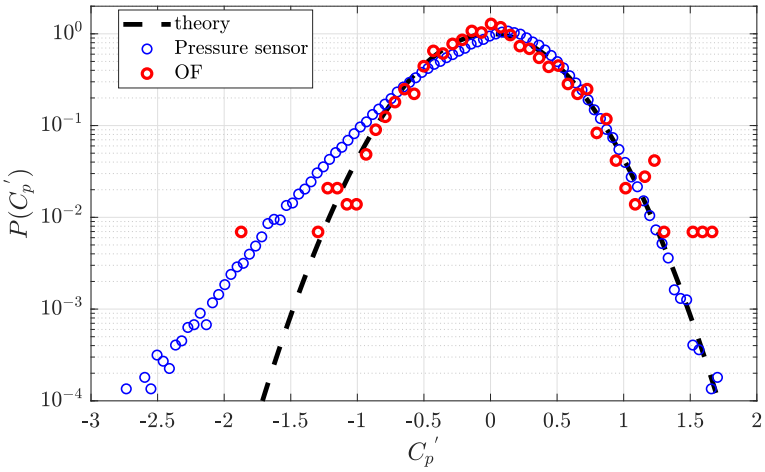

FIGURE 6.16: Probability density function estimation comparison in between optical flow and base pressure sensors.

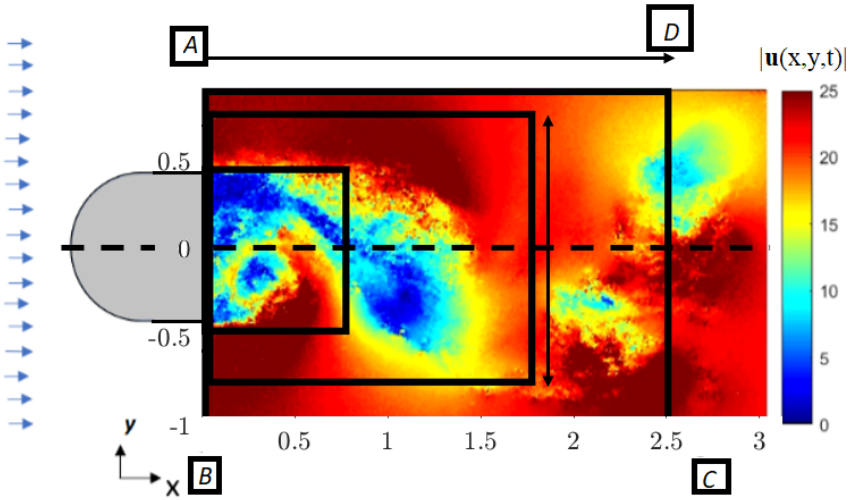

FIGURE 6.17: Global budget control volume sensitivity study: the size in the y direction is augmented symmetrically from the centre, and the size in the x direction is augmented starting from the base of the body. Integral limits A,B,C,D and middle plane line.

in Shanmughan et al., 2020 for the details of the model). The measurements of the pressure scanner are compared with the pressure obtained with the PIV near the body base. The results are shown in figure 6.16, where the measurements from the pressure scanner are non Gaussian, in particular for the the low fluctuations of C_p which is characteristic of the vortex shedding. At the contrary, the pressure measured with PIV is essentially Gaussian. Note that both the amplitude and the standard deviation are well captured by our pressure reconstruction technique but the rare events, probably associated with strong vortex tilting are clearly not captured since they are not included in the formulation of the temporal derivative, nor the transverse velocity is used for computing the solution to the pressure itself.

Next, we consider the TKE budget to estimate the dissipation, which is characteristic from the smallest scales of the flow in a control volume. The aim is to assess the accuracy of the present method to obtain an accurate estimate of the smallest term in the balance (i.e. ε) based on the contribution from the other terms whose contributions are characterised by the large-scales motions in the flow.

6.4.4 Global dissipation calculation in an arbitrary control volume

The volume integral of the dissipation can be calculated in an arbitrary Control Volume (CV) in the near-wake region using equation (6.21) in divergence form as

$$\int_A \left(U_j \overline{k'} + \overline{u'_j p'} + \frac{1}{2}\overline{u'_i u'_i u'_j} - \frac{1}{Re}\frac{\partial \overline{k'}}{\partial x_j} \right) n_j \, \mathrm{d}A = \int_V \overline{u'_i u'_j}\,\overline{S_{i,j}} - \varepsilon \, \mathrm{d}V \tag{6.24}$$

where A is the surface area over which the budget is calculated. As noted in the previous subsection, the molecular viscous term is three orders of magnitude smaller than the other terms and is neglected for the rest of the analysis.

Here we use a parrallelipedic CV, shown in figure 6.17 and once the quantities are projected onto the surfaces of the CV, the turbulence kinetic energy budget simplifies to

$$-\int_V \varepsilon \, dV = \int_{AB,DC} \left(U\overline{k'} + \overline{u'p'} + \overline{u'k'} \right) n_x \, \mathrm{d}y + \int_{AD,BC} \left(V\overline{k'} + \overline{v'p'} + \overline{v'k'} \right) n_y \, \mathrm{d}x + \int_V \overline{u'_i u'_j} S_{i,j} \, \mathrm{d}V, \tag{6.25}$$

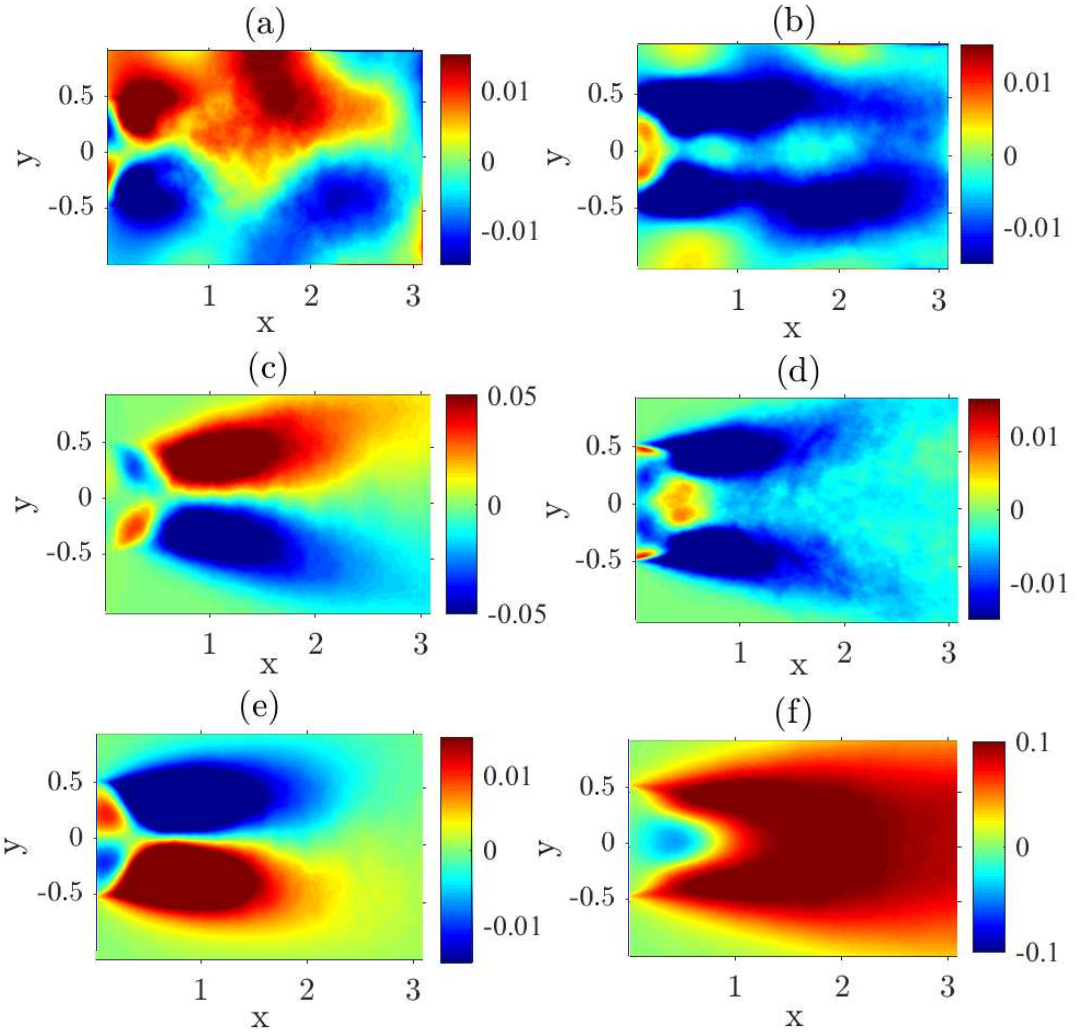

FIGURE 6.18: Global TKE budget terms: (a) $\overline{v'p'}$, (b) $\overline{u'p'}$, (c) $\overline{v'k'}$, (d) $\overline{u'k'}$, (e) $V\bar{k}$, (f) $U\bar{k}$ respectively. The full PIV domain is used as a CV in these results.

where the integral limits A,B,C,D of the CV are presented in figure 6.17. We mention that the presented global budget methodology only requires knowledge if the boundary values of the velocity and pressure, apart from the term of the production which is integrated in the volume (or in our case the surface since values are calculated per unit length). The evolution of the different terms of equation (6.25) along the middle line are shown in figure 6.19. We observe that the advection term in the x direction is dominant compared to all the other terms. We can also note that the solution is essentially symmetric, even for the turbulent diffusion term.

In the present dataset, the high resolution of the camera (29 Mpx) used for the PIV images also provided access to a direct calculation of the mean turbulence kinetic energy dissipation (see figure 6.12). Thus, the volume integral of the dissipation $\int_V \varepsilon \, dV$ is compared with the direct dissipation calculation from equation 6.21, in order to find the optimal CV and understand the departure induced by the errors from the isotropy assumption given in equation (6.22). In what follows, we compare the total direct budget calculation with the global budget as calculated in the variable size control volume, containing the recirculation area and the near-wake region. The CV is changed symmetrically from the middle plane regarding the y direction, and starting from the base of the body in the streamwise direction x as seen

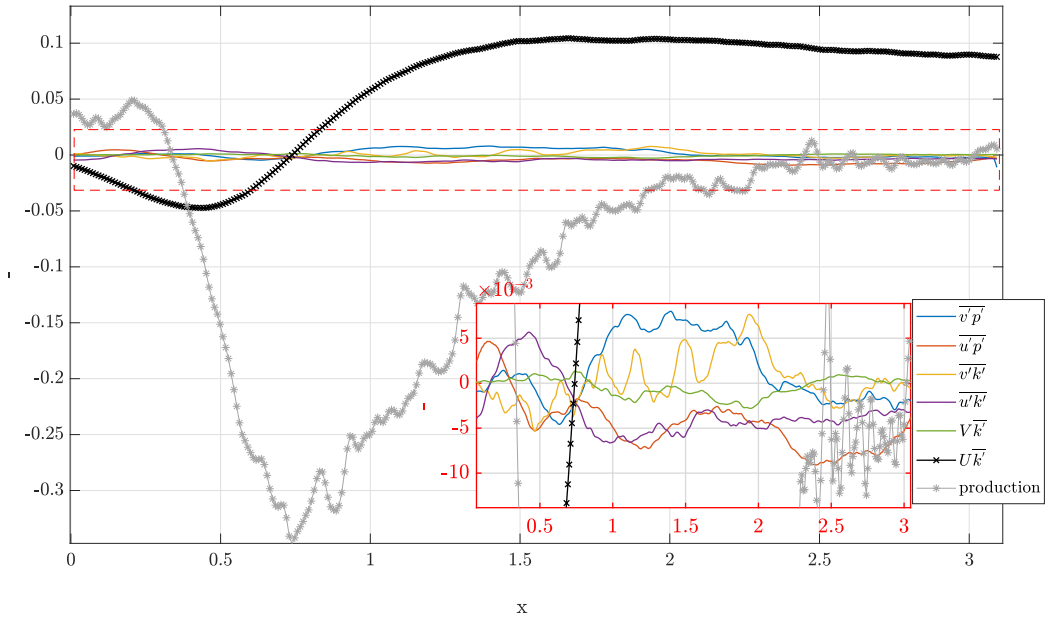

FIGURE 6.19: Global TKE budget terms along the central line, as presented in figure 6.18. A zoom representation for the non-dominant terms is presented in the bottom right corner.

in figure 6.17(a). Along the central line, the transport term is essentially balanced by the production term. The turbulent transport, the pressure diffusion are of the same order.

In figure 6.20(a), we can see the evolution of the different terms calculated on the boundaries and in the volume of the TKE budget for an increasing CV size in the x direction. As highlighted in the previous figure, the production is essentially balanced by advection. The remaining terms are magnified in figure 6.17 (b) where the turbulent transport, the pressure diffusion and the contributions from the upper and lower region are of the same order. Furthermore the terms on the upper and lower boundary nearly have the same magnitude and are somewhat symmetric although the CV is not exactly symmetric along the centre line.

The volume integral of the dissipation is finally compared in figure 6.21 estimated using the direct calculation method and the budget changing the CV size along x, with satisfying agreement for a CV longer than 2. The estimation is the least precise when $x \approx 1.25$ which

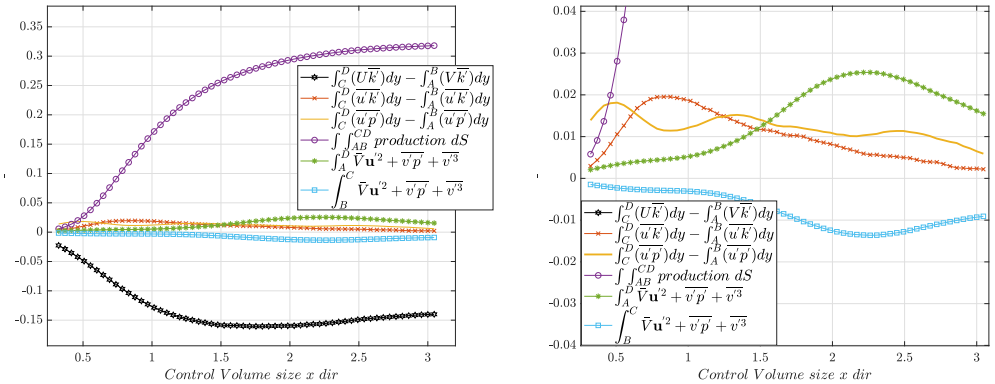

FIGURE 6.20: Contribution of different terms in the global TKE budget, augmenting the streamwise Control Volume size (left). A zoomed representation (right) reveals the evolution of the less dominant terms.

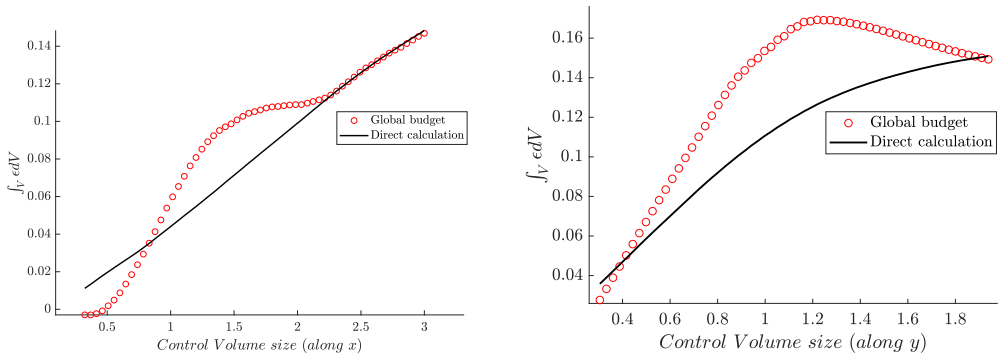

FIGURE 6.21: (left) Direct calculation of the dissipation (solid line) and global budget dissipation calculation (red circles) comparison changing the CV length in the x direction for a fixed $y = \pm 1$. (right) Volume integral of dissipation calculated by changing the size of the box in the y direction, symmetrically from the middle and where the CV length in the streamwise direction was kept constant at $x = 3$.

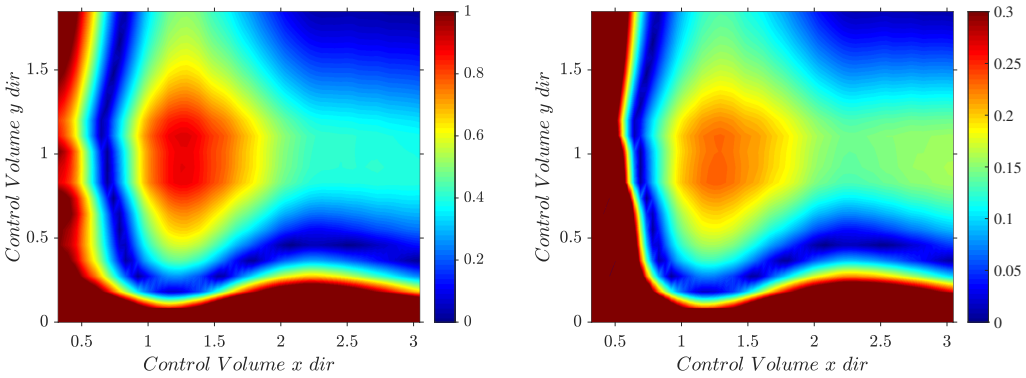

FIGURE 6.22: Volume integral of dissipation error calculation as in figure 6.21 changing both the size of the control volume in the y (symmetrically) and x direction (starting from the body). Relative error between global and direct budget calculation (reference) is presented (left) and relative difference normalized by the volume integral of the production term (right).

is very close to the length of the mean recirculation region. This region also corresponds to the region where the error is largest, as shown in figure 6.13(b) for the local budget.

The influence of the size of the CV in the y direction is presented in figure 6.21 (b), where the best approximation of the dissipation is obtained for a vertical size $y = 1.9$ which corresponds to the largest control volume available from our measurements.

Finally, figure 6.22(a) shows a contour map of the relative error on the dissipation estimation (i.e. $\left(\int_V \varepsilon_{est} - \varepsilon \, \mathrm{d}V\right) / \left(\int_V \varepsilon \, \mathrm{d}V\right)$) the influence of the CV size changing in both directions. A quite satisfying agreement between the direct calculation and the global budget calculation in the CV is observed when containing more than 2 body lengths in the streamwise direction (i.e. x) and 1.7 H in the vertical direction y. Figure 6.22(b) is equivalent to figure 6.22(a) but the error is now rescaled with the dominant term in the budget (cf. the production) and the error writes $\left(\int_V \varepsilon_{est} - \varepsilon \, \mathrm{d}V\right) / \left(\int_V \overline{u_i' u_j'} S_{i,j} \, \mathrm{d}V\right)$. In this case, the error remains essentially below 15%, except for $x \approx 1.25$ where three-dimensional effects of the turbulence the isotropy assumption may fall short provided the complex structure of the mean flow in this region.

6.5 Conclusions and perspectives

With a high-resolution camera and a pressure sensor as sole hardware resources, a novel methodology presented in this study shows the potential of 2D OF velocimetry to resolve spatial scales down to sub-Kolmogorov scales, calculate the acceleration term and reconstruct accurately the instantaneous pressure field in a plane. Two data sets were used to validate the method, a homogeneous synthetic turbulent dataset and an experimental turbulent wake of a D-shaped bluff body. Regarding the former, the velocity and pressure spectra as well as instantaneous acceleration fields showed good agreement with the equivalent DNS data. Regarding the latter, the methodology was validated on top of that with the TKE budget calculation, whose final error was smaller or equal to 10 % for most of the region of the wake, although measurements were limited to two components of the velocity from the PIV. The direct calculation volume integral of the dissipation was compared with the one calculated from the global budget in a CV of the near wake, with quite satisfying results. The CV size limits in the streamwise and vertical direction were also investigated. The spectra comparisons for the acceleration term showed deviations during comparisons with DNS-derived finite differences acceleration spectra. A perspective using a fourth order pressure reconstruction scheme is currently being investigated to possibly ameliorate this comparison.

Moreover, the present methodology to obtain the acceleration and pressure is only based on two-dimensional results. However, it provides an interesting tool to estimate pressure in a PIV plane, and this at a large scale which was difficult to achieve, specially for intrusive sensors measurements. Given that a DNS of high-Re turbulent bluff body wakes is often computationally intensive to obtain because of the complexity of the flow, the salient edges, and the broad range of time and length scales to resolve, we believe that such velocimetry experiments can open new alleys in the systematic and efficient studies of turbulent flows, where high-resolution and large acquisitions in time are required. Moreover, the present method no longer requires to acquire time-resolved measurements to obtain acceleration which is often technically challenging for high-definition CCD and CMOS cameras and difficult to implement.

The quality of the estimation could be further improved using for instance stereo or tomographic PIV. Both the Savitzky-Golay filter and the acceleration solver can be naturally extended in three dimensions with minor modifications to the present code. The extension of the acceleration solver from single snapshots from stereo-PIV measurements is presently under investigation and will be part of a follow-up study.

Part III

Modelling and system identification of a Turbulent Boundary Layer using data-driven methods

This part explores the feasibility of two data-driven methods in order to capture the dynamics of an experimental Turbulent Boundary Layer (TBL) flow. These methods are called data-driven because they require a large amount of data in order to first interpolate (learning part) and then extrapolate (validation part) correctly the dynamics behaviour of a particular system. No prior knowledge of the equations is needed, only a few sensors coming from PIV measurements. The first approach consists in a linear subspace identification method to model and predict the dynamics of turbulent coherent structures, using local upstream measurements. The second one, consists in a modern machine-learning learning approach, particularly a shallow artificial neural network, that performs a regression of local measurements and the global field dynamics.

Chapter 7

Transition to turbulence in the flat plate Boundary Layer flow

Due to its viscosity ν and the free stream U_∞, the Boundary Layer (BL) flow near the wall undergoes shear stress τ_w, as explained by Prandtl first. At low Reynolds numbers the dissipative effect of the viscosity is more important than the shearing: this is the laminar regime. Increasing the Reynolds number inverts the trend and the turbulent kinetic energy rises: this is the turbulent regime. It produces vorticity, which is diffused vertically and advected downstream; the boundary layer thickness δ grows consequently.

There are many paths to transition to turbulence in the zero pressure gradient BL flow, and they depend strongly on the incoming boundary conditions. Small free stream vortices penetrating or generated in the boundary layer can be transformed into the so-called Tollmien-Schlichting (T-S) waves by the natural instability. The critical Reynolds number based on the local displacement thickness is defined as:

$$Re_{\delta_0^*} = \frac{\delta_0^*(x)U_\infty}{\nu} \tag{7.1}$$

where U_∞ is the free-stream velocity, ν is the kinematic viscosity, x the streamwise coordinate (y and z being respectively the vertical and spanwise axis) and

$$\delta_0^* = \int_0^\infty (1 - \frac{u}{U_\infty})dy \tag{7.2}$$

is the local displacement thickness at the inlet of the PIV window, at $x_0 = 37$ cm from the leading edge. The critical Reynolds number is $Re_{\delta^*}^{crit} = 520$ (Klebanoff, Tidstrom, and Sargent, 1962a). The amplitude of these spanwise waves increases downstream until the emergence of alternating peaks and valleys, going from two-dimensional stable to three-dimensional unstable structure (Klebanoff, Tidstrom, and Sargent, 1962b). The waves finally break down into hairpin eddies, becoming then a fully turbulent flow with small-scale structures (spots, eddies) and intense fluctuations. This instability is referred as a receptivity problem, since it linearly amplifies small specific upstream perturbations (Kachanov, 1994). A typical visualisation experiment for this case is presented in figure 7.1. This path to transition to turbulence can be observed in experiments only where free-stream turbulence, vibrations, surface roughness and ambient noise have been carefully reduced to a minimum.

Another transition process may occur if the turbulence intensity of the incoming flow is of the order of 1% (Morkovin, 1985) or higher: the bypass transition. Groups of streaks are observed, which are streamwise structures periodically distributed in the spanwise direction (Matsubara and Alfredsson, 2001; Beneitez et al., 2019), for Reynolds numbers as low as $Rey_{\delta^*}(x)$ =300. It is called bypass, because it can bypass the T-S instability mechanism altogether. The characteristic spanwise length is usually a few times the BL thickness. In the wall-normal direction, the structures extend across the whole boundary layer. The streaks further downstream undergo wavy motions and collapse into turbulence (Schlatter et al., 2008),

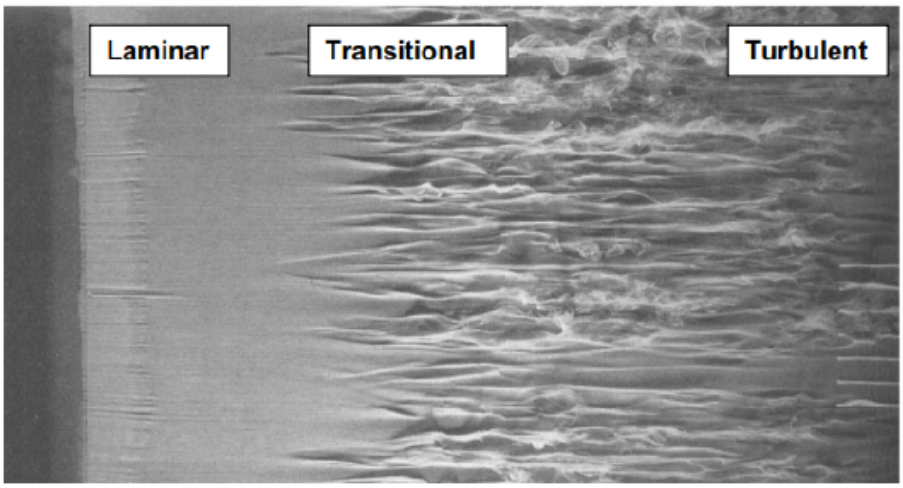

FIGURE 7.1: Boundary layer transition to turbulence along a flat plate under a Tollmien-Schlichting instability, visualisation experiment by Nichols (Nichols, 2010) . Laminar, transitional and turbulent regime.

like the T-S waves. This instability can be forced and observed in a laboratory environment, as Duriez, Aider, and Wesfreid, 2009 did to demonstrate the self-sustaining process between the steaks and the streamwise vorticity. An extensive review on boundary layer transition can be found in Lee and Jiang, 2019. Both transitions are not completely uncorrelated since the streaky structures of the bypass transition look like the 3D shape of the T-S waves and the natural transition spectrum signature is also identified in the streaks dynamics (Hughes and Walker, 2000). Coexistence of T-S waves and streaks can also be observed (Beneitez et al., 2019).

Delaying this transition is a good strategy to reduce the drag related to the skin friction. For instance, at moderate turbulence intensity, the T-S waves can be stabilized by streaks of low amplitude forcing (Cossu and Brandt, 2002; Fransson et al., 2006) or appear naturally (Martin et al., 2015). The modelling and instantaneous field reconstruction of a subcritical, wavy streak bypass transition is investigated in the present experiment, using visual sensors coming from the OF PIV. The transition was triggered using a finite amplitude pulsating jet perturbation described in section 7.1.1.

7.1 Turbulent Boundary Layer experimental setup

Experiments were carried out in a hydrodynamic channel driven by gravity. A divergent and a convergent sections, separated by honeycombs, stabilise the flow ; the turbulence intensity was $T_u = \sigma_u / U_\infty = 0.7\%$. The test section is 80 cm long and 15 cm wide in the spanwise direction (see figure 7.2). The flat plate along which the boundary layer growths entirely spans the test section width to manage 2D dynamics at best. The test section height height is $H = 8.5$ cm.

A homemade leading edge, designed as a NACA 0020 profile, is used to smoothly start the boundary layer. The origin is located at the beginning of the leading edge ($x = 0$), in the vertical symmetry plane ($y = 0$) and on the flat plat ($z = 0$). For the present study, the free-stream velocity range is $U_\infty = 0.188 m/s$ in the inlet of the PIV window $x_0 = x_w^* = 37\ cm$ downstream from the leading edge. This position, denoted x_W^* and illustrated in figure 7.2, is used to define the characteristic length of the flow $\delta_0^* = \delta^*(x_W^*)$ and the resulting Reynolds number taken as reference $Re_{\delta_0^*}$. In the same way, the dimensionless time is defined as $t^* = tU_\infty / \delta_0^*$. Velocities are non-dimensionalised by U_∞.

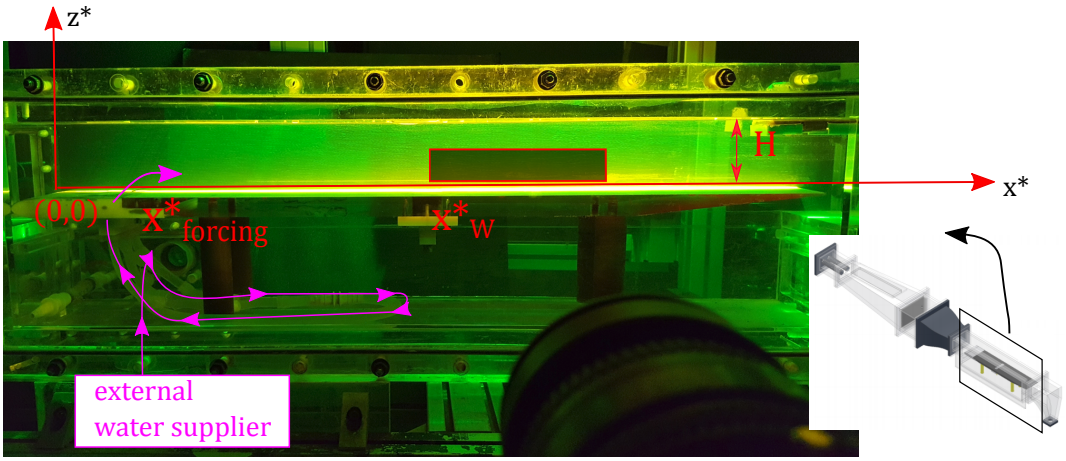

FIGURE 7.2: Experimental setup with the investigated PIV plane (red rectangle) starting at x^*_W and the forcing jet (pink arrow) at $x^*_{forcing}$. Sketch of the water channel is displayed on the bottom right. The origin of the (x,y) axis is placed in the leading edge.

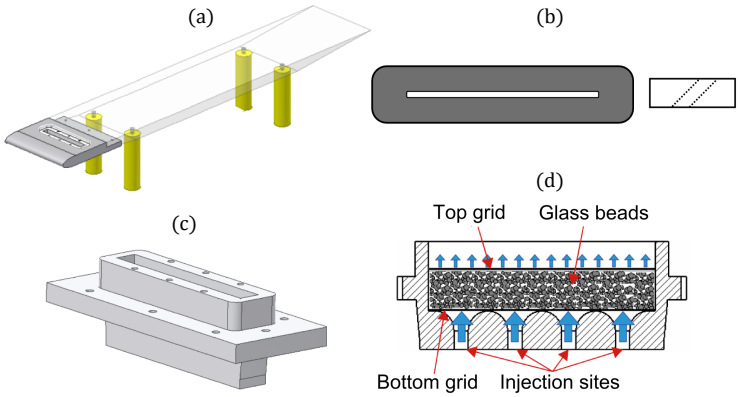

FIGURE 7.3: **(a)** Computer-aided design of the modified flat plate used in the water channel. **(b)** Inclined slot sketch. **(c)** 3D view and **(d)** side view of the jet injection system.

7.1.1 An experimental transition forcing mechanism

The flow for the maximum Re number of the channel followed a laminar profile. Hence, we designed an efficient way to transition to turbulence in the BL flow, using a finite amplitude pulsating jet perturbation. The perturbation is induced by a streamwise-inclined slotted jet, whose angle to the wall is 45° described in figures 7.3(a-d). The injection system is composed of glass beads between two pierced grids to avoid undesired structures. It is located at $x = 5\ cm$ downstream the leading edge, as shown in figure 7.2. The jet outlet has a rectangular cross-section which is 0.4 cm long (in the streamwise direction) and 9 cm wide (spanwise direction). Thanks to this geometry, the perturbation can be considered as homogeneous along the spanwise direction. As described in figure 7.5, the slotted jet is supplied by a pressurized water tank, monitored by an SMC ITV 1010 electro-pneumatic regulator to control the jet velocity $u_{forcing}$, which can be set regarding the frequency $f_{forcing}$, the amplitude $U_{forcing}$, and the duration $\delta T_{forcing}$. This setup enables to induce random perturbations by changing these parameters after each pulse. The command signal between the impulses remains at the value avoiding any perturbation generation, as if the slot does not exist.

The random 2D pulsating jet of finite amplitude is created by sending a square signal of

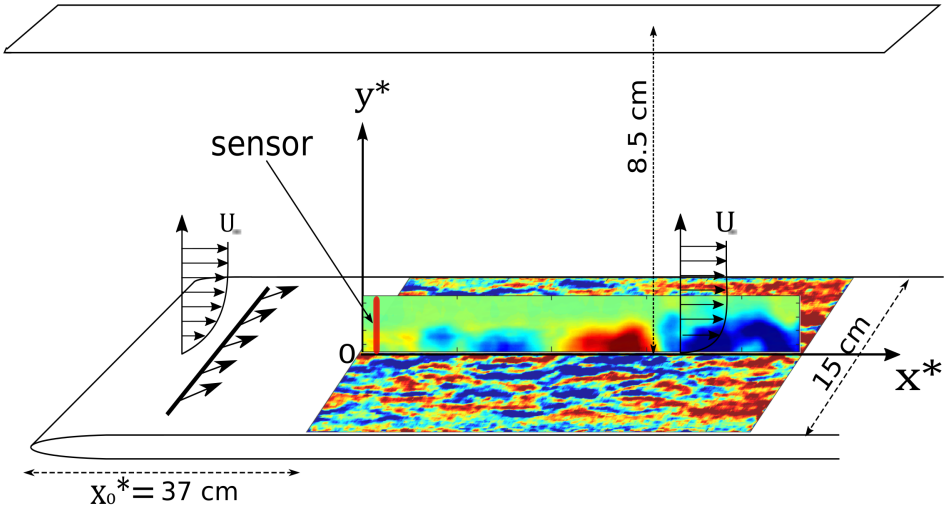

FIGURE 7.4: Flat plate geometry dimensions, perturbation slot and PIV window positions.

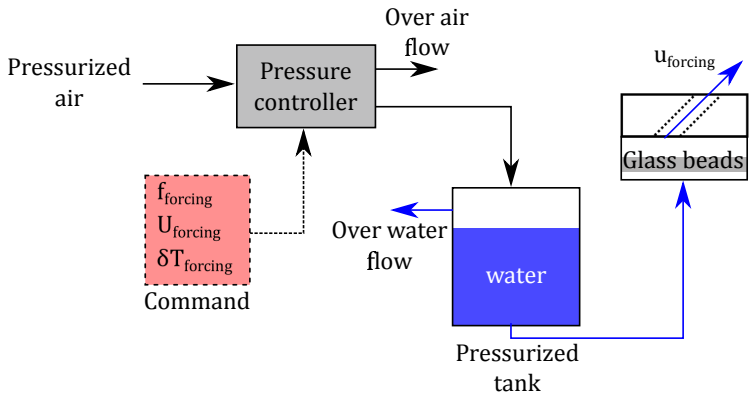

FIGURE 7.5: Jet supply circuit.

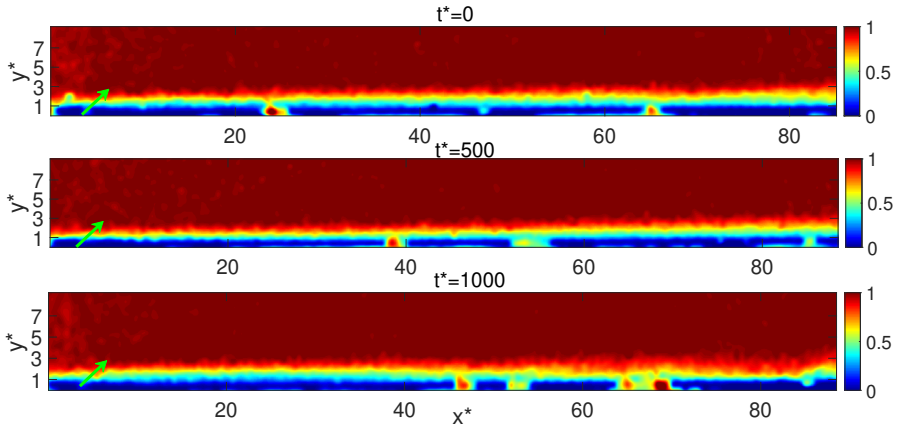

FIGURE 7.6: Generation or upstream vortical structures to perturb the boundary layer. Jet position is found in the green arrow, with 45 degree angle.

random frequency, to the pneumatic pressure controller. The random jet frequency was varied between 0 and 5 Hz for a total time of around 40 s. The initial vortical structures created by the spanwise invariant jet can be visualised in figure 7.6; they are initially of the order of the size of the boundary layer or smaller. These pulsating jets introduce streamwise rolls in the BL. Through the lift-up mechanism, they create streak groups organised in turbulent spots. The streaks are expanding in the spanwise direction and advected downstream. The full evolution of the streak energy in the streamwise direction is not possible due to the finite field of view of the camera. In a matter of $x = 100\ \delta_0^*$, wavy streaks are observed covering the full span, as found in figure 7.7. The experiment was repeated numerous times to cover all the frequency range of the forcing up to 5 Hz and ensure repeatability of the results.

7.1.2 Optical flow PIV

The flow is seeded with 20 μm neutrally buoyant polyamid seeding particles. The vertical symmetry plane of the test section is illuminated by a laser sheet created by a 8 W continuous laser beam passing through a cylindrical lens and generated by the *Genesis MX-6185* (Coherent, USA) operating at the wavelength 532 nm. A very thin layer of the fluorescent paint *FP Rhodamine 6G* has been applied on the surface illuminated by the laser sheet, in order to reduce the reflections. The snapshots of the illuminated particles are recorded by the camera PCO DIMAX-cs . An optical filter selecting only the laser frequency is mounted on the objective to reduce the light noise.

The two dimensional two components (2D-2C) velocity fields $v_x(x,z)$ and $v_z(x,z)$ (respectively the streamwise and the wall-normal components) are computed at the frequency $f_{PIV} = 150\ Hz$ using a Lucas-Kanade Optical Flow algorithm. The first version of the code has been developed at ONERA (Champagnat et al., 2011) and later modified, and adapted to the constraints of real-time measurements by Gautier & Aider (Gautier and Aider, 2013). A full description of the algorithm is presented in chapter 3.1. A kernel radius of 24 pixels was used for the gaussian blurring process of the algorithm, together with 3 pyramid levels. A low-pass filter has been applied to the raw data sets with a cutoff frequency f_{cut} at least ten times higher than the highest measured frequency of the forced boundary layer dynamics.

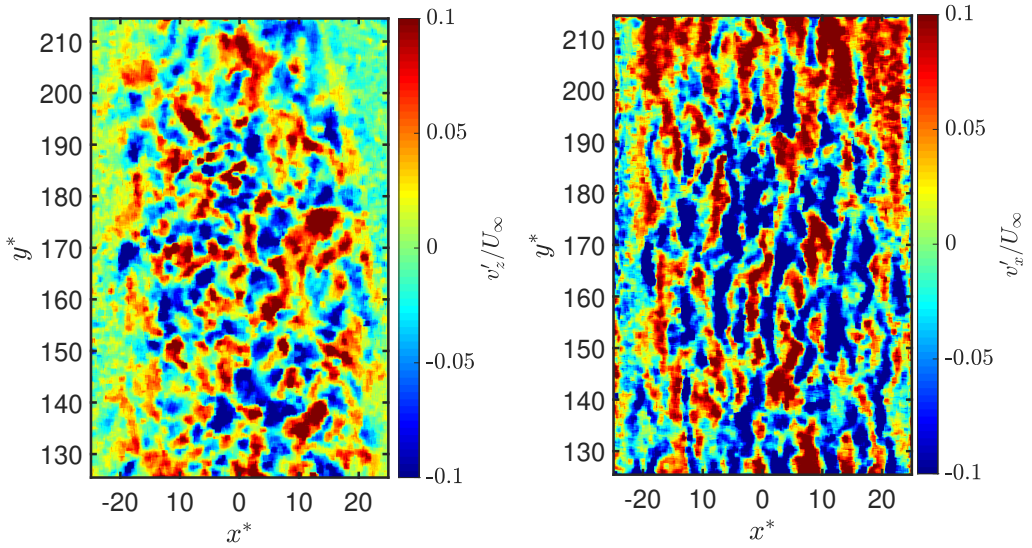

FIGURE 7.7: Instantaneous spanwise (left) and streamwise (right) velocity fluctuations in the horizontal plane TBL xy, for $z^* = 2$.

Chapter 8

Reduced-order modelling of a TBL flow using statistical learning

8.1 Introduction on dynamics estimators

Dynamics estimation in fluid mechanics is an important step in the process of flow control systems implementation. These methods go hand by hand with reduced-order modelling since the dimensionality of fluidic systems can be huge. For example, for PIV database consisting of 1 Mp snapshots, the dynamical system order is $O(10^6)$. Proper orthogonal (Berkooz and Titi, 1993) or Dynamic mode (Schmid, 2010) decomposition has been used for reducing the order of such systems.

Estimators can be static or dynamic. Static estimators are basically a mapping between optimal sensors and global flow dynamics at each time-step, without the notion of forecasting, or taking into account the effect of the history of the dynamics in the present state of the flow. The Linear Stochastic Estimation (LSE) techniques of Adrian (Adrian and Moin, 1988) were widely used to obtain static estimators, and particularly to characterise turbulent structures using multiple observations of nearby points (Adrian and Moin, 1988; Clark, Naghib-Lahouti, and Lavoie, 2014). A standard approach to obtain a dynamic estimator (when the system equations are known) is the Kalman filter method, which comes down to solving an algebraic Ricatti equation to obtain the estimator gain (B.Burl, 1998). Solving a Ricatti equation though, can be very computationally expensive for the full order system, so a reduced order model is usually needed. An extended Kalman filter method can also be used for optimal dynamic estimation of non-linear problems as well (Stengel, 1994).

In many complex or experimental applications though, where the system equations are unknown or a lot of system states hidden and unable to measure, System Identification (SI) can also help obtain successfully a dynamic estimator. This can be done just by using measurable input (sensor) and the output data available. Such data-based SI can be linear or non-linear. Linear SI as been widely used and proven robust and easier to implement (Favoreel, Moor, and Overschee, 2000; Guzmán, Sipp, and Schmid, 2014; Juillet, Schmid, and Huerre, 2013; Juillet, McKeon, and Schmid, 2014). Non-linear SI was applied by Loiseau et al. using the SINDy method for the case of cylinder flow for Re=100 (Loiseau, Noack, and Brunton, 2018). The discrete empirical interpolation method has also been used for nonlinear model order reduction (Pando, Schmid, and Sipp, 2015). Non-linear machine learning methods can also can also be used for SI. Güemes Jiménez, Discetti, and Ianiro, 2019 used wall shear stress measurements and a convolutional Neural Network to reconstruct the large scale motions in a turbulent channel flow. Wang et al. used deep neural networks for reduced-order modelling of an ocean gyre and flow past a cylinder (Wang et al., 2018).

Turbulent structures are inherently non-linear. However, coherent structures always exist in such flows. It has been shown that coherent structures in nonlinear flows can be identified using a linear framework. Resolvent analysis has been used for this complicated task (Thomareis and Papadakis, 2018). To perform this estimation based on linear equations

though, an extra eddy viscosity model can be needed, which makes the process more complex (Illingworth, Monty, and Marusic, 2018; McKeon and Sharma, 2010). In this work, we obtain a dynamic estimator for turbulent structures using a linear, statistical learning SI approach. The estimator is implemented on an experimental PIV dataset of a non-linear flow: a TBL flow under a bypass streak instability.

The section is organised as follows: First, we start with a description of the methodology, which consists in a system order reduction followed by a subspace SI algorithm. This algorithm creates a link between upstream local sensors and entire perturbation field dynamics and discovers a reduced-order state-space model. Then, the results and different parameter sensitivity studies are presented before turning into discussion and conclusions.

8.1.1 From streak dynamics to a linear time-invariant system

Statistical learning refers to a vast set of statistical tools used to understand data. They can be divided in to supervised or unsupervised. Supervised learning consists of building a statistical model for prediction, or estimation, of a specific output based on one or more inputs. In unsupervised statistical learning, there are inputs but no supervising output; nevertheless we can still learn relationships and and identify structures and features from such data. In the current study we focus on a supervised algorithm.

As proposed first time by Guzmán, Sipp, and Schmid (2014) for the BL flow under the TS instability, and later applied by Guzmán-Iñigo, Sodar, and Papadakis (2019) for the wake of an aerofoil, the same scheme of statistical learning identification and field reconstruction is applied here, for the Turbulent Boundary Layer. First, a POD is applied in the time-resolved PIV dataset, and then a statistical learning method (N4SID) is applied to identify a linear state-space model. The statistical learning method will use system realisations from an experimental PIV dataset.

The complete dynamics of a forced amplifier flow are represented by the incompressible NS equations including an unknown upstream forcing term $\boldsymbol{F_w} w(t)$:

$$\partial_t \boldsymbol{V} + \boldsymbol{V}.\nabla\boldsymbol{V} = -\nabla\boldsymbol{P} + Rey^{-1}\Delta\boldsymbol{V} + \boldsymbol{F_w} w(t), \nabla.\boldsymbol{V} = 0 \tag{8.1}$$

where the velocity $\boldsymbol{V}$ and the pressure $\boldsymbol{P}$ are dimensionless and the physical meaning of $w(t)$ is given in the following section. Expressing the velocity and the pressure in equations 8.2 such as $\boldsymbol{V} = \boldsymbol{V}_{base} + \boldsymbol{v'}$ and $\boldsymbol{P} = \boldsymbol{P}_{base} + \boldsymbol{p}$, where $\boldsymbol{V}_{base}$ and $\boldsymbol{P}_{base}$ are respectively the velocity and the pressure when $w = 0$ (base-flow), and $\boldsymbol{v'}$ and $\boldsymbol{p}$ are the velocity and pressure disturbances, leads to

$$\partial_t \boldsymbol{v'} + \boldsymbol{V}_{base}.\nabla\boldsymbol{v'} + \boldsymbol{v'}.\nabla\boldsymbol{V}_{base} = -\nabla\boldsymbol{p} + Rey^{-1}\Delta\boldsymbol{v'} + \boldsymbol{F_w} w(t), \nabla.\boldsymbol{v'} = 0 \tag{8.2}$$

where linear perturbation dynamics are assumed.

The objective is thus to obtain the following linear time invariant (LTI) multiple-input-multiple-output (MIMO) system:

$$x(n+1) = \mathscr{A}x(n) + \mathscr{B}u(n) + w(n), \tag{8.3a}$$

$$y(n) = \mathscr{C}x(n) + \mathscr{D}u(n) + v(n), \tag{8.3b}$$

where $y(n)$ is the system output, $x(n)$ is the system state, $u(n)$ is the system input, $w(n)$ is the state noise, $v(n)$ is the sensor noise, and $\mathscr{A}$, $\mathscr{B}$, $\mathscr{C}$ and $\mathscr{D}$ are the system matrices. $w(n)$ and $v(n)$ being unknown, the state space model described in equations 8.3 rather predicts an estimated output denoted y_e when $w = v = 0$. The system matrices are consequently chosen to minimize the difference between the estimated output, and the measured output y. We point out that the states $x(n)$ do not need to have a physical interpretation.

8.1.2 POD reduced-order model

N consecutive velocity fields $\{\boldsymbol{V(n)}\}_{n=1...N}$ are computed to form the so-called "learning" data set. The proper orthogonal decomposition (POD) of this data set enables to build a ranked and orthonormal basis containing N modes (Lumley, 1967; Sirovich, 1987) thanks to the snapshots method. The first K modes $\{\boldsymbol{\Phi_k}\}_{k=1...K}$ with $K \leq N$ are chosen to compute the approximated velocity field $\tilde{\boldsymbol{V}}\boldsymbol{(n)}$

$$\tilde{\boldsymbol{V}}\boldsymbol{(n)} = \sum_{k=1}^{K} \langle \boldsymbol{\Phi_k}, \boldsymbol{V(n)} \rangle \boldsymbol{\Phi_k}, \tag{8.4}$$

where the scalar product $\langle , \rangle$ is the energy-based inner product. By gathering all the POD coefficients $a_k(n)$, defined as $a_k(n) = \langle \boldsymbol{\Phi_k}, \boldsymbol{V(n)} \rangle$, the system output is obtained through the reduced state vector $Y(n) = [a_1(n)\ a_2(n)\ ...\ a_K(n)]^T$. The modes dynamics are contained in their coefficients. The dynamics of the estimation $Y_e(n)$ of the reduced state vector $Y(n)$ can therefore be captured from sensor measurements $s(n)$ by

$$Y_e(n+1) = \tilde{A}_s Y_e(n) + \tilde{L} s(n), \tag{8.5a}$$

$$s(n) = \tilde{C} Y_e(n), \tag{8.5b}$$

where $\tilde{A}_s$ is the linear evolution matrix, $\tilde{L}$ is the observer matrix, while $\tilde{C}$ is the measurement matrix. These matrices are determined using system identification techniques based on the input-output relation only and described hereafter. Assuming $\mathscr{D} = 0$, the matrices of the desired LTI MIMO system in equations 8.3 are related to equations 8.5 through $\tilde{A}_s = \mathscr{C}\mathscr{A}\mathscr{C}^{-1}$ and $\tilde{L} = \mathscr{C}\mathscr{B}$. Actually, the model has to consider the physical perturbations rather than the measurements in equation 8.5 and also the noise in equation 8.5 to capture the real dynamics

$$Y_e(n+1) = \tilde{A}_w Y_e(n) + \tilde{B}_w w(n), \tag{8.6a}$$

$$s(n) = \tilde{C} Y_e(n) + g(n), \tag{8.6b}$$

where $\tilde{B}_w w(n)$ is the unknown driving term and $g(n)$ is the measurement noise. The real linear evolution matrix $\tilde{A}_w$ is directly computed from the other matrices, using equations 8.6, 8.5 and 8.6

$$\tilde{A}_w = \tilde{A}_s + \tilde{L}\tilde{C}. \tag{8.7}$$

8.1.3 Subspace System identification

The SI comprises two steps, summarized in figure 8.2 : the statistical learning and the validation.

The POD coefficients are first computed from the learning data set, and are defined as output y. A subspace identification algorithm (Qin, 2006) is applied to calculate the linear state-space model matrices of the linear time-invariant system 8.3. the so-called "N4SID" algorithm (Van Overschee and De Moor, 1994; Van Overschee and De Moor, 1995) is well suited for this step. During the learning step, the system states x(n) are extracted and the (extended) observability matrix, with rank equal to N_x is obtained. The crucial component in this step is the singular value decomposition of a weighted matrix. Then the matrices A, B and C, are calculated (to within a similarity transformation) from the system states x(n) by a least squares regression. We note that the order N_x can be specified by the user and it has been investigated in the next chapter. Initial states are treated as independent parameters to be calculated together with the state-space model parameters. The learning data set must contain enough snapshots to build an efficient reduced-order model. The POD coefficients

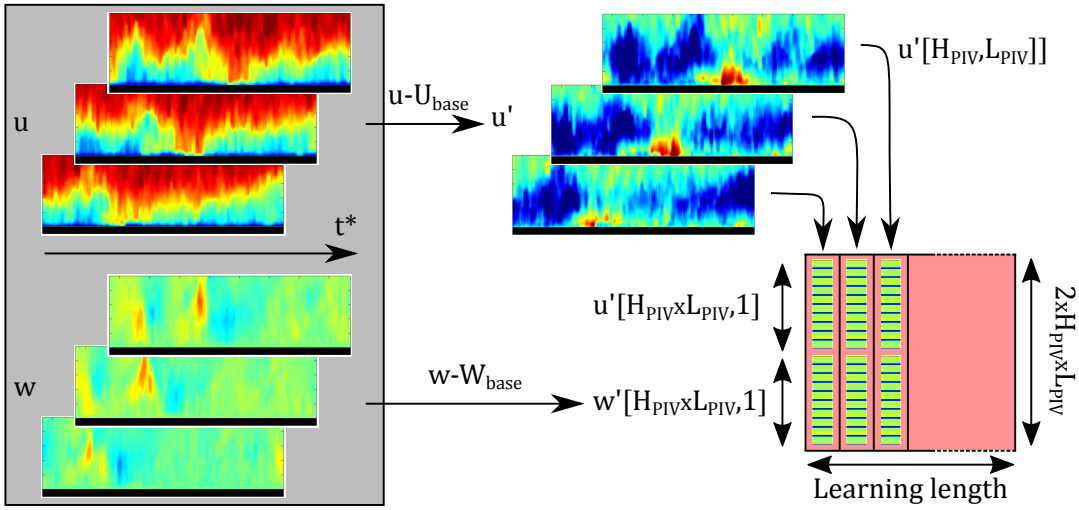

FIGURE 8.1: Sketch of the learning matrix (red) construction from the data set (gray).

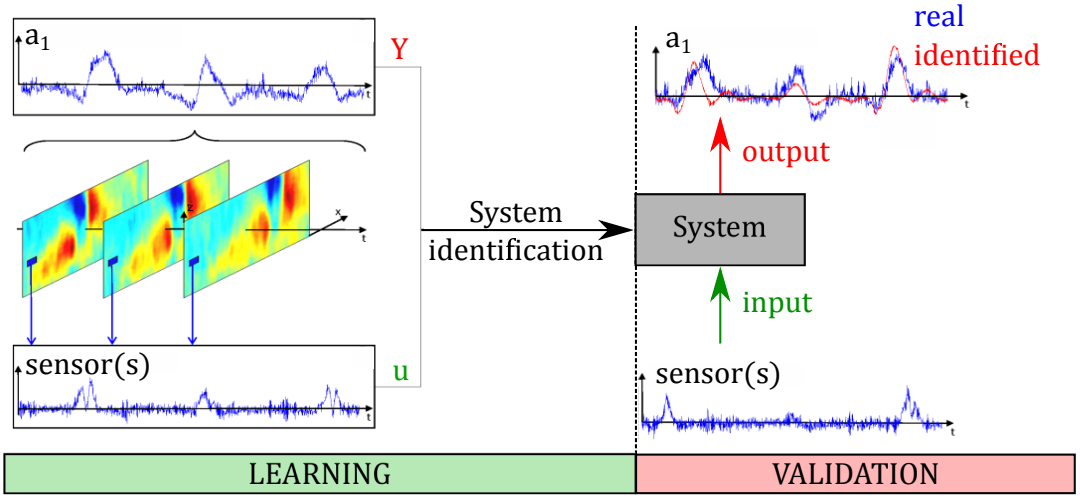

FIGURE 8.2: Sketch of a system identification method using POD coefficients a_i as output.

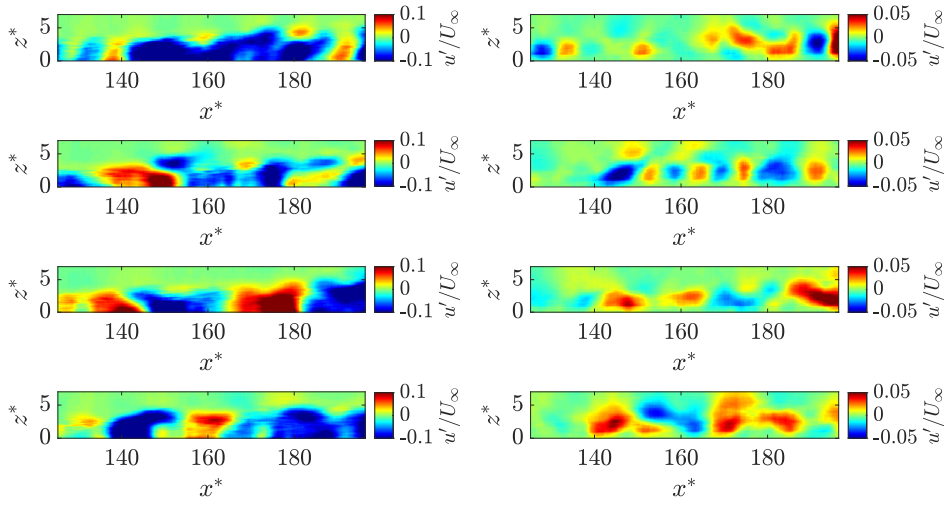

FIGURE 8.3: Successive instantaneous streamwise (left) and vertical (right) fluctuation velocity components of the velocity fields.

are defined as output and an appropriate sensor as input of the learning step ; their number must by as high to obtain all the important dynamics of the flow but not too high in order for the learning process to fail. A new dataset, that does not contain measurements used for the learning process is then used, the validation dataset. It is a standard measure in data-driven methods in order to avoid overfitting and test the extrapolation capability. The predicted output POD coefficients are again compared to the experimental ones ones.

8.1.4 Flow characterisation

The free-stream velocity in the present experiment was $U_\infty = 0.188 m/s$. The incoming boundary layer was laminar, with a displacement thickness at $x_0 = 37\ cm$ $\delta_0^* = 2.95 mm$. The corresponding Reynolds number is $Re_{\delta_0^*}(x) = 488$. The shape factor of the unperturbed flow was $H = 2.35$ and for the forced flow is $H = 1.33$, which is typical of a turbulent flow.

A transition forcing mechanism, using upstream pulsating jets, was utilised to create the turbulent boundary layer, which is analytically described in section 7.1.1. Groups of wavy streaks were observed covering the full span, as presented in the same section; their signature in the vertical field can be found in figure 8.3. The coherent structure advection speed is calculated by the inclination angle of the space-time diagram. In plot 8.4 we can also see the evolution of the total fluctuation kinetic energy of the streamwise direction along time, for both planes xz and xy ; the structure advection speed was found 0.7-0.8 U_∞.

The POD energy and the normalized POD modes of the streamwise velocity v_x^* are given in figure 8.5. The first 16 modes accumulate more than 85% of the total energy, the first one being at 23.1%. The first POD mode corresponds to the three-dimensionality of the streaks, due to their waviness. That way, structures can disappear or enter the plane, and this elongated streaky structure appears with a low oscillation frequency (see first POD coefficient). That way it does not come in pairs like the other convective modes. Hence, it was foreseen that it could not be fully modelled with the current method. Dynamics of this mode cannot connect with the dynamics of other modes, and this can be seen in the cross-correlation between the POD coefficient of these modes in figure 8.6. Pairing modes are 2-3, 4-6 , 7-8. Modes 15-16 are also in pairs and show more complex and higher frequency streak interaction.

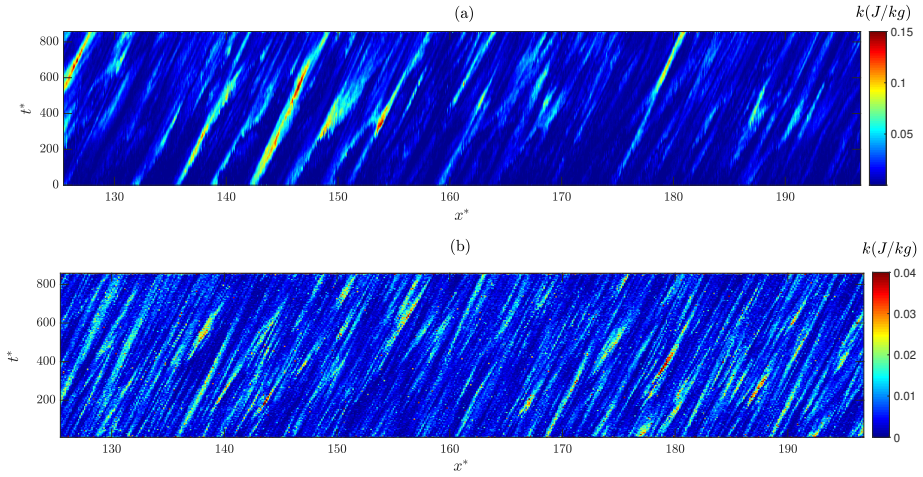

FIGURE 8.4: Space-time diagram of the sum of PKE in each position in the streamwise direction, for the vertical xz (a) and the horizontal xy (b) planes.

8.2 Estimation results

The total perturbation (or fluctuation) kinetic energy (PKE) k^* time-series, together with the POD coefficient time-series are chosen as criteria to study the validation of the algorithm.

The retaining learning data set is composed of $N = 3000$ velocity snapshots sampled at $f_{PIV} = 150Hz$ with a spatial resolution of 0.115 mm.px^{-1}. The validation dataset consisted of 1500 snapshots. The length of the learning data set is related to the occurrence of recorded events. The fluctuation fields are gathered in the learning matrix, as explained in figure 8.1. The size of this matrix was reduced by spatially down-sampling the fields and/or sub-sampling the data set. In our case we subsampled by 2, keeping every second pixel in the image in order to reduce the size of the matrices and computational time. A data standardisation was applied in the input and output data before the training process to help handling possible different signal scales. The computational time on a standard desktop (CPU Intel Xeon 5650 @ 2.66 GHz) was in the order of O(10) minutes depending on the model order, reaching up to 3 hours of learning maximum for the highest order number. This made analytical parameter sensitivity studies a difficult task.

8.2.1 Reduced-order model and validation

The reduced-order state-space model is finally computed using the algorithm N4SID, implemented in MATLAB. Different model orders $N_{order} \in [1:100]$ have been tested, since there is no explicit rule to select it. Even if the validation data set is recorded with the same settings as the ones generating the perturbations, it is independent from the learning data set. A blog diagonal modal form was chosen for matrix $tildeA_w$. To evaluate the global accuracy of the prediction for the validation data set, the PKE is computed from the POD coefficients as $k^*_{POD} = \sum_i a_i^2$ (Guzmán, Sipp, and Schmid, 2014). The difference between the real POD coefficients and the ones estimated by the ROM is then calculated via the error in the total PKE, defined as

$$k_{error} = 100 \frac{||k^*_{POD,real}(t^*) - k^*_{POD,model}(t^*)||}{||k^*_{POD,real}(t^*)||}. \tag{8.8}$$

Figure 8.12 gives the resulting k_{error} with respect to N_{order} for the sensor $s = [\langle v_x'^* \rangle_{\Omega_S}, \langle v_z'^* \rangle_{\Omega_S}]$, as well as 4 other sensors. It reveals that the best sensor is the double velocity sensor, with $k_{error} = 40.7\%$ for $N_{order} = 70$. The results of the POD coefficient time series prediction for

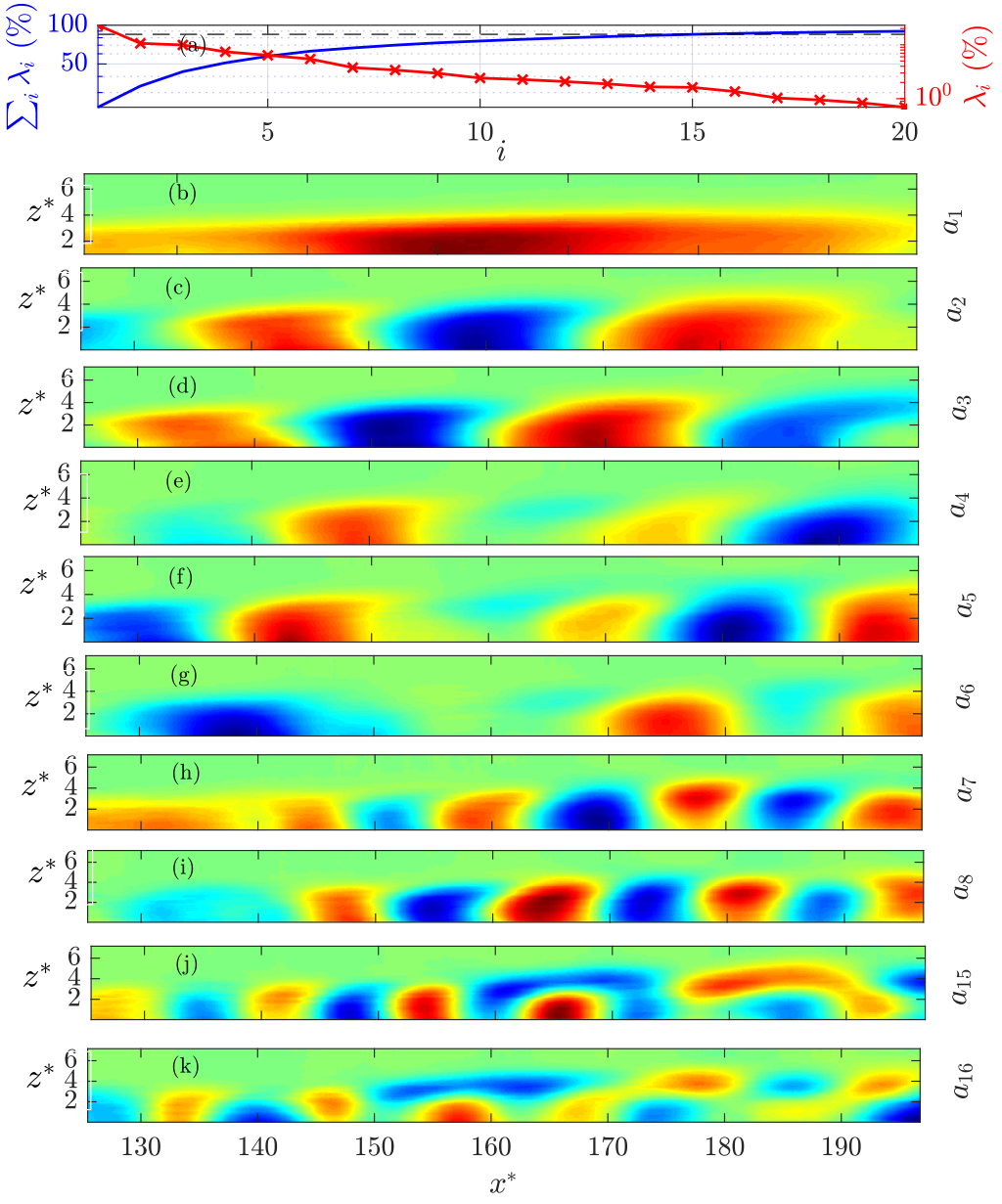

FIGURE 8.5: **(a)** POD energy (red) and accumulated energy (blue). The 85%-threshold is displayed (dashed black).**(b-k)** Normalized POD modes : $\Phi_{1-8}, \Phi_{15}, \Phi_{16}$.

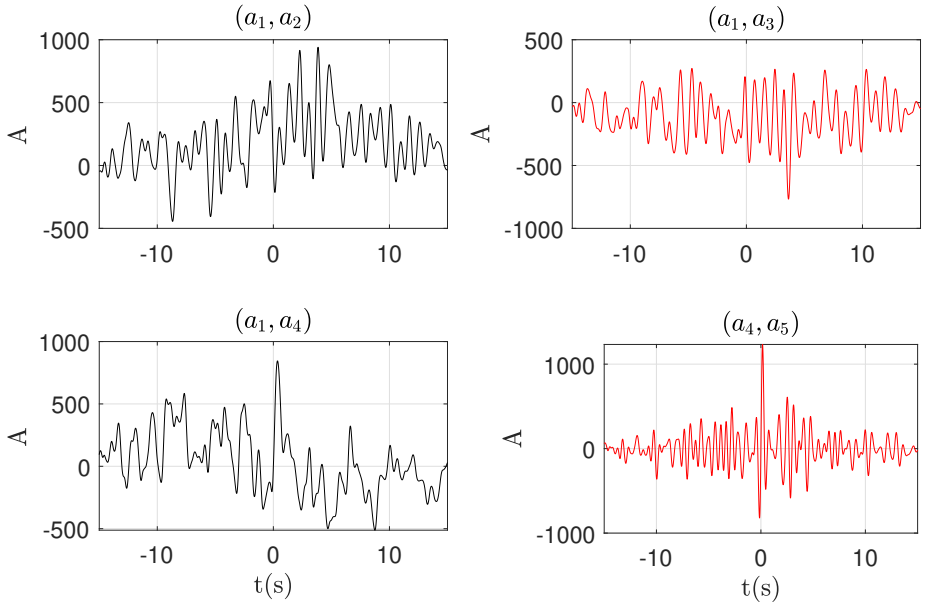

FIGURE 8.6: Signal cross-correlation of 3 POD modes with the first one(1st with 2nd 3rd and 4th), and cross correlation of the pair 4th and 5th. No significant signal correlation is observed with the first mode and any other.

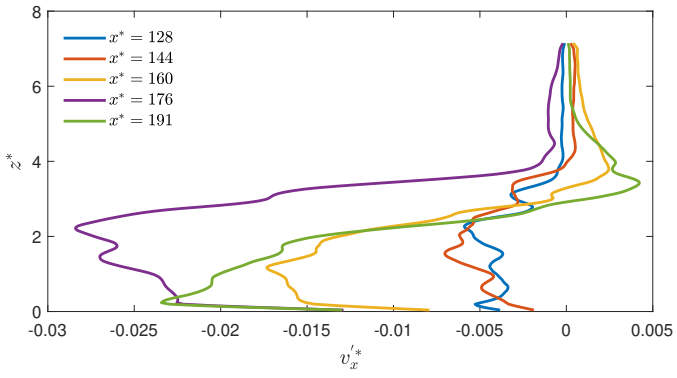

FIGURE 8.7: Instantaneous streamwise fluctuation profiles at different streamwise positions.

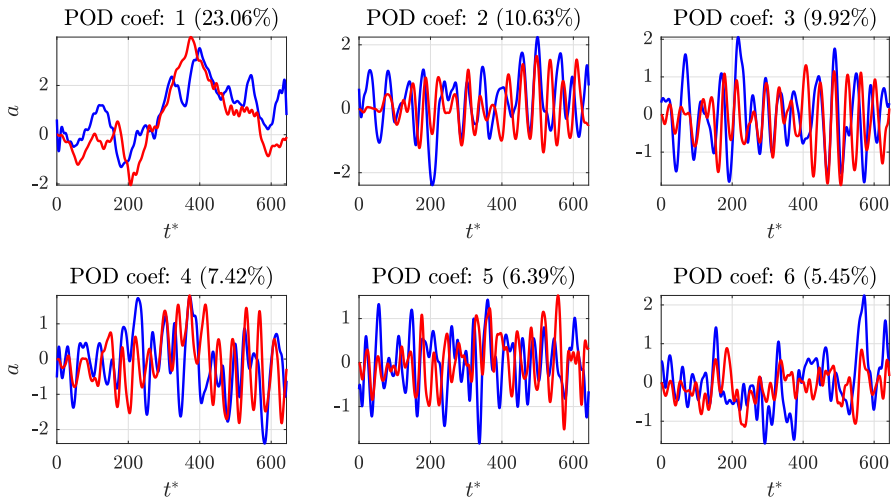

FIGURE 8.8: First six POD coefficient time series for validation dataset: dynamic observer(red) and experiment(blue). Optimal sensor and model parameters used.

the validation dataset can be found in figure 8.8. Unfortunately, although the main oscillation frequencies are captured, the amplitudes are not predicted with satisfying agreement.

For this state order, figure 8.9(a) compares the PKE resulting from the output POD coefficients of the model (red) and the real ones (blue). The amplitudes do not match exactly during the validation step, but the model effectively captures most of the dynamics of the fluctuations. It misses though two important PKE peaks at $t^* = 580$ and $t^* = 630$. The minimization of such fluctuations are a good objective for a closed-loop control. An advected coherent structure is depicted by three successive instantaneous fields in figures 8.10(a,d,g). Their corresponding POD reconstructions are given in figures 8.10(b,e,h). As expected from figure 8.5(a), most of the large-scale structures are well contained by those 16 POD modes, and the noise of the velocity fields is filtered by their projection onto the POD modes. Lastly, the corresponding output fields from the model are shown in figures 8.10(c,f,i). The fields appear visually to be rather close to their real projections, confirming the results obtained with the PKE. The estimated error arises also from the fact that initial conditions during prediction are starting from random values and hence are estimated wrongly in the first steps.

8.3 SI parametric investigation

The method has 3 main parameters to chose for best learning and validation fit. The model order, the number of outputs (POD rank) and the nature and number of the sensors and its positioning.

8.3.1 Influence of the sensors

Instead of a wall sensor, as in the numerical work of Guzmán, Sipp, and Schmid (2014), a different sensor has been used in the present experiment. Different values such as the vorticity ω_y and the λ_{Ci}-criterion, have been monitored directly from the local fluctuations of the velocity fields in the region of the instantaneous PIV snapshot. The size and location of the sensor may play a role in the efficiency of the learning process because the former will act as a spatial filter and the later will be crucial for its ability to detect relevant flow variations (Guzmán, Sipp, and Schmid, 2016).

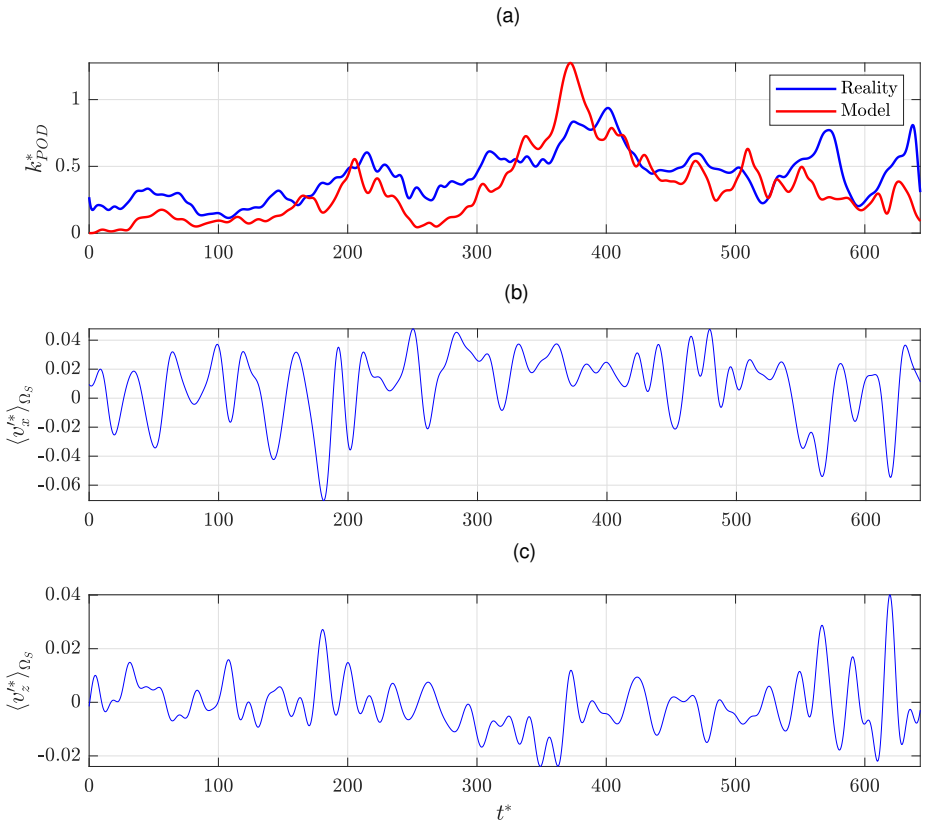

FIGURE 8.9: **(a)** PKE from the POD coefficients k^*_{POD} for the real validation data (blue) and the output of the dynamic observer (red). Time series of **(b)** the streamwise and **(c)** the normal components averaged over Ω_S.Optimal sensor and model parameters used.

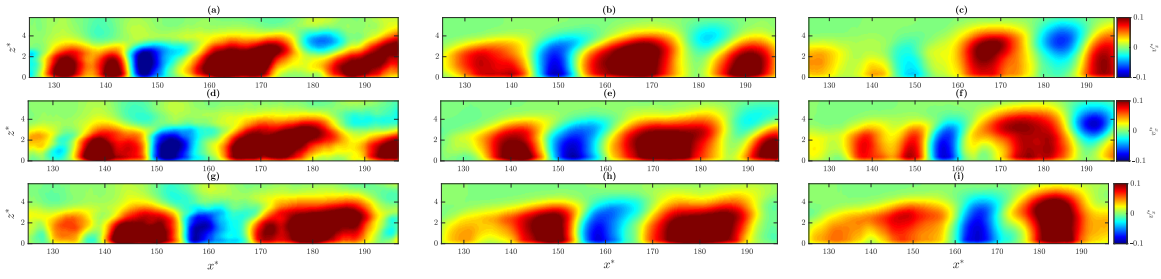

FIGURE 8.10: Real (left), reconstructed by POD (middle) and model-estimated (right) streamwise component of successive instantaneous velocity fields (from top to bottom) separated of $\Delta t^* = 5$. Validation dataset fields are presented.

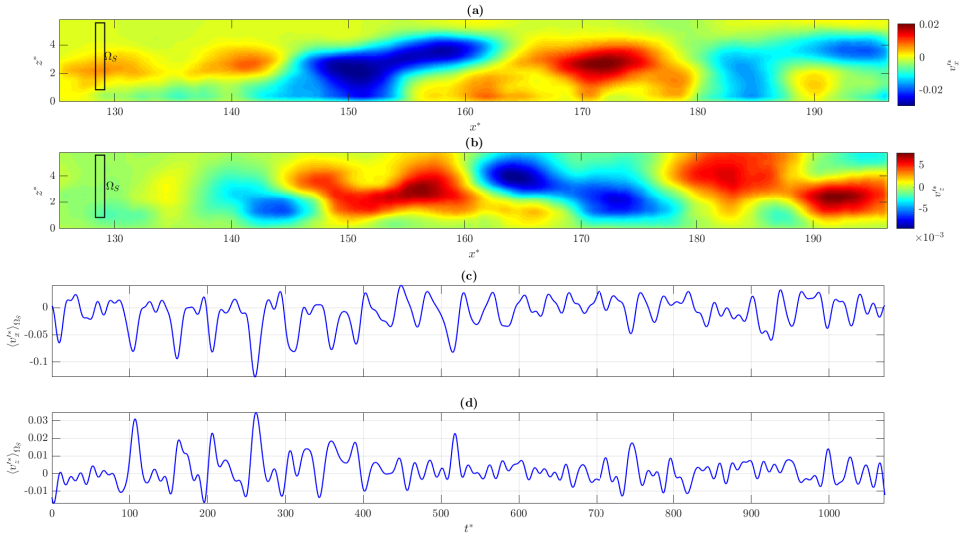

FIGURE 8.11: Instantaneous **(a)** streamwise and **(b)** vertical components of the fluctuating velocities at $t^* = 310$, together with the sensors area Ω_S (rectangles). Time series of **(c)** the streamwise and **(d)** the vertical components of the fluctuating velocity, both space-averaged over Ω_S.

The sensors $s_{1:J}$ used are directly derived from the velocity fields. Various natures, positions and numbers of sensors have been tested. The streamwise $v_x'^*$ and the vertical components $v_z'^*$ are first both monitored in the same region Ω_S placed upstream at $x_s^* = 128$ as shown in figures 8.11(a) et (b). They constitute the sensor $s = [\langle v_x'^* \rangle_{\Omega_S}, \langle v_z'^* \rangle_{\Omega_S}]$, which was optimal as we show further in the article. The sensor does not contain the ten first pixels (interrogation window radius) closest to the wall to limit noisy data. It is also not too large too avoid a smoothing effect. The width of the window is 10 and the height 60 pixels. The position of Ω_S has been chosen to detect the perturbations incoming in the PIV window as upstream as possible. A downstream sensor is avoided in purpose in the present study since the final objective will be the design of a feed-forward control.Other sensors have been tested: the velocity components alone, the swirling strength criterion λ_{Ci} alone, then combined with the streamwise component. As shown in figure 8.12, the streamwise and vertical velocity proved the best sensors for $N_{order} = 70$, whereas it is the vortex identification criterion together with the vertical velocity gave also almost equivalent results.

8.3.2 Influence of the model order

In general, a higher model order increases the number of system parameters to have an optimum fit. In system identification of experimental data though, the contained noise actually might make a high-order model try to model the noise during the learning process, hence actually increasing the error. A parametric sensitivity study of the model order is presented in 8.12.

8.3.3 Influence of number of POD coefficients and sensor position on observability

For a system to be observable, the requirement that the input s(n) and the state Y(n) are well correlated must be satisfied. This leads to the expression: $s = \widetilde{\boldsymbol{C}}\,\boldsymbol{Y}$. The measurement matrix

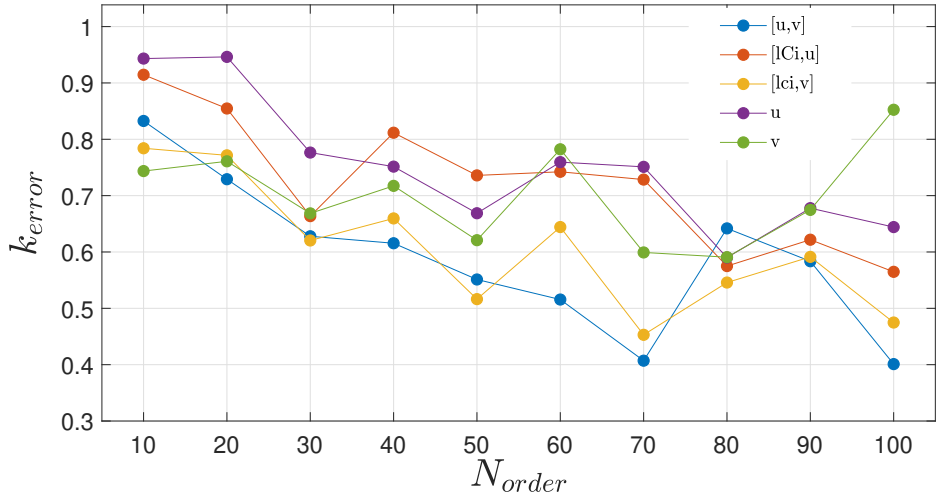

FIGURE 8.12: Difference between the real PKE and the one estimated by the ROM computed with various state orders N_{order} for different sensors. Validation dataset error presented.

$\widetilde{\boldsymbol{C}}$ can be calculated using a least squares method applied to the learning dataset as follows:

$$\widetilde{\boldsymbol{C}} = [s(1)s(2)...s(J)]\ [Y(1)Y(2)...Y(K)]^{\dagger} \tag{8.9}$$

where † denotes the Moore-Penrose pseudo-inverse matrix.

The resulting sensor $s_{POD}(K)$ is then compared to the real sensor s by defining an error as follows:

$$s_{POD,error}(K) = \frac{||s_{POD}(K) - s||}{||s||}. \tag{8.10}$$

Figure 8.13 shows the observability error results for the considered sensors at different streamwise positions. Taking a low number of POD modes into account leads to slightly better results for the sensors localized in the slightly more downstream part of the PIV window. Generally, we see that a minimum number of 15-20 POD modes are required from the observability of the POD basis. Using more than 40 modes leads to an equivalent error regarding all the positions, with a slight better performance of around 3 % of the downstream positions. As mentioned also though above, sensors have to be kept as upstream as possible in order to perform feed-forward control in the future.

8.4 Conclusions

A dynamic estimator method proposed firstly by Guzmán, Sipp, and Schmid (2014) and Guzmán-Iñigo, Sodar, and Papadakis (2019) has been implemented for an experimentally investigated transitional flow: the forced TBL flow, under a bypass transition. The inputs-sensors data have been obtained from optical flow PIV measurements. Sensors consisted in calculating a double visual sensor: the streamwise fluctuating velocity and either the vertical fluctuating velocity or the swirling strength criterion in an upstream window of the flow. The PKE increase induced by the streaks propagating along the flat plate has been identified and model, though with less than acceptable agreement between the model and the real flow. The sensor position and observability, model order and number of states were rigorously investigated. The non-linearity and weak three-dimensionality of the flow though is what makes

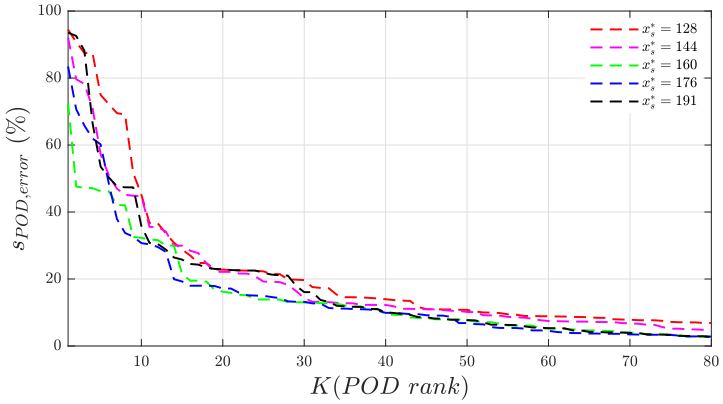

FIGURE 8.13: Relative error between the real and the POD sensor at different streamwise positions, and for different number of POD modes.

this modelling task complicated and not feasible with satisfying agreement; two important peaks of the PKE evolution were missed during the prediction process.

Moreover, the computation of the POD modes and coefficients required large usage of memory regarding the dense fields obtained via optical flow. The high data density inherent to this velocimetry method may thus become a drawback in the present case, as it was foreseen by Champagnat et al. (2011). Nonetheless, spatially down-sampling the field turns out to be a good solution, giving the choice (if the hardware allows it) between high space accuracy and lower computation cost for the estimation of the reduced-order model. A larger PIV window (or the use of a second camera) would be beneficial to capture the streak energy evolution. The description of the flow dynamics would be improved but it would consequently increase the system state order. This would require to change the camera objective to keep the spatial accuracy without extending the number of vectors and therefore the size of the learning matrix.

8.5 Perspectives

The motivation of the presented work is its extension to flow control, in order to suppress the captured coherent structures and reduce the PKE. Further works will therefore concern the closed-loop control based on the proposed dynamic estimator (Ottonelli, 2014; Guzmán, Sipp, and Schmid, 2014), since the actuator is already installed in the experiment. The region investigated contains indeed a slotted jet designed like the one forcing the streaks, which was covered with a plate visible in figure 7.2. The reduction of the PKE may be finally a good objective to fix to the built system since it can also be tracked in real-time. The presented methodology is also currently under investigation for the horizontal plane xy fields like the ones presented at figure 7.7. Distributed sensors in the spanwise direction are probably needed for this complicated task.

On a different direction but with a similar goal, an artificial neural network methodology has been already tested successfully in the same experimental dataset. The goal this time was not to obtain a model, but to reduce the order of the studied system and reconstruct the instantaneous velocity fields using the same visual sensors; all details and description of the method are described in the next chapter; it will be proven that it provide an ameliorated alternative for such system identification purposes.

Chapter 9

System order reduction and velocity field reconstruction of the TBL flow using Artificial Neural Networks

The content of this chapter is based on the article: *A.Giannopoulos, J.L. Aider, Data-driven order reduction and velocity field reconstruction using neural networks: The case of a turbulent boundary layer, Featured Article, Phys. Fluids 32, 095117 (2020).*

We present a data-driven methodology to achieve identification of coherent structures dynamics and system order reduction of an experimental Turbulent Boundary Layer (TBL) flow. The flow is characterized using time-resolved Optical Flow Particle Image Velocimetry, leading to dense velocity fields that can be used both to monitor the overall dynamics of the flow and to define as many local visual sensors as needed. A Proper Orthogonal Decomposition (POD) is first applied to define a reduced-order system. A non-linear mapping between the local upstream sensors (inputs-sensors) and the full-field dynamics (POD coefficients) as outputs is sought using an optimal Focused Time-Delay (FTD) Artificial Neural Network (ANN). The choices of sensors, ANN architecture and training parameters are shown to play a critical role. It is verified that a shallow ANN, with the proper sensor memory size, can lead to a satisfying full-field dynamics identification, coherent structure reconstruction, and system order reduction of this turbulent flow.

9.1 Introduction

Current experimental methods such as Particle Image Velocimetry (PIV) or numerical methods such as Large Eddy Simulations (LES), used to characterize 3D non-stationary flows, produce a large amount of data leading to high-order systems. It is generally necessary to use an order reduction to derive some information that could be handled either to model or control the targeted flow. Data-driven methods are nowadays becoming more and more efficient and reliable even for fluid mechanics research (Guzmán-Iñigo, Sodar, and Papadakis, 2019; Deng et al., 2019). Among successful applications, one can cite statistical learning (Guzmán, Sipp, and Schmid, 2014) or machine learning (Wang et al., 2018; Gautier et al., 2015; Rabault and Kuhnle, 2019) algorithms. More recently Artificial Neural Networks (ANNs) have been used extensively for fluid mechanics, because of their architecture flexibility, needed for reduced-order modelling (Pawar et al., 2019), turbulence modelling (Zhu et al., 2019; Maulik et al., 2018; Xie et al., 2019), as well as for field reconstruction of complex non-linear flows (Liu et al., 2020a). A short review on different applications of Deep Learning to Fluid Dynamics can be found in (Nathan Kutz, 2017). Nevertheless, applying identification or modelling algorithms to experimental fluid mechanics is still challenging because of various noises leading

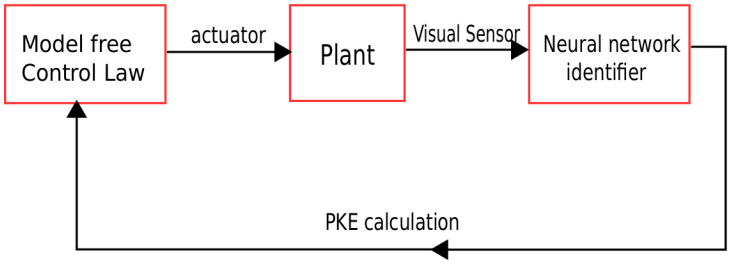

FIGURE 9.1: Control scheme for minimizing perturbation kinetic energy using a neural-network identifier

to non physical errors as well as a limited number of sensors and the complexity of the experimental setup. Large datasets with both good spatial and temporal resolutions are needed for successful applications of these data-hungry methods to experiments.

In an inverted flag flow experiment, Deng et al. (Deng et al., 2019) applied an ANN identification method to reconstruct time-resolved velocity fields from a handful of velocity sensors. It was also proven recently that ANNs can be used to predict the dynamics and reconstruct the time-resolved fields of an experimental Backward-Facing Step (BFS) flow (Giannopoulos and Aider, 2020b). We apply in this study a similar methodology to an experimental TBL flow, with the objective to identify correctly the dynamics, reconstruct the velocity field and predict the total Perturbation Kinetic Energy (PKE) of the full velocity field. The ANN algorithm will be used first to identify the global dynamics from upstream local sensors and second to reduce drastically the order of the system to a handful of easily measurable quantities. Such an algorithm would be an ideal part of a model-free control loops (Gautier et al., 2015) aiming at reducing the PKE field, as shown in the Fig. 9.1.

9.2 Artificial Neural Networks

Artificial Neural Networks (ANNs) can provide a non-linear mapping between one set of inputs-signals (that are easily measurable) and some corresponding output signals (that may be hard to measure in a final application, but still valuable for monitoring or control purposes) (Goodfellow, Bengio, and Courville, 2016). Great progresses have been made lately due to the ability to handle very large data-sets, the advancements of Graphics Processing Units (GPU) parallel programming, and the increasing availability of multiple optimized toolboxes. A short review of applications of deep ANN to fluid mechanics can be found in Nathan Kutz (2017). ANNs can be divided into Feed-Back (or recurrent) and Feed-Forward. They can also be discriminated according to their depth, either shallow or deep, depending on the number of hidden layers (one or more). Finally, they can be divided into static or dynamic, if the output of the current step depends on the previous steps as well, giving it a notion of memory.

In the case of a feed-forward ANNs, the output of any layer only modifies the next layer, not the previous ones. On the other hand, in a recurrent ANN the system output is calculated from its previous past time-steps along with the input at the current time-step (eq. 9.1), hence introducing a notion of output memory in the network.

$$y_t = f_{w,b}(y_{t-1}, x_t) \tag{9.1}$$

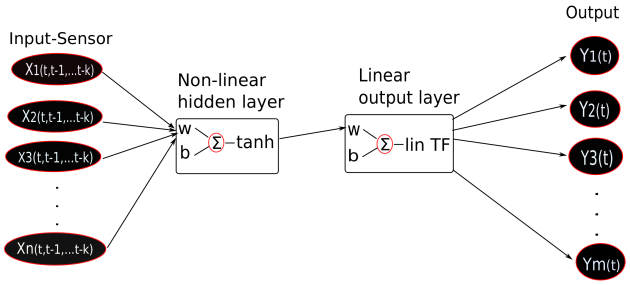

FIGURE 9.2: An example of a FTD ANN to perform a non-linear mapping from N inputs to M outputs.

One category of recurrent ANNs are the Long-Short Term Memory (LSTM) networks. They are gradient-based recurrent NNs used for supervised learning both in classification and prediction problems (Vlachas et al., 2018). They were first developed by Hochreiter and Schmidhuber (1997) to solve the vanishing or exploding gradient problem of the back-propagated error (Bengio, Simard, and Frasconi, 1994). In an LSTM architecture, the network is left to learn alone which past neuron contributions are important. They do so using a sophisticated gate-neuron that determines if the input is important enough or if it should be forgotten and when it should output its value.

9.2.1 Focused time-delay Artificial Neural Networks

The neural network used in the present System Identification (SI) study is a fully-connected FTD ANN, which was first introduced for speech recognition (Waibel et al., 1989). It is basically a standard feed-forward architecture along with a tapped constant time-delay (of time-step size k) in the input (see Fig. 9.2). The term “focused" comes from the fact that the notion of memory is introduced only in the input (sensors), and not in the output like in LSTM ANNs. They are used to model long-range temporal dependencies by keeping a number of k past measurements of the input at each time step x_t. This leads to the following expression for the output of the system :

$$y_t = f_{w,b}(x_t, x_{t-1}, ..., x_{t-k}) \tag{9.2}$$

where w and b are weight and bias parameters. They have been used for rainfall prediction (Charaniya and Dudul, 2012) as well as for effective acoustic modelling (Huang et al., 2019), in deeper architectures.

For the above network with a non-linear activation function f_1 in the hidden layer and a linear activation function f_2 in the linear layer, the equation giving the k_{th} neuron output of a single hidden layer network connected to the j_{th} neuron of the previous layer is:

$$y_k = \mathbf{f_1}\left(\sum_{j=0}^{N_2} w_{kj}^{(2)} \mathbf{f_2}\left(\sum_{i=0}^{N_1}\left(w_{kj}^{(1)} x_i + b_i\right)\right) + b_j\right) \tag{9.3}$$

where N_1 is the number of neurons in the first (hidden) non-linear layer and N_2 the number of neurons in the second (linear) layer. Regarding the choice of the non-linear activation function f_1, the tan-sigmoid or hyperbolic tangent function is used:

$$tanh(x) = \frac{e^{2x} - 1}{e^{2x} + 1} \tag{9.4}$$

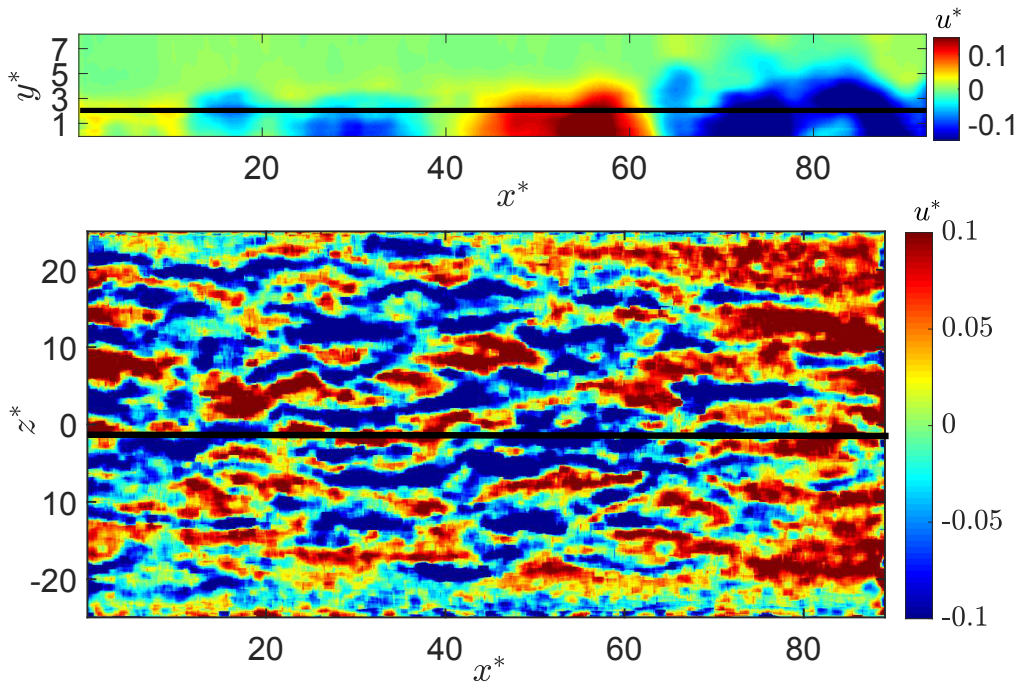

FIGURE 9.3: Instantaneous streamwise velocity fluctuation field of the TBL experiment. Vertical field for $z^* = 0$ (top) and horizontal field for plane $y = 2\ d_0^*$ (bottom). Streamwise velocity streaks can be clearly observed.

A widely used training process of the ANN (meaning finding the optimum weights and biases connecting the neurons of different layers) consists in dividing the data-set between a training data-set, a validation data-set and a testing dataset. For the training data-set we chose one set of weights (randomly initialized in the first iteration) connecting the layers and we use the same weights for each time step to calculate the output of the model. The error of the real vs the model-generated output signal is computed and the weights and biases are updated according to different back-propagation schemes (in our case the Scaled Conjugate Gradient method). The above process is called one “epoch". We continue the process for as many epochs as needed until a satisfactory fit error is achieved. The second data-set is used to test the performance of the network on new data and verify the achieved error, hence avoiding overfitting. The testing dataset is used to provide a single blind evaluation after the training of the network, providing an unbiased evaluation of the training process.

In the following, we first present the experimental setup as well the main characteristics of our TBL flow. The choice of the sensors of the ANN is then discussed and parametric studies of different training parameters are presented. The efficiency of the ANN for the dynamics identification and velocity field reconstruction is illustrated before turning to the discussion and conclusion.

The dynamics identification and coherent structure reconstruction of a subcritical bypass transition is investigated in the present experiment. The transition is triggered using a finite amplitude pulsating jet (as described in the experimental setup section 7.1.1). Groups of wavy streaks are observed as shown on Fig. 9.3. In the following all the spatial variables are non-dimensionalized using the displacement thickness at the beginning of the PIV window δ_0^* (at $x_0 = 37$ cm), for the unperturbed flow and noted (x^*, y^*, z^*). The velocity components are non-dimensionalized with the freestream velocity U_∞ and noted (u^*, v^*, w^*). Consequently, we refer to the dimensionless time $t^* = tU_\infty / \delta_0^*$.

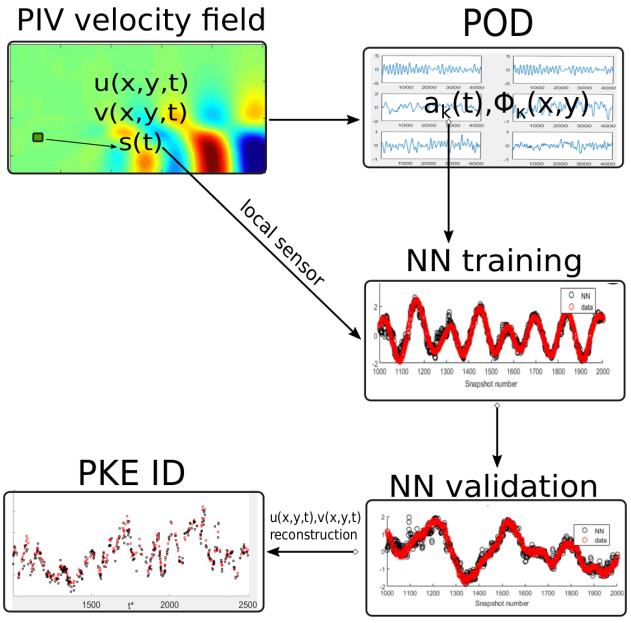

FIGURE 9.4: Block diagram showing the different steps used for the experimental perturbation energy identification through POD and training/validation steps.

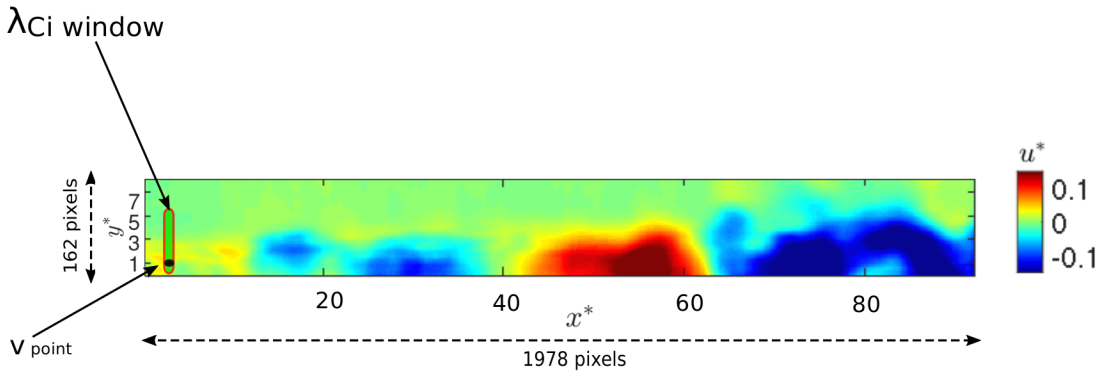

FIGURE 9.5: Location of the double visual sensors shown over the time-averaged unperturbed streamwise velocity field $\overline{u}$.

PIV length (cm)	23.39
Snapshot size (pixels)	162x1978
Spatial resolution (mm/px)	0.116
# Snapshots	6400
Acquisition time (s)	41.3

TABLE 9.1: PIV experiment parameters

9.3 Time-resolved PIV measurements

The flow was seeded with 20 μm neutrally buoyant polyamide particles, illuminated by a laser sheet created by a 10 W continuous laser (MX-6185, Coherent, USA) operating at 532 nm. A thin layer of fluorescent paint (FP Rhodamine 6G, Dantec) was applied to the illuminated surface, absorbing the laser wavelength to avoid reflections and to allow correct near-wall measurements. The camera used was a PCO DIMAX-cs with a sampling frequency of 150 Hz. An narrow-band optical filter centered around 532 nm was mounted on the camera to avoid any optical noise.

The velocity field is calculated from the acquisition of successive snapshots of the vertical laser sheet in the middle of the test section using a home-made optical-flow algorithm. The first version of the code has been developed at ONERA (Champagnat et al., 2011) and later modified, optimized and adapted to the constraints of real-time measurements (Gautier and Aider, 2015b). The advantage of this algorithm compared to a standard FFT-PIV algorithm is its high computational speed when implemented on GPUs with CUDA functions (C.Pan et al., 2015). The code has been used many times both for time-resolved PIV measurements with a high spatial resolution (Varon et al., 2017) as well as for closed-loop flow control experiments (Gautier and Aider, 2013; Gautier, 2014; Gautier and Aider, 2015a; Varon et al., 2019).

The vertical (x, y) PIV plane was chosen for the present identification because a larger experimental dataset was available, as seen in figure 7.4. Indeed, only the boundary layer region contains relevant information for the identification algorithm so that only the lower part of the snapshots are used, which allows a significant reduction of computational time. Also, the distribution of streaks in the spanwise direction was found homogeneous for the specific forcing. The extension of the method in the horizontal plane and for different boundary layer forcing scenarios could also be investigated. The parameters of the PIV experiments used in the following are summarized in table 9.1. One should keep in mind that the optical flow algorithm leads to dense vector fields with one vector per pixel.

9.3.1 Transition forcing mechanism

Experiments were carried out in an hydrodynamic channel in which the flow is driven by gravity. The flow is stabilised by divergent and convergent sections separated by honeycombs leading to a turbulence intensity of 0.6 %. A NACA 0020 profile is used to smoothly start the boundary layer. The test section is 80 cm long with a rectangular cross-section 15 cm wide and 8.5 cm high as shown in Fig. 7.4. The unperturbed flow is a laminar boundary layer. The Reynolds number measured at the inlet of the PIV window is $Re_{\delta^*} = 409$ for a freestream velocity $U_\infty = 0.188\ m.s^{-1}$. No natural instability was observed without forcing. The displacement thickness at $x_0 = 37\ cm$ is $\delta_0^* = 2.5\ mm$ leading to a shape factor $H_0 = 2.34$, typical of a laminar boundary layer.

In order to evaluate the potential of ANN on a non-linear flow, the transition to turbulence of the boundary layer is forced using a finite amplitude pulsating jet perturbation. The perturbation is induced by a spanwise slotted inclined (45°) jet as shown on Fig. 7.4. The injection system is optimized to obtain an homogeneous velocity along the spanwise direction. It is located at $x = 5$ *cm* downstream the leading edge, as shown in Fig. 7.4. The jet outlet has a rectangular cross-section which is 0.4 *cm* long (streamwise direction) and 9 *cm* wide (spanwise direction). The jet is supplied by a pressurized water tank, monitored by a SMC ITV 1010 electro-pneumatic regulator to control the jet frequency $f_{forcing}$ and amplitude $U_{forcing}$. The frequency of the perturbation was random ($0 < f_{forcing} < 5Hz$), for a constant maximum amplitude. The experiments were repeated multiple times showing the same Proper Orthogonal Decomposition (POD) mode structures.

The shape factor H of the forced boundary layer is $H = 1.31$, which is typical of a turbulent flow. The boundary layer thickness range in our PIV window was $\delta_{99} = [0.01 - 0.016]$ and the skin friction coefficient range $C_f = [0.0062 - 0.0072]$. The wall coordinate in figure 9.3, bottom, was $y^+ = [1.39 - 1.63]$. The coherent structure advection velocity u_{adv} has been estimated around 0.75 U_∞ (based on a space-time diagram of a horizontal profile of the streamwise velocity perturbation inside the boundary layer).

9.3.2 Proper Orthogonal Decomposition

Decomposing a dynamical system in modes of decreasing importance can help reducing the order of the variables of the system. N consecutive instantaneous velocity fields $\{\boldsymbol{U}(n) = (u^*, v^*)\}_{n=1...N}$ were computed from consecutive flow snapshots with an acquisition frequency $f_{ac} = 150\,Hz$. By calculating the mean field $[\overline{u}, \overline{v}]$ we were able to obtain the velocity fluctuations $u'(t) = u^*(t) - \overline{u}$ and $v'(t) = v^*(t) - \overline{v}$, which contained all the dynamics and were used to create the reduced-order system. The fluctuation matrices organised in columns for each time-step were used to form the so-called “snapshot matrix" to be decomposed. The reduced-order system is obtained using POD, which has been used extensively in fluid mechanics (Borée, 2003; Mendez et al., 2017). It allows us to build a ranked and orthonormal basis containing N modes (Lumley, 1967; Sirovich, 1987). The first M modes $\{\boldsymbol{\Phi_m}\}_{m=1...M}$ with $M \leq N$ containing a sufficient percentage of the total energy is then chosen to compute the approximated velocity field $\tilde{\boldsymbol{U}}(\boldsymbol{n})$:

$$\tilde{\boldsymbol{U}}(\boldsymbol{n}) = \sum_{m=1}^{M} \langle \boldsymbol{\Phi_m}, \boldsymbol{U}(\boldsymbol{n}) \rangle \boldsymbol{\Phi_m} = \sum_{m=1}^{M} a_m(n) \boldsymbol{\Phi_m} \tag{9.5}$$

where the scalar product $\langle \cdot, \cdot \rangle$ is the energy-based inner product. The system output to be identified is obtained through the reduced state vector containing the M POD coefficients $a_m(n)$:

$$Y(n) = [a_1(n)\ a_2(n)\ ...\ a_M(n)]^T \tag{9.6}$$

The full-field dynamics are now contained in their POD coefficients $a_m(t)$. The balance between the order and accuracy of the POD reduced-order system is crucial, because for a large number of POD modes the SI methods are much more likely to fail.

9.3.3 Overview of the method

In the present SI method we first apply a POD to the time-resolved PIV snapshot matrix, to perform a first system order compression. Then we proceed to train a FTD ANN for the non-linear mapping between local upstream sensors and the dynamic POD coefficients. All the dynamics information is then included in a 2 easily measurable quantities. More

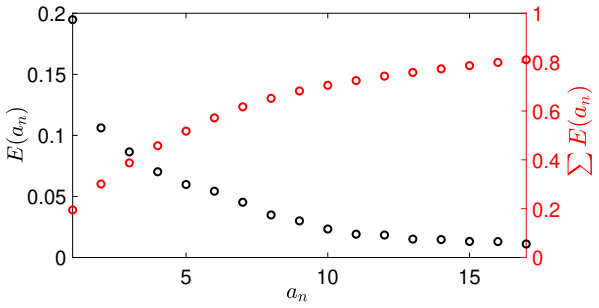

FIGURE 9.6: Energy of each POD modes together with the cumulative total energy of the POD modes up to 80 % of the total energy.

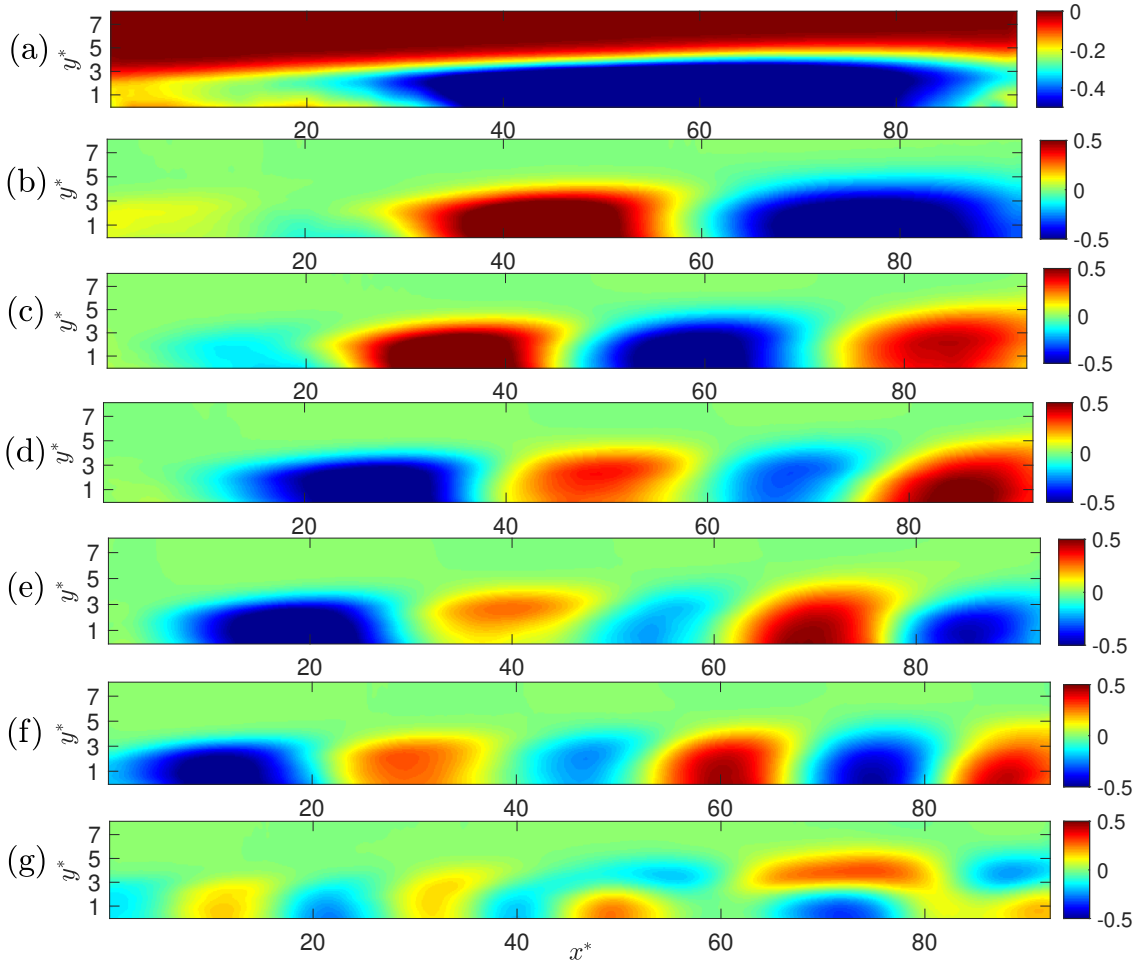

FIGURE 9.7: 1^{st} to 6^{th} (a-f) and 13^{th} (g) POD mode structures.

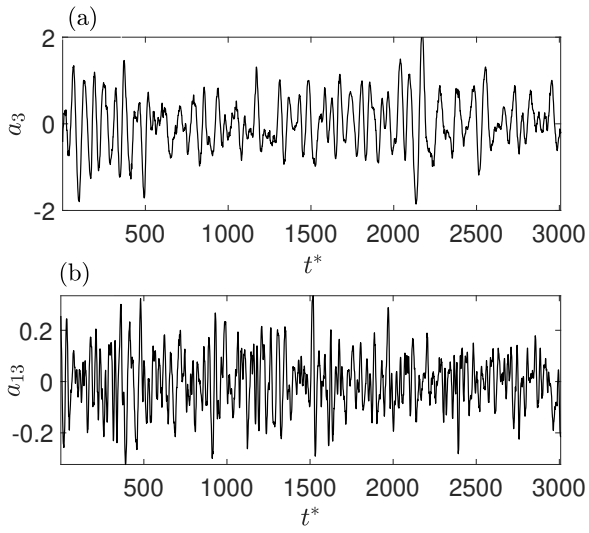

FIGURE 9.8: Evolution of 3^{rd} (a) and 13^{th} (b) dynamic POD coefficient.

specifically, the available time-resolved PIV dataset is divided into the learning or training part, the validation part and the testing part. During the training step, the parameters of the model (weight, bias) are updated accordingly using an appropriate learning algorithm which takes into account the error between the expected output and the model-generated output via a back-propagation learning algorithm, in our case the scaled conjugate gradient. After each weight and bias update, an epoch has passed. As many epochs as needed are used to obtain a satisfying fit error. Then, during the validation step, the model generated outputs are compared with the new data, this time expecting equivalent fit results as during the training step. Large validation fit errors yield over-fitting; meaning that the network does not provide a generalizable extrapolative solution for new input data. The correctly trained network will allow the accurate prediction of the PKE at any moment using just a few local PIV sensors. The different steps of the overall identification process are summarized on the diagram shown in Fig. 9.4.

9.3.4 Validation Criterion

To evaluate the efficiency of the identification, one has to define a relevant quantitative criterion to compare the POD coefficient time-series results obtained with the different ANN architectures to the ones obtained experimentally. In the present study, we compute the mean-squared error (MSE) at each time-step n for each POD coefficient $a_m(n)$:

$$MSE_m = \frac{1}{N}\sum_{n=1}^{N}\left(a_{exp,m}(n) - a_{NN,m}(n)\right)^2 \tag{9.7}$$

Then the averaged MSE for all the coefficients ($M = 17$) time-series gives the final evaluation error for the specific ANN architecture:

$$MSE = \frac{1}{M}\sum_{m=1}^{M} MSE_m \tag{9.8}$$

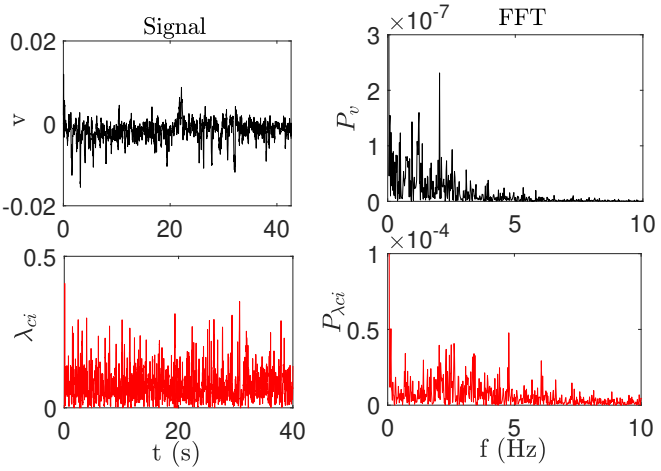

FIGURE 9.9: Time-series and power spectrum of velocity (s_1) and swirling strength (s_2) sensor.

9.4 Sensors definition

First, we obtained the full dataset of $N = 6400$ consecutive snapshots, acquired with a sampling frequency of 150 Hz. A POD was applied using the snapshot method. 17 POD modes were needed to obtain satisfying results with at least 80 % the total energy. The energy of the individual POD modes as well as their cumulative energy are shown in Fig. 9.6. The spatial structure of the third and 13^{th} POD modes can be found in Fig. 9.7 while their time evolution is shown in Fig. 9.8. We clearly see the similarity of the 3^{rd} POD mode with the large-scale coherent structures visualized in the instantaneous field of Fig. 9.3.

9.4.1 Choice of the sensor

The visual sensors will be the inputs in the identification process. The choice of the sensor(s) is then a critical step. There are many possible type of sensors as well as many possible size and locations. The first step is to choose the physical nature of the sensor which should be based on the two components of the instantaneous 2D velocity field measured at each time-step. It can be simply one of, or the two components of the velocity field, or the velocity magnitude measured in a given window defined in the PIV field. Because of their simplicity, they are the first sensors we will test.

As we are interested in the dynamics of coherent structures advected into the boundary layer, one can also choose to compute the vorticity field. As the vortical structures are embedded into the boundary layer, it is better to use more refined detection criteria, like the Q criterion or the λ_{Ci} criterion, which are well adapted to the identification of vortical structures inside a shear layer.

In the following, we will use the swirling strength λ_{Ci} criterion, which was first introduced by Chong, Perry, and Cantwell, 1990 who analyzed the velocity gradient tensor $\mathscr{D} = \overrightarrow{\nabla}\overrightarrow{u}$ and proposed that the vortex core could be defined as a region where $\nabla\mathbf{u}$ has complex conjugate eigenvalues. It was subsequently improved by Zhou et al., 1999 and by Chakraborty, Balachandar, and Adrian, 2005. It was also successfully applied by Cambonie and Aider, 2014 to visualize the 3D vortices created by a Jet in Cross-Flow measured by Volumetric Velocimetry or by Gautier and Aider, 2015a in a closed-loop flow control experiment

n_1	**MSE**	**Sensor choice**
75	0.05	[λ_{ci} , v']
110	0.11	v'
90	0.32	λ_{ci}

TABLE 9.2: Comparison of the validation data-set fit error obtained with a single velocity input, a single swirling strength input and their combination. Using the combination of the inputs minimises the MSE and the number of neurons.

using a similar visual sensor. For 2D data, λ_{Ci} can be computed quickly and efficiently using eq. (9.9) when such a quantity is real (else $\lambda_{Ci} = 0$):

$$\lambda_{Ci} = \frac{1}{2}\sqrt{4\det(\nabla \mathbf{u}) - \mathbf{tr}(\nabla \mathbf{u})^{\mathbf{2}}} \tag{9.9}$$

9.4.2 Influence of number of sensors

On one hand, reducing the number of sensors leads to a reduction of the number of inputs (and outputs) which generally would make the training of the system simpler. On the other hand we may loose valuable dynamics information, helpful for the identification process. A compromise has to be found. A combination of two inputs has been tested: first, the wall-normal velocity measured at one point (averaged over the five neighbouring pixels) and second, the swirling strength vortex identification criterion λ_{Ci} (as a sum of all the pixels in a 15 pixels-wide window). The combination of the 2 inputs was found to give better results compared to the velocity sensors alone or the swirling strength alone or the local vorticity and velocity combination. The main MSE results can be found in table9.2.

The swirling strength window allows a good detection of all the advected vortices. The spectra of the two sensors (Fig. 9.9) show that the velocity sensor detects the large structures passing in the neighbourhood with a frequency close to 1 Hz, while the swirling strength criterion gives us more information about the high frequency dynamics up to 4.8 Hz. Some frequencies can be found in both spectra, like a clear 2.32 Hz peak.

The efficiency of the combination of the two sensors can be explained through the cross-correlation of the sensor signals with the time-series signals of the POD coefficients, as illustrated in Fig. 9.10. One can clearly see that the 3_{rd} POD coefficient is weakly correlated with the swirling strength sensor, while it is strongly correlated to the velocity sensor. On the opposite the 13_{th} POD coefficient, which contains higher frequencies (see Fig. 9.8), is strongly correlated with the swirling strength sensor. This could be one of the reasons why the training using these two sensors is much more accurate than using a single sensor.

9.4.3 Influence of position and size of the sensor

The width of the swirling strength window plays an important role to obtain good SI results. If it is too large, it creates an unnecessary smooth event, while if too small it can be too noisy, especially for gradient variables computed from experimental data. A good compromise was found for 0.7 y^*. The height of the window was chosen large (5 y^*), so that it contains entirely the advected structures in the wall-normal direction, as observed in the POD modes.

The choice of the position of the sensors is also crucial. In general, the sensors should be located as upstream as possible in order to measure and predict early the downstream dynamics. The final position of the chosen sensors is shown in Fig. 9.5.

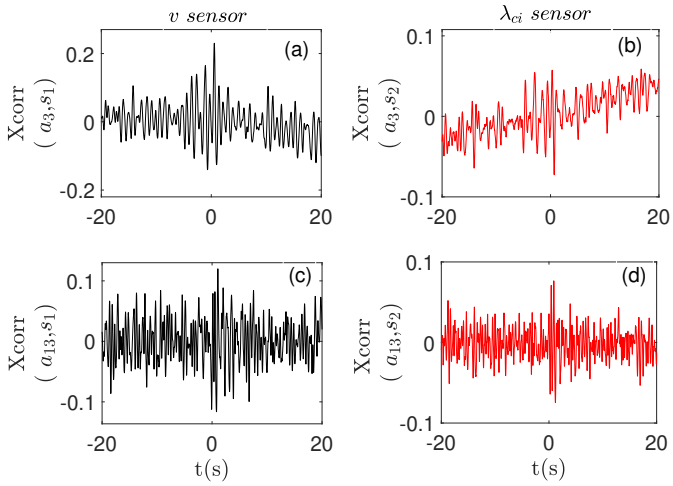

FIGURE 9.10: Cross-correlation of the velocity (s_1) and swirling strength (s_2) sensors with 3rd (a,b) and 13th (c,d) POD coefficient.

9.5 ANN parameter sensitivity studies

The architecture and parameters of the ANN can be changed to avoid overfitting and improve the training process, mainly by choosing the appropriate number of neurons in the hidden layer. The depth of the network (meaning number of hidden layers) can also be increased if needed. Generally a deeper network (using the same number of total neurons) will allow the identification of more complex features and information. The drawback is that the successful training can become very tricky, especially since it increases significantly the computational time for the training as well as the complexity of the network. This makes training parameter sensitivity analysis almost impossible.

In the FTD ANNs used in the present study the input time-delay (meaning the size of the sensor memory) can also be chosen accordingly to improve training and validation fit. It was found critical for the success of the training. The training process had a very low computational time: it was of the order of $O(1)$ minute using a Intel Xeon E5-2630 CPU running at 2.2 GHz. This allowed for a full parametric study to find the optimal time delay k for the inputs and the minimum number of neurons for the hidden layer.

For all the ANN calculations (training, validation) the MATLAB Deep Learning Toolbox was used. A basic scheme of the final FTD ANN can be shown in Fig. 9.11. An anti-causal zero phase low-pass moving average (over four time-steps) filter has been applied to each pixel time-series. The maximum frequency of the forced BL dynamics was 5 Hz, so seven times lower than the low-pass filter cutoff frequency.

We mention that training with Long-Short term memories recurrent network architectures was found inefficient in our case, with a strong increase of the computational time. A simple shallow Time-Delay ANN scheme with 75 neurons gave the best results. This actually contradicts the result of Olekan et al. (2016) who have found out that deep architectures are more efficient than single hidden layer models for noisy data sets. In our case a single hidden layer model was sufficient. The ANN used contained a tan-sigmoid transfer function. As a standard time-delay neural network it also contained an output layer with a linear transfer function to the output.

9.5.1 Training parameters

The full data-set is divided into 3 parts: training or learning (85% of the snapshots), validation (10% of the snapshots) and over-fitting test data-set (5% of the snapshots) as summarized

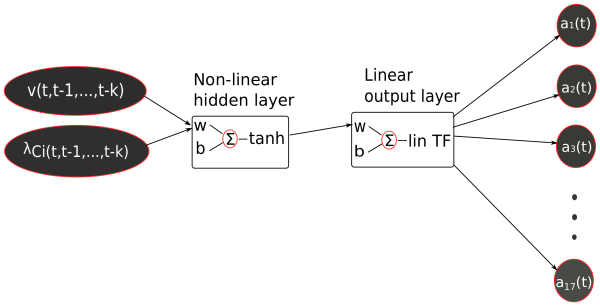

FIGURE 9.11: Structure of the FTD ANN used for this study, with 2 inputs-sensors ($v_\prime$ and λ_{Ci}), a k time-delay, 1 hidden layer with 75 neurons and M outputs (in our case $M = 17$ POD modes).

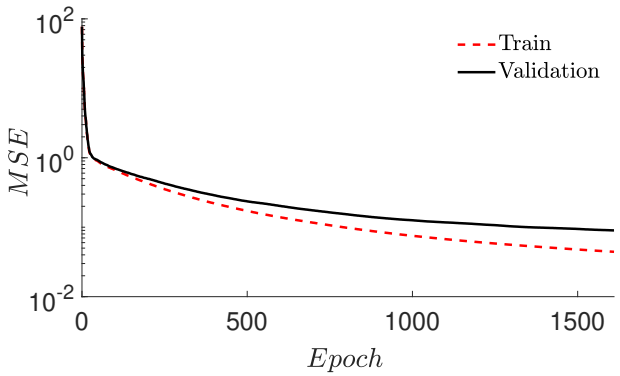

FIGURE 9.12: Training and validation mean-squared error for each epoch of the training process.

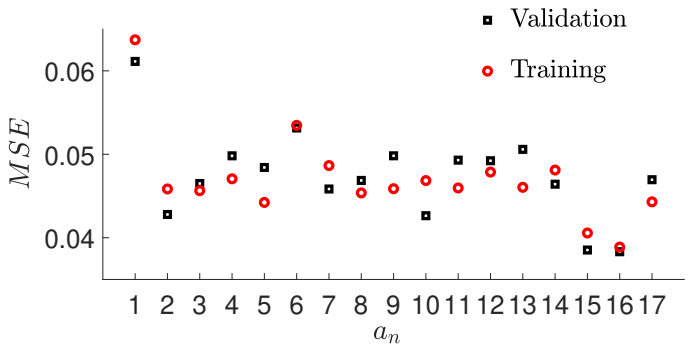

FIGURE 9.13: Training and validation MSE for each POD coefficient time series.

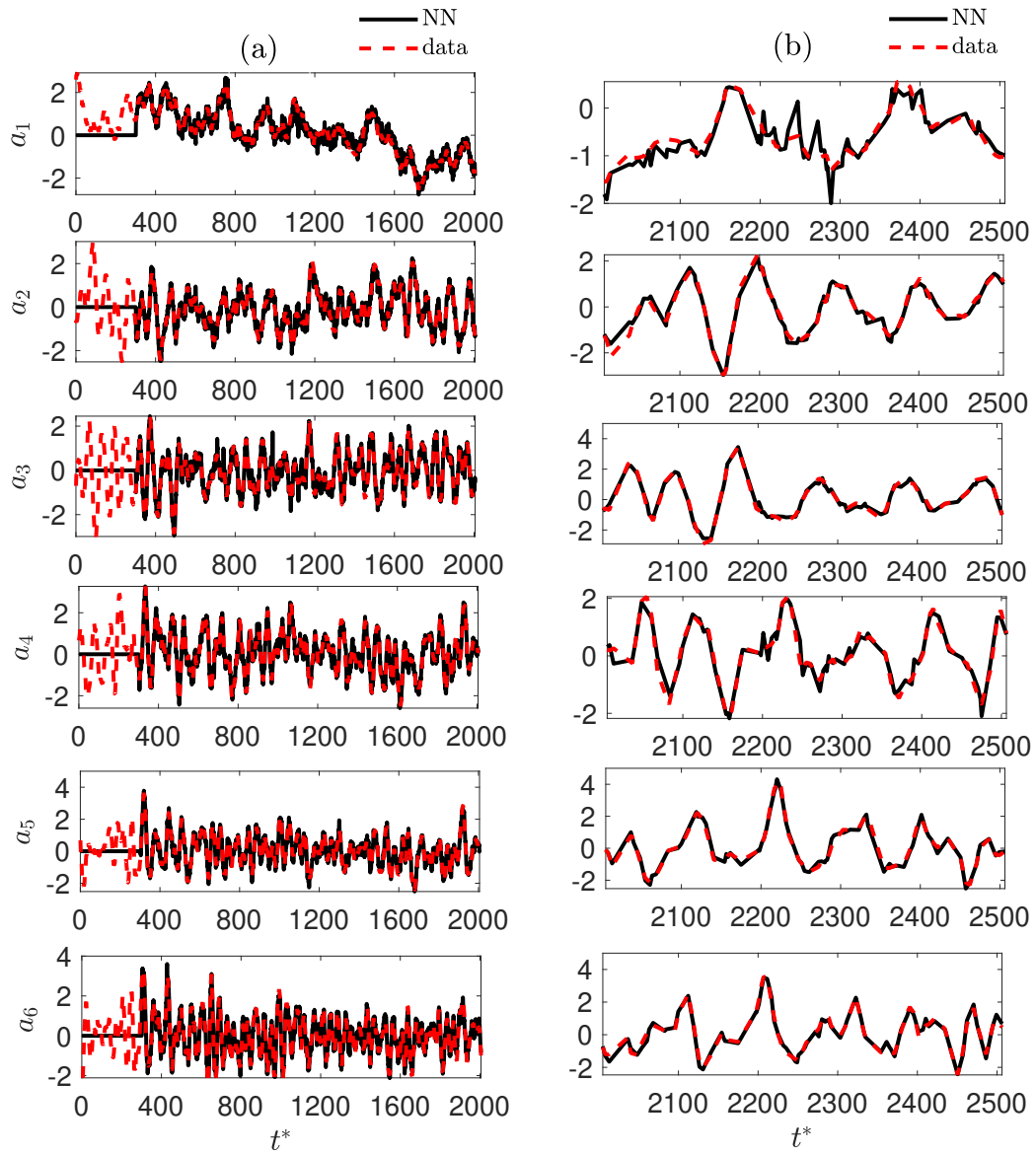

FIGURE 9.14: Comparison of the 1st to 6th POD coefficients time-series obtained from experimental data with the ones obtained with the ANN for training(a) and validation (b) datasets. The network zero signal due to time-delay is evident in the training set.

# Inputs	2
# Outputs	17
# Training Snapshots	5440 (85%)
# Validation Snapshots	640 (10%)
# Overfitting check snapshots	320 (5%)

TABLE 9.3: Neural network training parameters configuration

in Table 9.3. The third data-set is used as an early stopping criterion to test if a rising error is observed during the training process. As a common practice the data are shuffled randomly before the beginning of the training process. It avoids bad models if the data are initially classified. It also makes fitting faster because neighbouring points are not similar. Block consecutive data-set division failed to give good fit results. We also mention that a data standardisation was applied before the training process which also helps when different inputs or outputs have different scales. Lastly, we mention that the weights and biases of the network are initialised randomly for the first epoch.

The optimum number of neurons for the hidden layer was found to be 75 and the best sensor time-delay corresponded to $k = 300.8 \times t^{\star}$ snapshots (or around 4 s). The evolution of MSE with the epoch number is shown in Fig. 9.12 for both training and validation. The MSE decreases sharply for the first epochs and more smoothly for increasing epochs. The optimum architecture and training parameters are summarized in the table 9.4.

Network layer structure	2-75-17-17
Activation function	Hyperbolic Tangent
Loss function	MSE
Training method	Scaled Conjugate Gradient
Time-delay(s)	4

TABLE 9.4: Final choice for the neural network parameters.

In Fig. 9.13 we can see hat the MSE for each POD coefficient is around 5 % for most of the coefficients and for both training and validation, which is very satisfactory. In Fig. 9.14 we compare the time-series of the six first POD modes with the time-series obtained in the training step (a) and in the validation step (b). Both training and validation data are in very good agreement with the experimental data.

9.5.2 Influence of the sensor memory

The influence of the time-delay in the inputs, is illustrated on the plot of the evolution of the MSE as a function of the time-delay shown in Fig. 9.15. We observe that the sensor memory is critical for the correct dynamics identification: a minimum of $k = 150 \times t^{\star}$ time units is required to obtain for the first time a correct identification with an MSE lower than 50%. A sensor memory of $300.8 \times t^{\star}$ breaks the error limit of 5%. The interpretation of the physical meaning of an optimal neural network is often useful, but not frequently studied. In our case we observe that an abrupt error drop occurs in the region of the sensor memory size of $t^{*} = 150 \times t^{\star}$; using the structure advection velocity we obtain a characteristic length scale of 112.2 x^{*}, which is 1.22 times the size of our PIV domain (92 x^{*}). This shows that the optimal memory size is actually a function of the sensor position, the structure advection velocity and the size of the domain of which we are identifying the dynamics.

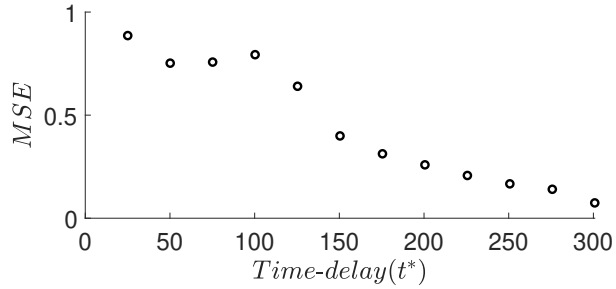

FIGURE 9.15: Network validation performance as a function of the time-delay in the sensors. Increasing the size of the sensor memory decreases the error in a linear way, after approximately 150 time units.

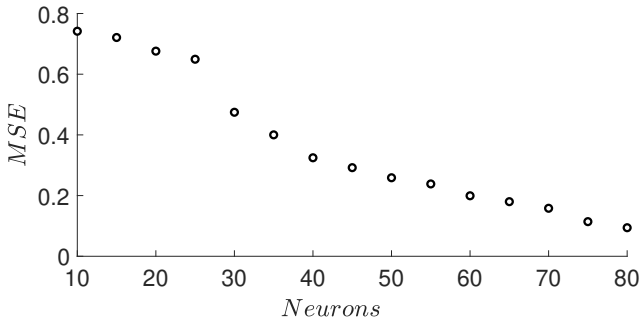

FIGURE 9.16: Network validation performance as a function of the number of neurons in the hidden layer.

9.5.3 Influence of the number of neurons in the hidden layer

Keeping an optimal constant time delay of 600 time-steps or 300.8 t*, we can study the sensitivity of the validation errors as a function of the number of neurons in the hidden layer, as shown in Fig. 9.16. A minimum of 70 neurons is needed to achieve an error of the order of 10 %. We also should keep in mind that increasing the number of neurons in the hidden layer increases drastically the number of parameters and the complexity of this fully connected architecture, even if the network is shallow.

9.5.4 Influence of the size of the training data-set

In Fig. 9.17 we show that decreasing the number of snapshots used for the training of the network leads to an increase of the number of neurons in the hidden layer needed for an equivalent validation error (keeping a constant time-delay of 301 time units t^*). Above a given number of snapshots, increasing the number of neurons does not help: it introduces overfitting hence increasing the validation error.

9.5.5 Optimal parameter results

Using the optimal time delay, the right number of neurons in the hidden layer and the proper combination of double upstream sensors, we can check the efficiency of the network in the POD coefficient signal prediction and the time-resolved instantaneous fields reconstruction. The dynamic coefficient signals are accurately predicted. In Fig. 9.14 it is clear that the fit error is similar for both training (left) and validation (right) datasets, which is strong evidence

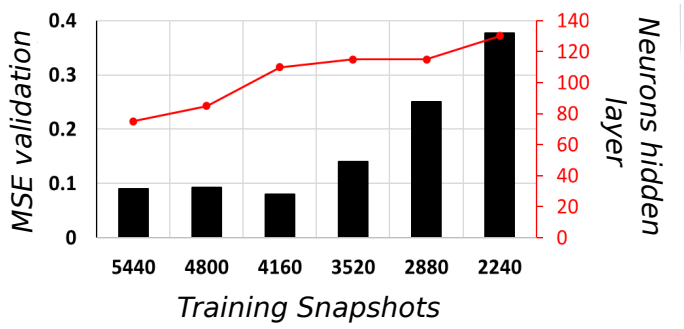

FIGURE 9.17: Network validation performance as a function of the number of snapshots used for the training.

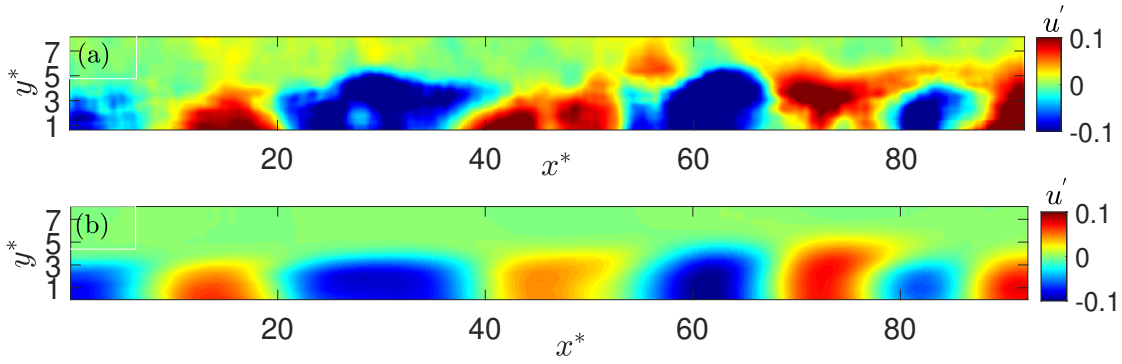

FIGURE 9.18: Instantaneous horizontal fluctuation velocity field comparison between experiment (a) and ANN-reconstructed field (b). Movie online. Time-steps are not consecutive due to the dataset shuffling process during the training-validation division.

that we avoided overfitting. In Fig. 9.18 we see that the main large coherent structures are well reconstructed.

Finally, the kinetic energy of these perturbations (PKE) computed for each pixel in the PIV window is defined as:

$$PKE(t) = \frac{1}{2}\left\|\left(u'(t), v'(t)\right)\right\|^2 \tag{9.10}$$

The sum of this quantity for each pixel is an interesting control quantity for the future model-free control scheme, since it is an indication of the total advected turbulent fluctuations intensity. So it is calculated and a compared, between ANN generated results and experiment. For the validation data-set, the optimal ANN architecture gives us a MSE of 10.46 %. The model and experimental time-series are in very good agreement as shown in Fig. 9.19.

9.6 Conclusions

A successful application of an ANN SI framework was presented for the case of an experimental TBL flow. FTD ANNs were proven flexible enough to achieve sufficient prediction precision, even for a high-order multiple-input multiple-output non-linear system. A non-linear mapping between upstream sensors and the global dynamics of the flow (in the form of POD coefficients) was presented. The cross correlation between sensors and coefficient

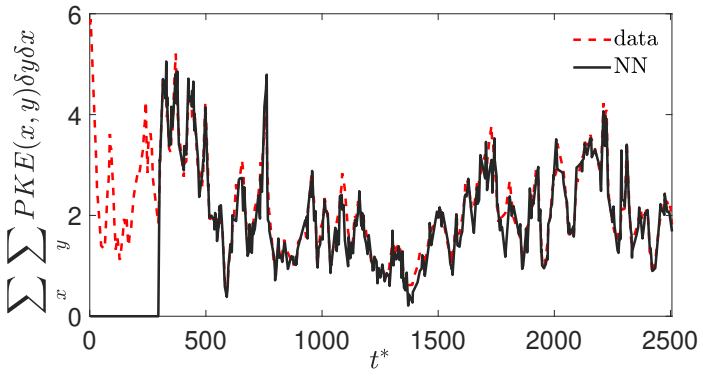

FIGURE 9.19: Comparison of the sum of PKE computed in the PIV window between decomposed experimental field and ANN-identified reconstructed field. Zero network signal is due to sensor time-delay.

signals was proven a useful tool for the choice of the optimal sensors. Different sensors correlate well with different coefficient signals. It was revealed why the collaboration of a swirling strength sensor and a local velocity sensor resulted in an accurate network training. The dynamics were identified, the turbulent coherent structures (wavy streaks) were reconstructed, and the system order was reduced to two easily measurable signals. A physical interpretation was given for the optimal sensor memory size in the final ANN architecture. The difficultly in the estimation of the coherent structures in this TBL flow arises due to streak wavyness and weak three-dimensionality. Still the ANN was proven efficient if the sensor memory size and number of neurons are properly chosen. The achieved fit accuracy is around 5%. The present study is the first step in identifying an efficient model-free control law like in Gautier et al. (2015) and Li et al. (2017), that comes from deep knowledge and precise prediction of the dynamics of each point in the velocity field. It will target the minimization of the PKE, since this quantity can be tracked in real-time. We also mention that the Reynolds number could also be integrated as an input, while the output could include POD coefficients for the different Reynolds numbers, hence going towards a system of variable velocity. The presented methodology could also be applied to the same turbulent flow but based on the horizontal (spanwise-streamwise) PIV plane (Fig. 9.3). Spanwise-distributed sensors and deeper networks are possibly needed for this complicated task but it clearly is now feasible.

A few comments can be made regarding a comparison with the dynamic observer method that used a statistical learning approach and was presented in the previous section: Even though the ANN does not provide a model but just a local-to-global regression, it showed remarkable adaptability on the weak-threedimensionality and waviness of the streaks, and successfully predicted every fluctuation energy peak with remarkable accuracy. Last but not least, the ANN approach required an order of magnitude less computational time and can be a valuable machine-diagnostic tool where no model is needed.

Part IV

Instabilities, dynamics and control of the Backward-Facing Step flow

Chapter 10

Transition to turbulence in the BFS flow

10.1 Classic 2D scenario

Noise-amplifier flows are fluid systems which are globally stable, but which selectively amplify the upstream perturbations coming from random environment noise via convective instability mechanisms (Huerre and Monkewitz, 1990; Chomaz, 2005). Typical examples are the flat plate Boundary Layer and Backward-Facing Step (BFS) flows (Armaly et al., 1983; Beaudoin et al., 2004b; Dergham, Sipp, and Robinet, 2013). Noise-amplifier flows play an important role in many industrial flows, like separated flows around airfoils (Darabi and Wygnanski, 2004) and the complex 3D wakes of ground vehicles (Aider et al., 2001; Beaudoin et al., 2004a).

The BFS flow, particularly, is considered a very important test-case for separated flows; separation is imposed by a sharp edge leading to a large recirculation bubble, secondary corner recirculating regions (in the bottom corners or the in the ceiling of the channel as well, for low vertical expansion ratios (Barkley, Gomes, and Henderson, 2002)) and a Kevin-Helmholtz (K-H) instability leading to high frequency emission of vortices. The recirculation bubble is usually associated to pressure drag (Dahan, Morgans, and Lardeau, 2012a). Its reduction is then a common objective to most flow control experiments targeting drag reduction (Gautier and Aider, 2014). It has been also found subject to a flapping motion, with a magnitude of frequency lower than the shedding frequency (Spazzini et al., 2001). A new boundary layer develops after the re-attachment of the flow, the position of which is important for heat and mass transfer purposes. Tihon et al. (Tihon, Legrand, and Legentilhomme, 2001) studied experimentally the re-attachment length for the Re number range [1200:12000]. It has been observed that the low-frequency flapping of the recirculation bubble, together with the K-H instability produces oscillations of this reattachment line (Dejoan and Leschziner, 2004).

In this spanwise-invariant description of the BFS flow we observe a convective instability surrounded by upstream and downstream regions of stability. A sketch of the main 2D observed phenomena, the recirculation length and reattachment zone can be found in figure 10.1. A LIF experiment performed at the PMMH lab showing the vortex shedding instantaneous snapshots for varying Re number can be found in figure 10.2. Since a very low Re number though, as low as $Re_h = 200$ (defined using the free-stream velocity and the step height), a 3D instability is observed (Armaly et al., 1983; Kaiktsis, Karniadakis, and Orszag, 1991; Beaudoin et al., 2004b), hence making recirculation area (RA) calculations strongly dependant on the measurement plane chosen. Particularly, Beaudoin et al. (Beaudoin et al., 2004b) showed for the first time experimentally a periodically modulated reattachment position in the spanwise direction, using PIV measurements.

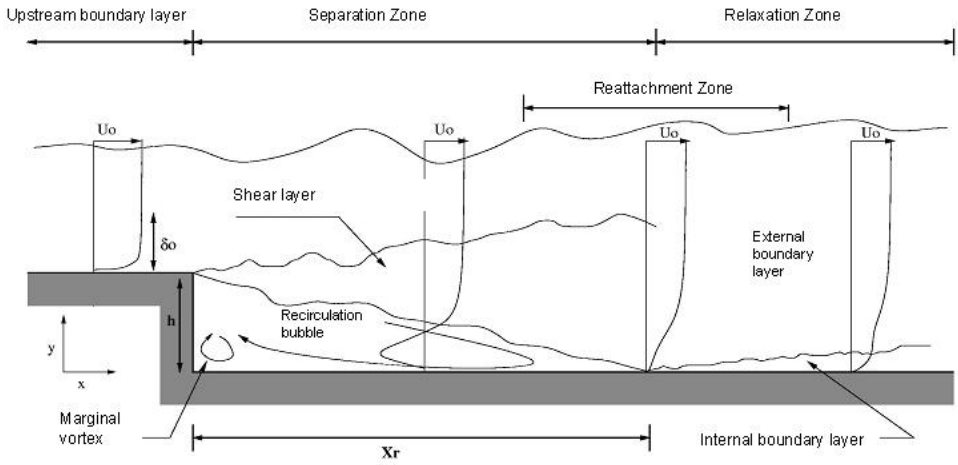

FIGURE 10.1: Main 2D-instability phenomena sketch of the BFS flow, as illustrated by Aider, Danet, and Lesieur, 2007.

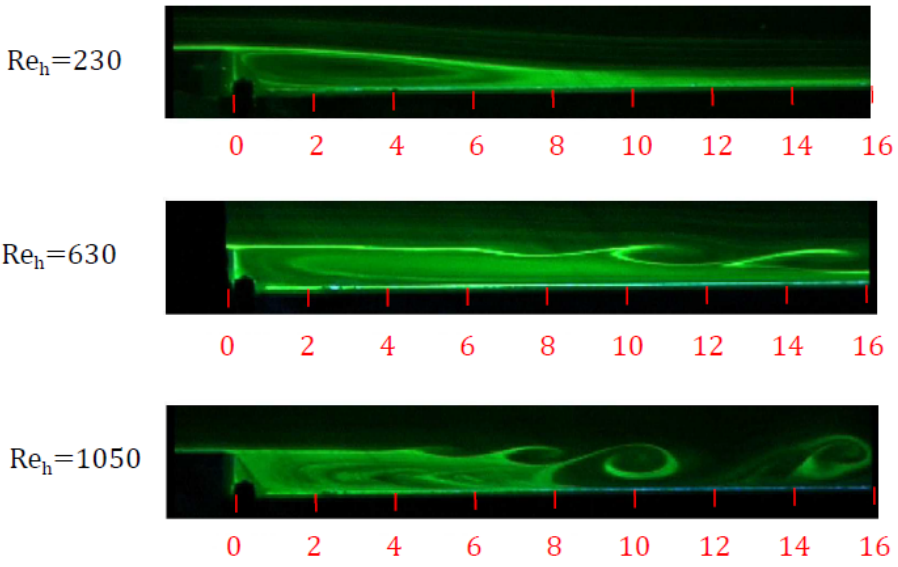

FIGURE 10.2: LIF experiment in the streamwise-wall normal direction varying the Re_h number from Beaudoin et al., 2004b. Development of K-H vortex shedding.

10.2 3D instabilities

Beaudoin et al. demonstrated experimentally that the radius of the local streamlines can vary the pressure along the boundary layer, triggering large scale streamwise longitudinal vortices. Numerically, numerous studies have been carried out (Blackburn, Barkley, and Sherwin, 2008; Wang, Wu, and Zhu, 2019; Lanzerstorfer and Kuhlmann, 2012) to study this instability; the grand majority of them dealing with low expansion ratios and a Poiseuille flow profile inlet and no slip upper boundary condition. These cases do not necessarily correspond to the phenomena observed in the open flow cases, like in ground vehicle applications, due to confinement effects. Barkley et al. (Barkley, Gomes, and Henderson, 2002) performed a linear stability analysis in such a numerical BFS flow and showed that a steady three-dimensional bifurcation observed at $Re_h = 748$. They argued that earlier transitions are due to artificial effect of the walls due to small aspect ratio. A study closer to the open flow case, using an expansion ratio of 0.83 and a non-reflective upper boundary condition was performed by Aider et al., using Large-eddy simulation scheme (Aider, Danet, and Lesieur, 2007). For a $Re_h = 5100$ and a turbulent incoming boundary layer, they showed the existence of coherent streamwise streaks creating a spanwise modulation, lasting 3-4 times the step size downstream the step. They argued that this spanwise modulation was responsible for the wavy modulation of the Kelvin-Helmholtz vortex rolls. A very similar 3D instability is also experimentally observed in a separated boundary layer by Passaggia, Leweke, and Ehrenstein, 2012b. By putting a bump in the flow and separating the boundary layer flow they observed a transverse instability and a low frequency RA flapping, similarly observed in the BFS flow. A lof of similarities can be found in the study by Faure et al. as well (Faure et al., 2009), where a similar Görtler instability occurs in an open cavity flow. A full study of the transition to unsteadiness of this flow was also investigated thoroughly numerically by Picella et al. (Picella et al., 2018), showing the occurrence of two successive bifurcations from which the first one, happening at Reynolds number $Re_h = 3430$, also associated with the emergence of (quasi-)steady Taylor Görtler vortices.

A surprisingly low number of experimental studies have been conducted. Experimentally, Kitzhofer et al.(Kitzhofer et al., 2009), again with a Poiseuille-profile inlet flow studied the BFS flow using volumetric velocimetry. The first and only experimental study regarding the 3D BFS flow instability using a Blasius boundary layer inlet BFS flow is by Beaudoin et al. (Beaudoin et al., 2004b). Using numerical results they showed the existence of an intrinsic unstable three-dimensional mode, due to a centrifugal instability in the vicinity of the reattached flow, in a region 8 times the step size away from the step position, outside of the recirculation bubble. Using Laser-induced Fluorescence (LIF) in the same setup they verified the existence of mushroom-like counter-rotating longitudinal vortices, as seen in figure 10.3.

The present study is directed towards the experimental investigation of this 3D instability for the Re_h number (based on the step height h and free-stream velocity) case from $Re_h = 290$ to 3080. The correct identification of the structure scales (as the Re_H number increase) is critical, in order to design simple open or closed-loop jet actuators that will optimally act on the flow. Shedding more light towards the understanding and controlling the BFS flow for drag reduction purposes could be proved important for the CO_2 diminishing goals of the European Union (EU-Council, 2014).

The chapter is organised as follows: We first present a description of the experimental setup and the 2D optical flow metrology that is used to further study this 3D instability, as studied in a low Re hydrodynamic channel. We then present experimental results on the characterisation of the BFS flow: the observed K-H as well the 3D instability observed in the spanwise direction. Afterwards, a novel open-loop control strategy using pulsating jets upstream of the step area is going to be presented, followed by a machine-learning dynamics prediction algorithm using local visual sensors.

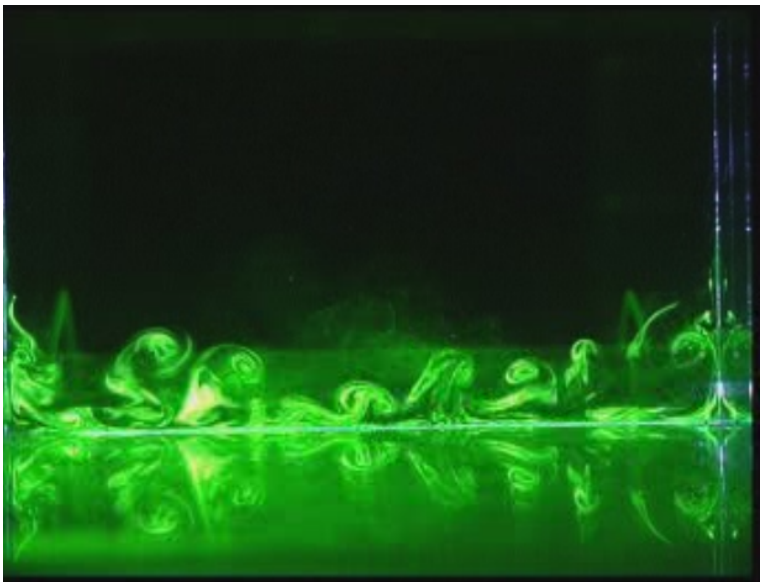

FIGURE 10.3: LIF experiment visualisation in the spanwise-wall normal direction from Beaudoin et al., 2004b. Counter-rotating streamwise vortices appearing due to streak formation.

Chapter 11

Experimental results on the 3D instability

11.1 Experimental setup

11.1.1 Hydrodynamic channel

Experiments have been carried out in a hydrodynamic channel in which the flow is driven by gravity, with a maximum free-stream velocity $U_\infty = 22\ cm.s^{-1}$. The flow is stabilised by divergent and convergent sections separated by honeycombs leading to a turbulence intensity less than 1 %. A NACA 0020 profile is used to smoothly start the boundary layer. The test section is 80 cm long with a rectangular cross-section $w = 15\ cm$ wide and $H = 10\ cm$ high (Fig. 11.1). The step height is $h = 1.5\ cm$. The maximum Reynolds numbers based on the step height is $Re_{h,max} = U_\infty h/\nu \approx 3080$. The vertical expansion ratio is $A_y = H/(h+H) = 0.82$ and the spanwise aspect ratio is $A_z = w/(h+H) = 1.76$.

The flow is seeded with 20 μm neutrally buoyant polyamide particles, which are illuminated by a laser sheet created by a 2 W continuous laser (MX-6185, Coherent, USA) operating at 532 nm. The Camera used was a 4 Mp PCO DIMAX-cs with an acquisition frequency up to $f_{ac} = 180\ Hz$. The camera has an embarked RAM giving a limit of 2000 images at 4Mp resolution, hence the total acquisition time was also limited by this factor. An narrow-band optical filter was mounted on the camera to visualise only the laser light reflected by the particles.

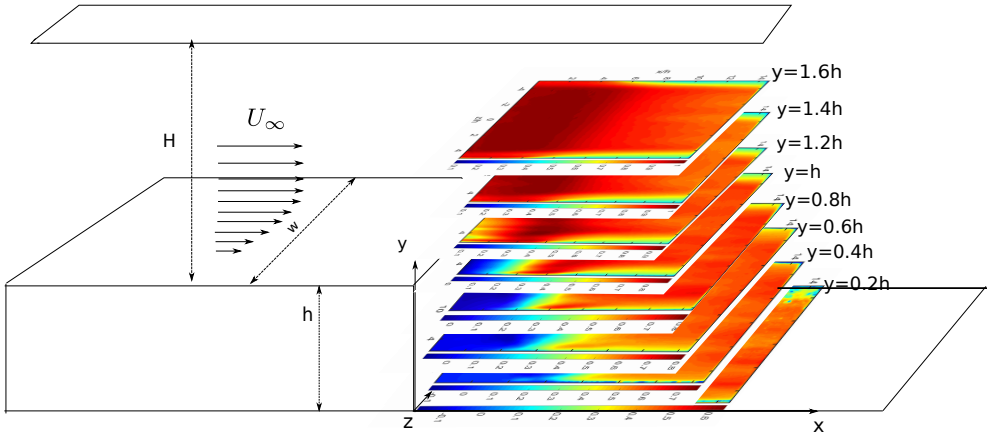

FIGURE 11.1: Sketch of the BFS geometry and 8 horizontal planes scanned with PIV. Results presented for $Re_h = 2709$.

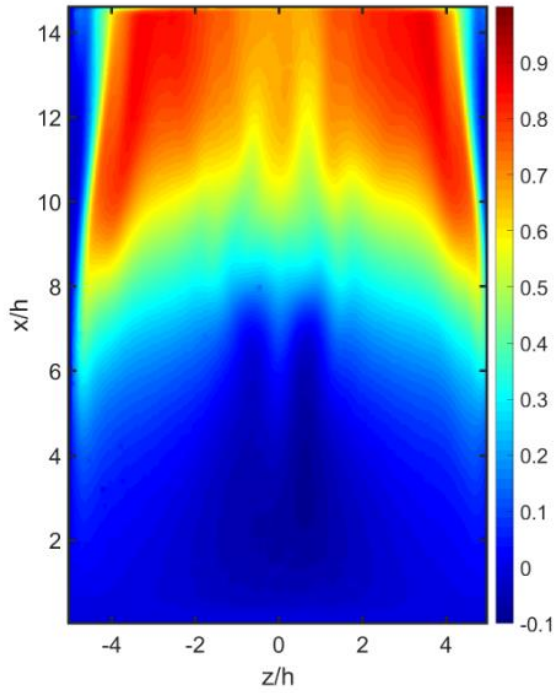

FIGURE 11.2: Mean streamwise velocity field at $y = 0.6\ h$, $Re_h = 1255$. First appearance of streaks near the middle plane.

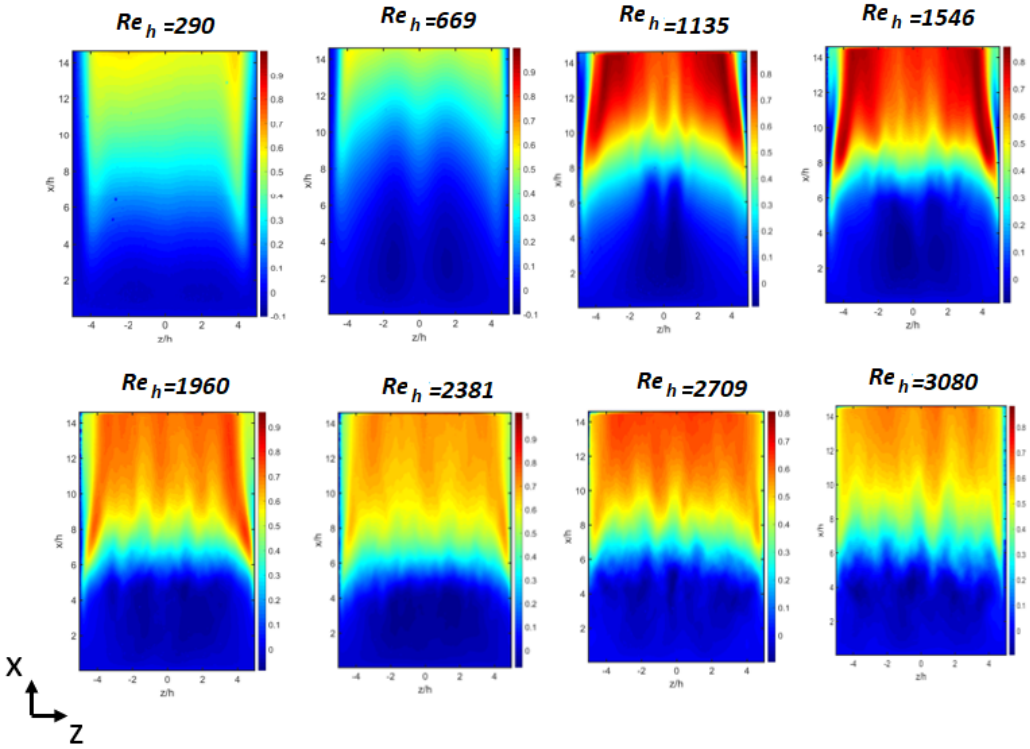

FIGURE 11.3: Mean streamwise velocity fields for various Re_h numbers, $y = 0.6\ h$; apprearance of spanwise periodic modulation due to streaks appearing after $Re_h = 669$.

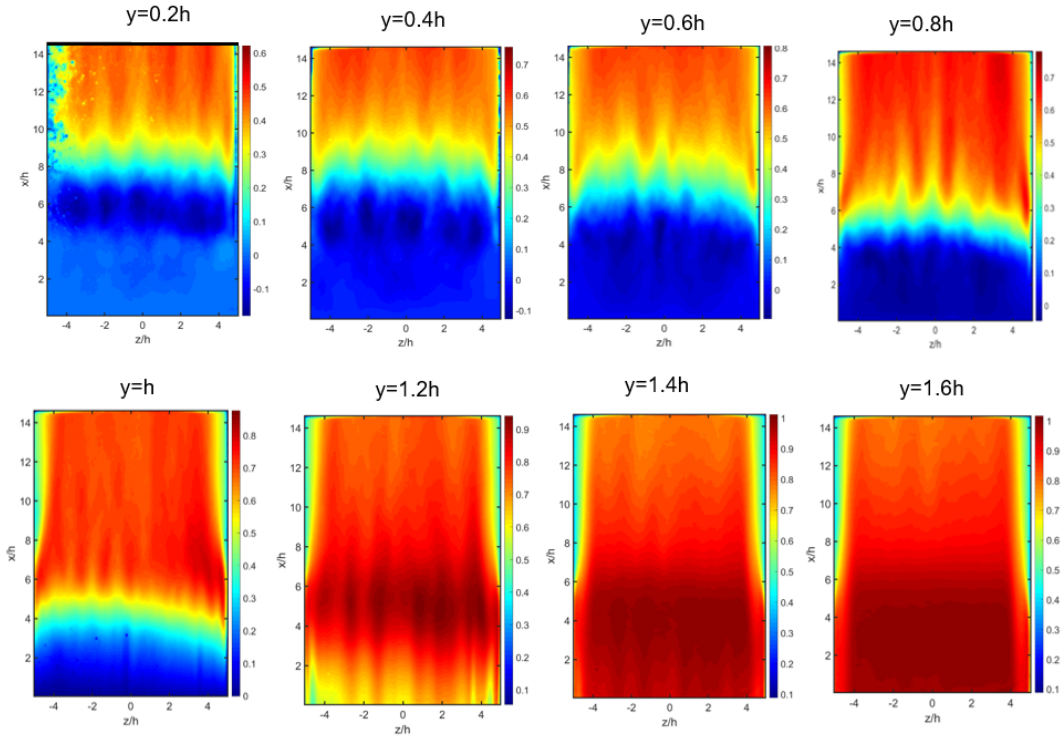

FIGURE 11.4: Mean streamwise velocity component fields for different horizontal planes changing the wall-normal height y. Results presented for $Re_h = 2709$, as for figure 11.1.

11.1.2 Optical flow measurements in the spanwise-streamwise plane

The time-resolved velocity fields are calculated from the acquisition of successive snapshots, using a home-made Lucas-Kanade Optical Flow (LKOF) algorithm. The first version of the code has been developed at ONERA (Champagnat et al., 2011) and later modified, optimised and adapted to the constraints of real-time measurements by Gautier & Aider (Gautier and Aider, 2013). Among the advantages of the LKOF algorithm compared to a standard FFT-PIV algorithm is the calculation of a dense velocity field with one vector per pixel. It also allows for high computational speed when implemented on a GPU with CUDA functions (C.Pan et al., 2015). The high spatial resolution is important for near-wall measurements while the high computation speed is important for real-time measurements that can be used as inputs in closed-loop flow control experiments (Gautier and Aider, 2015b). The code has been used many times both for time-resolved PIV measurements with a high spatial resolution (Varon et al., 2017), as well as for closed-loop flow control experiments (Gautier and Aider, 2013; Gautier et al., 2015). The PIV calculations in the present study were performed on a NVIDIA TESLA K80 GPU.

Eight horizontal, streamwise-spanwise plane xz were studied (at $y = 0.2 : 0.2 : 1.6\ h$). A sketch of the horizontal planes height positions can be seen in figure 11.1. The Reynolds number in the present experiment is $290 < Re_h < 3080$, corresponding to a maximum free-stream velocity $u_\infty = 25\ cm.s^{-1}$. The incoming boundary layer, is laminar and follows a Blasius profile.

11.2 Observed phenomena

The observed instability consists of a linearly unstable centrifugal instability (Saric, 1994; Beaudoin et al., 2004b), where the boundary layer interacts with the wall curvature leading to streamwise counter-rotating vortex rolls, or streaks. They streaks modulate the streawise velocity fields in the spanwise direction in a periodic manner. The lowest Re number to observe this instability in our channel was $Re_h = 1255$. The streak signature in the mean streamwise field can be found in figure 11.2, where the first pair of counter-rotating vortices appear in the center of the field. This first streak pair appearance for $Re_h = 1255$ is also associated with the birth of a turbulent spot. This turbulent spot observation is studied extensively in section 11.7.

An extrinsic side-wall structure appears close to the side walls at $z = 4\ h$ and $z = -4\ h$, existing from the lowest Re_H number studied at $Re_h = 290$. They are similar to the structures studied by Williams et al. ("Numerical simulations of laminar flow over a 3D backward-facing step"), Tylli (Tylli, Kaiktsis, and Ineichen, 2002) and Armaly et al. (Armaly et al., 1983) and are inevitable in hydrodynamic channels. They can be clearly observed in the streamwise mean field (figure 11.2). These extrinsic rolls could force this instability of the streaks to occur slightly subcritically, before the actual critical Re_h. For this reason we observe also a slight modulation of the streamwise field in $Re_h = 669$. They are similar to the adjacent Ekman structures in the endwalls of an experimental TaylorCouette flow (Czarny et al., 2003). These extrinsic wall effects actually might penetrate to some extent over the entire flow since they are superimposed wit the streaks (Benjamin, 1978).

The signature of the streaks can be observed through this spanwise modulation of the mean streamwise velocity for varying Re_h number in figure 11.3. We observe that the modulation extends to the full span for $Re_h = 1546$ and above. The scanning of different plane heights covering all the step and above can give access to the reconstruction of the streamwise velocity in the plane zy for different $x = const$ planes using the velocities of the multiple planes. The spanwise modulation for different streamwise distances is clearly revealed this way, as seen in figure 11.6. The observed spanwise modulation is very similar to the three-dimensional stall cells observed in two-dimensional airfoils (DellOrso, Tuna, and Amitay, 2016; Rodriguez and Theofilis, 2010). The vorticity calculation also reveals the longitudinal vortices center position, as seen in figure 11.7.

Another way to reveal the spanwise modulation having scanned all these multiple horizontal planes for $y = 0.2 : 0.2 : 1.6\ h$, is to plot the reconstructed 3D isosurfaces for different velocities. An example of such a reconstruction for $Re_h = 3080$ and different iso-velocities can be found in figures 11.14 and 11.8.

In the spanwise mean velocity fields we can observe large scale roll structures, of velocity one order of magnitude smaller than the small scale structures observed in the streamwise field. Their evolution with the Re_h number can be seen in figure 11.5. The large scale structures, which are in the form of convected quadrupole can be distinguished for the extrinsic wall structures before and after the bifurcation from their 2D Fourier amplitude analysis, as will be seen in next section. Before the instability, only the extrinsic wall vortices exist, and as the Re_h increases they are pushed more towards the side walls by the generation of streaks. At the point of the instability and onwards, the large scale roll increases in amplitude due to the quadrupole structures associated with the streaks, also observed in a channel flow transition to turbulence experiment (Lemoult et al., 2013). The separation of large and small scales is possible by using appropriate Butterworth filters, as will be seen in the next section. To find the appropriate filter limits we will use the 2D spatial Fast Fourier Transform (FFT) in the mean and instantaneous fields.

The interaction of the streaks with the K-H roll leads as well to a spanwise-wavy K-H roll as was previously observed by (Aider, Danet, and Lesieur, 2007). This wavyness

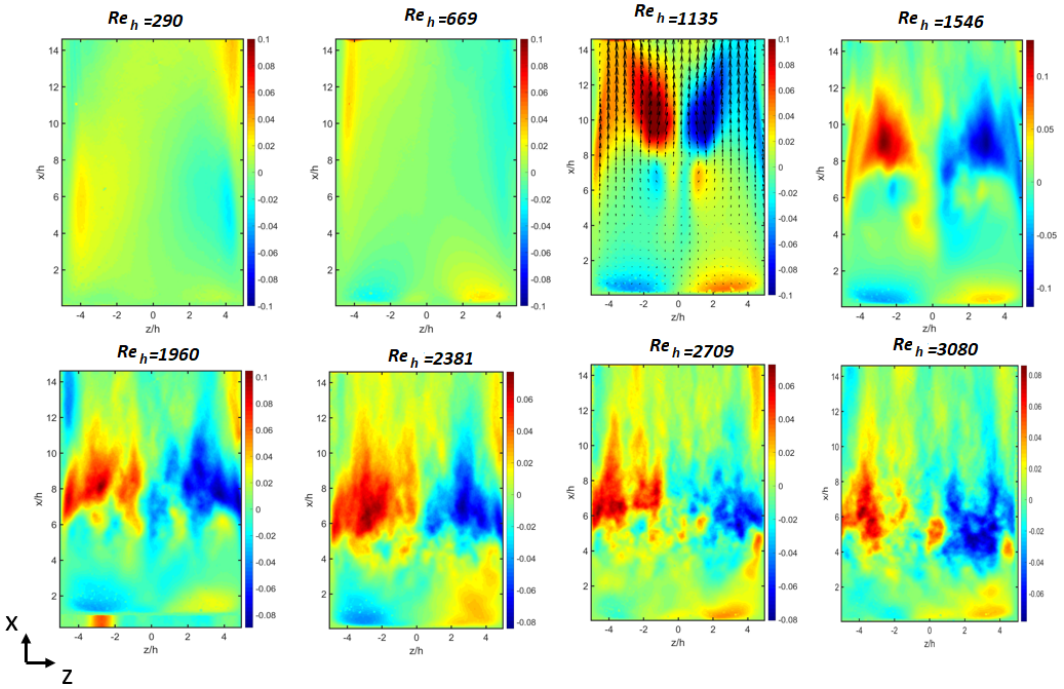

FIGURE 11.5: Mean spanwise fields for various Re_h numbers, $y = 0.6\ h$. Extrinsic wall structures always existing due to confinement; appearance of large scale roll structure after $Re_h = 669$.

was also observed in the streak structures for multiple heights as observed in figure 11.13. The spanwise modulation of the K-H roll due to the streaks is also studied using Proper Orthogonal Decomposition in the next paragraph. A sketch including schematically all the observed phenomena for the Re range $Re_h = 1255 - 3080$ can be found in 11.9.

11.3 Structure size analysis using 2D Fourier transform

The 2D Fourier transform of the mean and instantaneous fields was used to study the scales of the observed structures; the Fourier transform reveals a peak at the wavelength of the streaks and the large scale roll, as seen in figures 11.10 and 11.11 respectively. The results of the characteristic streak width as a function of the Re_h number are presented in figure 11.12. We observe that after $Re_h = 2000$ this length diminishes to about 2 cm or 1.3 h. A high-pass spatial filter applied in the streamwise fields can actually reveal more clearly the streak structure. For example for the case of $Re_h = 1960$, applying a Butterworth high pass filter at $k = 26$ in the streamwise mean field, we can really reveal naked the streaks structure and more precisely measure its size, as seen in figure 11.10. The size of the streaks will be proven very important for the design of an optimal pulsating jet actuator distribution to reduce the recirculation bubble size, as will be seen in paragraph 13.

This 2D Fourier spectrum study of the spanwise fields reveals the characteristic length of the large scale structures. We can see that the small scale structures that create the spanwise modulation of the streamwise field have an order of magnitude larger amplitude than the large scale structures (figures 11.16 and 11.15). A linear increase in both large and small scale amplitudes is observed as a function of Re_h, although after $Re_h = 2381$ the flow becomes more turbulent and this trend is lost for the streamwise fields analysis. For the case of the large scale structures appearing in the spanwise fields, by performing a linear fit before and after the instability, we can distinguish the superimposed extrinsic wall structures amplitude from

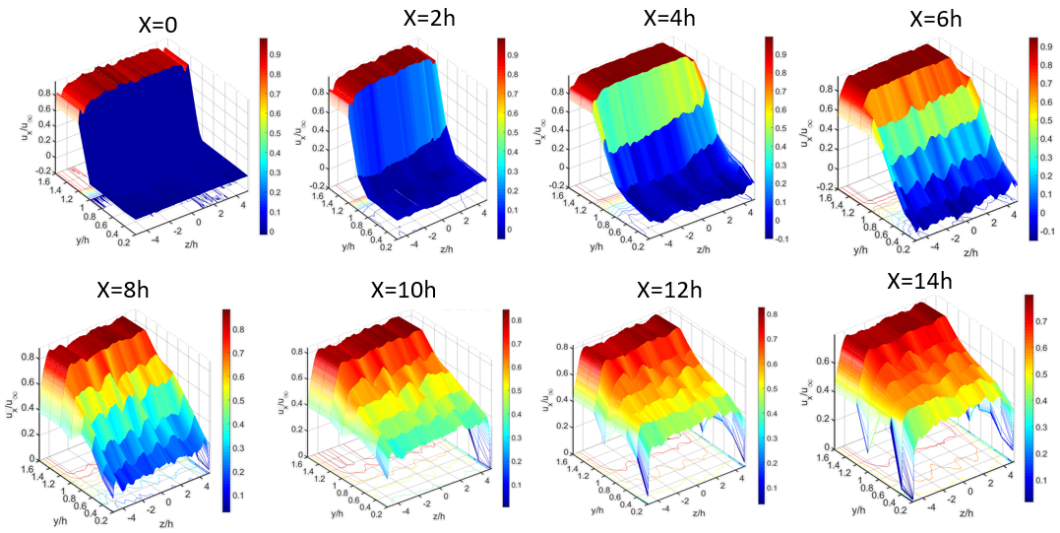

FIGURE 11.6: Mean streamwise velocity reconstruction for the plane yz, for different $x = const$. Development of the spanwise modulation in the streamwise direction: birth and death of streaks. $Re_h = 3080$

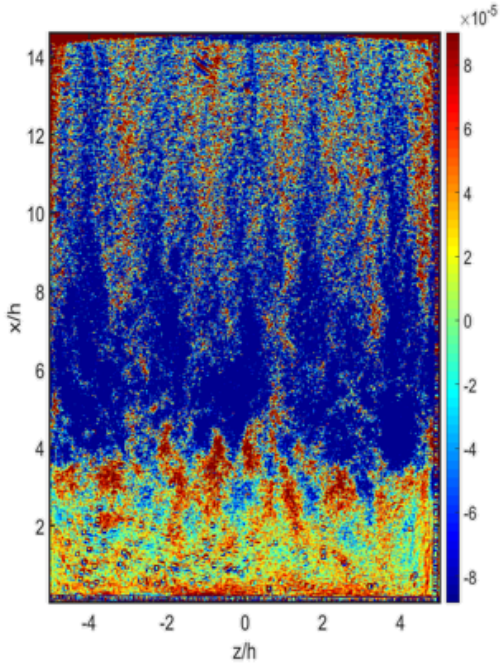

FIGURE 11.7: Mean vorticity field for $y = 0.6\ h$, $Re_h = 3080$.

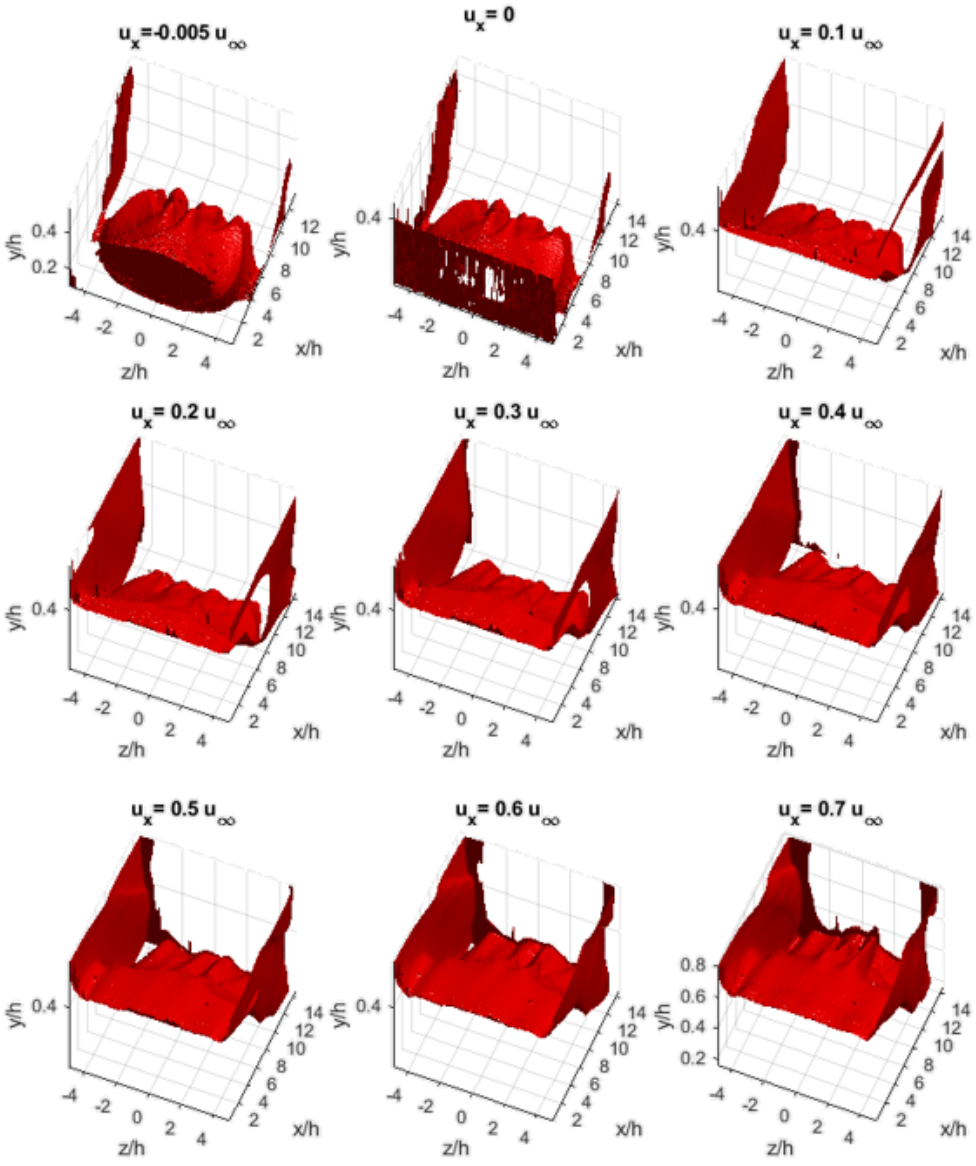

FIGURE 11.8: 3D isosurface of different streamwise velocities, $Re_h = 1135$. Spanwise modulation revealed.

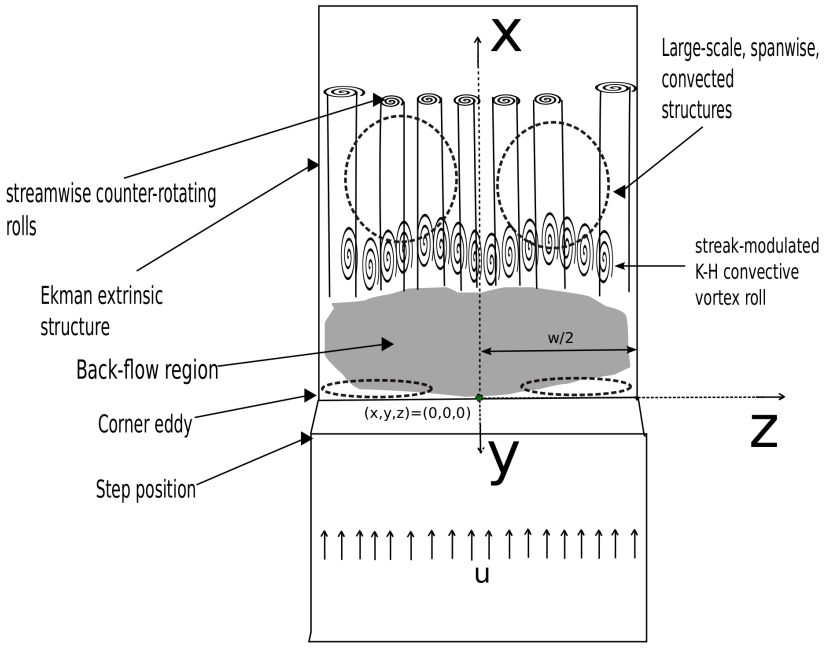

FIGURE 11.9: Sketch of the BFS geometry and main phenomena, plane xz. Coordinate system origin is placed in mid-span, bottom position.

the one of the large scale structures appearing after the instability. The Fourier amplitude plots is a good way to spot the critical Re number; more experiments are needed and are currently planed in order to precisely find the critical Re number for the 3D instability. For the experiments so far it can be spotted between $Re_h = [669, 1255]$, as seen in figure 11.16. A similar scenario of streamwise longitudinal vortices of small scale but large magnitude and large spanwise structures with small amplitude are found using the same 2D Fourier analysis in the transition in the Couette-Poiseille flow (Klotz, Pavlenko, and Wesfreid, 2021).

11.4 Defitinitons: Recirculation bubble, recirculation length and recirculation area

The detachment of the flow after the step leads to the creation of recirculation behind it. The volume of the recirculation bubble, is the space inside (below) the separation surface, inside which the fluid stays enclosed in. It can be defined as the point where the streamlines diverge, and is an area of relatively low pressure that contributes greatly to the drag (Beaudoin et al., 2004b). The recirculation bubble existing downstream a BFS has been studied using the recirculation length, which is the position of the re-attachment of the flow (Henning et al., 2007). Mathematically, it is described in equation 11.1. Reduction of this value can decrease the value of the drag as well, since in general the recirculation bubble is a region of low pressures (Armaly et al., 1983).

$$X_r = x\left(\tau_w = 0\right), \tau_w = \eta \left.\frac{\partial v}{\partial y}\right|_{y=0} \tag{11.1}$$

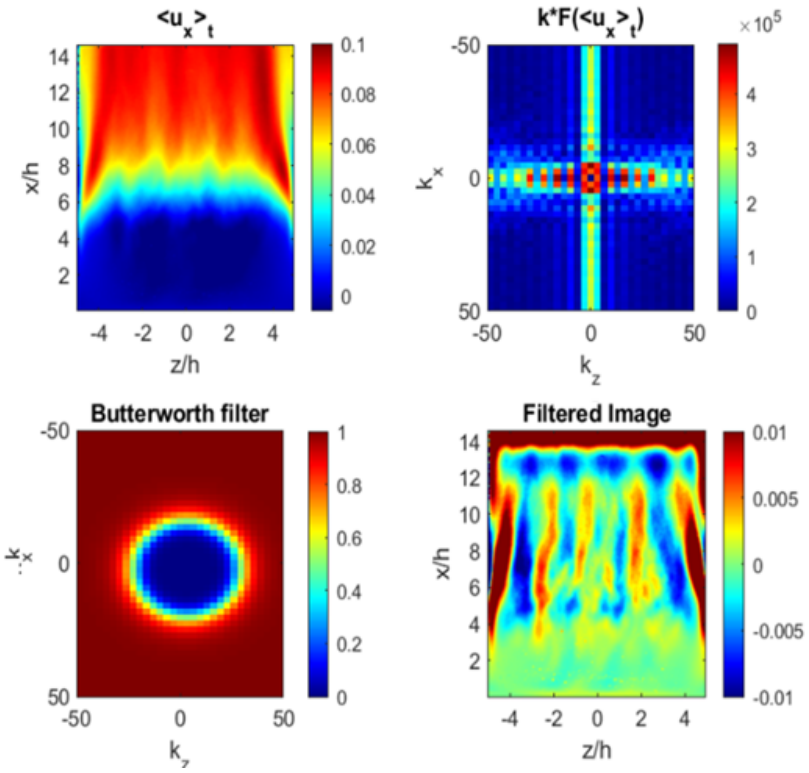

FIGURE 11.10: 2D Fourier transform and high-pass filter application in streamwise mean fields, $Re_h = 1960, y = 0.6\ h$.

The definition for the recirculation length X_r described in equation 11.1 is ill-suited to 2D velocity fields. The separation line is difficult to define using PIV, apart from the wall position where the velocity changes sign. Nonetheless, these near-wall measurements can be very tricky. A straightforward manner of qualifying recirculation in a 2D field is described in equation 11.2. It regards on the 2D RA definition of A_r as :

$$A_r(t) = \iint H(-u_x(t,x,z))dxdz \tag{11.2}$$

, where H is the Heaviside function. It has been seen that the dynamics of the the recirculation length are correctly recovered using the above definition (Gautier, 2014). We mention though that the time averaging operator does not commute with (3.2), this mean the time averaged RA $< A_r >_t$ does not correspond to the RA of the time averaged velocity field. This definition, which might underestimate slightly A_r (due to regions of positive streamwise component near the walls) is quite straight forward to calculate experimentally in real-time and contains the dynamics of the real bubble, along with the dynamics of the streaks and the corner eddies. Particularly, the corner eddies increase in size with the Re_H number, make the underestimation possibly larger. Nonetheless, this definition, has been set a multiple times as a minimization goal to be set in a closed-loop control scheme, like in the case of Gautier et al., 2015. We could also call this region "back-flow area" instead of RA.

The 3D recirculation bubble size calculation can shed important light in the 3D instability of the BFS flow (Armaly et al., 1983). This recirculation volume has been studied by Gautier, 2014 using 3D Particle Tracking Velocimetry, a method which is enormously computationally costly and requires huge amounts of disk space. A lighter method to study the time-averaged 3D bubble is presented in this chapter, and consists of scanning multiple 2D PIV planes in order to reconstruct the volume of the bubble.

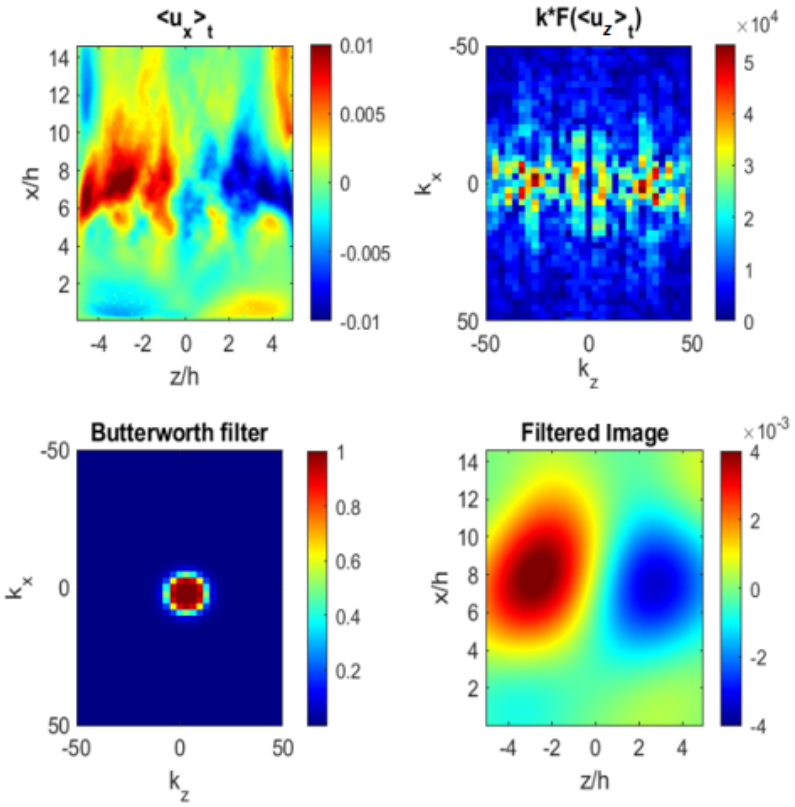

FIGURE 11.11: 2D Fourier transform and high-pass filter application in spanwise mean fields, $Re_h = 1960$, $y = 0.6\ h$.

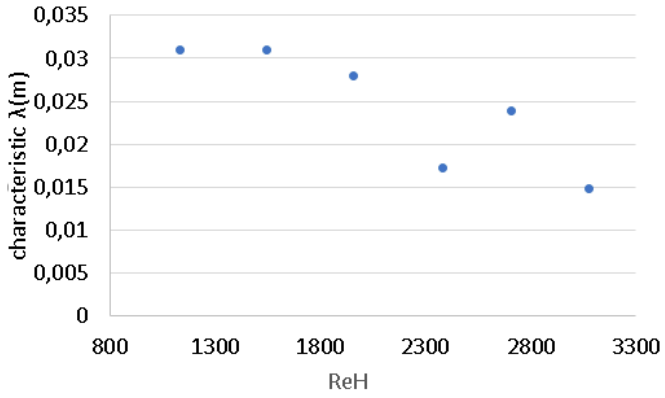

FIGURE 11.12: Mean field spanwise size of streaks, as a function of the Re_h number.

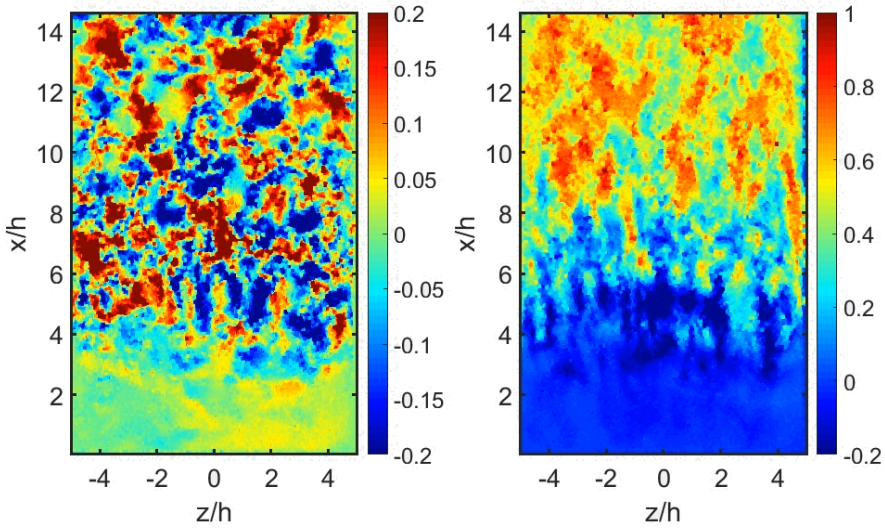

FIGURE 11.13: Mean streamwise and spanwise velocity field for Re=3080, $y = 0.6\ h$.

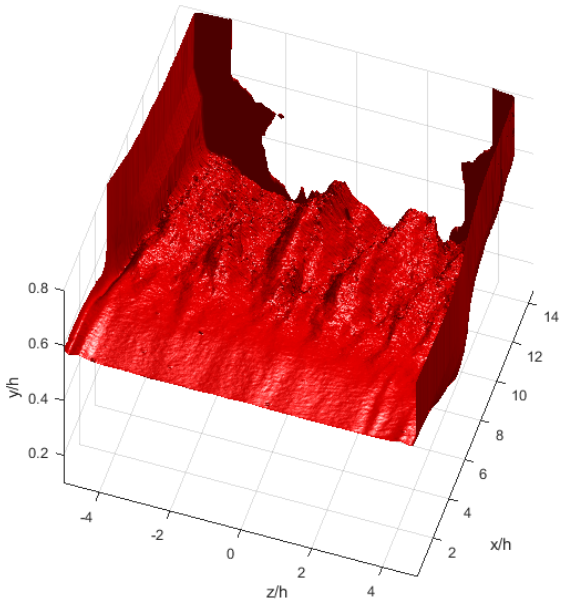

FIGURE 11.14: 3D isosurface of zero streamwise velocity $< u_x >_t = 0$, $Re_h = 3080$. A spanwise modulation signature appears together with the extrinsic wall structures.

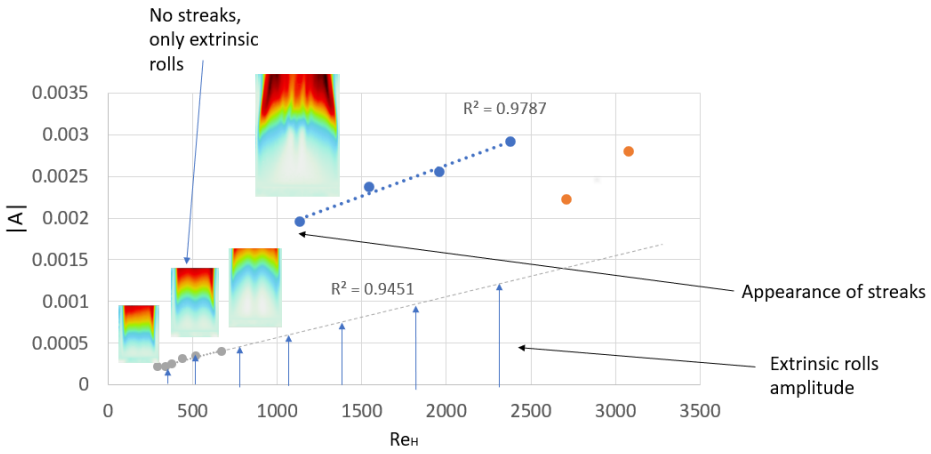

FIGURE 11.15: Fourier amplitude of spanwise component as a function of Re_h, for y=0.6h. Linear fitting can predict the effect of the extrinsic rolls after the instability occurs. Mean streamwise fields indicate the start of the streak appearance.

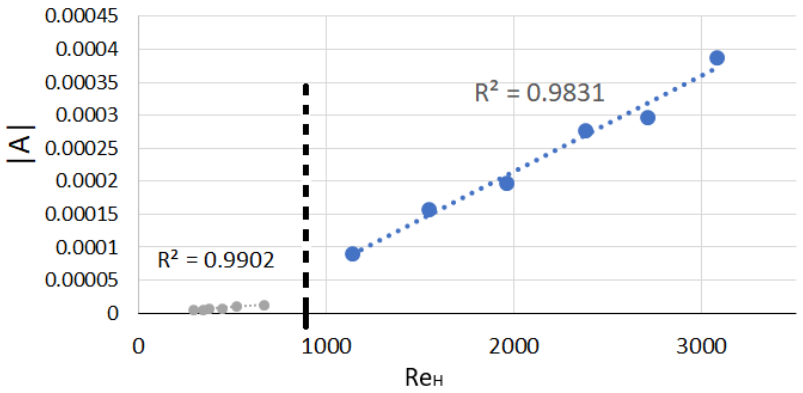

FIGURE 11.16: Fourier amplitude of streamwise component as a function of Re_h, for $y = 0.6h$. Linear fitting before and after the critical Re region.

11.4.1 Recirculation area dynamics

The RA downstream a BFS often serves as the minimization goal of a control scheme, since this can lead to a drag reduction or improve lift or vibrations in moving vehicles (Paschereit, Gutmark, and Weisenstein, 2000; Simpson, 1996). Its view on the horizontal plane $y = const$ gives a general view on the spatial streaky structures structures together with the K-H vortex roll and the RA. Measurements like the vertical recirculation length or RA for the streamwise-wall normal xy plane (z=const.) are strongly dependant on the plane chosen, which is the reason they cannot be compared easily from experiment to experiment in the bibliography. The RA dynamics include as well as the low frequency flapping or breathing of the recirculation bubble, which is of frequency of one order of magnitude less (Spazzini et al., 2001). The streaks show a wavyness which can also affect the RA measurement in the classic streamwise-wall normal plane.

The signature of all these dynamics can be studied using the different xz plane for different wall normal positions y. The higher horizontal planes have a stronger signature of the K-H roll and the planes inside the bubble show better the peaks of the recirculation area flapping and streak structures.

The results of the K-H vortex emission frequencies coming from the Fourier transform of the velocity time signals can be found for varying Re_h numbers in figure 11.18. An example of some Fourier transform plots can be found for three Re_h numbers in figure 11.17. The results of the measurements of the K-H vortices emission frequency agree in the vertical (xy), and horizontal (xz) measurements; the low-frequency flapping frequency of the RA could not be well captured though, due to the low number of acquisition time that was imposed by the embarked RAM of the camera.

In figure 11.19, we can see the mean RA for varying Re numbers. The xy plane for $z = 0$ (middle plane) and xz plane for $y = 0.6\ h$ from bottom were studied. We also note that the time averaging operator does not commute in equation 11.2; this meaning that the time averaged RA $< Ar >_t$ does not correspond to the RA of the time averaged velocity eld. For this reason the RA is calculated for each instantaneous field, and for each Re_h number 2000 fields or around 1 minute of measurements were acquired. The same peak is observed in the two measurement planes xy and xz, particularly for $Re_h = 669$ and $Re_h = 671$ respectively, as seen in figure 11.19. This peak is observed just before the appearance of the spanwise modulation and the longitudinal streaks. The same peak is recovered using the recirculation length measurement by Gautier et al. in the vertical xy plane (Gautier, 2014).In the vertical plane we are only seeing the effect of the K-H roll and RA, which is monotonously decreasing after the peak. In the horizontal plane xzthough, the flow after $Re_h = 1135$ is three-dimensional due to the wavyness of the streaks and the K-H roll, hence the contribution of K-H , streaks and large scale flows change this descending pattern. We mention that the size of the calculated RA in the 2 planes xy and xz is different due to the different PIV window size and dimensioning with the step size.

11.5 K-H vortex roll and streak interaction

The instability of the K-H co-rotating vortex rolls, due to the presence of the streaks can be studied using PIV in the horizontal planes $y = h$ or above. For this heights, there is a clear signature of the K-H roll creation and emission. The roll is deformed in the spanwise direction due to the presence of the streaks, which leads to interaction with the next incoming roll. An elliptic instability could also be present and affecting the roll interactions, but further investigation is needed in this direction before concluding. The K-H vortex rolls interaction was observed in the volumetric dye visualisation experiment in figure, 11.20 in which the front pair always destabilises and penetrates the previous roll. A large set of instantaneous

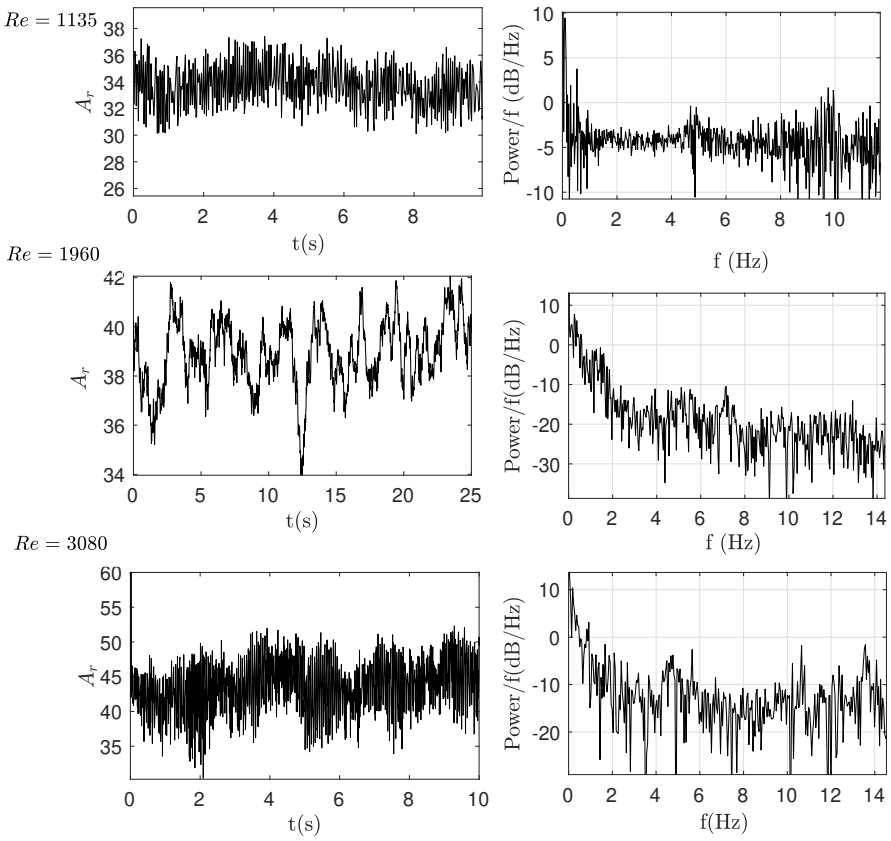

FIGURE 11.17: Time series and Fourier transform of RA signal for horizontal planes *xz*, for $y = 1.6\ h$.

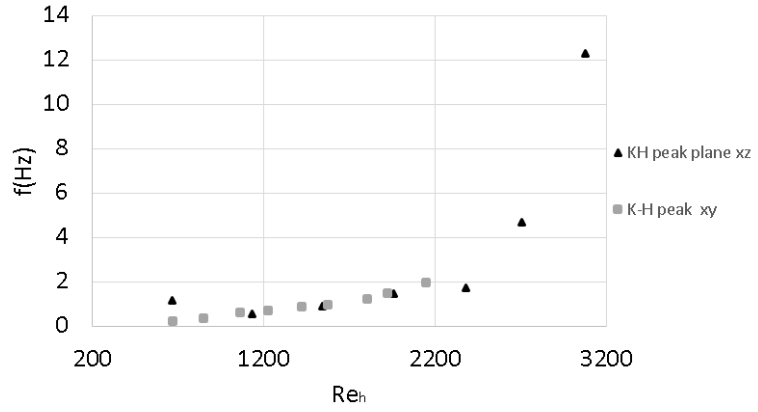

FIGURE 11.18: K-H vortex emmision frequencies calculated from PIV measurements in the xz and xy planes.

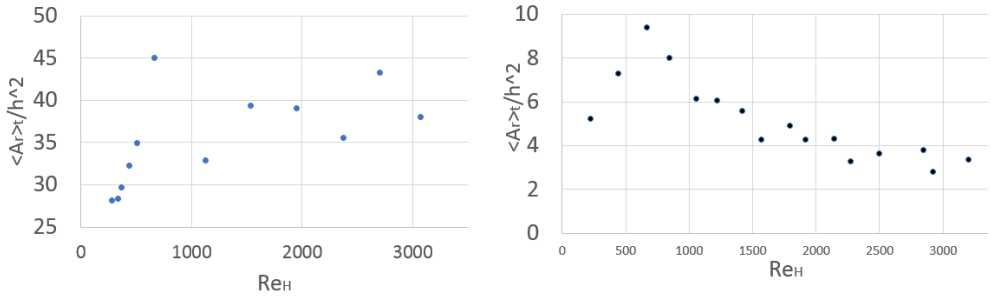

FIGURE 11.19: Mean recirculation area using horizontal (zx-left) and vertical (xy-right) plane measurements. Points are not connected because more measurements are needed to have the complete curve.

fields were examined and various spanwise modulations have been observed for the deformed vortex roll. Four characteristic K-H roll shapes can be found in figure 11.21. A Proper Orthogonal Decomposition (POD) was performed in this large time resolved PIV dataset for $y = 1.6\ h$; it revealed the K-H roll interaction modes for mode 6 and 13,together with the classical parallel equidistant vortex roll modes (modes $1-5$). The classical parallel rolls dominate due to their more frequent appearance; results can be seen in figure 11.22. A large number of image acquisitions could reveal the other roll pairing modes as well, but number of image acquired was limited to the embarked RAM of the camera and the acquisition frequency.

11.6 Conclusions and further perspectives

A preliminary study on the 3D instability of the BFS flow was studied using OF PIV. Different phenomena have been observed: longitudinal streaks of large amplitude and large scale spanwise structures of lower amplitude interact with the K-H vortex roll. This leads to a spanwise modulation of the streamwise velocity measured at different heights y from the bottom. The onset of the streak instability is placed after $Re_h = 700$ but more precise experiments are needed for the accurate definition. Extrinsic wall structures effect are observed since $Re_h = 100$ but their effect is limited in one step size maximum distance from the vertical walls; The study has validated again after Beaudoin et al., 2004b, that streamwise counter-rotating vortices appear downstream the BFS flow after the reattachment zone, which are superimposed with the co-rotating K-H vortex-rolls and the recirculation bubble. This study can shed more light in the 3D BFS instability of the open flow case, that has not been studied yet extensively experimentally by the community. More in-depth studies are needed to decide if we observe the same bifurcation as the one observed numerically by Blackburn, Barkley, and Sherwin, 2008. A water-channel of larger width, preferably mounted on an antivibratory optical table could be used. Further experiments in order to localise precisely the critical Reynolds number and disengage the vertical wall effects with the onset of the 3D instability are needed. The same study using a camera streaming directly to the computer using a PCI frame grabber, could also allow for a larger acquisition time and thus reveal well the low-frequency flapping phenomena of the RA. Future perspective studies could also include the investigation of the presented instability using stereo-PIV in order to obtain the missing component of the velocity, giving more insight in the true rather than the plane-projected dynamics of the structures.

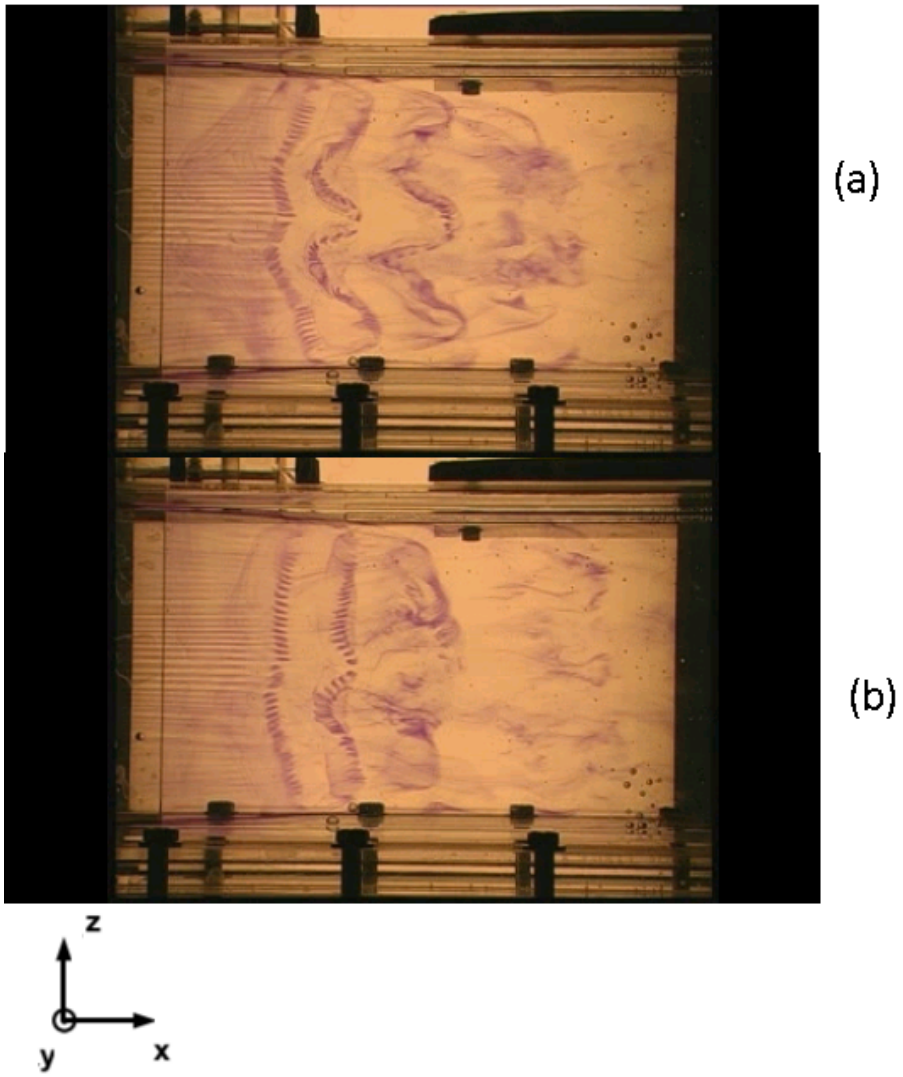

FIGURE 11.20: Instantaneous successive snapshots of dye visualisation on the xz plane of BFS flow for $Re_h = 1200$ from Beaudoin, 2004. Spanwise modulation of the K-H is observed.

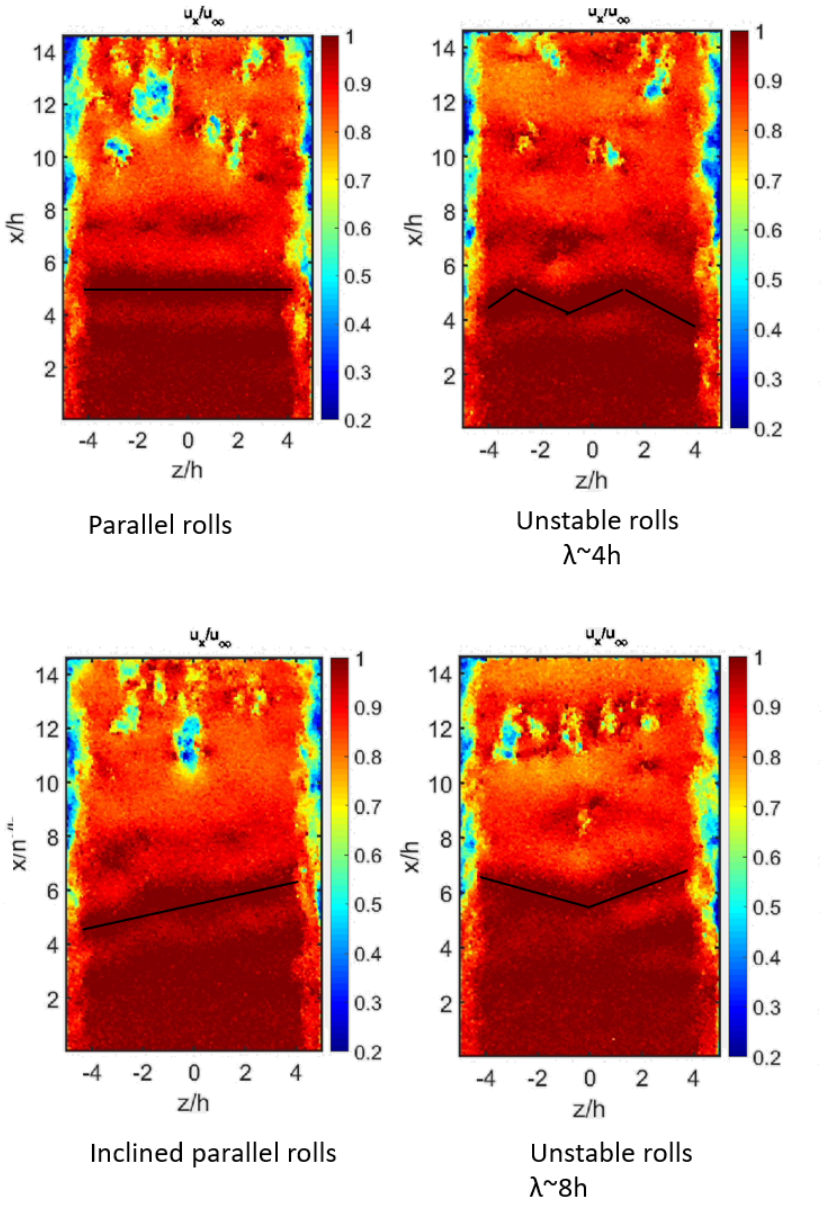

FIGURE 11.21: Different destabilisation processes of the K-H roll revealed through instantaneous streamwise velocity fields. Parallel, inclined, and spanwise modulated signatures appear at $y = 1.6\ h$

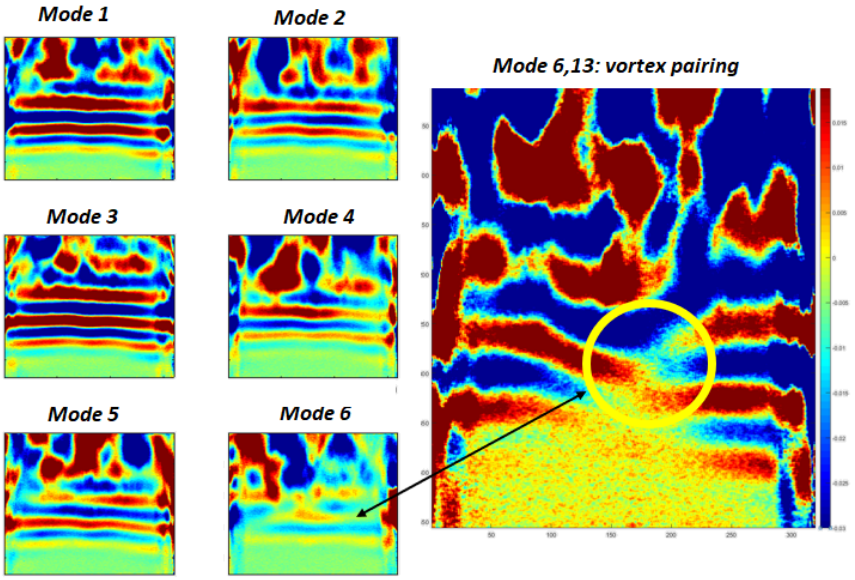

FIGURE 11.22: Proper orthogonal Decomposition of streamwise instantaneous fields, height $y = 1.6\ h$, $Re_h = 2709$.

11.7 Observation of turbulent spots in the BFS flow

The creation of turbulent spots are considered as one of the most intriguing features occurring in the process of the transition to turbulence in shear flows. Up to now it has been observed numerically or in well-controlled sub-critical shear-flow experiments like Poiseuille and Couette flows (Lemoult et al., 2014), in which they are triggered using proper perturbations or occur naturally. In this experimental study we show that turbulent spots can also arise spontaneously in the curved shear layer surrounding the recirculation bubble created downstream a Backward-Facing Step (BFS). We show that a single spot occurs at a critical Reynolds number, triggered by the natural perturbations contained inside the incoming boundary layer in the form of streaks of streamwise velocity. We also show that for larger Reynolds numbers multiple smaller turbulent spots are created around the recirculation bubble. The creation of turbulent spots triggered by streamwise velocity streaks appears like a key step in the transition to turbulence process of separated flows.

The first report on turbulent spots was made by Emmons (Emmons, 1951) in the transitional boundary layer. They were defined as isolated regions of strong fluctuations advected streamwise, growing in size and coalescing with neighbors. Later, Lindgren measured the velocity of their leading and trailing edges (Lindgren, 1969). They have since been reported numerous times in shear flows like the Couette flow (Lundbladh and Johansson, 1991; Couliou and Monchaux, 2018).

The BFS flow, particularly, is considered a very important test-case for separated flows; separation is imposed by a sharp edge leading to an low-frequency oscillating main recirculation area , secondary corner recirculating regions (in the bottom corners or the in the ceiling of the channel as well, for low vertical expansion ratios (Barkley, Gomes, and Henderson, 2002)) and a Kevin- Helmholtz instability leading to higher-frequency emission of vortices. A new boundary layer develops after the re-attachment of the flow, the position of which is important for heat and mass transfer purposes. Tihon et al. (Tihon, Legrand, and Legentilhomme, 2001) studied experimentally the re-attachment length for the Re number range [1200:12000]. In this spanwise-invariant description of the BFS flow we observe a convective

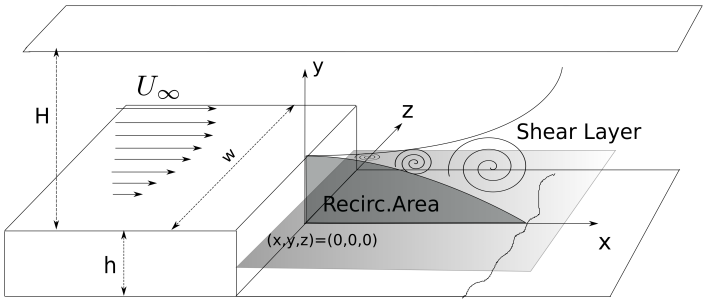

FIGURE 11.23: Sketch of the BFS geometry. Shear layer, recirculation area, re-attachment line and horizontal PIV window.

instability surrounded by upstream and downstream regions of stability.Since a very low Re number though, a 3D instability is observed (Armaly et al., 1983; Kaiktsis, Karniadakis, and Orszag, 1991; Beaudoin et al., 2004b), hence making recirculation area calculations strongly dependant on the measurement plane chosen. Particularly, Beaudoin et al. (Beaudoin et al., 2004b) showed for the first time a periodically modulated reattachment position in the spanwise direction, using PIV measurements. To our knowledge, there is no experimental proof of existence of turbulent spots in the BFS flow. Here we present and investigate such a case.

11.7.1 Experimental setup

Experiments have been carried out in a hydrodynamic channel in which the flow is driven by gravity, with a maximum free-stream velocity $U_\infty = 22\ cm.s^{-1}$. The flow is stabilised by divergent and convergent sections separated by honeycombs leading to a turbulence intensity of 0.8 %. A NACA 0020 profile is used to smoothly start the boundary layer. The test section is 80 *cm* long with a rectangular cross-section $w = 15\ cm$ wide and $H = 10\ cm$ high (Fig. 11.23). The step height is $h = 1.5\ cm$. The maximum Reynolds numbers based on the step height is $Re_{h,max} = U_\infty h/\nu \approx 3000$. The vertical expansion ratio is $A_y = H/(h+H) = 0.82$ and the spanwise aspect ratio is $A_z = w/(h+H) = 1.76$. The incoming boundary layer, downstream from the leading edge, is laminar and follows a Blasius profile. PIV is used to study the flow. The flow is seeded with 20 μm neutrally buoyant polyamide particles, which are illuminated by a laser sheet created by a 2 *W* continuous laser (MX-6185, Coherent, USA) operating at 532 *nm*. The Camera used was a 4 Mp PCO DIMAX-cs with an acquisition frequency $f_{ac} = 50\ Hz$. An narrow-band optical filter was mounted on the camera to visualize only the laser light reflected by the particles. The length of the PIV window 14.5 *h* and its spanwise width is 10 *h*.

The time-resolved velocity fields are calculated from the acquisition of successive snapshots in different horizontal y planes at $y = [0.2 : 0.2 : 1.6]h$, using a home-made Lucas-Kanade Optical Flow (LKOF) algorithm (Gautier and Aider, 2013).

11.7.2 Observations

The Reynolds number where the appearance of the first turbulent spot is $Re_h = 1135$, corresponding to a free-stream velocity $u_\infty = 7.13\ cm.s^{-1}$. The turbulent spot is created repetitively in the vertical position between $y = 0.4\ h$ and $y = 0.8\ h$. It is observed well in the instantaneous fields.

Experimental evidence implies that the position of the birth of these spots is not random: Reconstruction of the volumetric isosurface of $u_x = 0$, we can get an idea of where the birth happens regarding the recirculation bubble border. Superimposing this 3D surface with the

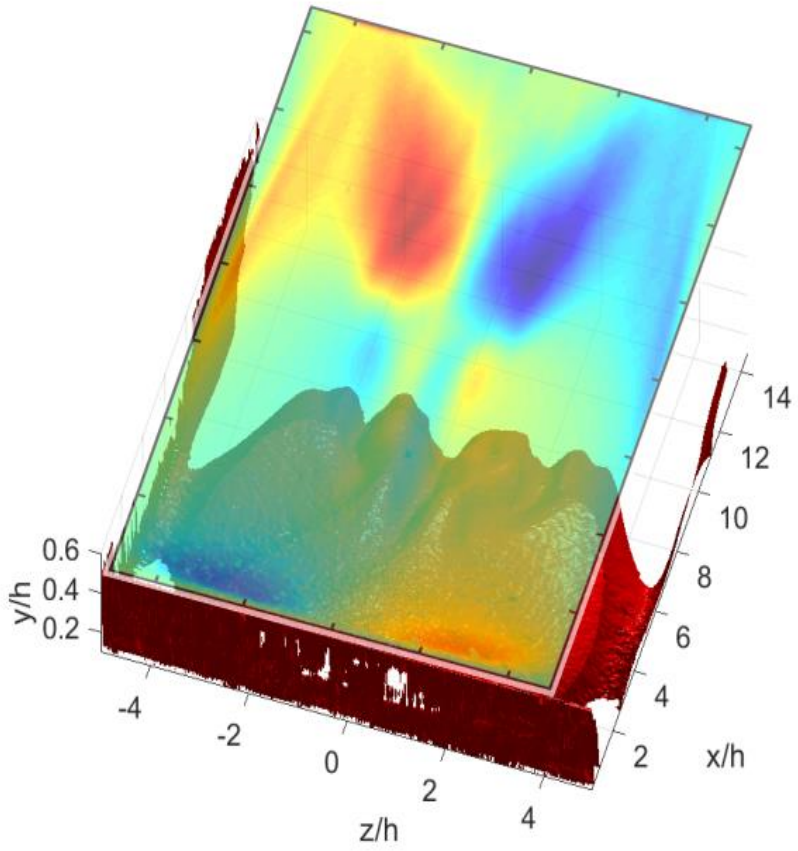

FIGURE 11.24: Superimposed isosurface $u_x = 0$ and contour of mean spanwise velocity u_y for $y = 0.6\,h$. Extrinsic structures appear in the wall and streak instability in the center. Large scale structures appear in the mean spanwise field. Appearance of turbulent spot in form of quadrupole.

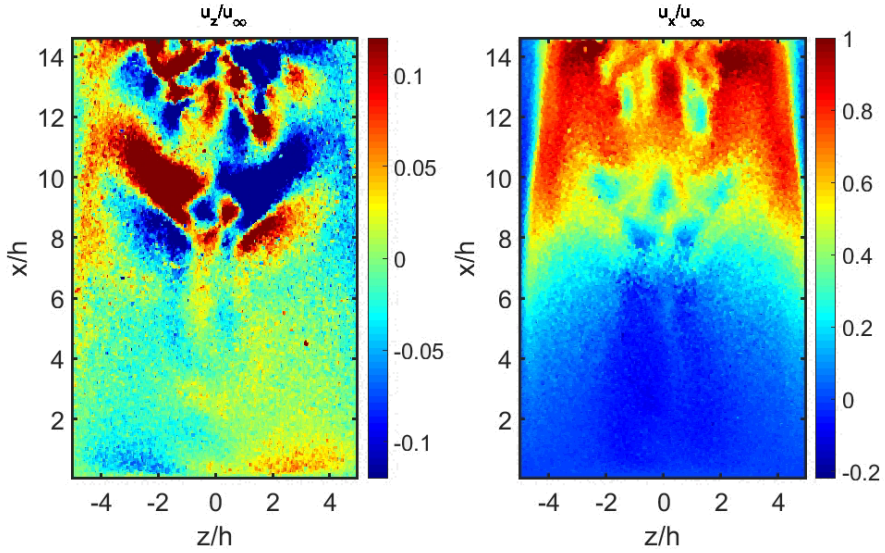

FIGURE 11.25: Characteristic instantaneous spanwise (left) and streamwise (right) velocity fields. The repetitive turbulent spot quadrupole nucleation is observed around position $x/h = 8$. Ekman structures are observed in the corners for $x = 0$ as well as the side walls, but without extending more than one step size.

mean streamwise field, where the exact position is well defined we can come to the conclusion below: birth of the spots is observed in the large curvature region of the recirculation bubble, where the streak start to form. This can be seen in figure 11.24 . The proper orthogonal decomposition also revealed the structures of the spot in the first two modes, as seen in figure 11.26. The energy of each mode was 12 %. A second observation, is that the number of turbulent spots are observed to be increasing with the Re number, as the number of streaks increases as well. Hence we suspect that there is a connection with the number of streaks and the occurrence spatial frequency.

Increasing the Re_h number, we can see more spot positions appearing, although less clearly since the flow becomes more 3dimensional and turbulent. An intensive search in the instantaneous fields is needed to verify this. Hence we suspect that the streak appearance is what facilitates the birth of these spots and accelerates the transition to turbulence.

11.7.3 Conclusions

Turbulent spot nucleation can be seen as a key mechanism in the transition to turbulence in the BFS flow. The number of nucleation spots increase with Re number, together with the increase of streak numbers, as seen in figure 11.27. Further experiments should be conducted to quantify the frequency of the appearance and relation with Re_h number. Volumetric PIV could actually shed more light in the exact position of birth of the spots and its relationship with the curvature of the recirculation bubble border. A comparison with a numerical simulation approaching the open-flow case (or at least a large vertical expansion ratio) could further verify these experimental findings.

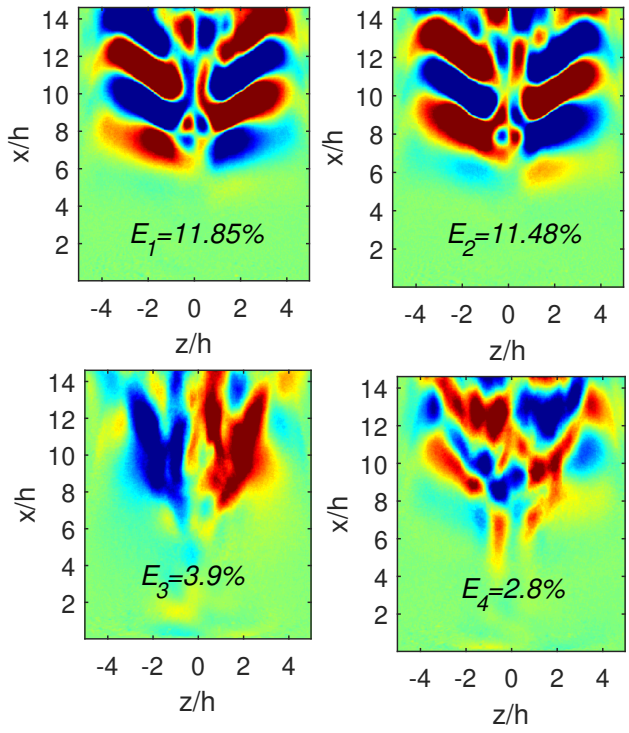

FIGURE 11.26: First 4 POD modes and their corresponding energies. $Re_h = 1135$ and plane $y = 0.6$

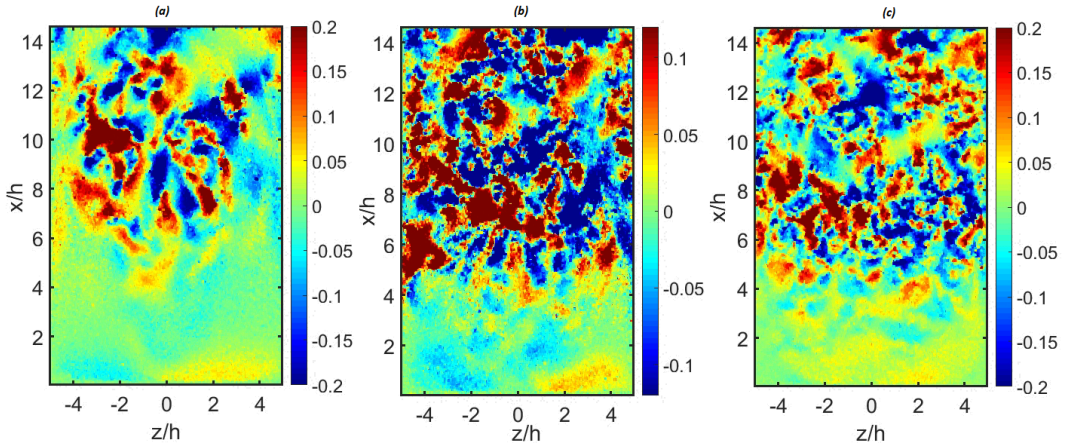

FIGURE 11.27: Turbulent spot nucleation as appearing in spanwise instantaneous fields. $Re_h = 1546$ (a), 1960 (b) and 2709 (c) respectively. Horizontal plane xz studied at $y = 0.6$

Chapter 12

Prediction of the dynamics of the BFS flow using neural networks

The content of this chapter is based on the article: *A. Giannopoulos, J-L Aider: Prediction of the dynamics of a backward-facing step flow using focused time-delay neural networks and particle image velocimetry data-sets, International Journal of Heat and Fluid Flow, Volume 82,https://doi.org/10.1016/j.ijheatfluidflow.2019.108533.*

The objective of this experimental work was to evaluate the potential of an artificial Neural Network (NN) to predict the full-field dynamics of a standard separated, noise-amplifier flow: the Backward-Facing Step (BFS) flow at $Re_h = 1385$. Different upstream local visual sensors, based on the velocity fields measured by time-resolved Particle Image Velocimetry, were tested as inputs for the Neural Network. The dynamic coefficients of a Proper Orthogonal Decomposition (POD) were defined as goals-outputs for this non-linear mapping. The coefficients time-series were predicted and the instantaneous velocity fields were reconstructed with satisfying accuracy using a Focused Time-Delay Neural Network (FTDNN). Using a time-delay appears like a crucial choice to ensure an accurate prediction of the dynamics of the BFS flow. A shallow FTDNN is sufficient to obtain good accuracy with low computational time. The influence of the choices of inputs-sensors, the size of the training data-set, the number of neurons in the hidden layer as well as the sensor delay on the accuracy of the predicted flow are discussed for this experimental fluid system.

12.1 Introduction

Shear layer flows like boundary layers (BL), mixing layers, jets or Backward-Facing Step (BFS) flows (Beaudoin et al., 2004b; Dergham, Sipp, and Robinet, 2013) are ubiquitous in nature as well as in industrial flows. One of their most important properties is that they are convectively unstable (Huerre and Monkewitz, 1990; Chomaz, 2005) and very sensitive to background noise. They are also called “noise-amplifier" flows because of their ability to amplify some specific frequency ranges.

Noise-amplifier flows play an important role in many industrial flows, like separated flows around airfoils (Darabi and Wygnanski, 2004) and the complex 3D wakes of ground vehicles (Aider et al., 2001; Beaudoin et al., 2004a). Most of the time they are responsible of loss of efficiency (increase of aerodynamic drag, lift crisis) or nuisances like aeroacoustic noises or fluid-structure interactions. Controlling shear flows is then crucial for many industrial applications. For instance, controlling the shear layers to reduce the wake of a bluff-body or a ground vehicle has been proved to be a valuable strategy to reduce the aerodynamic drag of ground vehicles (Aider, Beaudoin, and Wesfreid, 2009; Aider et al., 2014; Eulalie et al., 2018; Li et al., 2016; Grandemange et al., 2014).

Nevertheless, closed-loop flow control experiments are still challenges both for academic or industrial configurations. From a general point of view, the fist step is to choose sensors

and actuators before searching for a proper control law allowing the modification of the targeted flow by the actuators based on information coming from the sensors. One can choose arbitrarily the sensors and actuators and propose a closed-loop law based on some physical properties of the targeted flow, like the Kelvin-Helmholtz frequency of a shear layer (Gautier and Aider, 2015b). One can also use a Machine Learning algorithm to search for a proper control law (Gautier et al., 2015; Li et al., 2016; Debien et al., 2016; *Machine Learning Control-Taming Nonlinear Dynamics and Turbulence*). Ultimately the problem of the relevance of the sensors and their ability to represent the global dynamics of the flow becomes crucial. One can use statistical data-based System Identification (SI) techniques to try to find a relation between one or multiple sensors and the dynamics of the flow as shown by (Guzmán, Sipp, and Schmid, 2014; Varon et al., 2015). Another option is to use machine learning techniques to find the best combinations of sensors and a proper Reduced-Order system to recover most of the dynamics of the flow. This is the objective of this study.

In modern experimental and testing / diagnosing techniques, data-driven methods are becoming of great interest, since they don't require a priori knowledge of a model and the access to large data-sets is becoming easier. This is especially true when studying thoroughly non-stationary flows for different Reynolds numbers with various sensors such as Particle Image Velocimetry (PIV) or multiple Pitot / multiple hot-wire probes. Methods like statistical and machine learning algorithms, are becoming efficient and reliable for both academics or industrial applications. Regarding the machine learning family of algorithms NNs particularly, are attracting more and more attention in this "Big-Data" revolution.

In fluid systems, feed-forward artificial NNs have been used for data-driven reduced-order modelling (Müller, Milano, and Koumoutsakos, 1999; Wang et al., 2018; Pan and Duraisamy, 2018) with many results showing better field reconstruction than traditional POD methods (San, Maulik, and Ahmed, 2018; Erichson et al., 2019). They were also used by Mi, Ishii, and Tsoukalas, 1998 for experimental flow regime identification in multiphase flows. We mention that it has also been proved by Baldi and Hornik, 1989, that a linear NN can be equivalent to a Proper Orthogonal Decomposition (POD) basis structure. Convolutional NNs have also been used for the efficient real-time 2D and 3D inviscid simulations (Tompson et al., 2016) or along with pressure measurements for the velocity field prediction around a cylinder (Jin et al., 2018). Furthermore, if there are hints of deeper understanding of the underlying physics, simple shallow NNs can provide very good results in SI as well as for control laws creation (Lee et al., 1997; Herbert, Fan, and Haritonidis, 1996; J.Rabault et al., 2018). Their potential has been demonstrated early for modelling surface pressure and aerodynamic coefficients of 3-dimensional unsteady cases of aircrafts flows (Faller and Schreck, 1996). Finally, deep NNs are increasingly more important in the fluid mechanics community, especially for the modelling of complex turbulent flows. Srinivasan et al. Srinivasan et al., 2019 compared deep feed-forward and recurrent Long-Short Term Memory (LSTM) networks for turbulent shear flows prediction. Recently Deng et al. (Deng et al., 2019), used LSTM networks to reconstruct the POD coefficient time series using sub-sampled distributed velocity sensors in an inverted flag flow PIV experiment. A short review of applications of deep NN to fluid mechanics can be found in Nathan Kutz, 2017.

For complex flows, the number of degrees of freedom obtained from a 2D-2C (2 components in a 2D velocity field) optical-flow PIV measurement of a few millions pixels image is millions. Such a large system is impossible to handle and a reduced-order model (ROM) has to be identified. A dynamic observer can identify such a model based only on input-output measurements from measurable system quantities. As proposed firstly by Guzmán, Sipp, and Schmid, 2014 and verified experimentally for PIV data by Varon et al., 2015 it is possible to predict the full dynamics of a transitional flat-plate BL flow in the form of POD coefficients using a few local upstream sensors. The first step in their method was to create a successful reduced-order system using POD. The second step was to identify an optimal state-space

model using a statistical learning process (the so-called N4SID algorithm), in order to predict at any moment all the POD coefficients (outputs) by measuring one or two local variables upstream (sensors or inputs) in the flow. A similar approach was also presented in a paper from Beneddine et al. Beneddine et al., 2016, where the full frequency spectrum was obtained from local frequency information of the flow. Time-resolved field reconstruction was also successfully obtained for time-resolved PIV data of a round jet flow using point sensors and the mean flow Beneddine et al., 2017.

In the present study, we explore means of performing a local-to-global dynamics system identification (SI) using a NN architecture. We show we can successfully apply a machine learning data-driven identification process in a complex experimental fluidic data-set, in order to learn the relation between local upstream sensors and the global fluctuation dynamics of the system. A different data-set is used to validate the learning-training step. The predicted dynamics then allow the reconstruction of the full flow field, which would help design realistic, experimental controllers targeting the kinetic energy of the full fluctuation field. We show the importance of the various choices (from sensors, to NN parameters) in a successful SI of an experimental, time-resolved, separated flow.

The following chapter is organised as follows: first, we present the various artificial NNs that can be found in the literature. Then we present the experimental setup used to study the BFS flow. The choice of the NN architecture is then discussed. Different NNs have been tested; only one NN lead to satisfactory results with the least number of parameters and a reasonable computational time. Then the choice of the sensors as well as of the NN parameters like the training data-set size or the value of the time-delay are discussed. The efficiency of the chosen shallow NN architecture for such a SI is then demonstrated through validation data-sets comparisons between real and estimated POD coefficients time-series. Finally, the reconstructed time-resolved velocity fields are successfully compared with measured velocity fields, before turning to the conclusions.

12.2 Artificial Neural Networks

An artificial NN can provide a non-linear mapping between a set of inputs and a set of corresponding outputs. Great progresses have been made lately due to the availability of large data-sets, the increasing number of optimised toolboxes and also the improvements of Graphics Processing Units (GPU) parallel programming. This is the reason why NNs are becoming more and more popular nowadays.

The key component of a NN is the neuron or “perceptron". In general, one defines a weight w_i associated to each i^{th} neuron of the previous layer. To obtain the output of a perceptron from a set on N neurons, one computes the sum of the N inputs multiplied by their corresponding weight and adds a given bias b_i. An activation function f is then used to compute the output. A classic activation function is a step-function, but more refined functions are usually needed. To improve the efficiency of classic NNs, it is possible to add one or many “hidden" layers between the inputs and the outputs. It is theoretically proven that any continuous function can be approximated with a single hidden layer (Cybenko, 1989; Funahashi, 1989).

The simplest shallow, fully-connected NN architecture consists of an input layer (with n neurons), a single hidden layer (with an arbitrary number of n_1 neurons) and a linear layer (with $n_2 = m$ neurons) connected to the output, as shown in Fig. 12.1. A standard rule for the linear layer is to have the same number of neurons as the output layer. Regarding the choice of the number of neurons in the hidden layer, it can be as high as needed to increase accuracy, but without over-fitting. For a NN with a non-linear activation function f_1 in the

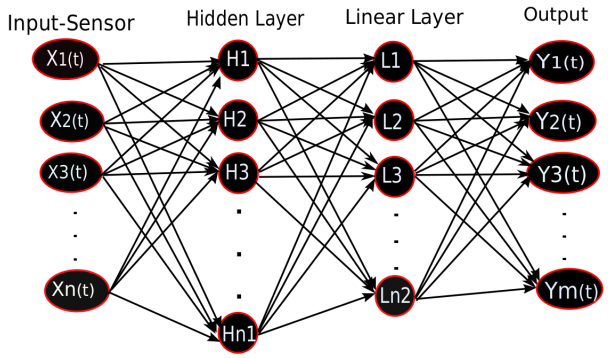

FIGURE 12.1: An example of a shallow NN non-linear mapping to monitor m outputs Y using the n sensors X in a feed-forward architecture, with n_1 neurons in the hidden layer.

hidden layer and a linear activation function f_2 in the linear layer, the equation giving the k_{th} neuron output of a single hidden layer network connected to the j_{th} neuron of the previous layer is:

$$y_k = \mathbf{f_1}\left(\sum_{j=0}^{n_2} w_{kj}^{(2)} \mathbf{f_2}\left(\sum_{i=0}^{n_1}(w_{kj}^{(1)} x_i + b_i) + b_j\right)\right) \tag{12.1}$$

where n_1 is the number of neurons in the first (hidden) non-linear layer and n_2 the number of neurons in the second (linear) layer. Regarding the choice of the non-linear activation function f_1, usually the popular tan-sigmoid or hyperbolic tangent function is used:

$$f_1(x) = \frac{e^{2x} - 1}{e^{2x} + 1} \tag{12.2}$$

The correct training process of the network (i.e. finding the optimal weights and biases connecting the neurons of different layers) consists of dividing the data-set into a training data-set and a validation data-set. Starting with the training data-set, the first set of weights connecting the layers is randomly initialised for this first iteration. The error of the real versus the model-generated output is computed and the weights and biases are updated according to different back-propagation schemes, in our case the Scaled Conjugate Gradient (SCG) method. In this case, the step size is adjusted at each iteration in order to minimise the performance function. The above process is called an “epoch". We continue the process for as many epochs as needed until a satisfactory fit error is achieved (Fig. 12.2). The second data-set is the “validation" data-set and is used to evaluate the performance of the network on new data and the corresponding error, hence avoiding over-fitting.

12.2.1 Neural Network types

NNs can be divided into Feed-Back (or recurrent) and Feed-Forward. They can also be discriminated according to their depth, either shallow or deep, depending on the number of hidden layers (one or more). Finally, they can be divided into static or dynamic, if the output of the current step depends on the previous steps as well, giving it a notion of memory.

In the case of a feed-forward NNs the output of any layer only modifies the next layer, not the previous ones. System identifications using feed-forward NNs have been a common practice since the 90s (Narendra and Parthasarathy, 1990; Reynold Chu, Shoureshi, and Tenorio, 1990). Recently, deeper feed-forward NNs have also been implemented in complex SI cases (Olekan et al., 2016).

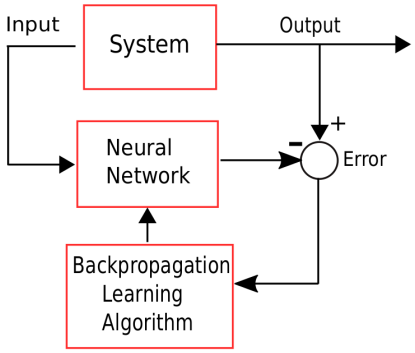

FIGURE 12.2: Block diagram of the NN System Identification training step.

On the other hand, in a feed-back NN the system output is calculated from its previous past time-steps along with the input at the current time-step like in equation 12.3:

$$y_t = f_{w,b}(y_{t-1}, x_t) \tag{12.3}$$

Recurrent NNs introduce a notion of memory in the output of the system. One specific family of recurrent NN is the Non-linear Auto-Regressive eXogenous (NARX) models. They are autoregressive because the outputs of the current time step depends on the output of a number of previous steps. They are exogenous because the output depends also on a number of inputs. The NARX models were first introduced by (Leontaritis and Billings, 1985) and used with NN with significant success by Chen, Billings, and Grant, 1990 for multiple non-linear SI cases. It is a natural extension of the Autoregressive Exogenous model (ARX), which has been extensively used in linear black-box SI.

Another category of recurrent NNs are the Long-Short Term Memory (LSTM) networks. They are gradient-based recurrent NNs used for supervised learning both in classification and prediction problems (Vlachas et al., 2018). They were first developed by Hochreiter and Schmidhuber, 1997 to solve the vanishing or exploding gradient problem of the back-propagated error. In an LSTM architecture, the network is left to learn alone the size of the memory of each neuron during the training process. They do so using a sophisticated gate-neuron that determines if the input is important enough or if it should be forgotten and when it should output its value.

12.2.2 Focused Time-Delay Neural Networks

Time-delays are frequently encountered in physical systems, and can be a source of instability in NNs. This is the reason why delayed NNs have become more attractive. Delays can be introduced in the output or the input of the NN and can be constant or time-varying (Yu, He, and Wu, 2018). The network used in the present SI study is a fully-connected Focused Time-Delay Neural Network (FTDNN) which was first introduced for speech recognition (Waibel et al., 1989). It is basically a standard feed-forward architecture along with a tapped constant time-delay (of time-step size k) in the input. The term “focused" comes from the fact that the notion of memory is introduced only in the input and not in the output like in LSTM NNs. They are used to model long-range temporal dependencies by keeping a number of k past measurements of the input at each time step x_t, leading to the following expression for the output of the system :

$$y_t = f_{w,b}(x_t, x_{t-1}, ..., x_{t-k}) \tag{12.4}$$

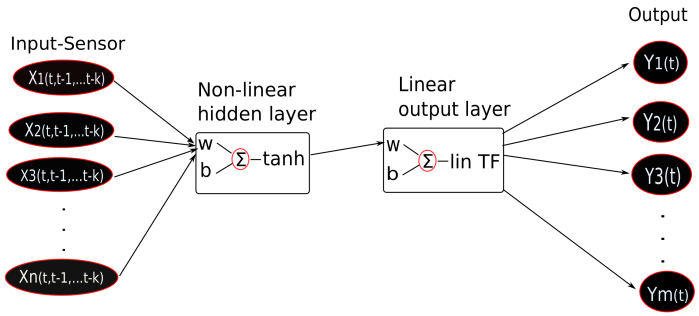

FIGURE 12.3: Example of a scheme of a FTDNN architecture with a hidden layer and an output layer.

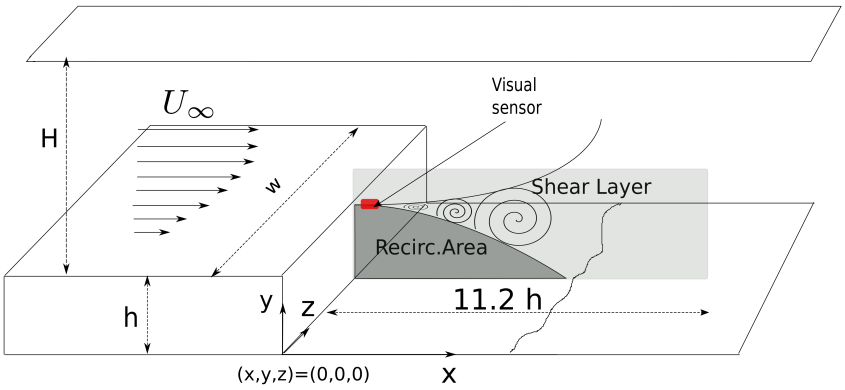

FIGURE 12.4: Sketch of the BFS geometry and main flow features (shear layer and recirculation bubble). The PIV window is shown in grey and the visual sensor location shown as a red dot.

where w and b are weight and bias parameters. A scheme of a FTDNN architecture is shown in Fig. 12.3. They have been used for rainfall prediction (Charaniya and Dudul, 2012) as well as for effective acoustic modelling (Huang et al., 2019), in deep architectures.

Fuzzy logic can also be integrated in NNs, as for the case of Takagi and Sugeno fuzzy-delayed NN. Shi et al. (Shi et al., 2018) proposed a new alterable sampled-data terminal method to investigate the reliable asynchronous filtering problem with time-varying parameters, stochastic intermittent faults and controller gain fluctuation. Modelling neutral delays in physical systems has led also to Neutral Neural network architectures. Li et al. (Li et al., 2019) studied the master-slave synchronisation in such NNs.

12.3 Experimental setup

12.3.1 Hydrodynamic channel

Experiments have been carried out in a hydrodynamic channel in which the flow is driven by gravity. The flow is stabilised by divergent and convergent sections separated by honeycombs, leading to a turbulence intensity of 0.8 %. A NACA 0020 profile is used to smoothly start the boundary layer. The test section is 80 cm long with a rectangular cross-section $w = 15$ cm wide and $H = 10$ cm high (see figure 12.4). The step height is $h = 1.5$ cm. The vertical expansion ratio is $A_y = H/(h+H) = 0.82$ and the spanwise aspect ratio is $A_z = w/(h+H) = 1.76$.

12.3.2 Optical Flow PIV measurements parameters

The flow is seeded with 20 μm neutrally buoyant polyamide particles, which are illuminated by a laser sheet created by a 2 W continuous laser (MX-6185, Coherent, USA) operating at 532 nm. A thin layer of fluorescent paint (FP Rhodamine 6G, Dantec) was applied to the illuminated surface to absorb the laser wavelength and avoid reflections and to allow correct near-wall measurements. The Camera used was a 4 Mp PCO DIMAX-cs with an acquisition frequency $f_{ac} = 150\ Hz$. An narrow-band optical filter was mounted on the camera to visualise only the laser light reflected by the particles. The length of the PIV window 11.2 h and its height is 3.7 h.

The time-resolved velocity fields are calculated from the acquisition of successive snapshots in the vertical symmetry plane at $z = w/2$, using a home-made Lucas-Kanade Optical Flow (LKOF) algorithm. The first version of the code has been developed at ONERA (Champagnat et al., 2011) and later modified, optimised and adapted to the constraints of real-time measurements by Gautier & Aider (Gautier and Aider, 2013). Among the advantages of the LKOF algorithm compared to a standard FFT-PIV algorithm is the calculation of a dense velocity field with one vector per pixel. It also allows for high computational speed when implemented on a GPU with CUDA functions (C.Pan et al., 2015). The code has been used many times both for time-resolved PIV measurements with a high spatial resolution (Varon et al., 2017), as well as for closed-loop flow control experiments (Gautier and Aider, 2013; Gautier et al., 2015; Gautier and Aider, 2015b). The PIV calculations in the present study were performed on a NVIDIA TESLA K80 GPU.

12.4 The Backward-Facing Step flow

12.4.1 Characterisation of the BFS flow

The objective of this study is to evaluate the potential of a NN SI method on experimental data of a shear-layer flow. We focus on a BFS flow which is a typical case of noise-amplifiers. Upstream perturbations are amplified in the shear layer leading to significant downstream disturbances. Separation is imposed by a sharp edge creating a strong shear layer where Kelvin-Helmholtz instability leads to vortex shedding (Fig. 12.4). Another important feature is the creation of a large separation bubble, which is usually associated to pressure drag (Dahan, Morgans, and Lardeau, 2012a). Its reduction is then a common objective to most flow control experiments targeting drag reduction. It is also considered as a benchmark case for the study of separated flows. For this reason it has been extensively studied both numerically and experimentally (Beaudoin et al., 2004b; Hung, Parviz, and John, 1997; Armaly et al., 1983). The Reynolds number in the present experiment is $Re_h = 1385$, corresponding to a free-stream velocity $u_\infty = 11\ cm.s^{-1}$. The incoming boundary layer, downstream from the leading edge, is laminar and follows a Blasius profile. The boundary layer thickness just upstream the step edge is $\delta_0 = 7mm = 0.47\ h$ corresponding to a shape factor $H = 2.3$, typical of a laminar boundary layer. The vortex shedding frequency is $f_{shed} = 1.13Hz$, which corresponds to a Strouhal number $St_h = \frac{f_{shed}h}{u_\infty} = 0.15$.

12.4.2 Detection of vortical structures

As we are interested in the growth and dynamics of coherent structures, one can choose to monitor the vorticity field. Since vortical structures are embedded into the shear layer, it is better to use more refined criteria, like the Q criterion or the λ_{Ci} criterion, which are well adapted to the identification of vortical structures inside a shear layer. The λ_{Ci} criterion was first introduced by Chong et al. Chong, Perry, and Cantwell, 1990, who analysed the

velocity gradient tensor $\mathscr{D} = \overrightarrow{\nabla}\overrightarrow{u}$ and proposed that the vortex core could be defined as a region where $\nabla\mathbf{u}$ has complex conjugate eigenvalues. It was subsequently improved by Zhou et al. Zhou et al., 1999 and by Chakraborty et al. Chakraborty, Balachandar, and Adrian, 2005. It was also successfully applied by Cambonie and Aider, 2014, to visualise the 3D vortices created by a Jet in Cross-Flow measured by Volumetric Velocimetry, and by Gautier et al. Gautier and Aider, 2015a in a closed-loop flow control experiment using a similar visual sensor. For 2D data, λ_{Ci} can be computed quickly and efficiently using equation 12.5, when such a quantity is real (else $\lambda_{Ci} = 0$):

$$\lambda_{Ci} = \frac{1}{2}\sqrt{4\det(\nabla\mathbf{u}) - \mathbf{tr}(\nabla\mathbf{u})^{\mathbf{2}}} \tag{12.5}$$

where “det" is the matrix determinant and “tr" is the trace of the matrix. An example of detection of vortical structures using the λ_{Ci} criterion is shown on Fig. 12.5 c. We mention, that the spatial mean λ_{Ci} has been proven to increase linearly with the Re_h number in the BFS flow, up to $Re_h = 3500$ (Gautier, 2014).

12.4.3 Proper Orthogonal Decomposition

Decomposing a dynamical system in modes of decreasing importance can help reducing the order of the variables of the system. $N = 4197$ consecutive instantaneous velocity fields $\{\boldsymbol{U}(n) = (u_x^*, u_y^*)\}_{n=1...N}$ were computed from consecutive flow snapshots with an acquisition frequency $f_{ac} = 150\,Hz$. The size of each snapshot-velocity field is 346×1010 pixels, with a spatial resolution of $0.166\,mm/pixel$. By calculating the mean field $[\overline{U}_x, \overline{U}_y]$ we were able to obtain the velocity fluctuations $u_x'(t) = u_x^*(t) - \overline{U}_x$ and $u_y'(t) = u_y^*(t) - \overline{U}_y$, which contained all the dynamics and were used to create the reduced-order system. The fluctuation matrices organised in columns for each time-step were used to form the so-called “snapshot matrix" to be decomposed. The reduced-order system is obtained using POD, which has been used extensively in fluid mechanics (Borée, 2003; Mendez et al., 2017). It allows us to build a ranked and orthonormal basis containing N modes (Lumley, 1967; Sirovich, 1987). The first M modes $\{\boldsymbol{\Phi_k}\}_{m=1...M}$ with $M \leq N$ containing a sufficient percentage of the total energy is then chosen to compute the approximated velocity field $\tilde{\boldsymbol{U}}(\boldsymbol{n})$:

$$\tilde{\boldsymbol{U}}(\boldsymbol{n}) = \sum_{m=1}^{M} \langle \boldsymbol{\Phi_m}, \boldsymbol{U}(\boldsymbol{n}) \rangle \boldsymbol{\Phi_m} = \sum_{m=1}^{M} a_m(n) \boldsymbol{\Phi_m} \tag{12.6}$$

where the scalar product $\langle \cdot, \cdot \rangle$ is the energy-based inner product. The system output to be identified is obtained through the reduced state vector containing the M POD coefficients $a_m(n)$:

$$Y(n) = [a_1(n)\ a_2(n)\ ...\ a_M(n)]^T \tag{12.7}$$

The full-field dynamics are now contained in their POD coefficients $a_m(t)$. The balance between the order and accuracy of the POD reduced-order system is crucial, because it was seen that for a large number of POD modes the SI methods are much more likely to fail.

The energies of the individual POD modes as well as their cumulative energy are shown in Fig. 12.6. One can see that more than 50 % of the energy is contained in the three first modes. The system size containing at least 80 % of the total energy was used. It corresponds to $M = 10$ modes $\boldsymbol{\Phi_m}$ and 10 POD coefficients a_m. The evolution of the $1^{st}, 3^{rd}$ and 5^{th} POD coefficients are shown in Fig. 12.7. We present the odd-numbered modes because since they are convective, they come in pairs. The characteristic frequency of the 1^{st} POD mode corresponds to the Kelvin-Helmholtz frequency, i.e. the shedding of the vortices in the shear layer.

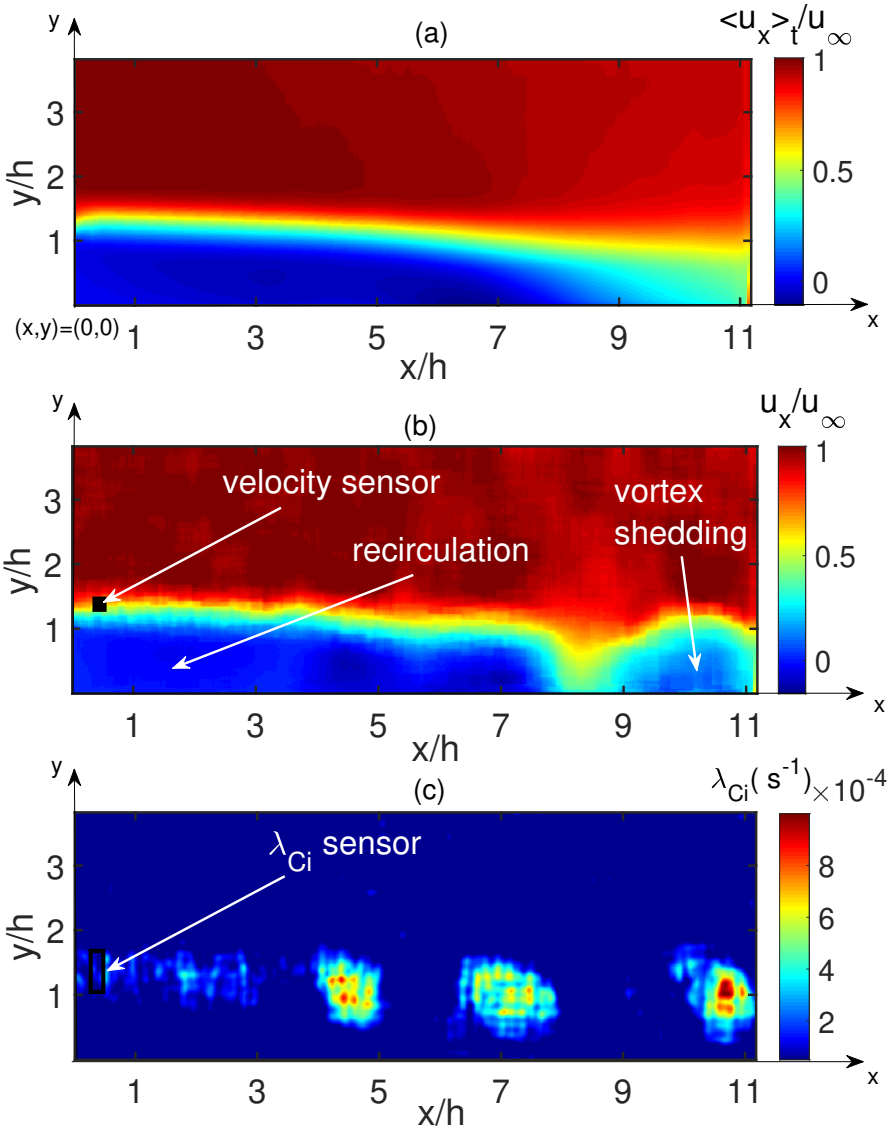

FIGURE 12.5: Illustration of the averaged streamwise velocity field (a), an example of an instantaneous streamwise velocity field (b) and of an instantaneous swirling strength field computed with the λ_{Ci} criterion (c). The position of the tested visual sensors is also shown on the figures (b, c). The flow principal direction is from left to right.

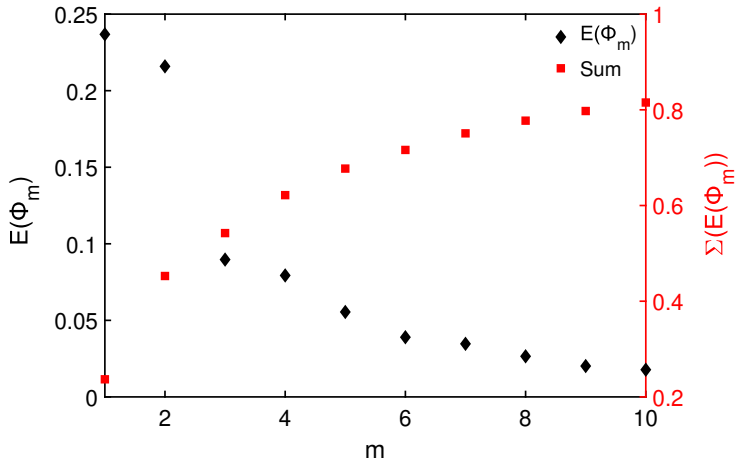

FIGURE 12.6: Energy of each POD modes and cumulative total energy of the POD modes up to 80 % of the total energy. First two POD modes correspond to the vortex shedding due to the Kelvin-Helmholtz instability.

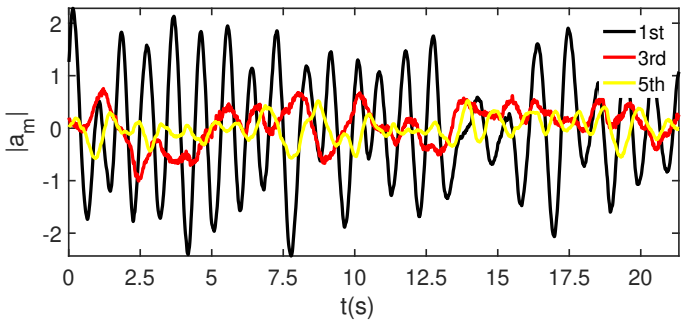

FIGURE 12.7: Time-series of 1^{st}, 3^{rd} and 5^{th} dynamic POD coefficients.The evolution of the 1^{st} coefficient has a peak frequency close to the K-H vortex shedding frequency.

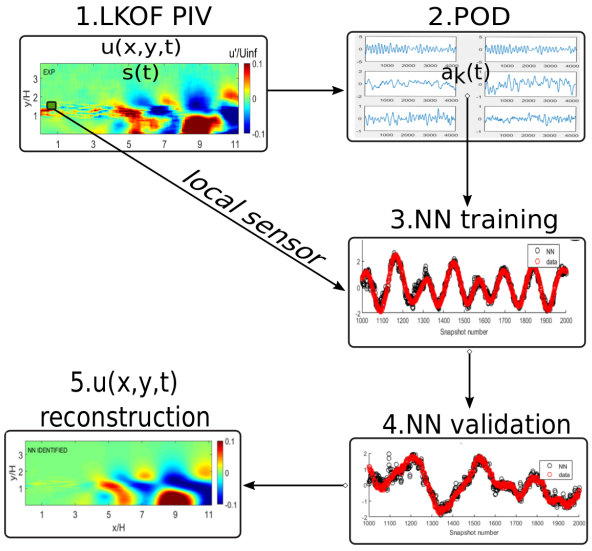

FIGURE 12.8: Sketch summarising the main steps of the identification procedure: from the time-resolved PIV experiment to a convincing reconstruction of the velocity fields using local upstream sensors.

12.5 System Identification steps

In the present study we explore the potential of artificial NNs for local-to-global dynamics SI applied to a shear layer flow. A full scheme of the identification process is summarised in Fig. 12.8. First, in the full data-set of time-resolved PIV experiment is decomposed to identify the dynamics in the form of POD coefficients. Then, in this data-driven identification process, we just rely on the input (optical sensors) - output offline measurements for a period of time from the operation of the system. Once the machine (in our case an artificial NN) has monitored a sufficient number of realisations (training data-set), it will identify the relationship between the given input-sensor and the goal-output. If the method is successful, then monitoring the sensor will allow us to predict successfully the full global dynamics (in the form of POD coefficients) of the system in a new, unknown to the machine, data-set (validation), with no further need for a time consuming field decomposition analysis. Then the time-resolved field can be reconstructed from the identified NN-generated POD coefficients, using only the local sensor measurements.

In the following sections we discuss the influence of the main parameters on the SI process. We will especially show the importance of the choice of the physical parameters (nature, number and location of the sensors) in the ability of the SI learning process to find the proper NN weights and biases for each neuron. We will also show how the choice of the NN parameters (number of neurons in the hidden layer, time-delay) plays a crucial role in the efficiency of the SI process.

12.5.1 Validation Criterion

To evaluate the efficiency of the identification, one has to define a quantitative criterion to compare the POD coefficient time-series results obtained with the different NN architectures to the ones obtained experimentally. In the following, we compute the mean-squared error

(MSE) at each time-step n for each POD coefficient $a_m(n)$:

$$MSE_m = \frac{1}{N}\sum_{n=1}^{N}\left(a_{exp,m}(n) - a_{NN,m}(n)\right)^2 \tag{12.8}$$

Then the averaged MSE for all the coefficients ($M = 10$) time-series gives the final evaluation error for the specific NN architecture:

$$MSE = \frac{1}{M}\sum_{m=1}^{M} MSE_m \tag{12.9}$$

12.6 Influence of the sensor-input definition

12.6.1 Choice of the input(s)

Our sensor consists of selected measurements from the time-resolved velocity field. Different inputs can be defined from these velocity measurements, or from velocity-derived variables like the vorticity or vortex identification criteria. First, it is necessary to choose the physical quantities measured by the sensor(s). As the optical sensors are the inputs in the identification process, their choice is a critical step. Our challenge is to identify vortices embedded in the shear layer, close to the BFS edge, in the receptivity region of the noise amplifier. For this reason, the sensors can either be one or the two components of the fluctuation velocity field, or more complex quantities based on the gradients of the velocity field, like the the λ_{ci} criterion.

12.6.2 Sensor position

The location of the sensor is critical. It should allow the detection of the perturbations during the initial phase of the reciptivity-amplification process of the shear layer (Guzmán, Sipp, and Schmid, 2014). So in such a noise-amplifier flow the sensor was placed as upstream in the velocity field as possible, right after the separation in the high-shear region, as shown in Fig. 12.5. The proximity to the wall also is important for the method to be realistically applicable if other measuring devices, like hot-wires, were to be tested in the future. The exact sensor location was finally chosen to be kept slightly away from the wall ($x = 0.25\ h$), in order to avoid possible noisy near-wall measurements. We mention that the flow field may be difficult to measure experimentally because of the large velocity gradients in the sensor region. Nonetheless, the good spatial resolution of the LKOF PIV measurements allows for the computation of gradient-based quantities like the vorticity or the swirling strength criterion.

12.6.3 Number and size of inputs

Reducing the number of sensors, as well as reducing the number of outputs, generally should make the training of the network simpler (lower order multiple input-multiple output regression). On the other hand, using less sensors may lead to a loss of valuable information about the flow, so a compromise has to be found. Single sensor configurations have been tested, i.e. either only vertical fluctuation velocity u_y or λ_{ci}, as well as combinations of two or three sensors.

The velocity component sensor s_1 is computed as an average in a five neighbouring pixels window. The swirling strength vortex identification input s_2 is defined from an ensemble of

n_1	**MSE Validation**	**Sensor choice**
50	0.065	[λ_{ci} , v]
90	0.085	v
105	0.3787	λ_{ci}

TABLE 12.1: Comparison of the validation data-set fit error obtained with a single velocity input, a single swirling strength input and their combination. Using the combination of the inputs minimises the MSE and the number of neurons.

velocity sensors included in a window: the sum of λ_{Ci} is computed over all the pixels in a $dx = 15$ pixels-wide window :

$$s_2 = \int_{y_1}^{y_2} \int_{x_1}^{x_2} \lambda_{Ci} dxdy \tag{12.10}$$

The height of the swirling strength window d_y has to be close to the thickness of the shear, so that the vortex activity can be properly monitored. A good compromise has been obtained with $dy = 0.5\ h$. The width of the swirling strength window also influences the quality of identification results. If it is too large, it creates an unnecessary smooth result, while if too small it can be too noisy, especially for gradient variables computed from experimental data. Finally, a window width of $d_x = 0.15\ h$ was used.

The SI error obtained using the different inputs separately or combined can be found in Table 12.1. One can see that the choice of the input(s) is indeed critical. Using a single swirling strength sensor leads to a large MSE (37.87%) together with a large number of neurons (105). Using a single velocity sensor as input reduces the MSE (8.5%) but still needs a large number of neurons (90). Finally, the best results are obtained with the combination of the two inputs: the MSE is minimum (6.5%) and the number of neurons is strongly reduced (50).

This result can be explained. Indeed, both sensors being placed inside the shear layer just after separation, they contain a lot of information. This region is rich in frequencies coming from the the initial receptivity and amplification process together with the shear layer instability. This is also a region where measurement noise coming from the PIV measurement will be maximum. Using both sensors helps the identification from the NN to be successful in separating the physical from the unwanted frequencies, leading to a strong improvement of the MSE fit (6.5%).

12.7 Results and discussion

12.7.1 Optimal NN identification procedure

The goal of the NN identification method is to predict at each time step n the POD coefficients $a_m(n)$ of the full field using local upstream sensors $s_j(n)$. The POD coefficients time-series have been calculated based on the PIV velocity fields. The sensors $s_j(n)$ were also monitored at the same time steps. The pairs $[a_m(n), s_j(n)]$ ($n = 1 : 4197$) is our identification data-set.

A FTDNN architecture has been chosen. Shallow and deeper LSTM architectures were also tested for this specific study without satisfying validation results. A possible explanation could be the spatial distance between the sensors and the dynamical structures to be predicted downstream which may requires a memory on the sensor side, not the output. Furthermore, the output comes from the decomposed field and thus contains significantly less frequencies than the sensor, which comes from the initial PIV data. That is because a POD

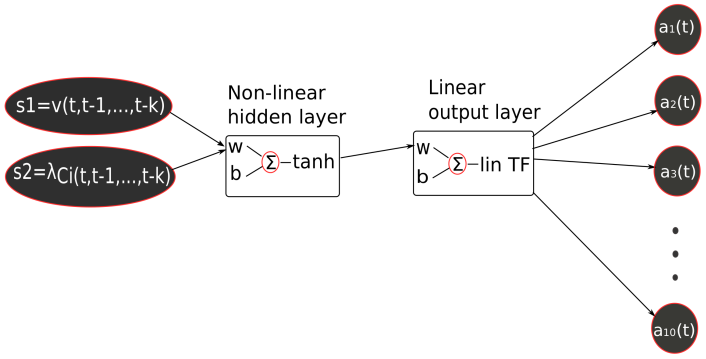

FIGURE 12.9: Structure of the optimal FTDNN non-linear mapping, with $j = 2$ inputs-sensors (velocity and λ_{Ci}), $k = 400$ steps of sensor memory (or 2.66 s), 1 hidden layer with $n_1 = 50$ neurons and $m = 10$ POD coefficients as outputs.

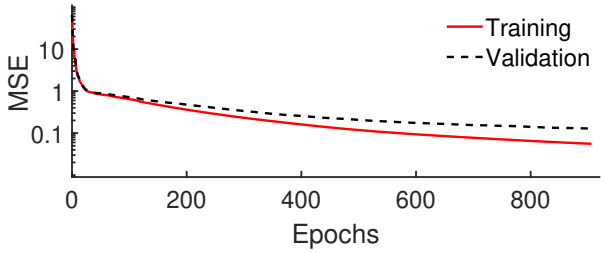

FIGURE 12.10: Training and validation MSE for each epoch of the training process.

introduces a filtering effect on the fields, while the shear layer specifically contains valuable high frequencies from the amplifying vortical structures.

Our objective was then to identify the optimal sensor-inputs s_j, the time delay k and the number of neurons in the hidden layer n_1. A basic scheme of the network is shown in Fig. 12.9. An anti-causal, zero phase, low-pass moving average (over four time-steps) filter has been applied to each pixel time-series, to reduce slightly the measurement noise. We mention that the cut-off frequency of the filter is more than 10 times the vortex shedding frequency. For all the NN calculations (training and validation) the MATLAB Deep Learning Toolbox was used Beale, Hagan, and Demut, 2018.

Network layer structure	2-50-10-10
Activation function	Hyperbolic Tangent
Loss function	MSE
Training method	Scaled Conjugate Gradient
Time-delay (s)	2.66

TABLE 12.2: Final choice for the optimal NN architecture and its training hyperparameters.

A NN should be as efficient as possible (according to the chosen criteria) and at the same time as simple as possible to easily check robustness and reduce computational time. Simplicity means minimising the number of layers and the number of neurons in each layer. The FTDNN networks tested used a tan-sigmoid transfer function and had a single hidden layer. In this case the NN is considered as “shallow".

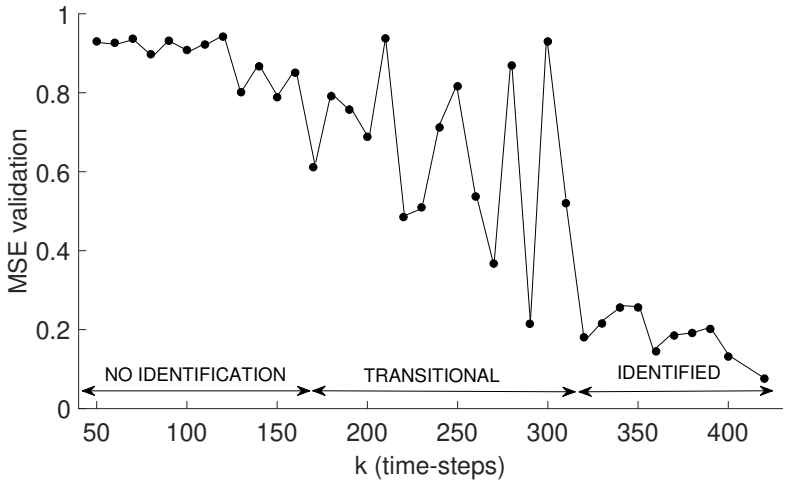

FIGURE 12.11: Evolution of the MSE as a function of the time-delay k in the sensor. Convergence is achieved for a memory size k higher than $n = 300$ time-steps.

The computational time for the training process, using a scaled conjugate gradient back-propagation algorithm, was of the order of $O(1)$ minute using a Intel Xeon E5-2630 CPU running at 2.2 GHz. The low computational time allowed a full parametric test to find the optimal time delay k for the input and the minimum number of neurons n_1 for the hidden layer.

For each NN architecture, the full data-set $[a_m(n), s_j(n)]$ $(n = 1 : 4197)$ has been divided into training (85% of snapshots), validation (10% of snapshots) and over-fitting check data-set (5% of snapshots). The third data-set is used to monitor if high over-fitting is observed during training. In this case the process is stopped immediately. As a common practice, the data-set is shuffled randomly before the beginning of the training process. It avoids bad models if the data are initially classified. It also makes fitting faster because neighbouring points are not similar. Block consecutive data-set division failed to give good fit results. We also mention, that a data standardisation was applied before the training process to help handling different inputs or outputs with different scales. Lastly, the weights and biases of the network are initialised randomly for the first epoch. No early stopping criterion has been used.

The number of neurons of the hidden layer n_1 was always changed iteratively, in order to find the optimal number leading to a minimisation of the mean-squared error (MSE). The same parametric study was carried out for the time-delay k, leading to a double loop parametric study from which the optimal combination of $[k, n_1]$ was found. The optimal number of neurons for the hidden layer was found to be $n_1 = 50$ and the best sensor time-delay corresponded to $k = 400$ time steps (2.66 s). A more detailed discussion about the time-delay parameter can be found below.

The results of the training performance as a function of the increasing epochs of the optimal architecture are shown in Fig. 12.10. 900 epochs were proved sufficient for a validation MSE lower than 10 % for all POD coefficients. The optimal architecture and training parameters are summarised in the Table 12.2. This simple shallow FTDNN architecture (see Fig. 12.9) avoids the complexity of deeper architectures which increases the computational time for the training process and the need for a large amounts of training data (Canziani, Paszke, and Culurciello, 2016), which are often difficult to obtain experimentally. This result verifies that shallow architectures can still provide satisfying results in many fluid mechanics applications (Srinivasan et al., 2019; Erichson et al., 2019; Tracey, Duraisamy, and Alonso,

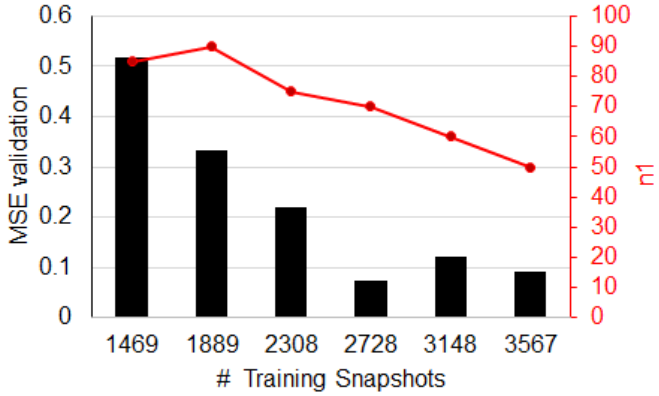

FIGURE 12.12: Network validation data-set performance as a function of the number of snapshots used for the training and the number of hidden layer neurons (n_1) used.

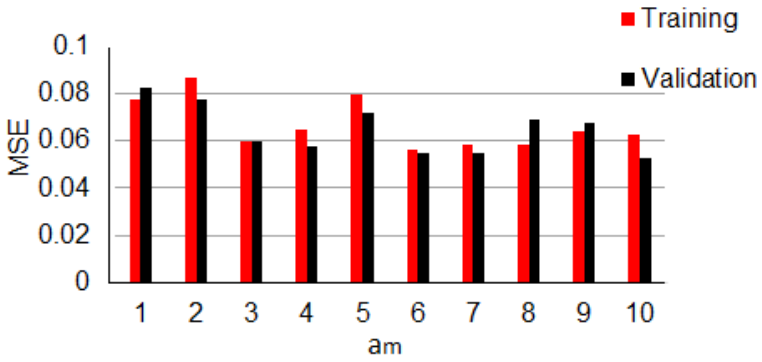

FIGURE 12.13: Training and validation MSE for each POD coefficient time series a_m.

2017).

12.7.2 Influence of the Time-Delay

The time-delay k in a FTDNN gives a notion of constant size memory in the sensors-inputs. It is crucial for the identification of downstream dynamics, while our sensors contain only information about the upstream dynamics in the Kelvin-Helmholtz instability region. The optimal time-delay in the inputs can be found through a parametric study whose objective is to minimise the MSE of the validation data-set, as shown in Fig. 12.11. Keeping a time delay of $k = 400$ steps or 2.66 s, we can achieve a validation fit error lower than 7%. This time-delay corresponds roughly to three oscillations of the 1st POD mode, which contains the highest amount of energy and corresponds to the Kelvin-Helmholtz vortex shedding.

The “memory" of these three events is crucial for the success of the algorithm. It explains why FTDNN with less memory or a standard feed-forward NN with zero time delay ($k = 0$) failed to identify the dynamics ($MSE > 90\%$). An intermediate transitional region with $k = 170$ up to $k = 300$ might actually give good identification results, but it strongly depends on the random weight-bias initialisation and random shuffling of data. Convergence is achieved only for $k > 300$ time-steps.

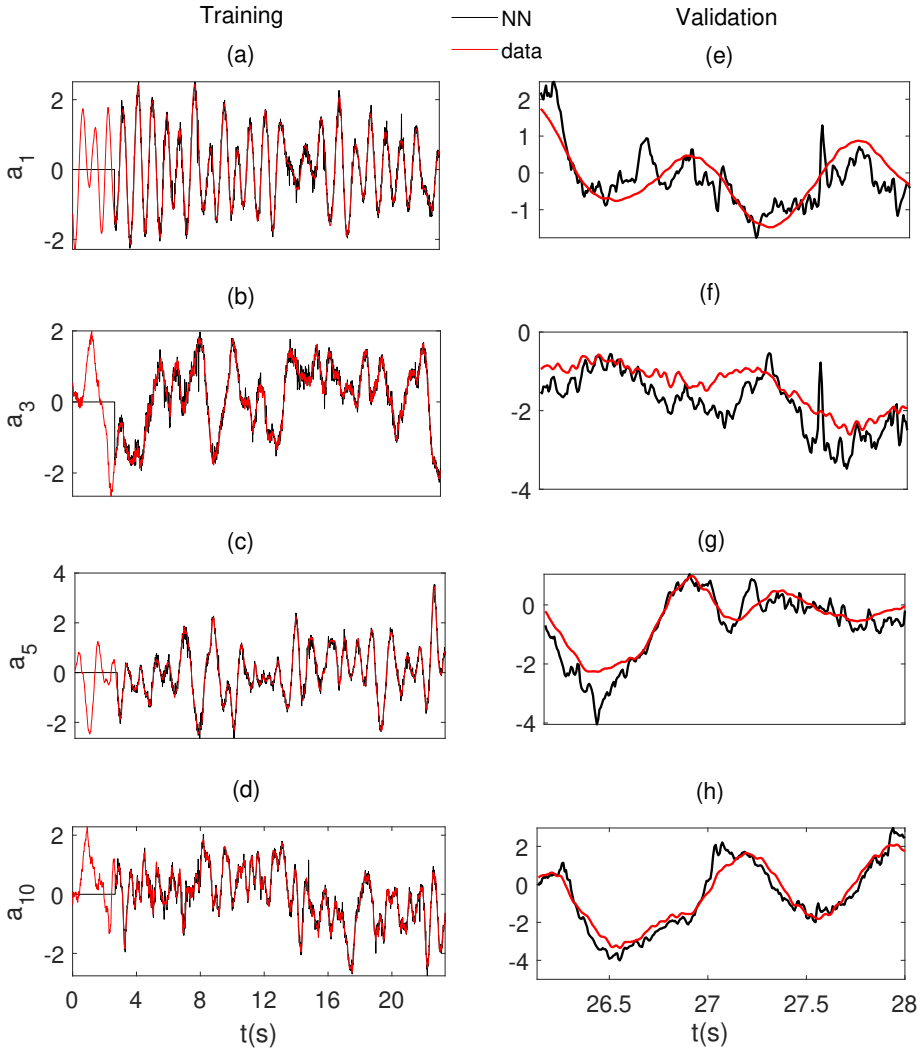

FIGURE 12.14: Comparison of the 1_{st} ,3_{rd}, 5_{th} and 10_{th} POD coefficient time-series obtained from experimental data with the ones obtained with NN for training (a, b, c, d) and validation (e, f, g, h) data-sets. The initial zero-response of the NN in the training data-set is due to the prediction time delay of the sensor.

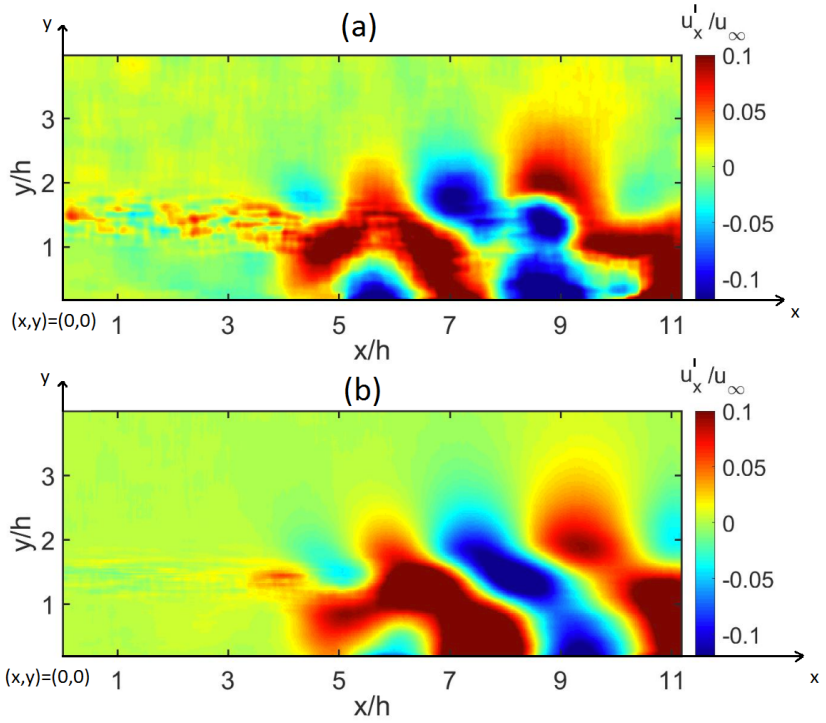

FIGURE 12.15: Comparison between experimental instantaneous streamwise fluctuation velocity field (a) and NN-reconstructed fields (b) using the double visual sensor and optimal NN architecture with $n_1 = 70$ neurons in the hidden layer and $N = 2728$ training snapshots. Movie online.

12.7.3 Influence of the size of the training data-set

As expected for any data-driven method, the more information is given to the machine the better. It will figure out more easily the optimal weights and biases for the mapping we ask it to perform. In Fig. 12.12 we can see that decreasing the number of snapshots used for the training of the network leads to an increase of the number of neurons in the hidden layer for an equivalent validation error (keeping a constant time-delay of $k = 400$ time steps). Below a given number of learning snapshots, increasing the number of neurons does not help. It just introduces over-fitting, and hence increases the validation error. The BFS flow PIV experiment for $Re_h = 1385$ is dominated by the vortex shedding frequency (more than 40% of energy in the first two POD modes). Comparing the number of events (or oscillations) with the accuracy of the identification shows that to obtain a MSE lower than 10% we need least 20 events to train the network.

12.7.4 Reconstruction of the instantaneous velocity fields

In Fig. 12.13 we present the MSE fit results of 10 POD coefficients, using the optimal architecture. We can see that the MSE for each POD coefficient is equivalent for all the coefficients at both training and validation, which proves we avoided over-fitting. In Fig. 12.14 we also present the time-series of four POD coefficients, as measured from the experiment compared with the time-series obtained in the training step (a-d) and in the validation step (e-h). We used for this figure a training data-set of $N = 2728$ snapshots, with two visual sensors and the NN using $n_1 = 70$ neurons in the hidden layer and $k = 400$ time-steps sensor delay. Both training and validation time-series are found in good agreement.

Projecting the NN-predicted POD coefficients a_m to the POD modes Φ_m allows the reconstruction of the instantaneous fluctuation velocity fields of all time steps of the validation data-set. It is then possible to compare the predicted velocity field with the real experimental fields. The instantaneous experimental velocity field is compared to the one reconstructed with the optimal double visual sensor information as shown in Fig. 12.15 and corresponding video. One can see that most of the main features of the BFS flow are recovered with correct amplitudes and spatial organisation throughout the velocity field. Some smaller structures in the shear layer have reduced amplitude, due to the 80% energy threshold used during the time-resolved field decomposition, as well as the NN identification process error itself.

12.8 Conclusions and perspectives

A successful application of a NN System Identification method to a time-resolved PIV experiment of a typical noise-amplifier flow has been presented. We were able to predict with satisfying precision the global dynamics of the flow (in the form of POD coefficients), using visual sensors coming from local velocity measurements. A shallow FTDNN architecture was sufficient to recover the overall dynamics of the flow. There was no need for sophisticated LSTM gates or more than one hidden layers, which would increase the training complexity and the computational time.

This demonstrates the feasibility to reduce the order of such fluid systems from $O(10^6)$ (for typical LKOF PIV measurements) to only a handful of useful variables, which is crucial for control purposes. The final NN architecture allows us to predict the dynamics of the flow using local, upstream visual probes, without the need for time-consuming full-field decomposition analysis or intrusive measuring devices like hot-wires or Pitot tubes. It was demonstrated that the combination of the swirling strength and local velocity inputs leads to a satisfying training and validation fit when comparing the POD coefficient time-series, even though these sensors were located in a high-gradient and difficult to measure region of the flow (early in the receptivity-amplification process of the noise-amplifier). The accuracy of the method was also demonstrated through the reconstruction of the predicted instantaneous velocity fields. The NN training process was found to be very fast on a standard desktop computer ($O(1)$ minutes). The double sensor approach is simple and fast to compute and is ideal for a model-free closed-loop control scheme, like in Gautier et al., 2015; Li et al., 2017, with the objective to reduce the turbulent kinetic energy of the flow.

Because of its accuracy and its computational efficiency, the Re_h number could also be integrated as an input, while the output could include POD coefficients from the different Re_h numbers, making it even more useful for flow control purposes (San, Maulik, and Ahmed, 2018). Distributed sensors, upstream and/or downstream, could also help achieve this complicated task. A larger number of POD modes could be included for more precise representation of the initial experimental data-set as well. Reinforcement learning could also be a key factor for the robustness of the NN when experiment parameters, like Re_h number vary greatly.

Chapter 13

Control of the BFS flow

The BFS flow is a first simplistic but fundamental model of a shear flow that appears in the wake of vehicles (Gautier and Aider, 2014). Hence, its successful control can give important insights on drag reduction for vehicle aerodynamics applications. Control strategies can be divided in open and closed loop.

Passive or open-loop control strategies are generally attempted before searching for more complex means of control, and can shed more light in the dynamics of the flow as well. Passive control strategies regard on changing boundary conditions of the flow without the use of a sensor. Hence, monitoring cannot be achieved in case of changing of the flow conditions. Active control consists in adding momentum/energy into the flow to modify its characteristics using an actuator. A fundamental difference is also the fact that a sensor component is required to monitor the state of system. They are more robust but complicated and expensive; that is why they are rarely integrated in civilian vehicle applications (Heinz, King, and Gölling, 2010). The opportunity of open loop control is to design a robust but cheap way to reduce drag or control vehicle dynamics, so that civilian applications could broadly install it. This could help reduce the $C0_2$ emissions as demanded by recent European Union regulations (Parliament and EU, 2013). Various control strategies have been tested in the past for such applications. For example, Godart and Stanislas (Godard and Stanislas, 2006; Godard, Foucaut, and Stanislas, 2006), used passive vortex generators are used to control a decelerating boundary layer. In Aider et al. (Aider, Beaudoin, and Wesfreid, 2010) active vortex generators (trapezoidal tabs) in order to reduce the drag of a 3D bluff body.

Two effects contribute to the total drag of a body: skin friction and pressure loses, and at high *Re* separated flows the pressure is the dominant term. Hence, the reduction of the recirculation bubble and the increase of pressure recovery is of great importance, although the relationship between the 2 remains complex. Beaudoin et al.(Beaudoin et al., 2004b) showed that while the drag is monotonously increasing with the *Re* number, this is not the case for the recirculation length or recirculation area. This could be attributed to the 3D nature of the flow and the different phenomena that occur in the normal plane. Hence, there are hints that there is no guarantee that reducing the recirculation area reduces the drag (Dahan, Morgans, and Lardeau, 2012b). To shed more light in the 3D aspect of the recirculation bubble , the horizontal plane xz direction (streamwise-spanwise) was chosen in this study to perform PIV as seen in figure 11.23. The third direction is studied by scanning numerous wall-normal planes from $y = [0.2 : 0.2 : 1]\ h$, as seen in figure 11.1.

It has been proven that controlling the BFS flow could be effective when placing pulsating jet actuators on the wall before the step (Gautier and Aider, 2014; Gautier et al., 2015). Such actuators are quite easy to implement and remain the simplest way to effect actuation in a dense fluid such as water. The coexistence of jets in cross-flows are found in various natural and industrial processes such as air injection in gas turbines, thrust vector control for high speed vehicles and exhaust plumes for power plants, hence making their study even more relevant to industry (Karagozian, 2010; *Fifty years of jet in cross flow research* 1993). Past researchers in the laboratory of PMMH have performed rigorous studies regarding the effect

of jets on a cross-flow (Beaudoin et al., 2004b; Duriez, Aider, and Wesfreid, 2009; Cambonie, 2012).

Particularly, Gautier et al, using genetic programming closed-loop control and a spanwise-invariant jet, managed to reduce the size of the recirculation area by 80%. Such a closed-loop control system required one week of continuous experiments in order to find the optimal control law; apart from that, closed-loop control can be quite costly and complicated to integrate in a lot of engineering applications. Given the fact also that since a Re_h number of down to $Re_h = 400$ the BFS flow has a 3D nature due to the presence of streaks, spanwise distribution of jets should be considered and 3D jet structures should be created to control such a flow. The jet-slot size is key and was designed in the same lengthscale as the streaks observed, as presented in the next paragraph.

13.1 Open-loop control using spanwise-distributed jets

The work presented in this manuscript features wall jets as actuators. The reason for this is twofold: wall jets are relatively easy to implement and remain the simplest way to effect actuation in a dense fluid such as water. Furthermore, this work was part of a broader research effort by the instability, control and turbulence team at PMMH. Following a study regarding jet-cross-flow interactions made during the thesis of Cambonie, 2012, an optimal 3D jet distribution was chosen to apply an open-loop control scheme in the BFS flow. The jet is supplied by a pressurised water tank at 2 bars maximum, monitored by a SMC ITV 1010 electro-pneumatic regulator to control the jet frequency $f_{forcing}$ and amplitude $U_{forcing}$. The frequencies checked were $f_{forcing}$ =[1:1:5] Hz, with a duty cycle of 50 % and an amplitude of to 2 Volts max. This corresponded to a jet exit velocity of 0.3 U_{inf}.

The schematic of this jet distribution is presented in figure 13.3, where $\theta = 45\ deg$ and the number of slots was N=22. The distance was chosen $\alpha = 7mm$. The distance between each slot pair was chosen as the average of the streak spanwise size for $Re_h = 1960 - 3080$, as presented in the Fourier scales study presented in figure 11.12; nonetheless we mention that various different configurations have been also tested in the past (Cambonie, 2012). The selected configuration though has been shown to develop the primary longitudinal vortex arms as well as some secondary inner auxiliary arms. The latter tend to be intense but vanish much quicker; The primary vortex arms though have a strong long lasting effect on the boundary layer (Cambonie, 2012). A volumetric PIV analysis of a single pair of slots by Cambonie, 2012 shows the development of these arms in the presence of a laminar boundary layer, as presented in figure 13.1. The development of these arms in the streamwise distance from the exit slot can be seen in figure 13.2. We mention again that multiple horizontal planes were used to calculate the mean recirculation bubble volume for $y = [0.2 : 0.2 : 1]\ h$, as seen in figure 13.5. That way we are sure of the spatially accurate measurement of the back-flow region under the streak spanwise modulation, which is not the case if we measure only the vertical middle-plane xy.

13.2 Results

For the five horizontal planes scanned up to $y = h$, the RA (or back-flow region) is calculated using the following definition of negative streamwise velocity component:

$$A_r(t) = \iint H(-u_x(t,x,z))dxdz \tag{13.1}$$

, where H is the Heaviside function. The Re_h number for the results presented below is is $Re_h = 1960$. Keeping the jet amplitude constant, the optimal frequency to reduce the

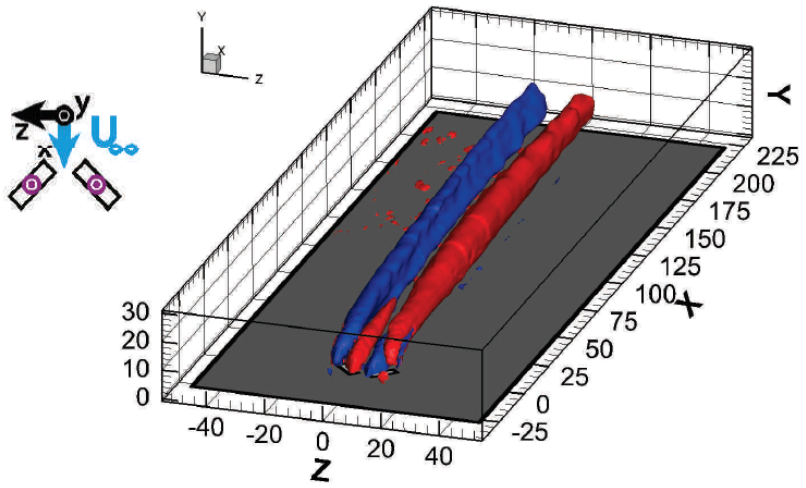

FIGURE 13.1: Isosurfaces of vortex swirling strength criterion of a single pair of slots of the selected jet configuration, and its interaction with a laminar boundary layer. Robust primary and unstable secondary vortex arms are observed. Plot from Cambonie, 2012.

recirculation bubble was found at 1 Hz, very close to the shedding frequency of the K-H rolls as presented in figure 11.18. The final maximum total relative reduction of the recirculation bubble with this simple control law was 64%. This can be seen in figure 13.4, where the total RA in the spanwise direction taken into account, not just one vertical plane which would be misleading. A volume reconstruction of the recirculation bubble from the multiple planes scanned before and after the pulsating jet control activation can also reveal this reduction as seen in figure 13.5. Furthermore, the isosurface results of streamwise velocity equal to -0.5 % the free-stream velocity are indicative of the recirculation bubble size, since the back-flow region is a region of negative streamwise velocity component. The controlled and uncontrolled isosurfaces for 1 Hz pulsating jets can be found in figure 13.6. The scheme was found robust up to $Re_h = 3080$, although more experiments are needed to test the robustness in higher Re numbers.

13.3 Conclusions and Perspectives

With sole resources a 2D-2C PIV system, without stereo nor volumetric PIV we present a method to study meticulously the full volumic rescirculation bubble, including the spanwise modulation of the 3D nature of the flow. An open-loop control system of pulsating jets at low frequencies was implemented to reduce the volume of the recirculation bubble. The jets were three-dimensional and distributed along the spanwise direction, upstream of the step.

The correct preparation of the incoming flow with this jet-cross flow boundary layer interaction led to a relative mean reduction of the recirculation bubble of 64% , a reduction which was calculated precisely taking into account the volume of a bubble and not only a vertical plane projection of it. Further parametric studies should be carried out to explore more control laws varying the frequency and amplitude of the jets; a genetic programming algorithm could be useful to scan optimally this parametric space and make the control strategy robust for a larger range of Re_h numbers. Nonetheless, the obtained result is quite impressive since using an open-loop method, we are approaching similar RA reduction results of a costly and complex closed-loop control methods achieved by genetic programming closed-loop control in the same setup , which was 80 % (Gautier et al., 2015).

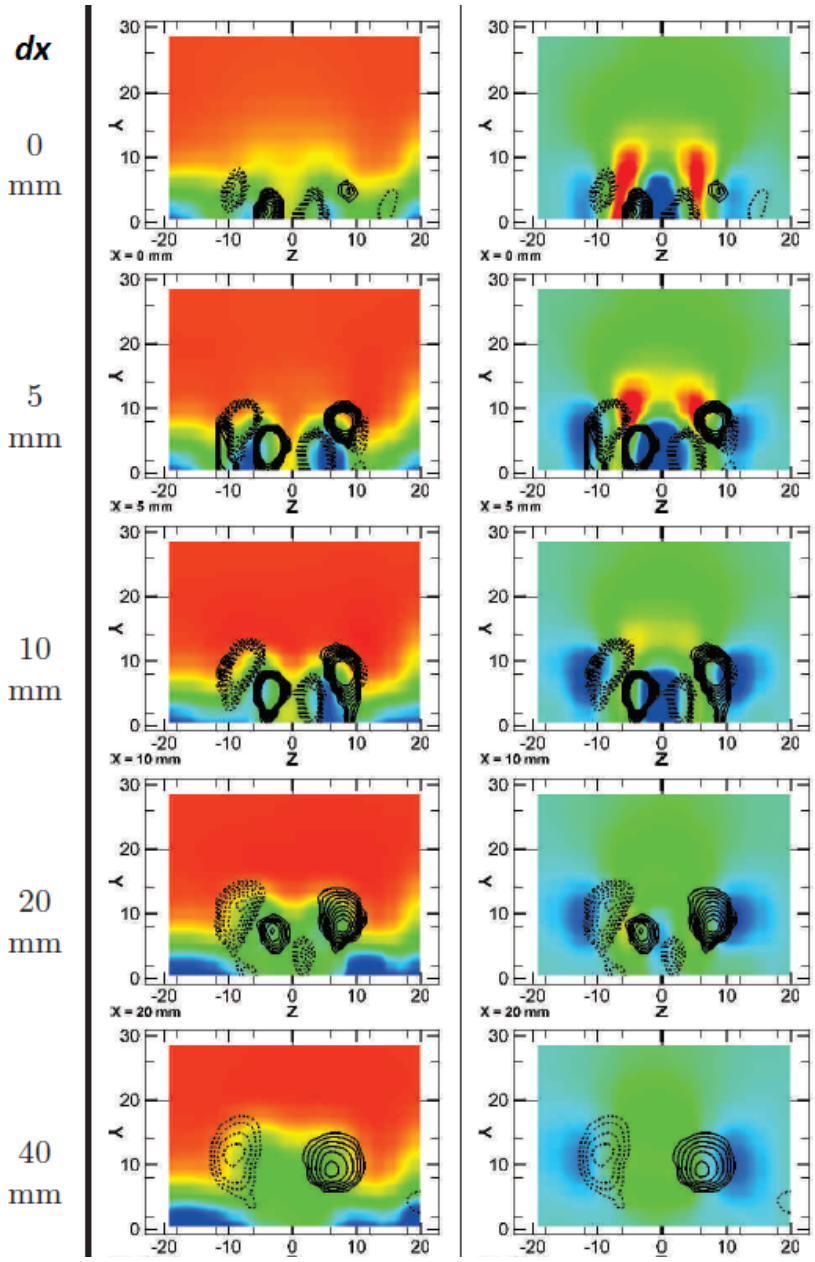

FIGURE 13.2: Horizontal and vertical velocity components of the jet-boundary layer superposition in the spanwise-wall normal plane, as a function of the streamwise distance *dx* from the jet exit. Development of primary arms, birth and death of inner auxiliary jet arms. Plot from Cambonie, 2012

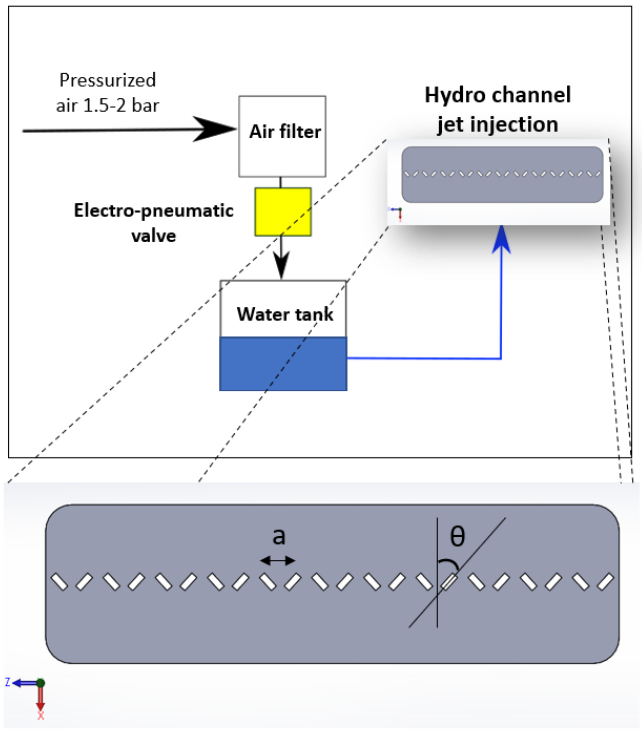

FIGURE 13.3: Synthetic jet scheme using a pressurised water tank. Jet distribution design.

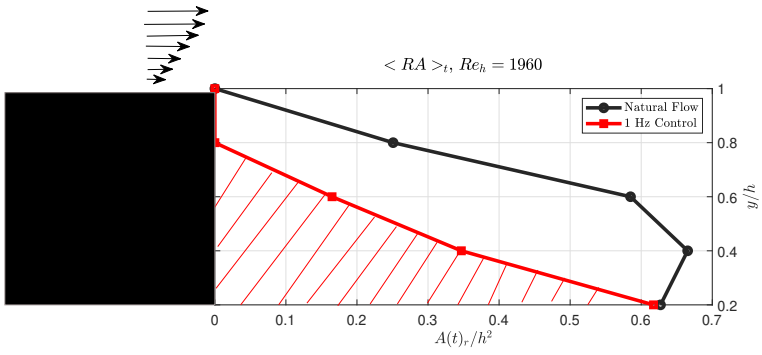

FIGURE 13.4: Recirculation bubble volume before and after pulsating jet control. This plot integrates information from all the span of the step and thus show a much better representation of the full recirculation bubble reduction.

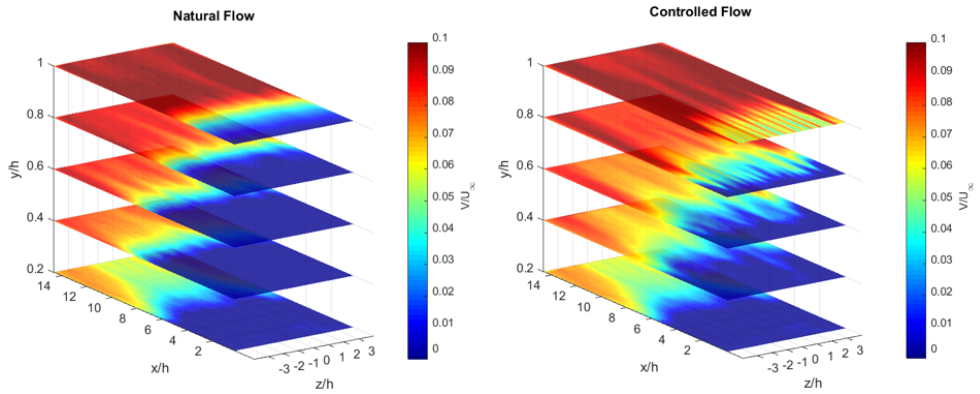

FIGURE 13.5: Time-averaged streamwise velocity component. Natural and controlled flow for 1 Hz pulsating jets. Dark blue regions correspond to the back-flow area.

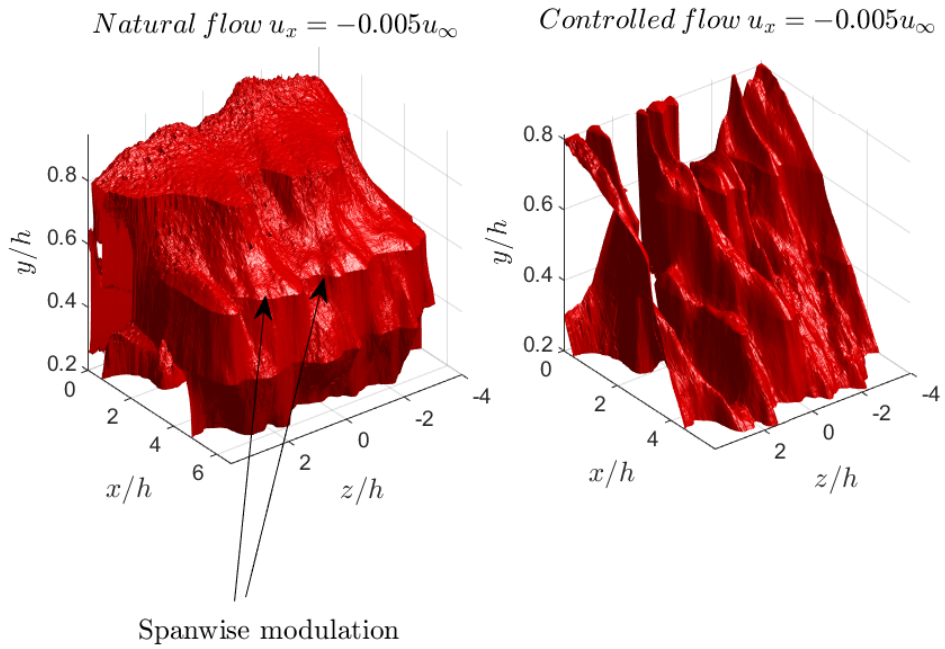

FIGURE 13.6: Velocity isosurfaces of negative velocity as an indication of the reduction of the total 3D recirculation bubble volume. Signature of the streak spanwise modulation of the flow appears in the natural flow; traces of this signature remain also after the control of 1 Hz pulsating jets is applied.

Nonetheless, in the present setup studying the streamwise-spanwise plane poses some important difficulties: The vertical position of the laser for the horizontal measurements poses stability problems in the NORCAN aluminum structure that it is installed. The small size of the step (1.5 *cm*) makes it difficult to be submilimetrically precise in the y position we set the plane to, due to the thickness of the laser sheet, which is around 1 *mm*. A setup with a larger step size would help scan more precisely more horizontal planes in the wall-normal direction. Volumetric PIV results could give access also to more accurate recirculation bubble size measurements and an important comparison with this 2D-2C PIV 3D reconstruction method. A work in progress is also underway to verify the robustness of the method for Re_h numbers higher than $Re_h = 3080$.

Part V

General conclusions

Chapter 14

Summarized thesis results

Optical Flow has been used by the fluid mechanics community as a velocimetry system more than 20 years less than Cross-Correlation PIV and for far fewer case studies. The present thesis regarded an integrated journey of an Optical Flow Velocimetry system in various benchmarking cases and novel applications.

The full development of an Optical Flow velocimetry system was described: its software (algorithm, GUI) and hardware parts (camera, workstation, laser synchronisation). The development took place in collaboration with the R & D team of Photon Lines; all the hardware components, together with the velocimetry algorithm coded in CUDA functions, were integrated in the software platform called Eyemotion, leading to a compact system with optimised data flow. Novel benchmarking test cases described in the present thesis showed its great potential for the application on turbulent flows; the gradients of the velocities were better resolved than state-of-the-art Cross-Correlation PIV, with an order of magnitude lower computational time on top of that. It was emphasised that the real-time computational frequency of the velocity fields can reach more than 100 fields per second, depending on the image size and PIV parameters. Moreover, it was shown that saving up to 50 % of disk space can be achieved as well during a PIV experiment, since the developed system has an innovative integrated option: the user is able to save velocity fields without saving the images.

Understanding turbulence is of uttermost importance for the optimisation of engineering applications in the transportation and energy industry. Such a precise velocimetry system, along with a large camera sensor, was proven that can give access to the study of small turbulent scales, down to sub-Kolmogorov range and reconstruct precisely the pressure and acceleration terms, for the case of a turbulent wake of a bluff body. More precisely, Optical Flow was proven successful to calculate the total budget of the Turbulent Kinetic Energy transport equation of the same flow using only 2D-2C PIV snapshots, with an impressive achieved error of less than 10 % in the wake region. Hence, these results aim towards highlighting the importance of the maximisation of the information we can gain from experiments, when studying turbulent flows. This methodology could have a great impact on the study of complex flows that are often difficult or impossible to simulate with Direct Numerical Simulations.

Furthermore, novel machine-learning tools were presented in order to reduce the order of large and complicated dynamical systems of turbulent flows. Such methods do not require previous knowledge of equations of a system, but solely require large amounts of data, which the proposed rapid Velocimetry system and an optimized experimental setup can provide easily today. These studies can be extremely useful for applications where simple diagnostic tools have to be implemented, in order to quickly monitor the state of a complex fluidic system, without complicated measurements that are often impossible to access anyway. The presented methods regarded two fundamental turbulent flows: the flat-plate turbulent Boundary Layer and the Backward-Facing Step flow for Re number up to $Re_h = 3090$. A handful of simple velocity sensors were placed near walls and optimal shallow neural networks were discovered and successfully trained; the flow dynamics were correctly correlated with the

sensors and the system order was reduced from order O(10) to O(1). Instantaneous velocity fields were successfully reconstructed as well. The simplicity and robustness of these methods, together with the low training time of the neural network (a few minutes), show great potential for their integration in modern engineering applications, and can potentially play an important role for the reduction of the CO_2 emissions of ground vehicles and aeroplanes, in accordance with the EU regulations (Parliament and EU, 2020).

Last but not least, the physics of the 3D instability of Backward-Facing Step flow, was described and studied using 2D-2C PIV and scanning multiple horizontal planes. A 3D reconstruction of the recirculation bubble volume was performed, and its relative reduction of 64 % was achieved using an upstream, pulsating jet, open-loop control strategy.

To summarise, the general conclusion of the present thesis comes down to the successful development and benchmarking of a promising Optical Flow Velocimetry system: sub-Kolmogorov turbulent scales were resolved, modern machine learning techniques were tested, instability and control studies were performed. A full journey of the exploitation of this system is now completed, but many more journeys are now to be explored.

Chapter 15

Conference participation list and related publications

During this fruitful thesis, i had the privilege of taking part in the following conferences with oral presentations, particularly:

- A. Giannopoulos, P.Chatelier, J-L Aider. A dense PIV system: a solution for rapid data assimilation. 3rd Workshop and Challenge on Data Assimilation &CFD Processing for PIV and LPT, Nov 2020, PARIS (en virtuel), France. pp.9 - 10. ffhal-03017749f.
- A. Giannopoulos, J.L.Aider, System identification using neural networks, GDR Flow separation control worksop, 20-21/11/19, ENSAM , Paris
- A. Giannopoulos, Prediction of the dynamics of noise-amplifier flows using Artificial Neural Networks, Laboratoire de Physique Statistique de l'Ecole Normale Superieure, group seminar organised by Professor A.Alexakis, 13/11/2019, Paris
- A. Giannopoulos, J.L. Aider. System identification using Neural Networks applied to experimental noise-amplifier flows characterized by real-time optical flow velocimetry. 17_{th} EUROPEAN TURBULENCE CONFERENCE (ETC17), Sep 2019, Torino, Italy.
- A. Giannopoulos, J.L. Aider, Neural Network System Identification in Noise-Amplifier Flows: an experimental study using Optical-Flow PIV, laboratory seminar of PMMH laboratory, 11/7/2019,Paris.
- A. Giannopoulos, J.L. Aider. Neural network system identification in noise-amplifier flows: an experimental study using optical-flow PIV data. 15_{th} International Conference on Fluid Control, Measurements and Visualization, 5/2019, Naples, Italy.

The list of workshops and summer/winter schools i had the chance to attend can be found below:

- Group De Recherche (GRD) Workshop in flow separation control ,France,19-20/11/2020
- Programming and Tuning Massively Parallel Systems + Artificial Intelligence summer school,25-29/6/19, BSC, Barcelona, Spain
- GDR Workshop in flow separation control, IMFT, Toulouse,France,8-9/11/2018
- Ethics and Integrity of scientific research, Sorbonne University(8h), 10/2018, Paris
- La Vision Particle Image Velocimetry Training (8h) : DaVis 10 software for intelligent imaging
- Workshop in Aerodynamics and Aeroacoustics of terrestrial vehicles (8h), CNRT-R2A, ONERA - Centre de Meudon, Paris, 6/6/2018

- Introduction to CUDA programming(40h) , Barcelona Supercomputing Center, Barcelona, Spain, 16-20/4/2018
- Ultra High Dynamic Range Imaging: latest advances of this rapidly evolving technology (14h) from some of the most influential HDR imaging leaders, 7-8/12/2017, Paris

The list of publications co-authored is found below:

- A.Giannopoulos, P.Y.Passaggia, N.Mazellier, J.L.Aider, Pressure reconstruction in turbulent flows : a comparative study between optical flow and cross-correlation for turbulent flows, to be submitted in Physical Review Fluids, 2021
- A.Giannopoulos, P.Y.Passaggia, N.Mazellier, J.L.Aider, On the optimal window size in optical flow and cross-correlation in particle image velocimetry :
  Application to turbulent flows, to be submitted in Experiments in fluids, 2021
- A.Giannopoulos, J.L. Aider, Data-driven order reduction and velocity field reconstruction using neural networks: The case of a turbulent boundary layer,featured article, Phys. Fluids 32, 095117 (2020); https://doi.org/10.1063/5.0015870
- A. Giannopoulos, J-L Aider: Prediction of the dynamics of a backward-facing step flow using focused time-delay neural networks and particle image velocimetry datasets, International Journal of Heat and Fluid Flow, Volume 82.
- A.Giannopoulos, J. Guzman, E.Varon, D.Sipp, P.Schmid, J.L.Aider , Experimental application of a dynamic observer to predict the transient boundary layer dynamics (considered to be submitted in Journal of Fluid Mechanics)
- A.Giannopoulos, J.-L.Aider, Observation of turbulent spots in a Backward-Facing Step flow (to be submitted in Physical Review Fluids)

I mention also that a series of non-scientific obligatory courses are demanded by the doctoral school; during the duration of the thesis i followed 90 hours of spanish language courses under Professor Isabela Hojman Prati of the Consorcio ELSE, and have successfully passed the official exams of level B1.1. Furthermore, i had the change to participate as well in the supervision of three internships of engineering students in the laboratory of PMMH, particularly:

- J.S.Pimienta, M2 Fluid mechanics, ENSAM Paris. Subject: Evaluation and benchmarking of Optical flow algorithm for scientific applications. 1/3/2020-31/8/20
- Simon Calonne, 5_{th} year of SUPAERO engineering school. Subject: Evaluation of acoustic actuators and genetic-programming closed loop control. 5/2019-6/2019.
- Soufiane Cherroud, 5_{th} year of SUPAERO engineering school, Subject: Characterisation of Backward -facing step flow using 2D2C Optical flow PIV measurements

Last but not least, since 2 years i have been a reviewer for the following journals:

- Physics of fluids (American institute of Physics)
- Journal of Physics: Conference Series
- Conference on Computer Science and Application Engineering

Bibliography

Adelson, Edward et al. (Nov. 1983). "Pyramid Methods in Image Processing". In: *RCA Eng.* 29.

Adrian, Ronald J. and Parviz Moin (1988). "Stochastic estimation of organized turbulent structure: homogeneous shear flow". In: *Journal of Fluid Mechanics* 190, pp. 531559. DOI: 10.1017/S0022112088001442.

Aider, J. L., J. F. Beaudoin, and J. E. Wesfreid (2009). "Drag and lift reduction of a 3D bluff-body using active vortex generators". In: *Exp.in Fluids* DOI 10.1007/s00348-009-0770-y, pp. 491–501.

Aider, J.-L. et al. (2001). "Experimental and numerical investigation of the flow around a simplified vehicle model". In: *Proc. Third MIRA International Vehicle Aerodynamics Conference*. Rugby, England.

Aider, J. L. et al. (2014). "Active flow control using pulsed micro-jets on a full-scale production car". In: *Int. J. of Flow Control* 6.1, pp. 1–20.

Aider, Jean-Luc, Jean-François Beaudoin, and José Eduardo Wesfreid (2010). "Drag and lift reduction of a 3D bluff-body using active vortex generators". In: *Experiments in Fluids* 48. ISSN: 1432-1114.

Aider, Jean-Luc, Alexandra Danet, and Marcel Lesieur (2007). "Large-eddy simulation applied to study the influence of upstream conditions on the time-dependant and averaged characteristics of a backward-facing step flow". In: *Journal of Turbulence* 8, N51. DOI: 10.1080/14685240701701000. URL: https://doi.org/10.1080/14685240701701000.

Armaly, B. F. et al. (1983). "Experimental and theoretical investigation of backward-facing step flow". In: *J. Fluid Mech.* 127, pp. 473–496.

Baldi, Pierre and Kurt Hornik (1989). "Neural networks and principal component analysis: Learning from examples without local minima". In: *Neural Networks* 2.1, pp. 53 –58. ISSN: 0893-6080.

Barkley, Dwight, M. Gabriela M. Gomes, and Ronald D. Henderson (2002). "Three-dimensional instability in flow over a backward-facing step". In: *Journal of Fluid Mechanics* 473, pp. 167190. DOI: 10.1017/S002211200200232X.

B.Burl, Jeff (1998). "Linear Optimal Control : H(2) and H (infinity) methods". In: Addison-Wesley Longman Publishing Co.

Beale, Mark Hudson, Martin T. Hagan, and Howard B. Demut (2018). "Deep Learning Toolbox User's Guide". In:

Beaudoin, J. F. et al. (Nov. 2004a). "Cavitation as a complementary tool for automotive aerodynamics". In: *EIF* 37.5, pp. 763–768.

Beaudoin, J.-F. et al. (2004b). "Three-dimensional stationary flow over a backwards-facing step". In: *Eur. J. Mech.* 38, pp. 147–155.

Beaudoin, Jean-François (2004). "Contrôle actif d'écoulement en aérodynamique automobile". Thèse de doctorat dirigée par Rouchon, Pierre et Wesfreid, José Eduardo Mathématique et automatique Paris, ENMP 2004. PhD thesis, 1 vol. (202 p.)

Beneddine, Samir et al. (2016). "Conditions for validity of mean flow stability analysis". In: *J.Fluid Mech.* 798, pp. 485–504. DOI: 10.1017/jfm.2016.331.

Beneddine, Samir et al. (2017). "Unsteady flow dynamics reconstruction from mean flow and point sensors: an experimental study". In: *Journal of Fluid Mechanics* 824, pp. 174201. DOI: 10.1017/jfm.2017.333.

Beneitez, Miguel et al. (2019). "Edge tracking in spatially developing boundary layer flows". In: *Journal of Fluid Mechanics* 881, pp. 164181. DOI: 10.1017/jfm.2019.763.

Bengio, Y., P. Simard, and P. Frasconi (1994). "Learning long-term dependencies with gradient descent is difficult". In: *IEEE Transactions on Neural Networks* 5.2, pp. 157–166.

Benjamin, Thomas Brooke (1978). "Bifurcation phenomena in steady flows of a viscous fluid. I. Theory". In: *Proceedings of the Royal Society of London. A. Mathematical and Physical Sciences* 359.1696, pp. 1–26. DOI: 10.1098/rspa.1978.0028. eprint: https://royalsocietypublishing.org/doi/pdf/10.1098/rspa.1978.0028. URL: https://royalsocietypublishing.org/doi/abs/10.1098/rspa.1978.0028.

Berkooz, Gal and Edriss S. Titi (1993). "Galerkin projections and the proper orthogonal decomposition for equivariant equations". In: *Physics Letters A* 174.1-2, pp. 94–102.

Blackburn, H., Dwight Barkley, and Spencer Sherwin (May 2008). "Convective instability and transient growth in flow over a bakward-facing step". In: *Journal of Fluid Mechanics* 603, pp. 271 –304. DOI: 10.1017/S0022112008001109.

Borée J., J. (2003). "Extended proper orthogonal decomposition: a tool to analyse correlated events in turbulent flows". Undetermined. In: *Experiments in Fluids* 35.2, pp. 188–192. DOI: 10.1007/s00348-003-0656-3.

Cai, S. et al. (2020). "Particle Image Velocimetry Based on a Deep Learning Motion Estimator". In: *IEEE Transactions on Instrumentation and Measurement* 69.6, pp. 3538–3554. DOI: 10.1109/TIM.2019.2932649.

Cai, Shengze et al. (Aug. 2019). "Particle Image Velocimetry Based on a Deep Learning Motion Estimator". In: *IEEE Transactions on Instrumentation and Measurement* PP, pp. 1–1. DOI: 10.1109/TIM.2019.2932649.

Camassa, Roberto et al. (2018). "Experimental investigation of nonlinear internal waves in deep water with miscible fluids". In: *J. Ocean Eng. and Marine Ener.* 4.4, pp. 243–257.

Cambonie, Tristan (2012). "Etude par vélocimétrie volumique d'un jet dans un écoulement transverse à faibles ratios de vitesses". Thèse de doctorat dirigée par Aider, Jean-Luc Mécanique des fluides Paris 6 2012. PhD thesis, 2 vol. (523 p.) URL: http://www.theses.fr/2012PA066606.

Cambonie, Tristan and Jean-Luc Aider (2014). "Transition scenario of the round jet in cross-flow topology at low velocity ratios". In: *Physics of Fluids* 26.8, p. 084101. DOI: 10.1063/1.4891850. eprint: https://doi.org/10.1063/1.4891850. URL: https://doi.org/10.1063/1.4891850.

Canziani, Alfredo, Adam Paszke, and Eugenio Culurciello (May 2016). "An Analysis of Deep Neural Network Models for Practical Applications". In:

Carlier, J (2005). "Second set of fluid mechanics image sequences. In: European Project Fluid image analysis and description, FLUID (2005)," in: *FLUID*. URL: http://www.fluid.irisa.fr/.

Chakraborty, P., S. Balachandar, and R. J. Adrian (2005). "On the relationships between local vortex identification schemes". In: *Journal of Fluid Mechanics* 535, pp. 189–214. DOI: 10.1017/S0022112005004726.

Champagnat, F. et al. (2011). "Fast and accurate PIV computation using highly parallel iterative correlation maximization". In: *Experiments in Fluids* 50, pp. 1169–1182. DOI: 10.1007/s00348-011-1054-x.

Charaniya, N.A. and Sanjay Dudul (Nov. 2012). "Focused Time Delay Neural Network Model for Rainfall Prediction Using Indian Ocean Dipole Index". In: pp. 851–855. ISBN: 978-1-4673-2981-1. DOI: 10.1109/CICN.2012.116.

Chen, S., S.A. Billings, and P.M. Grant (1990). "Non-linear system identification using neural networks". In: *Neural Networks* 51.6. DOI: 10.1080/00207179008934126.

Chomaz, J. M. (2005). "Global instabilities in spatially developing flows: non-normality and nonlinearity". In: *Annu. Rev. Fluid Mech.* 37, pp. 357–392.

Chong, M.S., A.E. Perry, and B.J. Cantwell (1990). "A general classification of 3-dimensional flow fields". In: *Physics of Fluids* 2, pp. 765–777.

Clark, H., Arash Naghib-Lahouti, and P. Lavoie (July 2014). "General perspectives on model construction and evaluation for stochastic estimation, with application to a blunt trailing edge wake". In: *Experiments in Fluids* 55. DOI: 10.1007/s00348-014-1756-y.

Cossu, Carlo and Luca Brandt (2002). "Stabilization of TollmienSchlichting waves by finite amplitude optimal streaks in the Blasius boundary layer". In: *Physics of Fluids* 14.8, pp. L57–L60. DOI: 10.1063/1.1493791. URL: http://dx.doi.org/10.1063/1.1493791.

Couliou, M. and R. Monchaux (Dec. 2018). "Childhood of turbulent spots in a shear flow". In: *Phys. Rev. Fluids* 3 (12), p. 123901. DOI: 10.1103/PhysRevFluids.3.123901. URL: https://link.aps.org/doi/10.1103/PhysRevFluids.3.123901.

C.Pan et al. (2015). "Evaluating the accuracy performance of Lucas-Kanade algorithm in the circumstance of PIV application". In: *Sci China-Phys Mech Astron* 58. DOI: 10.1007/s11433-015-5719-y.

Cybenko, G. (Jan. 1989). "Approximation by superpositions of a sigmoidal function". In: *Mathematics of Control, Signals and Systems* 2.4, pp. 303–314.

Czarny, Olivier et al. (2003). "Interaction between Ekman pumping and the centrifugal instability in TaylorCouette flow". In: *Physics of Fluids* 15.2, pp. 467–477. DOI: 10.1063/1.1534108. eprint: https://doi.org/10.1063/1.1534108. URL: https://doi.org/10.1063/1.1534108.

Dahan, Jeremy A., A. S. Morgans, and S. Lardeau (2012a). "Feedback control for form-drag reduction on a bluff body with a blunt trailing edge". In: *Journal of Fluid Mechanics* 704, pp. 360–387. DOI: 10.1017/jfm.2012.246.

— (2012b). "Feedback control for form-drag reduction on a bluff body with a blunt trailing edge". In: *Journal of Fluid Mechanics* 704, pp. 360387. DOI: 10.1017/jfm.2012.246.

Darabi, A. and I. Wygnanski (2004). "Active management of naturally separated flow over a solid surface. Part 2. The separation process". In: *Journal of Fluid Mechanics* **510**, pp. 105–129.

Davoust, S., L. Jacquin, and B. Leclaire (2012). "Dynamics of m = 0 and m = 1 modes and of streamwise vortices in a turbulent axisymmetric mixing layer". In: *Journal of Fluid Mechanics* 709, pp. 408444. DOI: 10.1017/jfm.2012.342.

Debien, Antoine et al. (Feb. 2016). "Closed-loop separation control over a sharp edge ramp using genetic programming". In: *Experiments in Fluids* 57.3, p. 40. ISSN: 1432-1114. DOI: 10.1007/s00348-016-2126-8. URL: https://doi.org/10.1007/s00348-016-2126-8.

Dejoan, A. and M.A. Leschziner (2004). "Large eddy simulation of periodically perturbed separated flow over a backward-facing step". In: *International Journal of Heat and Fluid Flow* 25.4, pp. 581–592. ISSN: 0142-727X. DOI: https://doi.org/10.1016/j.ijheatfluidflow.2004.03.004. URL: https://www.sciencedirect.com/science/article/pii/S0142727X04000499.

DellOrso, Haley, Burak A. Tuna, and Michael Amitay (2016). "Measurement of Three-Dimensional Stall Cells on a Two-Dimensional NACA0015 Airfoil". In: *AIAA Journal* 54.12, pp. 3872–3883. DOI: 10.2514/1.J054848. eprint: https://doi.org/10.2514/1.J054848. URL: https://doi.org/10.2514/1.J054848.

Deng, Zhiwen et al. (2019). "Time-resolved turbulent velocity field reconstruction using a long short-term memory (LSTM)-based artificial intelligence framework". In: *Physics of*

Fluids 31.7, p. 075108. DOI: 10.1063/1.5111558. eprint: https://doi.org/10.1063/1.5111558. URL: https://doi.org/10.1063/1.5111558.

Dergham, G., D. Sipp, and J. C. Robinet (2013). "Stochastic dynamics and model reduction of amplifier flows: the backward facing step flow". In: *J. Fluid Mech.* 719, pp. 406–430.

Ding, Liuyang et al. (July 2013). "Multiple-pulse PIV: numerical evaluation and experimental validation". In:

Dosovitskiy, A. et al. (2015a). "FlowNet: Learning Optical Flow with Convolutional Networks". In: *2015 IEEE International Conference on Computer Vision (ICCV)*, pp. 2758–2766. DOI: 10.1109/ICCV.2015.316.

— (2015b). "FlowNet: Learning Optical Flow with Convolutional Networks". In: *2015 IEEE International Conference on Computer Vision (ICCV)*, pp. 2758–2766.

Duriez, Thomas, Jean-Luc Aider, and José Eduardo Wesfreid (Sept. 2009). "Self-Sustaining Process through Streak Generation in a Flat-Plate Boundary Layer". In: *Phys. Rev. Lett.* 103 (14), p. 144502. DOI: 10.1103/PhysRevLett.103.144502. URL: https://link.aps.org/doi/10.1103/PhysRevLett.103.144502.

Duriez, Thomas, Steven L Brunton, and Bernd R Noack. *Machine Learning Control-Taming Nonlinear Dynamics and Turbulence*. Springer.

Elsinga, G.E. et al. (Feb. 2004). "Assessment and Application of Quantitative Schlieren Methods: Calibrated Color Schlieren and Background Oriented Schlieren". In: *Experiments in Fluids* 36, pp. 309–325. DOI: 10.1007/s00348-003-0724-8.

Emmons, H. W. (1951). "The laminar-turbulent transition in a boundary layer." In: *J. Aerosp. Sci* 18, pp. 490–498.

Erichson, N. Benjamin et al. (2019). "Shallow Learning for Fluid Flow Reconstruction with Limited Sensors and Limited Data". In: *arXiv*.

EU-Council, European (2014). "European Council, European Council of 23 and 24 October 2014 conclusions". In:

Eulalie, Yoann et al. (Apr. 2018). "Active flow control analysis at the rear of an SUV". In: *International Journal of Numerical Methods for Heat '&' Fluid Flow* 28, pp. 00–00. DOI: 10.1108/HFF-06-2017-0230.

Faller, William E. and Scott J. Schreck (1996). "Neural Networks: Applications and Opportunities in Aeronautics". In: *Prog. Aerospace Sci.* 32, pp. 433–456. DOI: 0396-0421(95)00011-9.

Faure, Thierry et al. (Sept. 2009). "Three-dimensional centrifugal instabilities development inside a parallelepipedic open cavity of various shape". In: *Experiments in Fluids* 47, pp. 395–410. DOI: 10.1007/s00348-009-0671-0.

Favoreel, Wouter, Bart De Moor, and Peter Van Overschee (2000). "Subspace state space system identification for industrial processes". In: *Journal of Process Control* 10.2, pp. 149–155. ISSN: 0959-1524. DOI: https://doi.org/10.1016/S0959-1524(99)00030-X. URL: http://www.sciencedirect.com/science/article/pii/S095915249900030X.

Fifty years of jet in cross flow research (Nov. 1993).

Foucaut, Jean-Marc, Johan Carlier, and Michel Stanislas (2004). "PIV optimization for the study of turbulent flow using spectral analysis". In: *Measurement Science and Technology* 15.6, p. 1046.

Fransson, Jens H. M. et al. (2006). "Experimental study of the stabilization of Tollmien-Schlichting waves by finite amplitude streaks". In: *IUTAM Symposium on Laminar-Turbulent Transition*. Ed. by Rama Govindarajan. Dordrecht: Springer Netherlands, pp. 299–304. ISBN: 978-1-4020-4159-4. DOI: 10.1007/1-4020-4159-4_41.

Funahashi, Ken-Ichi (1989). "On the approximate realization of continuous mappings by neural networks". In: *Neural Networks* 2.3, pp. 183–192. DOI: 10.1016/0893-6080(89)90003-8.

Gallaire, François, Matthieu Marquillie, and Uwe Ehrenstein (2007). "Three-dimensional transverse instabilities in detached boundary layers". In: *Journal of Fluid Mechanics* 571, p. 221.

Gautier, N. and J.-L. Aider (2013). "Control of the separated flow downstream of a backward-facing step using visual feedback". In: *Proceedings of the Royal Society A: Mathematical, Physical and Engineering Sciences* 469.2160, p. 20130404. DOI: 10.1098/rspa.2013.0404.

— (2014). "Feed-forward control of a perturbed backward-facing step flow". In: *Journal of Fluid Mechanics* 759, pp. 181196. DOI: 10.1017/jfm.2014.518.

— (Jan. 2015a). "Frequency-lock reactive control of a separated flow enabled by visual sensors". In: *Experiments in Fluids* 56.1, p. 16. DOI: 10.1007/s00348-014-1869-3. URL: https://doi.org/10.1007/s00348-014-1869-3.

— (2015b). "Real-time planar flow velocity measurements using an optical flow algorithm implemented on GPU". In: *Journal of Visualization* 18.2, pp. 277–286. DOI: 10.1007/s12650-014-0222-5.

Gautier, N. et al. (2015). "Closed-loop separation control using machine learning". In: *J.Fluid.Mech* 770, pp. 442–457.

Gautier, Nicolas (2014). "Flow control using optical sensors". In: *Mechanics of the fluids*.

George, William K, Paul D Beuther, and Roger EA Arndt (1984). "Pressure spectra in turbulent free shear flows". In: *J. Fluid Mech* 148, pp. 155–191.

George, William K. and Michel Stanislas (2020). *On the noise in statistics of PIV measurements*. arXiv: 2010.10768 [physics.flu-dyn].

Giannopoulos, A. et al. (2021). "On the optimal window size in optical flow and cross-correlation in particle image velocimetry : Application to turbulent flows". In: *Exp. Fluids (Submitted)*.

Giannopoulos, Antonios and Jean-Luc Aider (2020a). "Data-driven order reduction and velocity field reconstruction using neural networks: The case of a turbulent boundary layer". In: *Physics of Fluids* 32.9, p. 095117. DOI: 10.1063/5.0015870. eprint: https://doi.org/10.1063/5.0015870. URL: https://doi.org/10.1063/5.0015870.

— (2020b). "Prediction of the dynamics of a backward-facing step flow using focused time-delay neural networks and particle image velocimetry data-sets". In: *International Journal of Heat and Fluid Flow* 82, p. 108533. ISSN: 0142-727X. DOI: https://doi.org/10.1016/j.ijheatfluidflow.2019.108533. URL: http://www.sciencedirect.com/science/article/pii/S0142727X19308665.

— (2020c). "Prediction of the dynamics of a backward-facing step flow using focused time-delay neural networks and particle image velocimetry data-sets". In: *International Journal of Heat and Fluid Flow* 82, p. 108533. ISSN: 0142-727X. DOI: https://doi.org/10.1016/j.ijheatfluidflow.2019.108533. URL: http://www.sciencedirect.com/science/article/pii/S0142727X19308665.

Godard, G., J.M. Foucaut, and M. Stanislas (2006). "Control of a decelerating boundary layer. Part 2: Optimization of slotted jets vortex generators". In: *Aerospace Science and Technology* 10.5, pp. 394–400. ISSN: 1270-9638. DOI: https://doi.org/10.1016/j.ast.2005.11.006. URL: https://www.sciencedirect.com/science/article/pii/S1270963805001628.

Godard, G. and M. Stanislas (2006). "Control of a decelerating boundary layer. Part 1: Optimization of passive vortex generators". In: *Aerospace Science and Technology* 10.3, pp. 181–191. ISSN: 1270-9638. DOI: https://doi.org/10.1016/j.ast.2005.11.007. URL: https://www.sciencedirect.com/science/article/pii/S127096380500163X.

Goodfellow, Ian, Yoshua Bengio, and Aaron Courville (2016). *Deep Learning*. http://www.deeplearningbook.org. MIT Press.

Grandemange, M et al. (Sept. 2014). "Characterization of the flow past real road vehicles with blunt afterbodies". In: *International Journal of Aerodynamics* 24.1/2, pp. 24–42. URL: https://hal-ensta.archives-ouvertes.fr/hal-01164775.

Guzmán, Iñigo Juan, Denis Sipp, and Peter J. Schmid (2014). "A dynamic observer to capture and control perturbation energy in noise amplifiers". In: *Journal of Fluid Mechanics* 758, pp. 728–753.

— (2016). "Recovery of the inherent dynamics of noise-driven amplifier flows". In: *Journal of Fluid Mechanics* 797, pp. 130–145.

Guzmán-Iñigo, Juan, Markus Sodar, and George Papadakis (Nov. 2019). "Data-based, reduced-order, dynamic estimator for reconstruction of nonlinear flows exhibiting limit-cycle oscillations". In: *Physical Review Fluids* 4. DOI: 10.1103/PhysRevFluids.4.114703.

Güemes Jiménez, Alejandro, Stefano Discetti, and Andrea Ianiro (Dec. 2019). "Sensing the turbulent large-scale motions with their wall signature". In: *Physics of Fluids* 31, p. 125112. DOI: 10.1063/1.5128053.

Hain, Rainer, Christian J Kähler, and Cam Tropea (2007). "Comparison of CCD, CMOS and intensified cameras". In: *Exp. Fluids* 42.3, pp. 403–411.

Harker, Matthew and Paul O'Leary (Aug. 2013). "Regularized Reconstruction of a Surface from its Measured Gradient Field". In: *Journal of Mathematical Imaging and Vision* 51. DOI: 10.1007/s10851-014-0505-4.

Heinz, Notger, Rudibert King, and Burkhard Gölling (Apr. 2010). "Robust Closed-Loop Lift Control on an Industry-Relevant Civil Aircraft Half Model". In: vol. 108, pp. 125–139. ISBN: 978-3-642-11734-3. DOI: 10.1007/978-3-642-11735-0_9.

Henning, Lars et al. (2007). "Feedback Control Applied to the Bluff Body Wake". In: *Active Flow Control: Papers contributed to the Conference "Active Flow Control 2006", Berlin, Germany, September 27 to 29, 2006*. Ed. by Rudibert King. Berlin, Heidelberg: Springer Berlin Heidelberg, pp. 369–390. DOI: 10.1007/978-3-540-71439-2_23.

Herbert, T, X Fan, and Joseph Haritonidis (Jan. 1996). "Laminar flow control with neural networks". In: 242, pp. 87–91.

Hochreiter, S. and J. Schmidhuber (1997). "Long short-term memory". In: *Neural Computation*, pp. 1735–1780.

Horn, Berthold and Brian Schunck (Aug. 1981). "Determining Optical Flow". In: *Artificial Intelligence* 17, pp. 185–203. DOI: 10.1016/0004-3702(81)90024-2.

Huang, Xiaorong et al. (May 2019). "Deeper Time Delay Neural Networks for Effective Acoustic Modelling". In: *Journal of Physics: Conference Series* 1229, p. 012076. DOI: 10.1088/1742-6596/1229/1/012076. URL: https://doi.org/10.1088%2F1742-6596%2F1229%2F1%2F012076.

Huerre, P. and P.A. Monkewitz (1990). "Local and Global Instabilities in Spatially Developing Flows". In: *Annual Review of Fluid Mechanics* 22.1, pp. 473–537. DOI: 10.1146/annurev.fl.22.010190.002353.

Hughes, J. D. and G. J. Walker (2000). "Natural Transition Phenomena on an Axial Compressor Blade". In: *Turbo Expo 2000: Power for Land, Sea, and Air. Volume 3: Heat Transfer; Electric Power; Industrial and Cogeneration. Munich, Germany, May 811, 2000*. ASME. DOI: 10.1115/2000-GT-0264.

Hung, L., M. Parviz, and K. John (1997). "Direct numerical simulation of turbulent flow over a backward-facing step". In: *J. Fluid Mech.* 330, pp. 349–374.

Illingworth, S.J, J. P. Monty, and I. Marusic (2018). "Estimating large-scale structures in wall turbulence using linear models". In: *Journal of Fluid Mechanics* 842, pp. 146–162.

Jensen, Atle and Geir K Pedersen (Oct. 2004). "Optimization of acceleration measurements using PIV". In: *Measurement Science and Technology* 15.11, pp. 2275–2283. DOI: 10.1088/0957-0233/15/11/013. URL: https://doi.org/10.1088/0957-0233/15/11/013.

Jin, Xiaowei et al. (2018). "Prediction model of velocity field around circular cylinder over various Reynolds numbers by fusion convolutional neural networks based on pressure on the cylinder". In: *Physics of Fluids* 30.4, p. 047105. DOI: 10.1063/1.5024595. URL: https://doi.org/10.1063/1.5024595.

J.Rabault et al. (2018). "Artificial Neural Networks trained through Deep Reinforcement Learning discover control strategies for active flow control". In: *physics.flu-dyn*. DOI: arXiv:1808.07664v5.

Juillet, Fabien, BJ McKeon, and Peter J Schmid (2014). "Experimental control of natural perturbations in channel flow". In: *Journal of Fluid Mechanics* 752, pp. 296–309.

Juillet, Fabien, Peter J. Schmid, and Patrick Huerre (2013). "Control of amplifier flows using subspace identification techniques". In: *Journal of Fluid Mechanics* 725, pp. 522565. DOI: 10.1017/jfm.2013.194.

Kachanov, Y. S. (1994). "Physical Mechanisms of Laminar-Boundary-Layer Transition". In: *Annual Review of Fluid Mechanics* 26.1, pp. 411–482. DOI: 10.1146/annurev.fl.26.010194.002211. URL: https://doi.org/10.1146/annurev.fl.26.010194.002211.

Kähler, Christian J, Sven Scharnowski, and Christian Cierpka (2012). "On the resolution limit of digital particle image velocimetry". In: *Experiments in fluids* 52.6, pp. 1629–1639.

Kaiktsis, Lambros, George Em Karniadakis, and Steven A. Orszag (1991). "Onset of three-dimensionality, equilibria, and early transition in flow over a backward-facing step". In: *Journal of Fluid Mechanics* 231, pp. 501528. DOI: 10.1017/S0022112091003488.

Karagozian, A.R. (2010). "Transverse jets and their control". In: *Prog. Energy Combust. Sci.* 36, pp. 531–553.

Kindere, J. W. Van der et al. (2019). "Pressure from 2D snapshot PIV". In: *Experiments in Fluids* 60.

Kitzhofer, Jens et al. (Sept. 2009). "Volumetric Measurement of the Transitional Backward Facing Step Flow". In:

Klebanoff, P. S., K. D. Tidstrom, and L. M. Sargent (1962a). "The three-dimensional nature of boundary-layer instability". In: *Journal of Fluid Mechanics* 12.1, pp. 134. DOI: 10.1017/S0022112062000014.

— (1962b). "The three-dimensional nature of boundary-layer instability". In: *Journal of Fluid Mechanics* 12.1, pp. 134. DOI: 10.1017/S0022112062000014.

Klotz, L., A.M. Pavlenko, and J.E. Wesfreid (2021). "Experimental measurements in plane CouettePoiseuille flow: dynamics of the large- and small-scale flow". In: *Journal of Fluid Mechanics* 912, A24. DOI: 10.1017/jfm.2020.1089.

Koengeter, J. (1999). "PIV with high temporal resolution for the determination of local pressure reductions from coherent turbulence phenomena". In: *Experiments in Fluids* 29.

Kurtulus, Dilek, Fulvio Scarano, and Laurent David (Feb. 2007). "Unsteady aerodynamic forces estimation on a square cylinder by TR-PIV". In: *Experiments in Fluids* 42, pp. 185196. DOI: 10.1007/s00348-006-0228-4.

Kähler, Christian J. et al. (2016). "Main results of the fourth international PIV Challenge". In: *Experiments in Fluids* 57.

Lanzerstorfer, Daniel and Hendrik C. Kuhlmann (2012). "Global stability of the two-dimensional flow over a backward-facing step". In: *Journal of Fluid Mechanics* 693, pp. 127. DOI: 10.1017/jfm.2011.399.

LaVision (2021). *DAVIS 10 software solution for digital imaging*. URL: https://www.lavision.de/en/products/davis-software/.

Le Besnerais, Guy and Frederic Champagnat (Oct. 2005). "Dense optical flow by iterative local window registration". In: vol. 1, pp. I –137. ISBN: 0-7803-9134-9. DOI: 10.1109/ICIP.2005.1529706.

Lee, Changhoon et al. (1997). "Application of neural networks to turbulence control for drag reduction". In: *Phys. Fluids* 9, pp. 1740–1747. DOI: 1070-6631.

Lee, Cunbiao () and Xianyang () Jiang (2019). "Flow structures in transitional and turbulent boundary layers". In: *Physics of Fluids* 31.11, p. 111301. DOI: 10.1063/1.5121810. URL: https://doi.org/10.1063/1.5121810.

Lemoult, Grégoire et al. (Nov. 2013). "Turbulent spots in channel flow: An experimental study: Large-scale flow, inner structure and low-order model". In: *The European Physical Journal E*. DOI: 10.1140/epje/i2014-14025-2.

Lemoult, Grégoire et al. (Apr. 2014). "Turbulent spots in channel flow: an experimental study: large-scale flow, inner structure and low-order model". In: *The European physical journal. E, Soft matter* 37.4, p. 25. ISSN: 1292-8941. DOI: 10.1140/epje/i2014-14025-2.

Leontaritis, I. J. and S. A. Billings (1985). "Input-output parametric models for non-linear systems Part I: deterministic non-linear systems". In: *International Journal of Control* 41.2, pp. 303–328. DOI: 10.1080/0020718508961129.

Li, Ruiying et al. (Sept. 2016). "Feedback control of bimodal wake dynamics". In: *Experiments in Fluids* 57.10, p. 158. DOI: 10.1007/s00348-016-2245-2.

Li, Ruiying et al. (July 2017). "Drag reduction of a car model by linear genetic programming control". In: *Experiments in Fluids* 58.8, p. 103. ISSN: 1432-1114. DOI: 10.1007/s00348-017-2382-2.

Li, Tao et al. (2019). "Hybrid-delay-dependent approach to synchronization in distributed delay neutral neural networks". In: *Applied Mathematics and Computation* 347, pp. 449 – 463. ISSN: 0096-3003. DOI: https://doi.org/10.1016/j.amc.2018.11.019. URL: http://www.sciencedirect.com/science/article/pii/S0096300318309925.

Lindgren, E. Rune (1969). "Propagation Velocity of Turbulent Slugs and Streaks in Transition Pipe Flow". In: *The Physics of Fluids* 12.2, pp. 418–425. DOI: 10.1063/1.1692497. eprint: https://aip.scitation.org/doi/pdf/10.1063/1.1692497. URL: https://aip.scitation.org/doi/abs/10.1063/1.1692497.

Liu, Bo et al. (2020a). "Deep learning methods for super-resolution reconstruction of turbulent flows". In: *Physics of Fluids* 32.2, p. 025105. DOI: 10.1063/1.5140772. eprint: https://doi.org/10.1063/1.5140772. URL: https://doi.org/10.1063/1.5140772.

Liu, Tianshu et al. (2015a). "Comparison between optical flow and cross-correlation methods for extraction of velocity fields from particle images". In: *Experiments in Fluids* 56. DOI: https://doi.org/10.1007/s00348-015-2036-1.

Liu, Tianshu et al. (Aug. 2015b). "Comparison between optical flow and crosscorrelation methods for extraction of velocity fields from particle images". In: *Experiments in Fluids* 56, p. 166. DOI: 10.1007/s00348-015-2036-1.

Liu, Tianshu et al. (Feb. 2020b). "Hybrid Optical-Flow-Cross-Correlation Method for Particle Image Velocimetry". In: *Journal of Fluids Engineering* 142.5. 054501. DOI: 10.1115/1.4045572. eprint: https://asmedigitalcollection.asme.org/fluidsengineering/article-pdf/142/5/054501/6518386/fe_142_05_054501.pdf. URL: https://doi.org/10.1115/1.4045572.

Loiseau, Jean-Christophe, Bernd R. Noack, and Steven L. Brunton (2018). "Sparse reduced-order modelling: sensor-based dynamics to full-state estimation". In: *Journal of Fluid Mechanics* 844, pp. 459490. DOI: 10.1017/jfm.2018.147.

Lourenco, L (2000). "TRUE resolution PIV: a mesh-free second order accurate algorithm". In: *10th Int. Symp. on Applications of Laser Techniques in Fluid Mechanics (Lisbon), 2000*.

Lumley, J. L. (1967). "The Structure of Inhomogeneous Turbulent Flows". In: *Atmospheric turbulence and radio propagation*. Ed. by A. M. Yaglom and V. I. Tatarski. Moscow: Nauka, pp. 166–178.

Lundbladh, Anders and Arne V. Johansson (1991). "Direct simulation of turbulent spots in plane Couette flow". In: *Journal of Fluid Mechanics* 229, pp. 499516. DOI: 10.1017/S0022112091003130.

Marquillie, Matthieu and UWE Ehrenstein (2003). "On the onset of nonlinear oscillations in a separating boundary-layer flow". In: *Journal of Fluid Mechanics* 490, p. 169.

Marquillie, Matthieu, Uwe Ehrenstein, Jean-Philippe Laval, et al. (2011). "Instability of streaks in wall turbulence with adverse pressure gradient". In: *Journal of Fluid Mechanics* 681.205-240, p. 30.

Martin, Juan A. et al. (2015). "Numerical Studies of Non-linear Intrinsic Streaks in the Flat Plate Boundary Layer". In: *Procedia IUTAM* 14. IUTAM ABCM Symposium on Laminar Turbulent Transition, pp. 479 –486. ISSN: 2210-9838. DOI: 10.1016/j.piutam.2015.03.076. URL: http://www.sciencedirect.com/science/article/pii/S2210983815001029.

Matsubara, M. and P. H. Alfredsson (2001). "Disturbance growth in boundary layers subjected to free-stream turbulence". In: *Journal of Fluid Mechanics* 430, pp. 149168. DOI: 10.1017/S0022112000002810.

Maulik, R. et al. (2018). "Data-driven deconvolution for large eddy simulations of Kraichnan turbulence". In: *Physics of Fluids* 30.12, p. 125109. DOI: 10.1063/1.5079582. eprint: https://doi.org/10.1063/1.5079582. URL: https://doi.org/10.1063/1.5079582.

Mazellier, Nicolas, Luminita Danaila, and Bruno Renou (2010). "Multi-scale energy injection: a new tool to generate intense homogeneous and isotropic turbulence for premixed combustion". In: *J. Turb.* 11, N43.

McKeon, B. J. and A. S. Sharma (2010). "A critical-layer framework for turbulent pipe flow". In: *Journal of Fluid Mechanics* 658, pp. 336–382.

Mendes, Luís, Alexandre Bernardino, and Rui M.L. Ferreira (2020). "piv-image-generator: An image generating software package for planar PIV and Optical Flow benchmarking". In: *SoftwareX* 12, p. 100537. ISSN: 2352-7110. DOI: https://doi.org/10.1016/j.softx.2020.100537. URL: https://www.sciencedirect.com/science/article/pii/S2352711020300339.

Mendez, M.A. et al. (2017). "POD-based background removal for particle image velocimetry". In: *Experimental Thermal and Fluid Science* 80, pp. 181 –192. ISSN: 0894-1777.

Meunier, P. and T. Leweke (2003a). "Analysis and treatment of errors due to high velocity gradients in particle image velocimetry". In: *Exp. Fluids* 35.5, pp. 408–421.

— (2003b). "Analysis and treatment of errors due to high velocity gradients in particle image velocimetry". In: *Experiments in Fluids* 35.5, pp. 408–421.

Mi, Y., M. Ishii, and L.H. Tsoukalas (1998). "Vertical two-phase flow identification using advanced instrumentation and neural networks". In: *Nuclear Engineering and Design* 184, pp. 409–420.

Morkovin, M. V. (1985). "Bypass transition to turbulence and research desiderata". In: *Transition in Turbines*, pp. 161–204.

Müller, S., M. Milano, and P. Koumoutsakos (1999). "Application of machine learning algorithms to flow modeling and optimization". In: *Annual Research Briefs*, pp. 169–178.

Narendra, K. S. and K. Parthasarathy (Mar. 1990). "Identification and control of dynamical systems using neural networks". In: *IEEE Transactions on Neural Networks* 1.1, pp. 4–27. ISSN: 1045-9227. DOI: 10.1109/72.80202.

Nathan Kutz, J (Mar. 2017). "Deep learning in fluid dynamics". In: *Journal of Fluid Mechanics* 814, pp. 1–4. DOI: 10.1017/jfm.2016.803.

Nichols, Robert (Sept. 2010). *Turbulence Models and Their Application to Complex Flows*.

Olekan, Ogunmolu et al. (2016). "Nonlinear Systems Identification Using Deep Dynamic Neural Networks". In: *CS*.

Olsen, MG and RJ Adrian (2000). "Out-of-focus effects on particle image visibility and correlation in microscopic particle image velocimetry". In: *Experiments in fluids* 29.1, S166–S174.

Ottonelli, Claudio (2014). "Apprentissage statistique de modèles réduits non-linéaires par approche expérimentale et design de contrôleurs robustes: le cas de la cavité ouverte". PhD thesis. Ecole Polytechnique X, France.

Oudheusden, B W van (Jan. 2013). "PIV-based pressure measurement". In: *Measurement Science and Technology* 24.3, p. 032001. DOI: 10.1088/0957-0233/24/3/032001. URL: https://doi.org/10.1088/0957-0233/24/3/032001.

Pan, Shaowu and Karthik Duraisamy (Dec. 2018). "Long-Time Predictive Modeling of Nonlinear Dynamical Systems Using Neural Networks". In: *Complexity* 2018, pp. 1–26. DOI: 10.1155/2018/4801012.

Pando, Miguel Fosas de, Peter J. Schmid, and Denis Sipp (2015). "Nonlinear Model-order Reduction for Oscillator Flows Using POD-DEIM". In: *Procedia IUTAM* 14, pp. 329 –336. ISSN: 2210-9838. DOI: https://doi.org/10.1016/j.piutam.2015.03.056.

Parliament, European and council of the EU (2013). "DECISION No 1386/2013/EU OF THE EUROPEAN PARLIAMENT AND OF THE COUNCIL of 20 November 2013 on a General Union Environment Action Programme to 2020 "Living well, within the limits of our planet """. In: *Official Journal of the European Union*.

— (2020). "Long-term low greenhouse gas emission development strategy of the EU and its Member States". In: *Official Journal of the European Union*.

Paschereit, Christian, Effie Gutmark, and Wolfgang Weisenstein (June 2000). "Excitation of Thermoacoustic Instabilities by Interaction of Acoustics and Unstable Swirling Flow". In: *Aiaa Journal - AIAA J* 38, pp. 1025–1034. DOI: 10.2514/2.1063.

Passaggia, Pierre-Yves and Uwe Ehrenstein (2018). "Optimal control of a separated boundary-layer flow over a bump". In: *arXiv preprint arXiv:1801.05890*.

Passaggia, Pierre-Yves, Thomas Leweke, and Uwe Ehrenstein (2012a). "Transverse instability and low-frequency flapping in incompressible separated boundary layer flows: an experimental study". In: *Journal of fluid mechanics* 703, p. 363.

— (2012b). "Transverse instability and low-frequency flapping in incompressible separated boundary layer flows: an experimental study". In: *Journal of Fluid Mechanics* 703, pp. 363373. DOI: 10.1017/jfm.2012.225.

Passaggia, Pierre-Yves et al. (2020). "Estimating pressure and internal-wave flux from laboratory experiments in focusing internal waves". In: *Experiments in Fluids* 61.11, pp. 1–29.

Pawar, S. et al. (2019). "A deep learning enabler for nonintrusive reduced order modeling of fluid flows". In: *Physics of Fluids* 31.8, p. 085101. DOI: 10.1063/1.5113494. eprint: https://doi.org/10.1063/1.5113494. URL: https://doi.org/10.1063/1.5113494.

PhotonLines (2021). *Eyemotion Imaging Software*. URL: http://seefastechnologies.com/software-components/eyemotion.

Picella, F. et al. (2018). "Successive bifurcations in a fully three-dimensional open cavity flow". In: *Journal of Fluid Mechanics* 844, pp. 855877. DOI: 10.1017/jfm.2018.169.

pytorch (2021). *An open source machine learning framework that accelerates the path from research prototyping to production deployment*. URL: https://pytorch.org/.

Qin, S.J. (2006). "An overview of subspace identification". In: *Comp. & Chem. Eng.* 30.10, pp. 1502–1513.

Quénot, Georges, Jaroslaw Pakleza, and Tomasz Kowalewski (1998). "Particle Image Velocimetry with Optical Flow". In: *Experiments in Fluids* 25.3, pp. 177–189. DOI: 10.1007/s003480050222. URL: https://hal.archives-ouvertes.fr/hal-00953823.

Rabault, Jean, Jostein Kolaas, and Atle Jensen (Nov. 2017a). "Performing particle image velocimetry using artificial neural networks: a proof-of-concept". In: *Measurement Science and Technology* 28.12, p. 125301. DOI: 10.1088/1361-6501/aa8b87. URL: https://doi.org/10.1088%2F1361-6501%2Faa8b87.

— (Nov. 2017b). "Performing particle image velocimetry using artificial neural networks: a proof-of-concept". In: *Measurement Science and Technology* 28.12, p. 125301. DOI: 10.1088/1361-6501/aa8b87. URL: https://doi.org/10.1088%2F1361-6501%2Faa8b87.

Rabault, Jean and Alexander Kuhnle (2019). "Accelerating deep reinforcement learning strategies of flow control through a multi-environment approach". In: *Physics of Fluids* 31.9, p. 094105. DOI: 10.1063/1.5116415. eprint: https://doi.org/10.1063/1.5116415. URL: https://doi.org/10.1063/1.5116415.

Raffel, M., Christian Willert, and Juergen Kompenhans (Jan. 1998). *Particle Image Velocimetry: A Practical Guide*. ISBN: 3-540-63683-3. DOI: 10.1007/978-3-662-03637-2.

Rapaka, Narsimha R., Bishakhdatta Gayen, and Sutanu Sarkar (2013). "Tidal conversion and turbulence at a model ridge: direct and large eddy simulations". In: *Journal of Fluid Mechanics* 715, pp. 181209. DOI: 10.1017/jfm.2012.513.

Reynold Chu, S., R. Shoureshi, and M. Tenorio (1990). "Neural Networks for System Identification". In: *IEEE Control Systems Magazine* 10.3, pp. 31–35.

Rodriguez, D. and V. Theofilis (2010). "Structural changes of laminar separation bubbles induced by global linear instability". In: *Journal of Fluid Mechanics* 655, pp. 280305. DOI: 10.1017/S0022112010000856.

Ruhnau, P. et al. (Jan. 2005). "Variational optical flow estimation for particle image velocimetry". In: *Exp. Fluids* 38, pp. 21–32. DOI: 10.1007/s00348-004-0880-5.

Sadeghioon, Ali et al. (Aug. 2014). "Design and Development of a Nonintrusive Pressure Measurement System for Pipeline Monitoring". In: *Journal of Pipeline Systems Engineering and Practice* 5, p. 04014001. DOI: 10.1061/(ASCE)PS.1949-1204.0000169.

San, Omer, Romit Maulik, and Mansoor Ahmed (2018). "An artificial neural network framework for reduced order modeling of transient flows". In: *Communications in Nonlinear Science and Numerical Simulation* 77. DOI: 10.1016/j.cnsns.2019.04.025.

Saric, W S (1994). "Görtler Vortices". In: *Annual Review of Fluid Mechanics* 26.1, pp. 379–409. DOI: 10.1146/annurev.fl.26.010194.002115. eprint: https://doi.org/10.1146/annurev.fl.26.010194.002115. URL: https://doi.org/10.1146/annurev.fl.26.010194.002115.

Sartor, Fulvio, Gilles Losfeld, and Reynald Bur (Sept. 2012). "PIV study on a shock-induced separation in a transonic flow". In: *Experiments in Fluids* 53, pp. 815–827.

Scarano, Fulvio and M.L. Riethmuller (Apr. 2012). "Advances in iterative multigrid PIV image processing". In: *Experiments in Fluids* 29, S051–S060. DOI: 10.1007/s003480070007.

Schlatter, Philipp et al. (2008). "On streak breakdown in bypass transition". In: *Physics of Fluids* 20.10, p. 101505. DOI: 10.1063/1.3005836. URL: http://dx.doi.org/10.1063/1.3005836.

Schmid, Peter (2010). "Dynamic mode decomposition of numerical and experimental data". In: *Journal of Fluid Mechanics* 656, pp. 5–28.

Schmidt, B. E. and J. A. Sutton (2019). "High-resolution velocimetry from tracer particle fields using a wavelet-based optical flow method". In: *Exp. Fluids* 60.3, p. 37.

Schmidt, Bryan and J. Sutton (Jan. 2020). "Improvements in the accuracy of wavelet-based optical flow velocimetry (wOFV) using an efficient and physically based implementation of velocity regularisation". In: *Exp. Fluids* 61. DOI: 10.1007/s00348-019-2869-0.

Seong, jee hyun et al. (Oct. 2019). "Velocity refinement of PIV using global optical flow". In: *Exp. Fluids* 60. DOI: 10.1007/s00348-019-2820-4.

Shanmughan, Roshan et al. (2020). "Optimal pressure reconstruction based on planar particle image velocimetry and sparse sensor measurements". In: *Exp. Fluids* 61.11, pp. 1–19.

Shi, Kaibo et al. (2018). "Reliable asynchronous sampled-data filtering of TS fuzzy uncertain delayed neural networks with stochastic switched topologies". In: *Fuzzy Sets and Systems*. ISSN: 0165-0114. DOI: https://doi.org/10.1016/j.fss.2018.11.017. URL: http://www.sciencedirect.com/science/article/pii/S0165011418309436.

Simpson, Roger L. (1996). "Aspects of turbulent boundary-layer separation". In: *Progress in Aerospace Sciences* 32.5, pp. 457 –521. ISSN: 0376-0421. DOI: https://doi.org/10.1016/0376-0421(95)00012-7. URL: http://www.sciencedirect.com/science/article/pii/0376042195000127.

Sirovich, Laurence (1987). "Turbulence and the dynamics of coherent structures". In: *Quarterly of Applied Mathematics* 45, pp. 561–571.

Spazzini, P. G. et al. (2001). "Unsteady behaviour of back-facing step flow". In: *Experiments in Fluids* 30, pp. 551–561.

Srinivasan, P. A. et al. (May 2019). "Predictions of turbulent shear flows using deep neural networks". In: *Phys. Rev. Fluids* 4 (5), p. 054603. DOI: 10.1103/PhysRevFluids.4.054603. URL: https://link.aps.org/doi/10.1103/PhysRevFluids.4.054603.

Stanislas, M, K Okamoto, and C K hler (July 2003). "Main results of the First International PIV Challenge". In: *Measurement Science and Technology* 14.10, R63–R89. DOI: 10.1088/0957-0233/14/10/201. URL: https://doi.org/10.1088%2F0957-0233%2F14%2F10%2F201.

Stanislas, M, K Okamoto, and C Kahler (Sept. 2003). "Main results of theFirst International PIV Challenge". In: *Measurement Science and Technology* 14.10, R63–R89. DOI: 10.1088/0957-0233/14/10/201. URL: https://doi.org/10.1088%2F0957-0233%2F14%2F10%2F201.

Stanislas, M. et al. (2005). "Main results of the Second International PIV Challenge". In: *Experiments in Fluids* 39, pp. 170–191.

Stanislas, M. et al. (2008). "Main results of the third international PIV Challenge". In: *Experiments in Fluids* 45, pp. 27–71.

Stengel, Robert F. (1994). "Optimal Control and Estimation". In: Dover Publication Inc., New York.

Stoica, Petre and Randolph Moses (Jan. 2005). "Spectral Analysis of Signals". In: *Prentice Hall*.

Thielicke, William and Eize J. Stamhuis (Oct. 2014). "PIVlab – Towards User-friendly, Affordable and Accurate Digital Particle Image Velocimetry in MATLAB". In: *Journal of Open Research Software* 2.

Thomareis, N. and G. Papadakis (July 2018). "Resolvent analysis of separated and attached flows around an airfoil at transitional Reynolds number". In: *Phys. Rev. Fluids* 3 (7), p. 073901. DOI: 10.1103/PhysRevFluids.3.073901. URL: https://link.aps.org/doi/10.1103/PhysRevFluids.3.073901.

Tihon, Jaroslav, Jack Legrand, and P. Legentilhomme (Nov. 2001). "Near-wall investigation of backward-facing step flows". In: *Experiments in Fluids* 31, pp. 484–493. DOI: 10.1007/s003480100300.

Tompson, Jonathan et al. (July 2016). "Accelerating Eulerian Fluid Simulation With Convolutional Networks". In: *Proceedings of the 34th International Conference on Machine Learning*.

Tracey, Brendan D., Karthikeyan Duraisamy, and Juan J. Alonso (2017). "A Machine Learning Strategy to Assist Turbulence Model Development". In: *53rd AIAA Aerospace Sciences Meeting*. DOI: 10.2514/6.2015-1287.

Tsuji, Yoshiyuki and Yukio Kaneda (2012). "Anisotropic pressure correlation spectra in turbulent shear flow". In: *Journal of fluid mechanics* 694, p. 50.

Tylli, Niclas, Lambros Kaiktsis, and Beat Ineichen (2002). "Sidewall effects in flow over a backward-facing step: Experiments and numerical simulations". In: *Physics of Fluids* 14.11, pp. 3835–3845. DOI: 10.1063/1.1506163. eprint: https://doi.org/10.1063/1.1506163. URL: https://doi.org/10.1063/1.1506163.

Van Overschee, P. and B. De Moor (1994). "Subspace algorithms for the identification of combined deterministic-stochastic systems". In: *Automatica* 30.1, pp. 75–93.

— (1995). "A unifying theorem for three subspace system identification algorithms". In: *Automatica* 31.12, pp. 1853–1864.

Varon, E. et al. (2015). "Experimental application of a Dynamic Observer to capture and predict the dynamics of a flat-plate boundary layer". In: *Proc. of the 15th European Turbulence Conference (ETC15)*. Delft, The Netherlands.

Varon, Eliott et al. (Mar. 2017). "Chaotic dynamics of large-scale structures in a turbulent wake". In: *Phys. Rev. Fluids* 2 (3), p. 034604. DOI: 10.1103/PhysRevFluids.2.034604.

Varon, Eliott et al. (2019). "Adaptive control of the dynamics of a fully turbulent bimodal wake using real-time PIV". In: *Experiments in Fluids* 60.8, p. 124.

Vig, DhruvăK., AlexăE. Hamby, and CharlesăW. Wolgemuth (2016). "On the Quantification of Cellular Velocity Fields". In: *Biophysical Journal* 110.7, pp. 1469 –1475. ISSN: 0006-3495. DOI: https://doi.org/10.1016/j.bpj.2016.02.032. URL: http://www.sciencedirect.com/science/article/pii/S0006349516300339.

Vlachas, Pantelis et al. (Feb. 2018). "Data-Driven Forecasting of High-Dimensional Chaotic Systems with Long-Short Term Memory Networks". In: *Proceedings of the Royal Society A: Mathematical, Physical and Engineering Science* 474. DOI: 10.1098/rspa.2017.0844.

Waibel, A. et al. (1989). "Phoneme recognition using time-delay neural networks". In: *IEEE Transactions on Acoustics, Speech, and Signal Processing* 37.3, pp. 328–339. ISSN: 0096-3518. DOI: 10.1109/29.21701.

Wang, Fang fang, Shi qiang Wu, and Sen lin Zhu (2019). "Numerical simulation of flow separation over a backward-facing step with high Reynolds number". In: *Water Science and Engineering* 12.2, pp. 145 –154. ISSN: 1674-2370. DOI: https://doi.org/10.1016/j.wse.2019.05.003.

Wang, Hongping, Guowei He, and Shizhao Wang (Oct. 2020). "Globally optimized cross-correlation for particle image velocimetry". In: *Exp. Fluids* 61. DOI: https://doi.org/10.1007/s00348-020-03062-x.

Wang, Z. et al. (2018). "Model identification of reduced order fluid dynamics systems using deep learning". In: *Int J Numer Meth Fluids* 86, pp. 255–268. DOI: 10.1002/fld.4416.

Westerweel, Jerry (Jan. 1993). "Digital Particle Image Velocimetry - Theory and Application". In:

Westerweel, Jerry, Gerrit E Elsinga, and Ronald J Adrian (2013). "Particle image velocimetry for complex and turbulent flows". In: *Annual Review of Fluid Mechanics* 45, pp. 409–436.

Williams, P. T. and A. J. Baker. "Numerical simulations of laminar flow over a 3D backward-facing step". In: *International Journal for Numerical Methods in Fluids* 24.11 (), pp. 1159–1183. DOI: 10.1002/(SICI)1097-0363(19970615)24:11<1159::AID-FLD534>3.0.CO;2-R.

Xie, Chenyue et al. (2019). "Artificial neural network mixed model for large eddy simulation of compressible isotropic turbulence". In: *Physics of Fluids* 31.8, p. 085112. DOI: 10.

1063/1.5110788. eprint: https://doi.org/10.1063/1.5110788. URL: https://doi.org/10.1063/1.5110788.

Yu, Hui-Jun, Yong He, and Min Wu (2018). "Delay-dependent state estimation for neural networks with time-varying delay". In: *Neurocomputing* 275, pp. 881 –887. ISSN: 0925-2312. DOI: https://doi.org/10.1016/j.neucom.2017.09.029. URL: http://www.sciencedirect.com/science/article/pii/S0925231217315448.

Zhou, J. et al. (1999). "Mechanisms for generating coherent packets of hairpin vortices". In: *J Fluid Mech* 387, pp. 535–396.

Zhu, Linyang et al. (2019). "Machine learning methods for turbulence modeling in subsonic flows around airfoils". In: *Physics of Fluids* 31.1, p. 015105. DOI: 10.1063/1.5061693. URL: https://doi.org/10.1063/1.5061693.